Parametric controls for modular quantum computing and quantum devices

by

Pinlei Lu

Bachelor of Science, Wuhan University, 2015

Master of Science, University of Pittsburgh, 2017

Submitted to the Graduate Faculty of

the Dietrich School of Arts & Sciences in partial fulfillment

of the requirements for the degree of

Doctor of Philosophy

University of Pittsburgh

2022

UNIVERSITY OF PITTSBURGH

DIETRICH SCHOOL OF ARTS AND SCIENCES

This dissertation was presented

by

Pinlei Lu

It was defended on

April 15th 2022

and approved by

Prof. Michael Hatridge, Department of Physics and Astronomy

Prof. Gurudev Dutt, Department of Physics and Astronomy

Prof. Roger Mong, Department of Physics and Astronomy

Prof. Brian Batell , Department of Physics and Astronomy

Prof. Susan Fullerton, Department of Chemical and Petroleum Engineering

Parametric controls for modular quantum computing and quantum devices

Pinlei Lu, PhD

University of Pittsburgh, 2022

In superconducting quantum information, qubits are made from low-loss superconducting capacitors, inductors, and transmission lines in combination with nonlinear Josephson elements. In superconducting circuits, the Hamiltonian of the system is very flexible, allowing us to build very nonlinear circuits, like qubits, or very linear circuits, like parametric amplifiers, or anything in between, simply by changing the size of the Josephson junctions we use. The challenge is both to explore which circuits are feasible to realize in the laboratory and embody just the right Hamiltonian to result in a desired quantum behavior. On the other hand, parametric controls, as an approach acts on the Hamiltonian parameter, provides even more potential of realizing different quantum devices for various scenario.

This dissertation begins with a discussion of the theory and simulation of quantum superconducting circuits, including circuit quantum electrodynamics and electromagnetic simulation. It next covers the nano-fabrication techniques I used during my PhD. It also contains a review of microwave measurement techniques for quantum circuits.

The thesis next details the experimental realization of a simple, two-mode, quantum-limited, Josephson junction based frequency comb, including both the theoretical analysis on the instability of the circuits and the experiments on frequency and time domain.

More, we have extended the Hamiltonian engineering techniques to realize a parametrically driven, modular architecture for coupling superconducting qubits. We have realized a 'tree' of microwave modes, which can mediate long-range interactions between individual bits by a series of parametric interactions. This architecture, in contrast to the current reliance on the field nearest-neighbor interaction, realizes a far denser of network of interaction between qubits, and thus makes the challenge of achieving large-scale quantum machines less daunting.

In the end, my research has shown that devices that are thought of as very different (qubits and amplifiers) can be built and controlled very similarly. In ongoing work detailed

in the final sections of this thesis, we have used our growing command of parametric control and Hamiltonian engineering to extend the idea of many-to-many connections among modes via a central SNAIL to realize a 4 transmon 'quantum module'.

Table of Contents

List of Tables

List of Figures

List of Symbols

Constants

e	Electric charge constant	$\equiv 1.602\ 176\ 634 \times 10^{-19}\,\mathrm{C}$
k_b	Boltzmann constant	$\equiv 1.380\ 649 \times 10^{-23}\,\mathrm{J \cdot K^{-1}}$
$\hbar$	Reduced Planck constant	$\approx 1.054\ 571\ 817 \times 10^{-34}\,\mathrm{J \cdot s}$
		$\approx 6.582\ 119\ 569 \times 10^{-16}\,\mathrm{eV \cdot s}$
Φ_0	Magnetic flux quantum	$\approx 2.067\ 833\ 848 \times 10^{-14}\,\mathrm{Wb}$
ϕ_0	Reduced flux quantum	$\equiv \frac{\Phi_0}{2\pi} \approx 3.291\ 059\ 784 \times 10^{-14}\,\mathrm{Wb}$

Chapter 2

ω_r	Resonance frequency
Z_r	Characteristic impedance
L	Oscillator's inductance
C	Oscillator's capacitance
Q	Charge on the capacitor
$\hat{Q}$	Quantized charge
Φ	Flux threading inductor
$\hat{\Phi}$	Quantized flux
$\hat{a}$	Annihilation operator
I_c	Junction's critical current
κ	Cavity bandwidth
E_J	Josephson energy
E_C	Charging energy
ω_q	Qubit frequency
C_S	Shunt capacitance
C_J	Junction's capacitance
$\hat{n}$	Charge number operation

Q_g	offset charge
α	Qubit anharmonicity
χ	Qubit-cavity dispersive shift
Q_{int}	Internal quality factor
Q_{ext}	External quality factor
Γ	Reflection coefficient
V^+	Signal propagating from left to right
V^-	Signal propagating from right to left
$\mathcal{F}$	Fourier transform
P_{dis}	Dissipation power
$\vec{J}_s$	Surface current
G	Conductance
W	Waves In Space Purcell Effect (WISPE) factor

Chapter 3

W	JJs' overlay width
L	Dolan bridge width
θ	Double angle deposition's angle
d_1	Thickness of MMA resist
d_2	Thickness of PMMA resist
A	Area of JJs
J_c	Current density of Josephson junction
I_c	Critical current of Josephson junction
φ_0	Reduced flux quantum
Δ	Superconducting energy gap
R_N	Josephson junction normal state resistance

R_J	Josephson junction room temperature resistance
L_J	Josephson junction inductance

Chapter 4

ω_c	Cavity frequency
ω_q	Qubit frequency
α	Qubit anharmonicity
g	Qubit-cavity coupling strength
κ	Cavity decay rate
χ	Qubit-cavity dispersive shift
T_m	Cavity measrument length
ψ	Ket state
φ_i	Accumulated real phase
ϕ_i	Accumulated virtual phase

Acknowledgments

This work was only possible through the effort and conscious guidance of many people and the years of prior researches upon which the included work was built.

The first person I want to appreciate is my advisor, Prof. Michael Hatridge. There are too many things I could list about his enthusiasm on physics, willingness to education, and everyday kindness. But the most valuable thing is that he opens the door of quantum computation for me. I still remember the first time I got interviewed by him when he described the quantum mechanics and flying qubits. That is also the first time I feel there is a world full of mystery waiting for me to explore. I will forever be grateful of the help he gives me and the perspectives he guides.

Also, I had the good fortune to be taught from Prof. Roger Mong during my graduate school. He always can explain difficult concepts and equations with remarkable ease, and his creativity with his willingness shines through in every conversation. By the way, I'm also really enjoying his thermodynamics class, where I first start understanding what's this course about.

I had the pleasure of working with several other professors during my Ph.D. from whom I learned a lot both in theory and experiments. First, Prof. Hakan Türeci, with whom I first plunged into the exciting experiments presented in this thesis. All the discussion him make me realize the complexity and the beauty of physics. Then, Prof. Wolfgang Pfaff, for teaching us more tricks on parametric control and coding idea. The software infrastructure he proposed show us a totally different world of programming possibilities.

In addition, I would like to thank my other committee members, Prof. Gurudeve Dutt, Prof. Brian Batell and Prof. Susan Fullerton, for taking time out of their busy schedules to guide me on my research. And their kindness advising also let me realize how big the physics world is, and there are always more question waiting us to solve.

Next, I want to thank all senior graduate student in Hatlab, Tzu-Chiao Chien, Olivia Lanes and Xi Cao, who have contributed significantly to previous and in-parallel work, without which these experiments would not have been possible. Tzu-Chiao has taught me lots of knowledge about fabrication and amplifier measurement, which becomes a very important part in my later study. Not only this, Tzu-Chiao also is the first friend I made

in the states, he has given me lots of support when I first came here, and I wish I can have one more dance with him in the future. And I also feel very lucky studying with Olivia, who gives me many valuable suggestions on both physics side and the etiquette in America. Last, I have also learned the basic of qubit measurement from Xi, who is always so patient teaching me all fundamental technology in the lab.

Moreover, I want to thank Chao Zhou, who has spent almost 4 years with me. We have together built the software platform, hardware setup, fabrication recipe, measurement protocol and in the end the modular quantum computer. I can never imagine without him, many accomplish during my Ph.D. would just be in vain. Also, working with Chao is always enjoyable and gratifying, I still remember how touch we were when the first time we saw Bell state in our quantum computer. If there is one thing I want to do before leaving Pittsburgh, that would be getting drunk again with Chao. Further, I feel very lucky I have met Mingkang Xia in my Fifth year. He is a very fast learner and soon starts helping me a lot on experiments in the later stage. He is literally the reason I can finish my dissertation on time, and also the hope my name can show up in the *Nature* article.

I would also like to thank Maria Mucci, who is always so passion and enthusiasm on many things. Even though we didn't have lots of chance working on the same project, however, every time we work together, I feel relaxing and inspiring. More importantly, without her, we even couldn't have the second fridge in the lab, let alone any following experiment I have done there.

On more experimental support side, Param Patel is another crucial friend in my research life. I'm really appreciated of him devoting his time exploring the fabrication details, especially tantalum deposition techniques. Also, he is always a happy person who gives us lots of joy in our lab life. Then, the help from Ryan Kaufman is so precious and prompt. I totally understand how hard it could be making an amplifier that is both workable and at the right frequency, that's why I feel so lucky that I can have a friend like Ryan in the lab.

One of the pity in the lab for me is that I didn't get enough time working with Israa Yusuf and Boris Mesits. They're brilliant, creative, and most importantly, they're excellent people. All the help they give me on my dissertation is really valuable, and I really do appreciate it. Israa, I think she is the most patient people I have known in this lab. All the

polishing, machining work she has done, I think it cannot be called it as a metal anymore, but a true art. Boris, he has the most detailed notebook I have ever seen, he inspires me on lots of sense not only in the lab work but also the way we handle our life. By the way, I'm still expecting the next soccer game we are going to play.

Evan McKinney, I don't want to thank him, because he still own me a beer. Fine, I agree he is a good person, an excellent researcher, a fine coder, a no-game man. All the conversions we have about computing architecture, machine learning and coding logic are always impressive and memorable. If he can have one more beer with me, I think we can be good friends.

During my Ph.D. I got several chances working with other Universities' friend. Saeed Khan, a very smart man who can always find the key problem of science. If I ever have any confusion in the theory understanding, talking to Saeed is always the best and efficient solution I can imagine. We have together finished the first project mentioned in this thesis, and he is also like a mentor to me, teaching me many tricks and techniques in the science field, including figure generating, cluster computer calculation, data analyzing and even scientific writing. I want to thank him again for all his help. Daniel Weiss is also a very talented theorist who has helped us understand much confusion in our Hamiltonian. And I'm truly indebted to him for helping us interpret various horrible theory.

I would also like to thank my family for supporting me through the whole process. First and most importantly, my wife, Jae J. We met the first year I started my graduate school, and we get married soon after. She has accompanied me during my whole PhD journey, and all the encouragement and support she gives me was never in a question. Also, I like to thank my parents, whose guidance in my childhood put me on track to succeed as an adult. With my mom always giving me tons of chances trying all different things and my dad showing me the power that we can conquer everything, I am forever indebted to them for my past and future achievements. Moreover, I want to thank my parents-in-law, who not only give me but my family lots of help during the COVID quarantine. It could be a real tough time for the last three year, however, all the supports I have received make me believe there should be nothing we cannot overcome in the future.

Lastly, I would like to thank my son, Jason, who was born during my graduate school.

He is always my source of pleasure and I want to be his friend in my rest of life.

In the very end of the acknowledgement, I want to take a second thank myself. I never imagine I could finish the Ph.D. when I first came to the states. There are multiple moments I was thinking about giving up, and that's why I also feel how lucky I am when this final moment come. If there is one thing I can tell myself in the future, I want to say, "Please try one more time, and always remember why you start."

1.0 Introduction

You can never represent yourself totally .... to seek self -knowledge is to embark on a journey which ... will always be incomplete, cannot be charted on a map, will never halt, cannot be described.
– Douglas Hofstadter

Due to the quarantine, I'll only be telling inside jokes.
- Meme from internet found at the start of the third year of COVID-19

Why do people want to read yet another dissertation related to quantum computation? What does a graduate student do in a superconducting quantum computing lab? How can so many seemingly random science projects relate to each other? If there is one element threading my whole graduate study, what is it? How will we organize a six-year study into just 200 pages? The purpose of this introductory chapter is trying to answer these question by going through my personal experience during my study. The intent is to give new students coming to this field some basic insights; if this can give you one extra perspective on your research, it will have been a worthwhile effort

My story begins in Sec. 1.1 with the basic understanding of quantum engineering and my current research direction. In Sec. 1.2, I will cover all research projects I have participated in and try to find a connection between them. Next, Sec. 1.3 presents an important element, parametric control, which overtook the Hatlab during my time in graduate school, and discuss why it could change the game in superconducting systems. Last, in Sec. 1.4, I'll lay out the overall structure of this thesis

1.1 Quantum engineering and quantum computation

Quantum mechanics famously allows objects to be in two places at the same time. The same principle can be applied to information, represented by bits: quantum bits can be both zero and one at the same time. The field of quantum information science seeks to engineer real-world devices that can store and process information using quantum states. It is be-

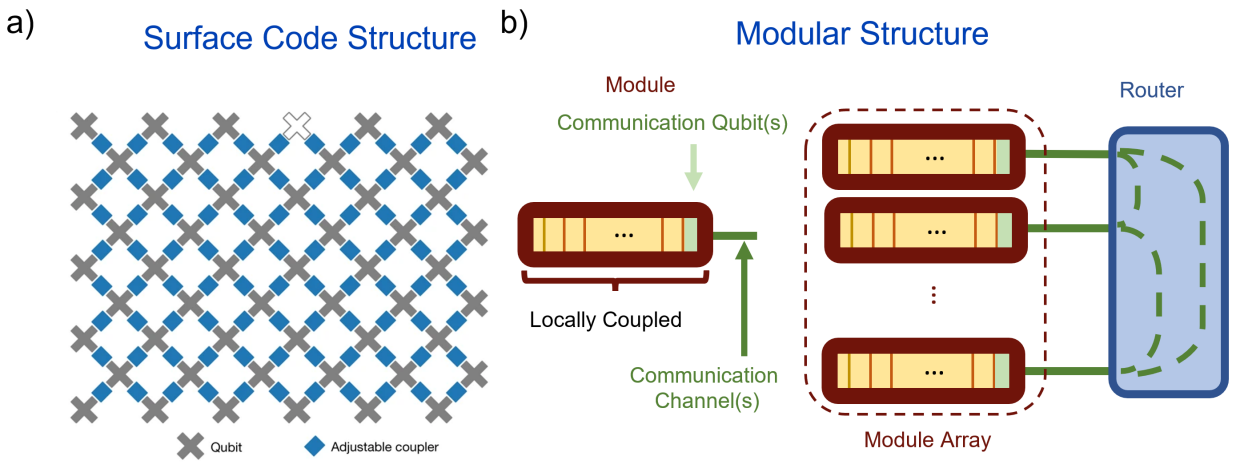

Figure 1: **Quantum architecture adapted from Ref. [4]** a) Surface-code structure; b) Modular structure.

lieved that computers operating according to such principles will be capable of solving some important problems exponentially faster than existing classical computers, while quantum networks have provable security guarantees. However, constructing such systems is a significant challenge, as quantum effects and hence quantum information, are extremely fragile, and typically die very quickly due to unwanted interactions with their environment.

For decades, quantum computing has been viewed as a futuristic technology–one will change the world if it ever evolves from the fantastical to the practical. However, machines must contain far more qubits than they do today to become useful. Moreover, we must protect quantum computers from errors by spreading information across multiple physical qubits, requiring still more qubits. Companies such as IBM and Google are currently mounting a direct assault on the problem by simply building bigger in their chosen architecture, the so-called surface code [1, 2, 3].

In academic research, we cannot match these efforts; on the other hand, it is not clear that we should try. Instead, we can best benefit the field by searching for new qubits, controls, and architectures that can allow us to shortcut this grind, producing machines that can operate better with far fewer qubits. As we do this, however, we must keep in mind that

single- and two-qubit experiments are not enough to truly prove ideas out, which must scale to the thousand plus qubit level. Instead, we must push ourselves to design systems that are both inventive enough to be interesting and big enough to be convincing.

In my research at the University of Pittsburgh, I have been working towards such a goal, seeking to create a quantum network with dense local couplings among multiple quantum objects. More importantly, these couplings not only have enough coherence to produce high-quality nearest-neighbour couplings [1, 2, 3], which the surface code is based on, also can be generally applied on multi-layer structure. That's why we chose modular quantum architecture as an alternative to connecting several small "quantum modules" via parametric coupling onto a quantum bus [5, 6, 7, 8]. In my most recent experiment[4] in partnership with Chao Zhou, we realized a parametrically driven, modular architecture for coupling superconducting qubits. We envision a "tree" of microwave modes that can mediate long-range interactions between individual bits through a series of parametric interactions. This architecture, in contrast to the current reliance in the field of nearest-neighbor pair-wise interactions builds a much denser network of gates between qubits, and thus makes the challenge of achieving large-scale quantum machines less daunting.

1.2 Different researches in superconducting quantum computing

On the other hand, studying in a superconducting quantum computing lab doesn't mean the only job is making a quantum computer. In my research I have tried multiple projects, including traveling wave gate design, quantum-limited amplifier operation, two-mode squeezed light readout, etc. I must admit during each process, I never thought they had deep connections with each other. However, at the end of the day, I have come to realize that each project, while different on the surface, relies on a common set of techniques and ways of thinking.

The first project I have participated is designing a traveling wave gate for the flying microwave photon qubits. Even though this project didn't turn into a device in the end, it was my entry point to circuit quantum electrodynamics (cQED) [9, 10, 11, 12, 13] which is the

single most important and powerful tool in superconducting systems. It is no exaggeration to say that most projects across so many groups and years, all start from circuit QED. It is the study of the interaction of nonlinear superconducting circuits, acting as artificial atoms or as qubits for quantum information processing, with quantized electromagnetic fields in the microwave frequency domain. Moreover, circuit QED has led to advances in the fundamental study of light-matter interaction, in the development of quantum information processing technology, and in the exploration of novel hybrid quantum systems [14]. With the help from Prof. Hatridge and Prof. Mong, we have explored lots of different combination of circuit design and Hamiltonian engineering with continue and discrete variables crossing the whole system. I analyzed the system from the very first Lagrangian to the different driven frame under different approximations. I have really come to appreciate the time we have spent together on understanding this theory, which gave me a very solid cornerstone for my next several projects.

Then, I got the chance of working with Tzu-chiao Chien and Olivia Lanes on parametric amplifier design which give me lots of chances studying simulation, fabrication and low-Q mode measurement [15]. This period of time helped me gather lots of experience as a quantum hardware researcher: the simulations which connect the Hamiltonian and physical objects and the fabrication which brings them reality. Next, we cool the samples down to cryogenic temperature ($< 20\,\mathrm{mK}$) and measure them with radio frequency (RF) instruments. All these experiences continued throughout my PhD, however, if there is one thing I learned from Tzu-chiao and Olivia, it is that every tiny step in the whole process matters in the end, including a small 3D structure overlap in fabrication and the fine details of the attenuation arrangement along the fridge input lines.

Later, I have participated in another project with Xi Cao and Gangqiang Liu on two-mode squeezed light readout. From this project, I started learning qubit measurement and operation [16]. One of my key contributions, together with Chao Zhou, was to develop the whole setup of qubit measurement based on FPGA-based Keysight electronics with Python operational code. During this process, I gained experience on both software programming and hardware design. Also, I realized that graduate school, especially in an experimental lab, required me to master not only quantum physics, but also plumbing, electricity, coding,

machining and so on. Also after this project, I have grown strong interest on quantum computation and parametric control

Next, I started an independent experimantal project in collaboration with a theory group from Princeton University, working with Saeed Khan and Prof. Hakan Tureci on a Josephson junction-based frequency comb. I used everything I had learned in my first years in the lab, and in close collaboration with Saeed, we together finished the project and I produced my first first-author publication [17]. This experience taught me how hard it could be to complete a whole science project, starting from the theory design, to the fabrication and measurement and repeating these over and over. The final part, writing the manuscript, was also a big challenge for me. In the end, however, it all pays off, since every tiny step in science is irreplaceable.

Finally, Chao Zhou and I have paved the way to build a modular quantum computer using parametric controls. This time, we almost start from scratch: the fridge input and output lines had to be carefully designed to protect the coherence of the system, plus a great deal of work on all filters, attenuators and isolators we have designed for packaging our machine. The quantum computer software platform required at least three major upgrades during the project, not only to catch up with the progress with the hardware, but also to suit the more and more complicated needs of our experiments. I still remember the day we first made a Bell state in the experiment, I felt so touched that I thought "this is something I want to do my whole life. And I believe this is also something I want more people to feel one time in their life."

1.3 Parametric control changes the game

Among my many projects while in graduate school, I find parametric controls to be the single thread tying all my projects together. However, the definition of this term can be a bit difficult. "A parametric oscillator is a driven harmonic oscillator in which the oscillations are driven by varying some parameter of the system at some frequency, typically different from the natural frequency of the oscillator." Above is from Wikipedia [18], the definition of

'parametric oscillator'. However, when people first hear about parametric control in quantum systems, I don't think this definitions helps them at all; or at least I personally felt confused by it for a period of time. After several years' study, I think a more accurate description is actually from optics. In the optical system, An optical parametric oscillator (OPO) is a parametric oscillator that oscillates at optical frequencies. It converts an input laser wave (called "pump") with frequency ω_p into two output waves of lower frequency (ω_s, ω_i) by means of second-order nonlinear optical interaction. The sum of the output waves' frequencies is equal to the input wave frequency: $\omega_p = \omega_s + \omega_i$. For historical reasons, the two output waves are called "signal" and "idler", where the output wave with higher frequency is the "signal" [19].

The reason I think this makes more sense is that two keywords it has mentioned: (frequency) 'convert' and 'nonlinear' interaction. Almost the first requirement of a parametric system is a nonlinear term in the Hamiltonian, which can be (counting the number of raising and lower operators) third order, fourth order, or even higher. Then, by sending a 'pump' tone into the system, these terms can generate some extra interaction not present in the undriven system, which includes but is not limited to: Rabi oscillation, photon conversion, amplification and so on. Actually, almost every experiment I have participated, there is one or more parametric interactions inside controlling the system.

For example, the very first example from Hatlab is quantum-limited amplification [20], and this is also a very classical application of parametric control in superconducting quantum system. By pumping the frequency summation of two modes with the third order nonlinearity in the system, the photon number in both modes can be amplified by 100 times more or even more with only a bit more than a half photon of added noise. In practice, this amplification process can also use fourth order term and not limited to single mode 'phase sensitive' amplification and two mode 'phase preserving' amplification [15, 21, 22, 23].

Then, later in our lab, Xi Cao and Maria Mucci have also developed a technique using parametric control to change a qubit's bath temperature (M. Mucci, X. Cao, et al. in preparation). Here, they use a third order nonlinearity to couple the qubit with a lossy mode, and then by pumping the transition between a qubit state and the lossy mode, they can drive the system and have the qubit to nearly any state they want.

Next, in our recent modular quantum computer experiment, we have again utilized parametric controls on qubit operation, including both single- and two- qubit gates [4], [M. Xia, et al. in preparation]. At the end of the day, for a 4-bit quantum system, we have used a single pump line realizing all ten possible operations: four families of single-qubit gates and six two-qubit gate pairs. The details we will cover in the following sections, but in as a preview: the third order term naturally enables singe qubit Rabi oscillations with two pump photons and two qubit interactions with one pump photon.

However, this is very far away from the end of parametric control in quantum systems. Just the experiments I can think about are following: *First*, parametric readout. Since we have already integrated parametric single-qubit gate and two-qubit gate together, why can't we also try parametric readout? There are dispersive terms hidden in the fifth order nonlinear terms, this could be a good target for design. *Second*, entanglement stabilization. There are already lots of non-Hermitian Hamiltonian engineering [24, 25] based on parametric controls. As we already can connect multiple desired modes and engineering system bath via parametric systems, I don't think this should be very far away. *Last*, One benefit of parametric control is that it doesn't limit the number of parametric tones in the system. Based on the single- and two- qubit gates, I think we can think more aggressively about multiple qubits gates, including three- or even four- qubit gates, which can boost quantum computing operational speed by requiring building larger unitaries directly instead of only relying on two-qubit gates.

1.4 Dissertation organization

My thesis is organized as follows: First, Chapter 2 builds the cornerstone of the whole structure, theory and simulation, where the theory focuses on circuit QED, and the simulation section presents how to transfer from a Hamiltonian into a physical object using simulation tools. Next, Chapter 3 is devoted to superconducting device fabrication which can bring the simulated object to the life. Next, in Chapter 4, I work through the basics of RF measurement on a cold sample. At the same time, I also introduce a crucial component

I spent a lot of time on during my graduate study: parametric gate tune up.

Chapter 5 described my first independent project, realizing a Josephson junction based frequency comb via quantum engineering. More specifically, we start by discussing the instabilities of a particular non-linear two-mode system; and then use a strong drive with weak nonlinearity to generate a comb spectrum in the frequency domain; the chapter concludes with comments about system coherence and chaos.

Next, in Chapter 6, I discuss our efforts to build a modular quantum computer using all techniques I have detailed up to this point, including Hamiltonian engineering, nanofabrication, and quantum architecture design together with lots and lots of parametric gate tuneup. I show how to make the first part of a modular quantum computer, a quantum state router, where we combine a waveguide and center SNAIL together.

Lastly, Chapter 7 discusses a bit about our ongoing progress on the second part of the modular quantum computer, a 4-bit quantum module, the conclusions I have drawn from my work, and ends with the my future outlook.

2.0 Theory and simulation

2.1 Circuit QED

In the 1980s the first Josephson junction-based superconducting circuits were invented to explore quantum mechanical effects at the macroscopic level[26]. Since the early 2000s, these circuits, have been realized as qubits and have been studied intensely for potential applications in quantum computation and quantum information science. While atomic cavity QED[27] inspired many of the early developments of these superconducting circuits, the truth that a superconducting system can be made to strongly and controllably interact with microwave photons and also store the quantized electromagnetic filed led to the creation of the field of circuit QED. Very soon, circuit QED plays an essential role in all current approaches to quantum information processing with superconducting circuits, and it allows the study and control of light-matter interaction at the quantum level in unprecedented details.

For over 20 years, circuit QED has been developed rapidly and systematically. While it built its success on strongly-coupled qubit-cavity experiments [9, 10, 11, 12, 13], it had also been firmly established as a versatile platform to realize a broader variety of quantum nonlinear systems [28]. Josephson-junction based superconducting circuits have also enabled devices from quantum-limited amplifiers [29, 30, 31, 32, 33] and single-microwave photon detectors [34, 35, 36, 37] with application ranging from quantum information processing to the search for dark matter axions, to hybrid quantum systems [14].

In this section, instead of reviewing the broad set of concepts realized from circuit QED, I'm going to focus on three major parts I have been studied and explored during my doctoral: superconducting circuit elements; measurement in circuit QED and parametric driven system.

2.1.1 Superconducting circuit elements

Since the first cooper pair box qubit has been invented in 2000 [38, 39], various kinds of superconducting circuit elements have been created for all different purposes, including quantum-limited amplifiers, photon detectors, fast switches and qubits. By changing the combination and the size of the capacitance, inductance and the most important part, the nonlinear inductance, Josephson-junction, the circuit can perform different functions, also weaken different kinds of noise effects. Here I am going to take several elements as examples explaining the philosophy behind circuit QED, and the applications of different combinations.

2.1.1.1 The quantum LC resonator and transmon in circuit QED

Before we describe something nontrivial, let's start from the easiest model, the LC resonator, to get the idea of circuit QED and make the symbols consistent.

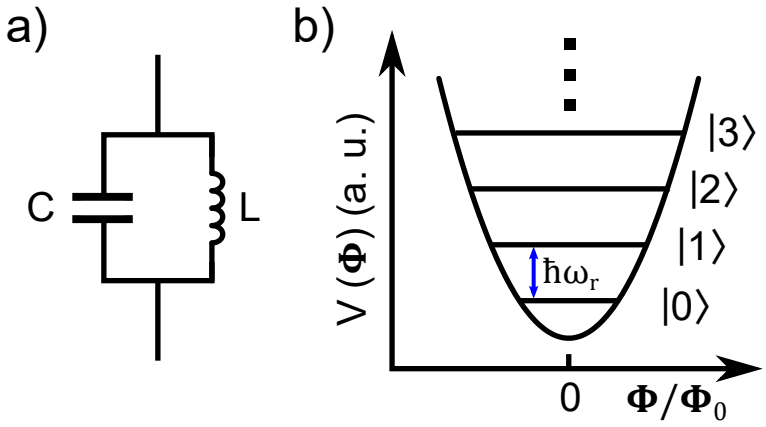

Figure 2: **The quantum LC oscillator.** a) Schematic of LC resonator. b) Harmonic potential versus flux of the LC circuit with $\Phi_0 = h/2e$ the flux quantum.

As shown in Fig 2a), an LC oscillator is characterized by its inductance L and capacitance C, where they can also be derived as angular frequency $\omega_r = 1/\sqrt{LC}$ and characteristic impedance $Z_r = \sqrt{L/C}$. The total energy of the circuit can be written as:

$$H_{LC} = \frac{Q^2}{2C} + \frac{\Phi^2}{2L}, \tag{1}$$

where Q is the charge on the capacitor and Φ is the flux threading the inductor. Here the definition of charge and flux are inherited from classical circuit, where $Q(t) = \int_{t_0}^{t} I(t')dt'$ and $\Phi(t) = \int_{t_0}^{t} V(t')dt'$ where the voltage and current are zero at time t_0.

Very naturally, this expression gives us an analogy of a mechanical oscillator with conjugate variables Q and Φ. Therefore, quantization will automatically apply to the Hamiltonian with the commutation relation:

$$[\hat{\Phi}, \hat{Q}] = i\hbar \tag{2}$$

Then, it is useful to further introduce the standard annihilation $\hat{a}$ and creation $\hat{a}^\dagger$ operators of the the LC oscillator, where they have been defined as:

$$\hat{\Phi} = \Phi_{\text{ZPF}}(\hat{a}^\dagger + \hat{a}) \qquad\qquad \hat{Q} = iQ_{\text{ZPF}}(\hat{a}^\dagger - \hat{a}) \tag{3}$$

with the characteristic magnitude of the zero-point fluctuations of the flux $\Phi_{\text{ZPF}} = \sqrt{\hbar Z_r/2}$ and the charge $Q_{\text{ZPF}} = \sqrt{\hbar/2Z_r}$. Now, the Hamiltonian can be rewritten as:

$$\hat{H}_{LC} = \hbar\omega_r(\hat{a}^\dagger\hat{a} + 1/2) \tag{4}$$

with eigenstates $\hat{a}^\dagger\hat{a}\,|n\rangle = n\,|n\rangle$ for $n = 0, 1, 2, ...$ Here, I want to emphasize that after the quantization of circuit, $\hat{a}^\dagger$ physically creates a photon of frequency ω_r stored in the circuit, and $\hat{a}$ destroy one.

Till here, we have completed quantization of LC oscillator. Before we move on, the very first question we ask is that is it possible to operate the circuit in a regime where quantum effects are important? For this to be the case, there are at least two conditions that must be satisfied:

First, the system need to decouple enough from the noisy world. In other words, the quality factor $Q = \omega_r/\kappa$, where κ is the bandwidth of the cavity, should be big enough that the energy levels are much narrower than their separation.

Second, the temperature of the system needs to be low enough. We should keep in mind the truth that, $1\,\text{GHz} \times h \sim 50mK \times k_b$, and the thermal energy k_bT of the environment should be way much smaller than the energy separation $\hbar\omega_r$.

With these two conditions satisfied, a simple LC oscillator can be operated in the quantum regime, which means that the circuit can be initialized in its ground state $|n = 0\rangle$ by waiting for several times (~ 5) of photon lifetimes $T_\kappa = 1/\kappa$.

2.1.1.2 Josephson junction (JJ) and JJ-based qubit

Now we can introduce some non-trivial elements into the system. Here, 'nontrivial' comes from the fact that even though the oscillator we discussed above can be prepared in the quantum mechanical ground state, it is still very hard to directly observe clear quantum behavior. Or in quantum computation language, without some degree of nonlinearity, encoding and manipulating quantum information in such system becomes almost impossible. Fortunately, now we can introduce one of the most important elements in superconducting circuit, Josephson junction (JJ), with decent nonlinearity while avoiding extra losses.

Here, I'm going to skip most of the details of the JJ, but emphasize two important Josephson relations:

$$I = I_c \sin\varphi \tag{5}$$

$$V = \frac{\Phi_0}{2\pi} \cdot \frac{d\varphi}{dt} \qquad \text{or} \qquad \varphi(t) = 2\pi \frac{\Phi(t)}{\Phi_0} = 2\pi \frac{\int dt' V(t')}{\Phi_0} \tag{6}$$

where the first one indicates the relation between supercurrent I and the phase φ difference between the superconducting condensates (superconducting order parameters), here I_c is the junction's critical current. And the second one reveals the time dependence of the phase different related to the voltage across the junction, where $\Phi_0 = h/2e$ is the flux quantum. Notice here, sometimes, we can see ϕ_0 in other articles, where $\phi_0 = \hbar/2e$ represents reduce flux quantum. And another thing here, superconducting phase φ is a compact variable, $\varphi = \varphi + 2\pi$, and Φ can take arbitrary real values with 'mod 2π'.

Taken together, Josephson relation actually connect current I and flux Φ, where geometric inductance has a very similar relation: $\Phi = LI$. For this reason, we also treated Josephson junction as a nonlinear inductor with following inductance:

$$L_J(\Phi) = \left(\frac{\partial I}{\partial \Phi}\right)^{-1} = \frac{\Phi_0}{2\pi I_c} \frac{1}{\cos\left(2\pi\Phi/\Phi_0\right)} \tag{7}$$

Notice here, the inductance of Josephson junction depends on flux Φ. Furthermore, we can make analogy of the energy stored in the linear inductor: $E = \int dtV(t)I(t) = \Phi^2/2L$, we have

$$E = \int dtV(t)I(t) = \int dt \left(\frac{d\Phi}{dt}\right) I = I_c \int dt \left(\frac{d\Phi}{dt}\right) \sin\left(\frac{2\pi\Phi}{\Phi_0}\right) = -E_J \cos\left(\frac{2\pi\Phi}{\Phi_0}\right) \quad (8)$$

With $E_J = \Phi_0 I_c/2\pi$ the Josephson energy. This quantity is proportional the rate of tunnelling of Cooper pairs across the junction.

After we have figured out the junction energy part, there are tons of freedom shunting the junction with all kinds of elements. The most common one is a capacitively shunted Josephson junction as shown in Fig. 3 a).

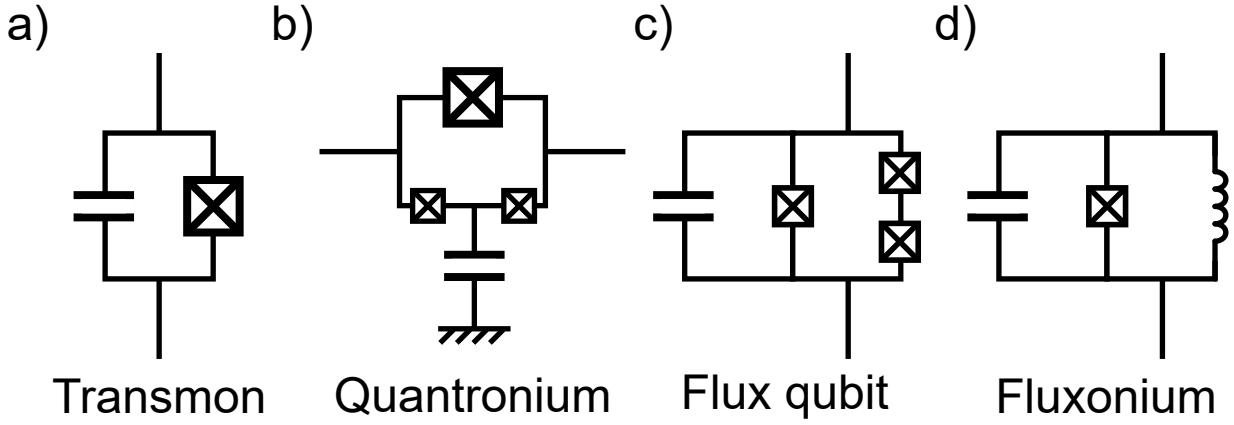

Figure 3: **JJ-based qubit.** By combining Josephson junction with other elements, there are lots of possibilities for all kinds of qubits. In general, different designs bring different sensitivity to the environment. Based on the requirement, we can choose different structure for use.

For this particular one, the quantized Hamiltonian reads:

$$\hat{H} = \frac{(\hat{Q} - Q_g)^2}{2(C_S + C_J)} - E_J \cos\left(\frac{2\pi}{\Phi_0}\hat{\Phi}\right) = 4E_C(\hat{n} - n_g)^2 - E_J \cos\hat{\varphi} \quad (9)$$

Where C_S and C_J are shunt capacitance and junction's capacitance, normally $C_S \gg C_J$, here we also define $C = C_S + C_J$. For the $\hat{Q}$ and $\hat{\Phi}$ are conjugate operators that are similar as the one in LC oscillator. In second equal sign, we have also defined $\hat{n} = \hat{Q}/2e$ as charge number

operator, the phase operator $\hat{\varphi} = (2\pi/\Phi_0)\hat{\Phi}$ and charging energy $E_C = e^2/2(C_S + C_J)$. Another parameter we haven't introduced is a possible offset charge $n_g = Q_g/2e$ due to capacitive coupling of the transmon to the external charges. This term is unavoidable for capacitive coupling element, however, by controlling the ration between E_J and E_C, we can change the system's sensitivity to the offset charge. A very famous work from J. Koch in 2007[40], where he carefully compare the relation between sensitivity and E_J/E_C. And in the end, he make the conclusion that when $E_J/E_C \gg 1$, the variance of the charge degree of freedom is large and the variance of its conjugate variable $\hat{\varphi}$ is correspondingly small. In this situation, it is instructive to rewrite Eq. 9 as:

$$\hat{H} = 4E_C\hat{n} + \frac{1}{2}E_J\hat{\varphi}^2 - E_J(\cos\hat{\varphi} + \frac{1}{2}\varphi^2) \tag{10}$$

And because $\Delta\hat{\varphi} = \sqrt{\langle\hat{\varphi}^2\rangle - \langle\hat{\varphi}\rangle^2} \ll 1$, therefore the Hamiltonian can be truncated to its first nonlinear correction:

$$\hat{H}_{\text{transmon}} = 4E_C\hat{n} + \frac{1}{2}E_J\hat{\varphi}^2 - 1/4!E_J\hat{\varphi}^4 \tag{11}$$

which is so-called the transmon energy.

Next, it is naturally to introduce creation and annihilation operators chosen to diagonalize the first two terms, where:

$$\begin{aligned}\hat{\varphi} &= \left(\frac{2E_C}{E_J}\right)^{1/4}(\hat{b}^\dagger + \hat{b}) \\ \hat{n} &= \frac{i}{2}\left(\frac{E_J}{2E_C}\right)^{1/4}(\hat{b}^\dagger - \hat{b})\end{aligned} \tag{12}$$

Now the equation finally leads to:

$$\hat{H}_{\text{transmon}} = \sqrt{8E_CE_J}\ \hat{b}^\dagger\hat{b} - \frac{E_C}{12}(\hat{b}^\dagger + \hat{b})^4 \approx \hbar\omega_q\hat{b}^\dagger\hat{b} - \frac{E_c}{2}\hat{b}^\dagger\hat{b}^\dagger\hat{b}\hat{b} \tag{13}$$

where $\hbar\omega_q = \sqrt{8E_CE_J} - E_C$. There is approximation where we only keep terms that have the same number of creation and annihilation operations. The approximation holds because any terms with an unequal number of $\hat{b}$ and $\hat{b}^\dagger$ will be oscillating in a frame rotating at ω_q. If the frequency of these oscillations is larger than the prefactor of the oscillating term, then this term rapidly averages out and can be neglected. This Rotating-Wave Approximation (RWA) is valid if $\hbar\omega_q \gg E_c/4$, an inequality that is easily satisfied in the transmon regime.

2.1.1.3 Exchange interaction between a transmon and an oscillator

Having introduced the two main characters in this section, the quantum harmonic oscillator and the transmon artificial atom, we are now ready to consider their interaction. As we have just described, because of the large size coming from the requirement of having a low charging energy (big capacitance), transmon qubit is very easily capacitively coupled to microwave resonators, as shown in Fig. 4.

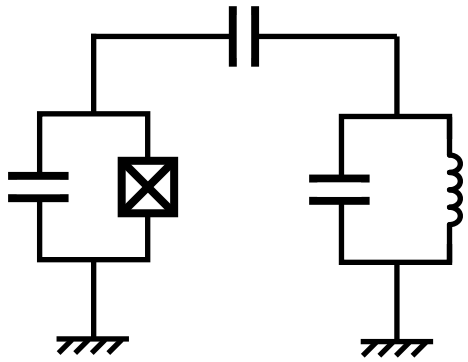

Figure 4: **Schematic representation of a transmon qubit coupled to a resonator**

There are tons of literature have systematically derived the Hamiltonian of the circuit. There are two of them I personally feel super useful and insightful during my graduate study: One is K. Geerlings's dissertation [41], and another one is a review of circuit QED [9]. I don't think it is necessary repeating the work, the only point I want to restate here is the result of the Hamiltonian:

$$\hat{H}/\hbar = \omega_r \hat{a}^\dagger \hat{a} + \omega_q \hat{b}^\dagger \hat{b} + \frac{\alpha}{2}\, \hat{b}^\dagger \hat{b}^\dagger \hat{b} \hat{b} + \chi \hat{a}^\dagger \hat{a} \hat{b}^\dagger \hat{b} \tag{14}$$

where $\alpha = -E_C$ is the anharmonicity of the qubit, and $\chi = -2\frac{g^2 E_C}{\Delta(\Delta-\alpha)}$ is the dispersive coupling between cavity and qubit.

We will discuss more details in Sec. 2.1.2 about how do we use this Hamiltonian to perform measurement in qubit-cavity system.

2.1.1.4 Superconducting Nonlinear Asymmetric Inductive eLement (SNAIL)

Except for the above JJ-based qubits, there are lots of other JJ-based elements that have been broadly used in quantum-limited amplifier, qubit coupler, bath engineering and so on. And one of the elements, that has been used several times during my graduate study, is Superconducting Nonlinear Asymmetric Inductive eLement (SNAIL) [42]. In this section, I'm going to carefully derive the Hamiltonian details related to SNAIL and introduce some basic applications people have utilized.

The SNAIL consists of a superconducting loop of n large Josephson junctions and a single smaller junction with tunneling energies E_J and αE_J respectively (again $E_J = \varphi_0^2/L_J$). The inductive energy of SNAIL can be written as:

$$U_{SNAIL}(\varphi) = -\alpha E_J \cos(\varphi) - nE_J \cos\left(\frac{\varphi_{\text{ext}} - \varphi}{n}\right) \tag{15}$$

where φ is the superconducting phase across the small junction, and $\varphi_{\text{ext}} = 2\pi\Phi_{\text{ext}}/\Phi_0$ is the reduced applied magnetic flux threading the SNAIL loop.

Through numerical minimization of Eq. 15, we analyze the SNAIL's mixing capabilities by Taylor expanding about the minimum φ_{min} to obtain the effective potential for $\tilde{\varphi} = \varphi - \varphi_{\text{min}}$:

$$U_{eff}(\tilde{\varphi})/E_J = c_2\tilde{\varphi}^2 + c_3\tilde{\varphi}^3 + c_4\tilde{\varphi}^4 + ... \tag{16}$$

Experimentally, we choose $n = 3$ for Dolan bridge fabrication process, and we specialize all further analysis to the case $n = 3$, so we can have all coefficients as:

$$\begin{aligned}
c_2 &= \frac{1}{6}\left(\cos\left(\frac{\varphi_{\text{ext}} - \varphi_{\text{min}}}{3}\right) + 3\alpha\cos(\varphi_{\text{min}})\right) \\
c_3 &= \frac{1}{54}\left(\cos\left(\frac{\varphi_{\text{ext}} - \varphi_{\text{min}}}{3}\right) - 9\alpha\cos(\varphi_{\text{min}})\right) \\
c_4 &= -\frac{1}{648}\left(\cos\left(\frac{\varphi_{\text{ext}} - \varphi_{\text{min}}}{3}\right) + 27\alpha\cos(\varphi_{\text{min}})\right)
\end{aligned} \tag{17}$$

Furthermore, quantization can be achieved in the canonical way by replacing the flux amplitudes of the equivalent oscillators by operators as:

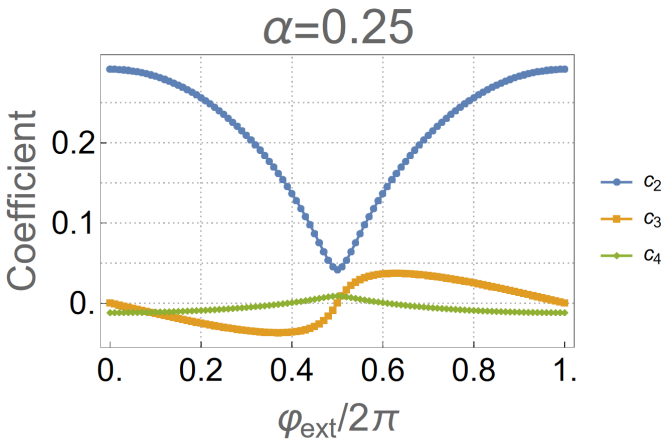

Figure 5: **SNAIL expansion coefficient.** Assume $\alpha = 0.25$ and $E_J = 1$, we numerically calculate all coefficients with different external flux threading the SNAIL.

$$\tilde{\varphi} = \sqrt{\frac{\hbar}{2} Z_{\text{eff}}} \left(a + a^\dagger\right) \tag{18}$$

In order to easily compare all terms' magnitude later, here we explicitly write down all the expansion of 2nd, 3rd, 4th order terms in the Hamiltonian.

$$\begin{aligned}
&c_2 \left(\sqrt{\frac{\hbar}{2} Z_{\text{eff}}}\right)^2 (a^\dagger + a)^2 + c_3 \left(\sqrt{\frac{\hbar}{2} Z_{\text{eff}}}\right)^3 (a^\dagger + a)^3 + c_4 \left(\sqrt{\frac{\hbar}{2} Z_{\text{eff}}}\right)^4 (a^\dagger + a)^4 \\
&= c_2 \frac{\hbar}{2} Z_{\text{eff}} \left(2a^\dagger a + a^\dagger a^\dagger + aa + 1\right) \\
&+ c_3 \frac{\hbar^{\frac{3}{2}}}{2\sqrt{2}} Z_{\text{eff}}^{\frac{3}{2}} \left(a^\dagger a^\dagger a^\dagger + 3a^\dagger a^\dagger a + 3a^\dagger aa + aaa + 3a^\dagger + 3a\right) \\
&+ c_4 \frac{\hbar^2}{4} Z_{\text{eff}}^2 \left(a^\dagger a^\dagger a^\dagger a^\dagger + 4a^\dagger a^\dagger a^\dagger a + 6a^\dagger a^\dagger aa + 4a^\dagger aaa + aaaa + 12a^\dagger a + 6a^\dagger a^\dagger + 6aa\right)
\end{aligned} \tag{19}$$

As we can see, there are multiple nonlinear terms in the Hamiltonian which may matter during the parametric process. I'm going to pick up several reasonable parameters and insert into the expression to compare the magnitude of these terms with external flux.

Assuming $\alpha = 0.25$, $\omega_s(\varphi_{\text{ext}=0}) = 5(2\pi)\,\text{GHz}$, $E_J = 2.166 * 10^{-22}$ ($L_J = 0.5\,\text{nH}$). Then we first can plot the modulation of SNAIL with flux:

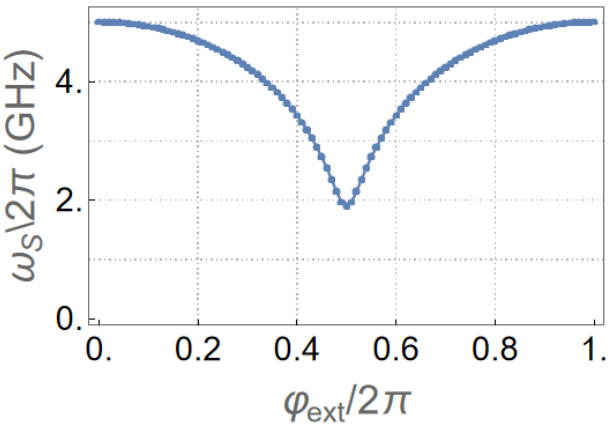

Figure 6: **SNAIL frequency modulation.** With the external flux threading the SNAIL, the frequency of SNAIL modulate from 2 to 5 GHz.

Next we can compare the following terms: 3rd order: $a^\dagger a^\dagger a^\dagger$, $a^\dagger a^\dagger a$, 4th order: $a^\dagger a^\dagger a^\dagger a^\dagger$, $a^\dagger a^\dagger a^\dagger a$, $a^\dagger a^\dagger aa$ with flux as shown in Fig. 7.

One thing need to be noticed here: by carefully tuning up the flux biasing the SNAIL, we can find a good point where Kerr terms approaches zero. However, in the parametric regime, when the circulating photon inside the SNAIL becomes larger, the even higher order terms show up, and the effective Kerr term can not be ignored in the system.

In the experimental scenario, we generally apply different pumping tone onto the device, which will result in different rotating frames. I'm going to analyze the details in different frames in section 2.1.3.

2.1.2 Measurement in circuit QED

Circuit QED has been developed as a super powerful tool in superconducting system, including circuit analysis, Hamiltonian engineering, electromagnetic field simulation and etc. And one other important application is the measurement, not only the steady state solution, but also dynamical response. Analyzing the physics process of measurement can give us a rough idea of quantum operation in the later sections.

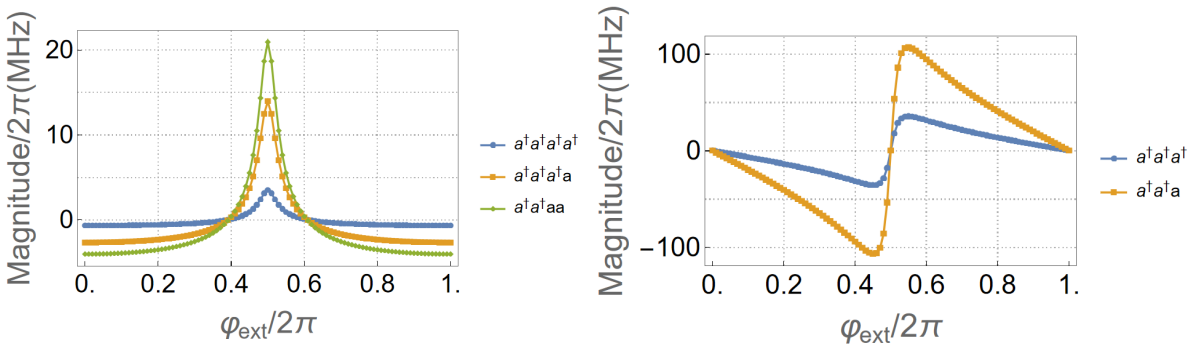

Figure 7: **SNAIL 3rd order and 4th order magnitude with flux.** We calculate the exact magnitude of the 3rd and 4th terms to have a straight idea of how big are these terms.

2.1.2.1 Steady state solution of cavity measurement

In this section, we start from measurement of a linear mode, focusing on comparing the classical method and quantum method with both reflection and transmission analysis. As shown in Fig. 8, we take a series LCR oscillator as the example, and use the classical method to calculate the cavity response [43].

From the parameter in the Fig. 8, we can first define following numbers:

$$\begin{aligned} Q_{\text{int}} &= \omega_0 L/R \\ Q_{\text{ext}} &= \omega_0 L/Z_0 \\ \omega_0 &= 1/\sqrt{LC} \end{aligned} \tag{20}$$

At steady state condition, the reflection can be written as:

$$\Gamma = \frac{V_0^-}{V_0^+} = \frac{Z_l - Z_0}{Z_l + Z_0} \tag{21}$$

where $Z_l(\omega) \approx R + j\ 2L\Delta$, and $\Delta = \omega - \omega_0$ to the first order. In order to compare with quantum method, the expression can be written in terms of Q_{int}, and Q_{ext}:

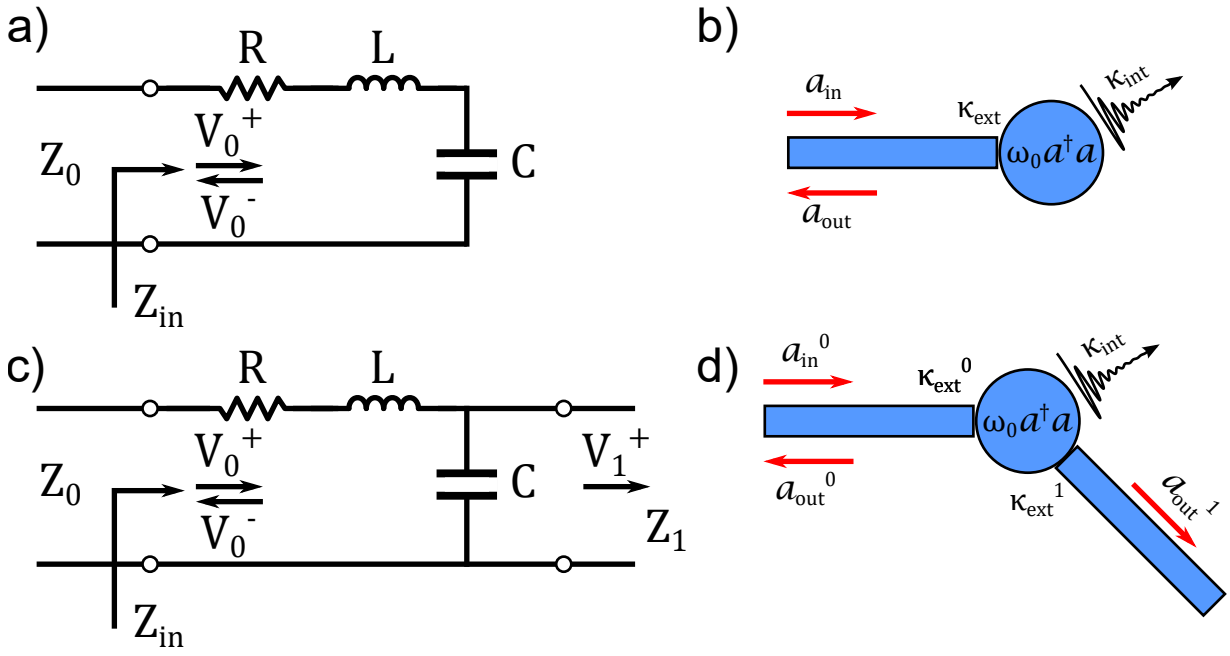

Figure 8: **Cavity measurement (steady solution).** a, c) Classical circuit representation of an RLC oscillation, where Z_0 is the transmission impedance, V_0^+, V_0^- are signal sending in and coming out, separately, and V_1^+ is the output of another port. b, d) Quantum schematic representation of a linear mode, where the frequency is ω_0, and the mode is represented by operator a; $a_{\text{in}}, a_{\text{out}}$ represent the input and output for each port.

$$\frac{V_0^-}{V_0^+} = \frac{R + j\ 2L\Delta - \omega_0 L/Q_{\text{ext}}}{R + j\ 2L\Delta + \omega_0 L/Q_{\text{ext}}} = \frac{\omega_0(1/Q_{\text{int}} - 1/Q_{\text{ext}}) + j\ 2\Delta}{\omega_0(1/Q_{\text{int}} + 1/Q_{\text{ext}}) + j\ 2\Delta} \tag{22}$$

At the same time, we can also derive the relation in quantum representation. Notice here the decay rate of each port is $\kappa = \omega_0/Q$. We start from equation of motion and input-output theory:

$$\begin{aligned} \dot{\hat{a}} &= \frac{i}{\hbar}[\hat{H}_{\text{sys}}, \hat{a}] - \frac{\kappa}{2}\hat{a} + \sqrt{\kappa_{\text{ext}}}\hat{a}_{\text{in}} \\ \hat{a}_{\text{out}} &= \hat{a}_{\text{in}} - \sqrt{\kappa_{\text{ext}}}\hat{a} \end{aligned} \tag{23}$$

For the $\hat{H}_{\text{sys}}$, we only consider it as a linear oscillator, where $\hat{H}_{\text{sys}} = \omega_0 \hat{a}^\dagger \hat{a}$. For the Heisenberg equation of motion, we want to add a comment here: The equation itself describes the time

evolution of the field amplitude $\hat{a}$ inside the cavity, and the amplitude $\hat{a}$ experiences decay at a rate $\kappa/2$, where $\kappa = \kappa_{\text{int}} + \kappa_{\text{ext}}$. At the same time, its fluctuations a constantly replenished via the quantum noise entering through the various port of the cavity with a total rate $\sqrt{\kappa_{\text{ext}}}$.

In order to solve the steady state solution, we can simply Fourier transform the equation of motion to get:

$$\begin{aligned} i\omega\hat{a}[\omega] &= i\omega_0\hat{a}[\omega] - \frac{\kappa}{2}\hat{a}[\omega] + 2\sqrt{\kappa_{\text{ext}}}\hat{a}_{\text{in}}[\omega] \\ (\kappa + 2i\Delta)\hat{a}[\omega] &= 2\sqrt{\kappa_{\text{ext}}}\hat{a}_{\text{in}}[\omega] \end{aligned} \tag{24}$$

Then use input-output theory to get an expression with only $\hat{a}_{\text{in}}$ and $\hat{a}_{\text{out}}$:

$$\begin{aligned} (\kappa + 2i\Delta)(\hat{a}_{\text{in}}[\omega] - \hat{a}_{\text{out}}[\omega]) &= 2\kappa_{\text{ext}}\hat{a}_{\text{in}}[\omega] \\ \hat{a}_{\text{out}}[\omega] &= \hat{a}_{\text{in}}[\omega]\left(\frac{\kappa_{\text{int}} - \kappa_{\text{ext}} - 2i\Delta}{\kappa_{\text{int}} + \kappa_{\text{ext}} - 2i\Delta}\right) \end{aligned} \tag{25}$$

At this point, we can easily see:

$$\frac{V_0^-}{V_0^+} = \frac{\hat{a}_{\text{out}}[\omega]}{\hat{a}_{\text{in}}[\omega]} \tag{26}$$

One interesting thing, if we look closer, we can find is that here $j = -i$, which is coming from electronic engineering convention. After we have the steady state solution, we can start playing around with the parameters and see what's the difference between different choices.

Here is an example where we change the ratio between external Q and internal Q. As we can see from Fig. 9 b), when $\kappa_{\text{ext}} < \kappa_{\text{int}}$, the port is under-coupled, and the phase wrap across the whole mode is smaller than π; if $\kappa_{\text{ext}} = \kappa_{\text{int}}$, the port is critical-coupled, and the phase wrap is exactly π; last, $\kappa_{\text{ext}} = \kappa_{\text{int}}$, the port is over-coupled, and the phase wrap is 2π. The reason we cared about the port coupling is that this can give us a straightforward idea about how good the port is. If $\kappa_{\text{ext}} < \kappa_{\text{int}}$, this may indicate the system has unwanted losses we didn't realize; If $\kappa_{\text{ext}} \gg \kappa_{\text{int}}$, it is either a lossy cavity designing for fast readout, or we may need a weak port to fit internal Q.

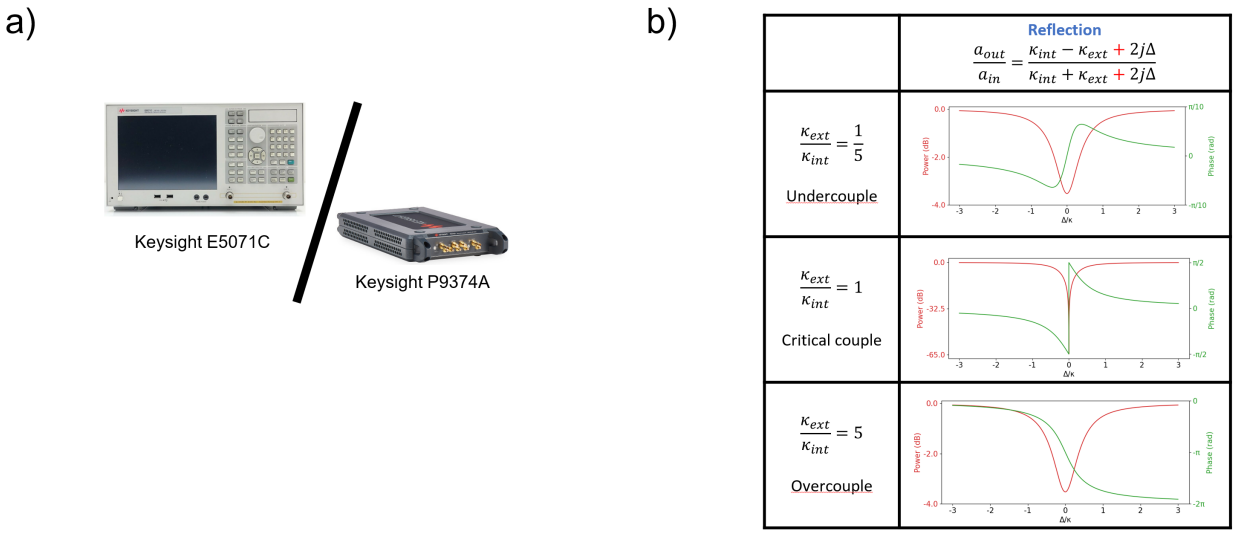

Figure 9: **Reflection measurement of cavity (frequency domain).** a) Vector Network Analyzer (VNA) is usually used for measuring steady state in frequency domain. b) Three different classical port coupling: under-couple, critical-couple and over-couple. For the complex part, we choose plus sign to match the result coming from VNA.

Similar idea for the transmission response. Here we skip the classical method, and use the quantum method to derive it again. Assume the signal send into port 0, and calculate both output from port 0 and port 1:

$$\begin{aligned}
\dot{\hat{a}} &= \frac{i}{\hbar}\left[\hat{H}_{\text{sys}}, \hat{a}\right] - \frac{\kappa}{2}\hat{a} + \sqrt{\kappa^0_{\text{ext}}} \\
\hat{a}^0_{\text{out}} &= \hat{a}^0_{\text{in}} - \sqrt{\kappa^0_{\text{ext}}}\hat{a} \\
\hat{a}^1_{\text{out}} &= \sqrt{\kappa^1_{\text{ext}}}\hat{a}
\end{aligned} \tag{27}$$

Then, the same Fourier transformation apply on the first equation and substitute $\hat{a}$ as propagation operators, and following two equations can be derived:

$$\begin{aligned}
\hat{a}^0_{\text{out}}[\omega] &= \hat{a}_{\text{in}}[\omega]\left(\frac{\kappa_{\text{int}} + \kappa^1_{\text{ext}} - \kappa^0_{\text{ext}} - 2i\Delta}{\kappa - 2i\Delta}\right) \\
\hat{a}^1_{\text{out}}[\omega] &= \hat{a}^0_{\text{in}}[\omega]\left(\frac{\sqrt{\kappa^0_{\text{ext}}\kappa^1_{\text{ext}}}}{\kappa - 2i\Delta}\right)
\end{aligned} \tag{28}$$

For the port 0, the only difference is now the external loss from port 1 becomes an internal loss for port 0. In another word, if we see from port 0, we couldn't identify if the information leaks from port 1 or from the internal. And for the transmission response $\hat{a}^1_{\text{out}}$, two external couplings have multiplied together, which means we cannot extract the port coupling separately. However, from the expression, we still can get totally decay rate from the bandwidth (BW).

2.1.2.2 Dynamic response of cavity measurement

After we have derived the steady state solution, the dynamic response is just a Fourier transform away. Let's take the reflection response as an example:

$$\hat{a}_{\text{out}}[t] = \mathcal{F}^{-1}\left[\hat{a}_{\text{out}}[\omega]\right] = \mathcal{F}^{-1}\left[\hat{a}_{\text{in}}[\omega]\left(\frac{\kappa_{\text{int}} - \kappa_{\text{ext}} - 2i\Delta}{\kappa_{\text{int}} + \kappa_{\text{ext}} - 2i\Delta}\right)\right] \tag{29}$$

Using convolution theorem: $\mathcal{F}^{-1}\{f \cdot g\} = \mathcal{F}^{-1}\{f\} \cdot \mathcal{F}^{-1}\{g\}$, we can analytically solve the time dynamics:

$$\hat{a}_{\text{out}}[t] = -\kappa_{\text{ext}} \int_{-\infty}^{t} \hat{a}_{\text{in}}(\tau) \exp\left[\left(\frac{\kappa}{2} + i\omega_0\right)(\tau - t)\right] d\tau + \hat{a}_{\text{in}}(t) \tag{30}$$

Similar idea for the transmission response:

$$\hat{a}^1_{\text{out}}[t] = -\sqrt{\kappa^0_{\text{ext}}\kappa^1_{\text{ext}}} \int_{-\infty}^{t} \hat{a}^0_{\text{in}}(\tau) \exp\left[\left(\frac{\kappa}{2} + i\omega_0\right)(\tau - t)\right] d\tau \tag{31}$$

Basically, the main difference between transmission and reflection is that the latter also has the incoming wave in it. That's why the transmission signal is purer than reflection and is better for the following amplifier (harder to saturate). In Fig. 10, we take a flat top signal as an example for incoming signal and calculate different responses under different conditions.

Notice here, after a period of time (≈ 3 to $5 \times 1/\kappa$), the response enter into steady state. Depending on the drive frequency we send into the system, the corresponding value should be consistent with the solution we get from steady state calculation.

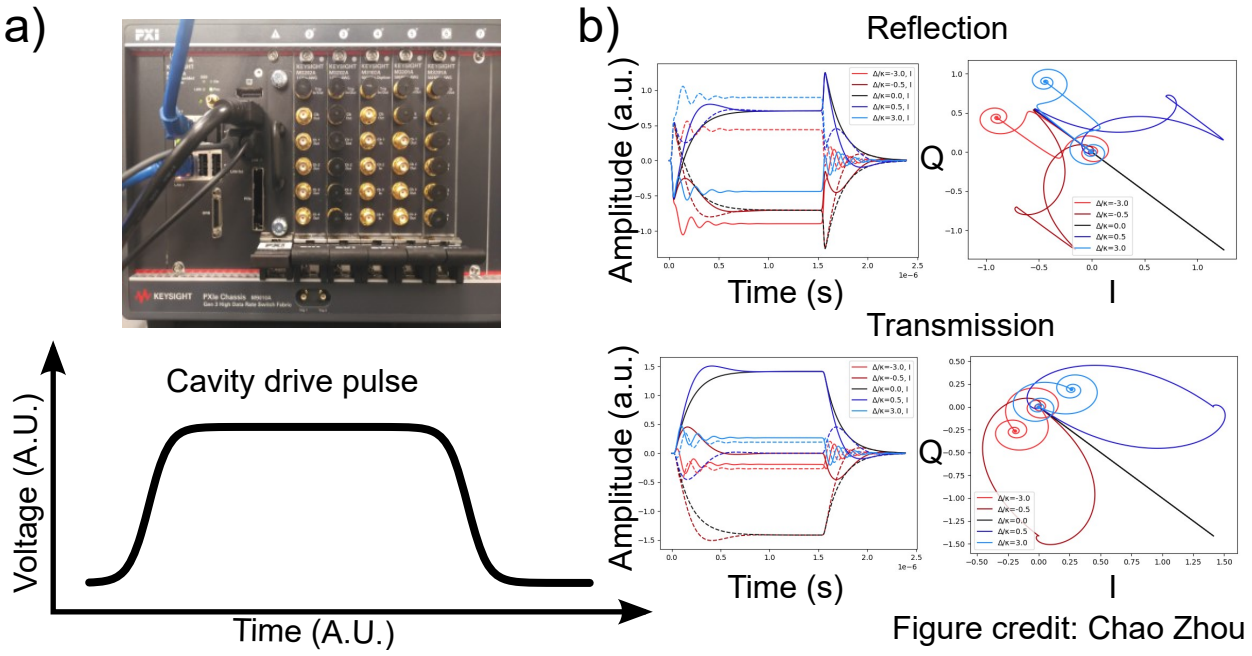

Figure 10: **Cavity measurement (time domain)** a). Time domain measurement instrument, including Arbitrary Waveform Generator (AWG) and digitizer. One example of the incoming signal is a finite flat top pulse; b) Different dynamical responses based on different conditions (Δ/κ).

2.1.2.3 Dispersive readout and qubit measurement

Next, we can consider a little more complicated system, a cavity dispersively coupled with a qubit. Considering the Hamiltonian as following:

$$\hat{H} = \omega_c \hat{c}^\dagger \hat{c} + \omega_q \hat{q}^\dagger \hat{q} + \alpha(\hat{q}^\dagger \hat{q}^\dagger \hat{q}\hat{q}) + \chi(\hat{q}^\dagger \hat{q} \hat{c}^\dagger \hat{c}) = (\omega_c + \chi\langle \hat{q}^\dagger \hat{q}\rangle)\hat{c}^\dagger \hat{c} + \omega_q \hat{q}^\dagger \hat{q} + \alpha(\hat{q}^\dagger \hat{q}^\dagger \hat{q}\hat{q}) \quad (32)$$

Where, ω_c, q are the resonance frequency of cavity and qubit, α is the anharmonicity of qubit and χ is the dispersive coupling between two modes. The critical term $\hat{q}^\dagger \hat{q} \hat{c}^\dagger \hat{c}$ changes the cavity resonance frequency depending on the occupation of qubit.

As shown in Fig. 11, when qubit in state $|g\rangle$ ($\langle \hat{q}^\dagger \hat{q}\rangle = 0$) and state $|e\rangle$ ($\langle \hat{q}^\dagger \hat{q}\rangle = 1$), the cavity shows different response.

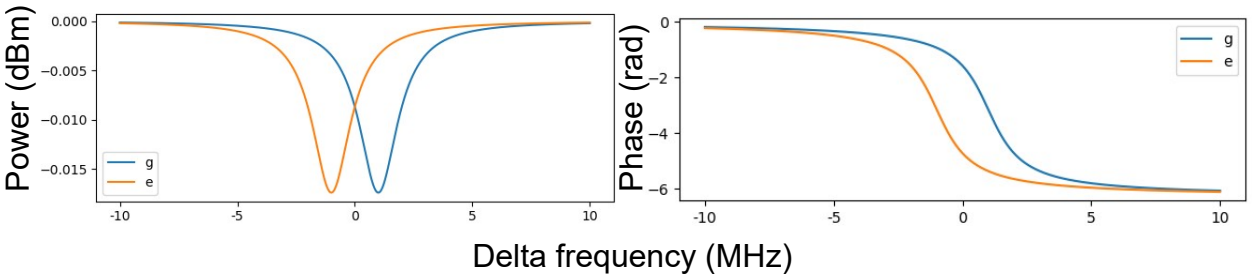

Figure 11: **Dispersive readout (steady solution).** When qubit has different population, the cavity has different resonance frequencies.

Because of this state-dependent resonance, it gives us an idea of measuring the state of qubit by measuring the response of cavity. If we recall the dynamic response of cavity, both reflection and transmission, there is a $\exp\left[\left(\frac{\kappa}{2}+i\omega_0\right)\right]$ term in the integration, which tells us the response depends on the resonance of the cavity. More specifically, assuming $\omega_c^g = \omega_c$ when qubit in ground state and $\omega_c^e = \omega_c - \chi$ when qubit in excited state, and we directly drive at $\omega_d = \omega_c - \chi/2$, then if $\kappa > \chi$, we can get two same magnitude response but different phase; if $\kappa \ll \chi$, the magnitude of the response is the same, but the phase is also the same (phase wrapping). In practice, if we want to have an optimized readout, the cavity drive frequency highly depends on χ/κ.

One example has been showing in Fig. 12, and another technique we generally do is integrating the whole cavity response (sometimes with a weighted function) to get a signal point on the I-Q plane. After thousands repetition, all points forming two Gaussian blobs where the centers corresponding to the two resonances' steady state solutions, and sigma represents half-photon noise after amplification.

2.1.3 Parametric driven system

Last but not least in this section, I want to discuss a very common technique during my graduate study, parametric driven system. A parametric driven system can be treated as a driven oscillator in which the oscillations are driven by varying some parameter of the system

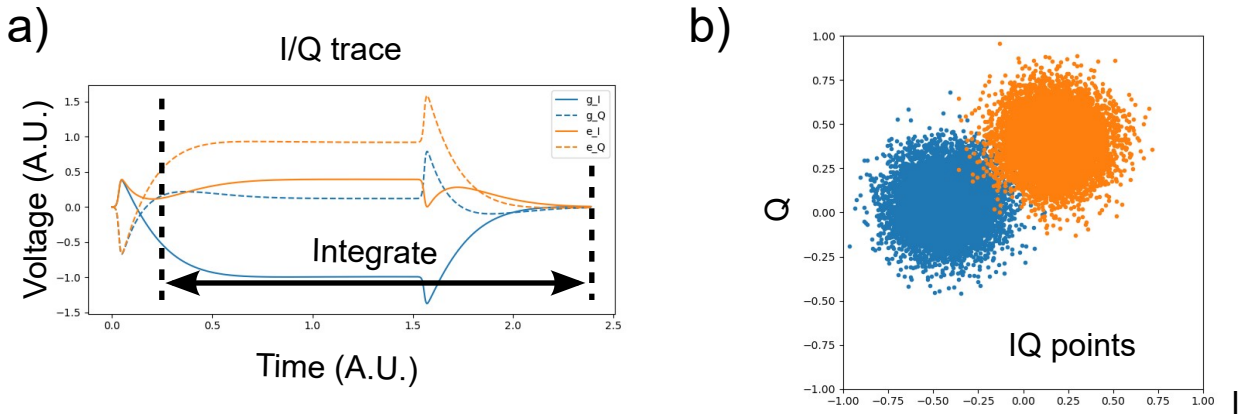

Figure 12: **Dispersive readout (dynamical solution).** a) Cavity response when qubit in different states; b) After integration, data has been plotted on I-Q plane.

at some frequency, typically different from the natural frequency of the oscillator. A simple example of a parametric oscillator is a child pumping a playground swing by periodically standing and squatting to increase the amplitude of the swing's oscillations.

In the quantum physics, a parametric system often comes with frequency conversion, photon amplification and circulation. And with some Hamiltonian engineering help, we find a parametric system can realize lots of application, such as parametric amplifiers, two-qubit gates, quantum state router and bath engineering.

Let's start from a simple example explaining the techniques of parametric system. In general, a parametric system's Hamiltonian can be divided into two parts: first, the oscillator modes, no matter linear or nonlinar modes; second, nonlinear term across the whole system. Here the nonlinear term could come from the modes themselves, like Josephson Ring Modulator (JRM), or from another mode coupling to all other oscillator modes. As shwon in Fig. 14, it is a simple three modes parametric system.

One thing I want to point out is that depending on the nonlinear terms we choose, it can be three-wave mixing, like SNAIL or JRM; or four-wave mixing, like Josephson junction coupler; or even high order nonlinear terms. Based on the operation we want, different numbers of pump photon will be sent into the coupler generating effective multi-body inter-

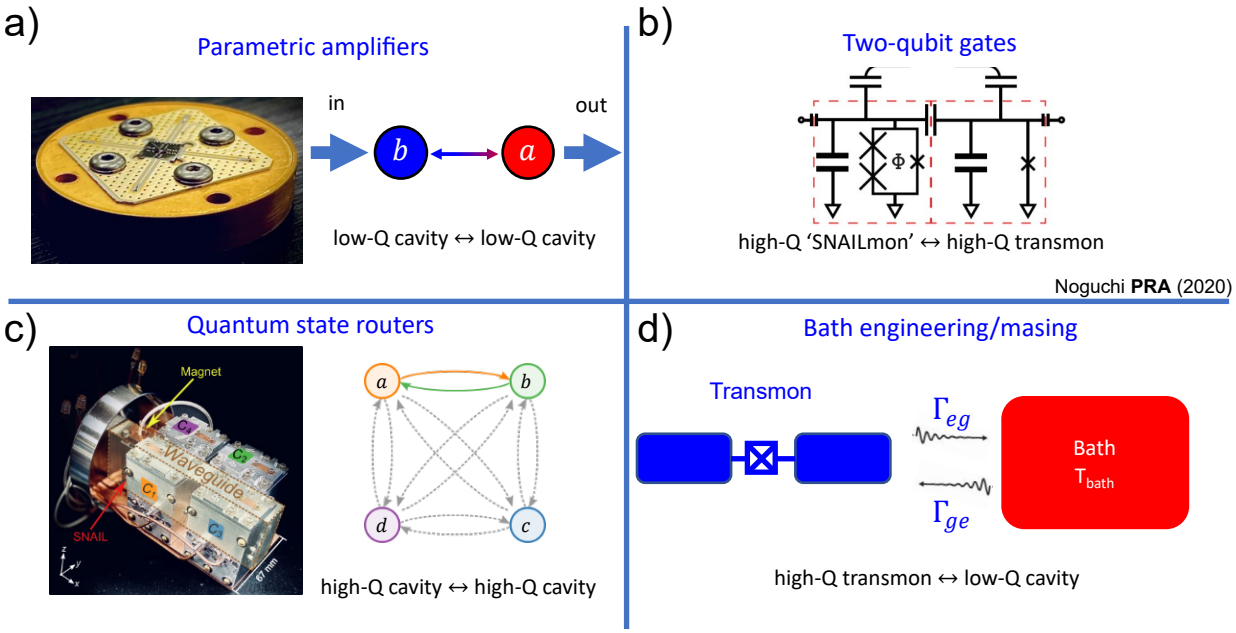

Figure 13: **Everything can be parametric.** Here are several examples involved with parametric system. a), c) and d) are systems we have realized in our lab, and we are currently making more.

actions. In the following text, I'm going to use a example where two linear modes coupled to a SNAIL mode to explain the idea of a parametric driven system and how we use the three-wave mixing term to generate an iSWAP gate.

The schematic representation is shown in Fig. 15, and the Hamiltonian can be written as:

$$\hat{H}_0/\hbar = \omega_1 \hat{c_1}^\dagger \hat{c_1} + \omega_2 \hat{c_2}^\dagger \hat{c_2} + g_{c_1 s}(\hat{c_1}^\dagger \hat{s} + \hat{c_1}\hat{s}^\dagger) + g_{c_2 s}(\hat{c_2}^\dagger \hat{s} + \hat{c_2}\hat{s}^\dagger) + \omega_s \hat{s}^\dagger \hat{s} + g_3(\hat{s} + \hat{s}^\dagger)^3 \quad (33)$$

We first ignore the nonlinear term and focus on the linear part. This step is quite similar as we described in Sec. 2.1.1.2, where we treat the nonlinear parts as perturbations in the Hamiltonian. The second order terms can be diagonalized first: then all three modes: $\hat{c_1}, \hat{c_2}, \hat{s}$ become dressed mode. Here for simplicity, we use the same operators for the dressed

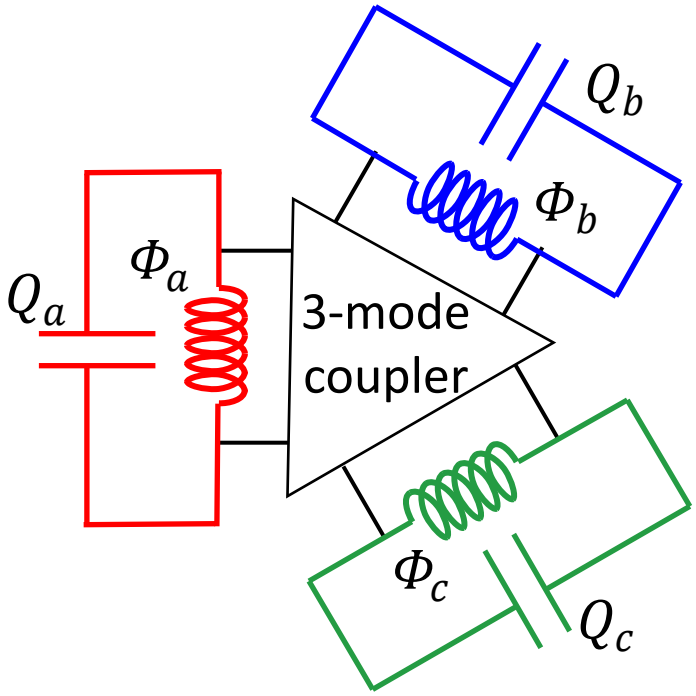

Figure 14: **Parametric coupling overview**. A classical three-wave mixing device. All three modes have been coupled together via the three-mode coupler in the middle. Thus, three-wave mixing terms are across the whole system with all combinations

Figure 15: **Schematic representation of three-body parametric system.** C_1 and C_2 are two linear modes which are both coupled to the center SNAIL mode.

modes. Next, for the nonlinear term, the dressed modes automatically inherits all third order nonlinearity with different coefficients. There are totally 24 different nonlinear terms after we expand the bracket, but most of them are relatively small in the rotation frame without

any other processing. The term we are going use for the parametric analysis is:

$$g_{c_1c_2s}\left(\hat{c_1}^\dagger \hat{c_2}\hat{s} + \hat{c_1}\hat{c_2}^\dagger \hat{s}^\dagger\right) \tag{34}$$

Here $g_{c_1c_2s}$ is the 3-wave-mixing coefficient. In the weak coupling regime where $(\frac{g}{\Delta})_{c_is} \lesssim 0.1$, the coefficient $g_{c_1c_2s}$ is approximately $g_3(\frac{g}{\Delta})_{c_1s}(\frac{g}{\Delta})_{c_2s}$, where $\Delta_{c_is} = \omega_{c_i} - \omega_s$.

The idea of parametric gate is that there is a hidden two-body interaction inside the three-body mixing term. To realize a photon conversion between two cavities, we apply a strong single-tone pump on the SNAIL at the frequency difference of two cavities, $\omega_p = |\omega_{c_1} - \omega_{c_2}|$. The time-dependent pumping term can be written as $\hat{\mathcal{H}}_P/\hbar = \epsilon(t)(\hat{s} + \hat{s}^\dagger)$, where $\epsilon(t)$ is represented by:

$$\epsilon(t) = \begin{cases} \epsilon^x(t)\cos(\omega_p t) + \epsilon^y(t)\sin(\omega_p t), & 0 < t < t_g \\ 0, & \text{otherwise,} \end{cases} \tag{35}$$

The total system Hamiltonian under pumping can be written as $\hat{H}' = \hat{H}_0 + \hat{H}_P$. To study the effect of this pumping term in the total Hamiltonian, we apply a unitary transformation on $\hat{H}$ with displacement operator:

$$D(t) = \exp[(zs^\dagger - z^* s)], \tag{36}$$

where $z = -\frac{(\epsilon^x + i\epsilon^y)/2}{\omega_p - \omega_s}e^{-i\omega_p t} + \frac{(\epsilon^x - i\epsilon^y)/2}{\omega_p + \omega_s}e^{i\omega_p t}$. This results in a new Hamiltonian $\hat{\mathcal{H}}^D$, in which the $\hat{\mathcal{H}}_P$ term is canceled and $\hat{s} \to \hat{s} - z$. Specifically, the 3-wave mixing term in Eq. 107 becomes:

$$g_{c_1c_2s}\hat{c_1}^\dagger \hat{c_2}\left(\hat{s}\frac{(\epsilon^x + i\epsilon^y)/2}{\omega_p - \omega_s}e^{-i\omega_p t} - \frac{(\epsilon^x - i\epsilon^y)/2}{\omega_p + \omega_s}e^{i\omega_p t}\right) + h.c. \tag{37}$$

Then we apply a rotating frame transformation at the frequency of all modes in the system:

$$R(t) = \exp\left[i\omega_s \hat{s}^\dagger \hat{s} + i\left(\omega_{c_1}\hat{c_1}^\dagger \hat{c_1} + \omega_{c_2}\hat{c_2}^\dagger \hat{c_2}\right)\right], \tag{38}$$

Note that $\omega_p = \left|\omega_{c_i} - \omega_{c_j}\right|$. All the other frequency differences in the system are assumed several bandwidth away from the pumping frequency. Then the only non-resonating term after the transformation is

$$\hat{H}^{\mathrm{RWA}} = \eta \; g_{c_1 c_2 s} \left(\hat{c}_1^\dagger \hat{c}_2 + \hat{c}_1 \hat{c}_2^\dagger \right), \tag{39}$$

where $\eta = (\epsilon^x + i\epsilon^y)\omega_s/(\omega_d^2 - \omega_s^2)$.

Eq. 39 shows that the pumping tone at $\omega_p = |\omega_{c_1} - \omega_{c_2}|$ activates the spontaneous photon conversion process between cavity modes c_1 and c_2. And the conversion speed mainly depends on the pumping strength. By controlling the length of the pump, $i\mathrm{SWAP}^{1/n}$ gates can be performed between the two modes. Moreover, this parametric pumping scheme is not limited on single process: if there are multiple modes in the system, multiple tones can be apply simultaneously to generate multi photon conversion or any other desired processes together.

2.2 Practical device simulation and its philosophy

After doing analysis above, now we finally have a circuit that can solve some particular questions. Next question that comes up naturally is that how we can realize it in real life. Then the very first step in solving this problem will be how do we transform a given schematic circuit into a real 2D or 3D object.

In the following sections, I'm going to use the example of the transmon + cavity system (i.e. Fig. 4) to explain the philosophy of simulation. Specifically, in Sec. 2.2.1, I'm going to discuss some choices of 2D/3D structures of linear mode, and a 'shoebox' cavity will be used explaining details in simulation; then in Sec. 2.2.2, two main ideas, black-box quantization and energy-participation-ratio, will be introduced to simulate most parameters of the transmon object, and again, a transmon in a 'shoebox' cavity will be used to discuss details.

2.2.1 Resonator mode

Continuing from Sec. 2.1.1.1, quantum harmonic oscillator can be made in different styles, and the LC oscillator could be one example. Another important example in circuit QED are microwave resonator, which can be divided into two main fields: 2D resonators, where

the electromagnetic field is confined in a planar structure, and 3D resonators, where in a three-dimensional volume.

Regarding 2D resonators, lots of discussions can already be found in different literature [43, 9], and I'm not going to explain details here. However, I'd still like to emphasize here, entering the quantum regime for a given mode m requires two condition: one is that $h\omega_m \gg k_B T$ and the other is the linewidth $\kappa_m \ll \omega_m$. Of course, after almost 20 years developing, both of conditions can already be easily realized in the experiment. However, there are still physical origin that not be fully understood. For example, dielectric losses at interfaces and surfaces can be important limiting factors to the internal quality factor of resonators. And one solution is to lower the ratio of the field energy stored at interfaces and surfaces to the energy stored in vacuum.

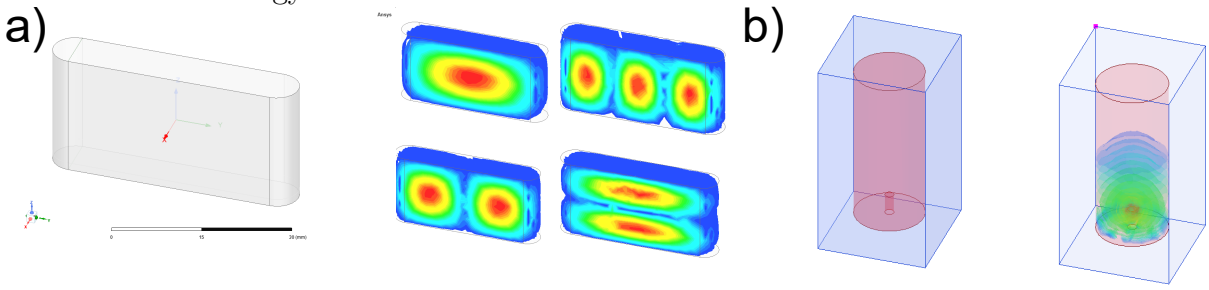

Figure 16: **'Shoe-box' cavity and coaxial cavity.** a) Schematic representation of a 'shoebox' cavity. The right-hand side shows the electronic field of first four TE_{mnl} modes obtained from Ansys HFSS. b) Schematic representation of a coaxial $\lambda/4$ cavity. And the electric field distribution shows the evanescent field rapidly decays from the top of the inner conductor.

That's why introducing 3D resonator could be a shortcut for this problem, since in three-dimension structure, the surface participation ration can be as small as 10^{-7} [44]. In practice, 3D resonators comes in many shapes and sizes for different practical purposes. As illustrated in Fig. 16, two popular designs, 'shoebox' and coaxial cavity, have often been used in designing 3D structure.

In 'shoebox' cavity, the resonator is just simply vacuum surrounded on all sides by superconductor, typically aluminum, to minimize surface losses. And the mode resonance is

the discrete set of TE and TM cavity modes of frequency [43]:

$$\omega_{mnl} = c\sqrt{\left(\frac{m\pi}{a}\right)^2 + \left(\frac{n\pi}{b}\right)^2 + \left(\frac{l\pi}{d}\right)^2} \quad , \text{ where } m, n, l \in \mathbb{Z} \tag{40}$$

where c is the speed of light, and a, b, d are the cavity dimensions. Of course, in most scenarios, the first fundamental mode will be used as the linear object. However, sometimes, by carefully designing the frequency distribution, a rectangular waveguide can also be treated as a coupling bus [4] or multimode Purcell filter [40]. On the other hand, coaxial $\lambda/4$ cavity let the electromagnetic field of the fundamental mode concentrating near the post, and exponentially decay from the top of the inner conductor.

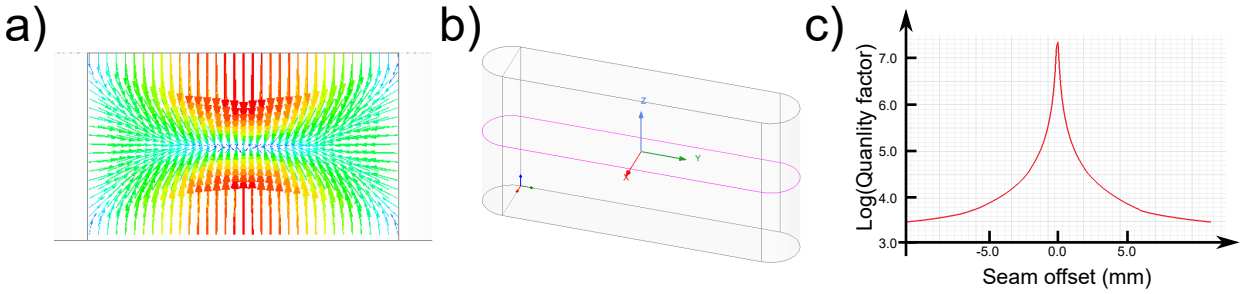

Figure 17: **Surface current and seam loss in 3D resonator.** a) The vector of surface current on the y-z plane of the inner conductor in the 'shoebox' cavity. b) Schematic representation of seam location on the cavity. c) The relation between common logarithm of quality factor and the seam position, here the seam offset is calculated based on the midpoint of z-axis on cavity.

Again, as shown in Fig. 16, from the distribution of electromagnetic field inside the 3D structure, we already have a rough idea about the thing we're going to build. And by changing the dimensions, the frequency of the designed mode can be as close as the theory required, and before introducing any loss elements, the quality factor will be infinitely large. However, in the real life, there are unavoidably different loss we need to consider in the simulation. and the very first one is the seam between metals. In Fig. 17 a), I have plotted the vector of current on the surface of the inner conductor in the 'shoebox' cavity. And in

the real life, due to the finite width of seam, there will be always current passing through the seam.

Now, we can also quantify the dependence of seam losses on the cavity geometry. The details can be found in Brecht et al. 2015 [45], here I'm going to summarize the expression in the following:

$$P_{\text{dis}} = \frac{1}{2G_{\text{seam}}} L \int_{\text{seam}} |\vec{J}_s \times \hat{l}|^2 dl. \tag{41}$$

$$\frac{1}{Q_i} = \frac{1}{\omega} \frac{P_{\text{dis}}}{E_{\text{tot}}} = \frac{1}{G_{\text{seam}}} \frac{L \int_{\text{seam}} |\vec{J}_s \times \hat{l}|^2 dl}{\omega \mu_0 \int_{\text{tot}} |\vec{H}|^2 dV} \tag{42}$$

The first one shows the relation between the dissipation power and the surface currents, and the seam has been treated as a distributed port around a path $\vec{l}$ with a total length L and total conductance G_{seam}. The second one assumes the only loss is coming from the seam, where the mode frequency is ω and E_{tot} is total energy over the volume V inside the cavity.

From these equations and the known field of the cavity, we can calculate the quality factor of the mode limited by the seam loss. For example, considering the TE_{101} mode of the 'shoebox' cavity, and we assume the seam is along y-axis, by sweeping the z-axis position, we can calculate the internal quality factor at different point, as shown in Fig. 17 c). From the simulation, for the 'shoebox' cavity, the best seam location is the mid-point along z-axis, and this also gives us the principles drawing the real metal for machining.

One last thing completing the 3D resonator design is the external coupling to the environment, or in other word, the wave port in the system. In most scenario, designing the wave port could be a tricky problem. However, it can also be summarized into a single question, how strong the coupling do you want for different modes? Let's take 'shoebox' cavity as the example again: if I want to measure the internal quality factor of the TE_{110} mode, and assume the only loss comes from the seam. Based on the fact that the internal Q is around 10^7, the external Q will be also approximately the same to measure that precision in the experiment.

Then by looking at the electric field distribution in Fig. 16 a), the rough position of the port will be around the corner of the cavity as shown in Fig. 18 a) to minimize the quality

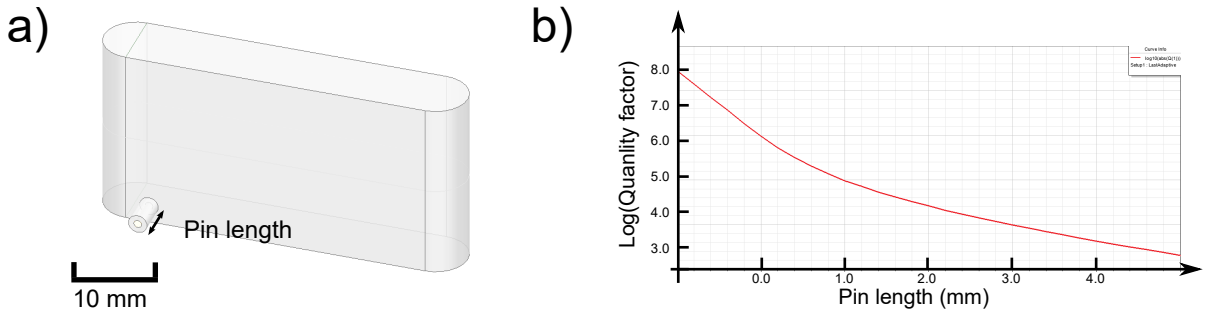

Figure 18: **Cavity probe and the corresponding quality factor.** a) External port position to minimize external Q. b) Relation between pin length and external quality factor (log scale), here, zero-point is based on the surface of inner conductor.

factor. Next, by sweeping the pin length, the corresponding length can be determined for the required external Q. However, in some scenarios, resonate mode is not the only mode that coupled to the external port. And for different purpose, different quantities will be calculated.

2.2.2 Transmon mode

After figuring out the shape of the resonator, in order to observe quantum behavior in the system, now we need to introduce some nonlinearity into the simulation. The general idea, instead of directly simulating nonlinearity, will be considering the coupling between multi modes. For example, if we want to put a transmon qubit into a 'shoebox' cavity, we actually model an LC oscillator, generally on a substrate (such as sapphire), and put it into the cavity. By calculating the effective impedance [46] or energy participation ratio [47], we can figure out the effect of nonlinearity applying onto the whole system.

Most of the math details have already been discussed in the previous sections. Here I'm going to use a specific example to introduce the steps of simulation. As shown in Fig. 19 a), transmon has been constructed as a capacitor shunted with a lumped inductor which forming two parts of the energy: E_J and E_C. From above analysis in Sec. 2.1.1.2, we already have an estimate on the magnitude of these two number, which makes our simulation easier. By

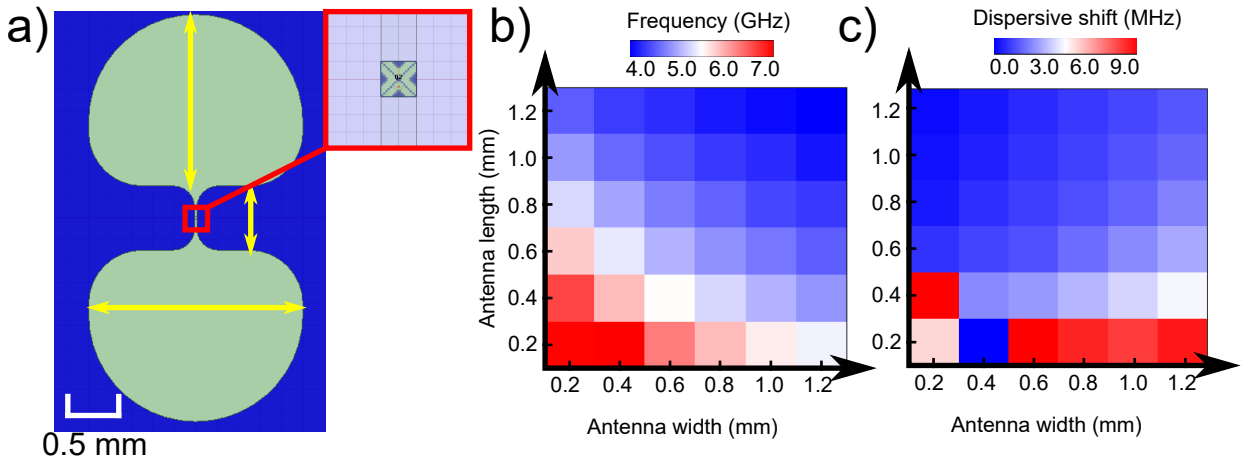

Figure 19: **Transmon design and its coupling.** a) Schematic of transmon design, where two big green pads forming the capacitor part of the mode also the antenna capturing cavity field; the small rectangular block is the lumped inductor representing Josephson-junction in the system. By changing the shape and size of antenna, also the magnitude of inductor, the frequency of transmon can be easily controlled. b) By sweeping the width and length of the antenna, the frequency can vary from 4 to 7 GHz. c) Similar idea, by changing the shape of antenna, the coupling between transmon and cavity will be different, resulting in different dispersive shift in the experiment.

changing the shape of the antenna (length, width and gap), the capacitance of the transmon will change. After assigning a lumped inductor with a reasonable inductance, the frequency of the mode will vary correspondingly. One example is shown in Fig. 19 b), where I change the antenna length and width, the frequency of the mode varies from 4 GHz to 7 GHz.

After that, the most important step is calculating the coupling between modes or in other word, dispersive shift between qubit and cavity. Despite the math details, the truth of coupling is actually the transmon antenna trying to capture the electric field of the cavity, which will be a dipole-field interaction. So again, the key factor affecting the magnitude of coupling will be the shape of the antenna and the position of the transmon itself. For the different experiments and purposes, we may pick up different couplings. And in most cases, another important parameter related to the coupling is the decay rate κ of the cavity mode,

which will be addressed later. Here, at this moment, we can just use the same scan in the last paragraph to show the idea of controlling the coupling in the system.

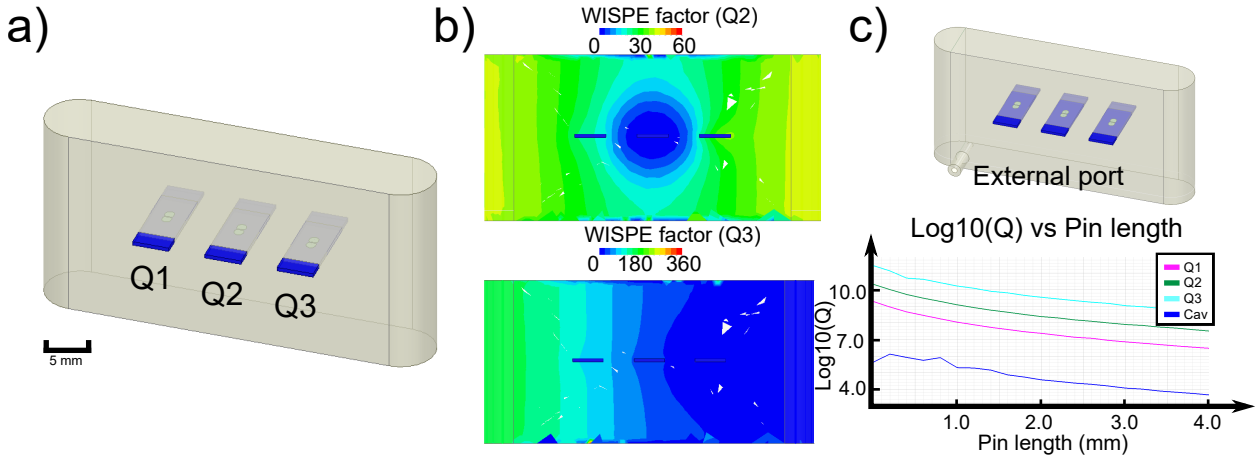

Figure 20: **Waves In Space Purcell Effect (WISPE).**

Finally, we can start considering where the port should be. Depending on the truth that we probably want to maximize the coherence of qubit, the port should be minuscule ($Q_{\text{ext}}^{\text{qubit}} \approx 10^8$) coupled to the qubit mode. At the same time, if we also want a fast readout for the resonator mode, the port will be reasonably strong ($Q_{\text{ext}}^{\text{cavity}} \approx 10^3$) coupled to the resonator mode. Or in summary, we can define a Waves In Space Purcell Effect (WISPE) factor:

$$W = \frac{\vec{E_c} \cdot \vec{E_q}}{|\vec{E_q}|^2} \tag{43}$$

where $\vec{E_c}$ and $\vec{E_q}$ are the electric fields of resonator and transmon, correspondingly. Then, by plotting W factor on the surface of the inner conductor inside the cavity, an optimized point where we can not only drive easily on the cavity but also keep the qubit coherence will be pinpointed. For example, continued from previous qubit and cavity design, we put two more qubits on the side inside the cavity for A-B comparison.

In Fig. 20 b), the W factor has been plotted on the surface of the cavity inner side. After the optimized point has been decided, by sweeping the pin length, the pin length will be determined to fulfill both conditions. As we can see in Fig. 20 b), in order to get the cavity external Q around 4000, the pin length will be 4 mm.

At this point, the simulations have almost done, we can proceed to the next step, bringing the simulation to real life, including machining and fabrication. In practice, there are still several loss points that could be easily overlooked. For example, the higher harmonic modes of the cavity, quasi-particles in Josephson junction [48], surface loss [49] and etc. With the development of superconducting system, we have started seeing people reach over milliseconds transmon modes and over seconds resonator modes. This still could be a very broad field waiting for people reaching another level.

3.0 Fabrication and Characterization

This chapter presents the superconducting fabrication techniques I have used during my graduate studies. Although the specifics may not be directly relevant to other fabrication projects and materials, I believe these recipes share some basic principles that can be easily adopted from one project to another. Many of the techniques in this chapter have already been discussed repeatedly in the literature; but there are usually steps missing or overlooked. Here I have tried to go through carefully and step-by-step the fabrication of Josephson junction with different styles, which could be a very good introduction for new students coming into this field or starting in the Hatlab.

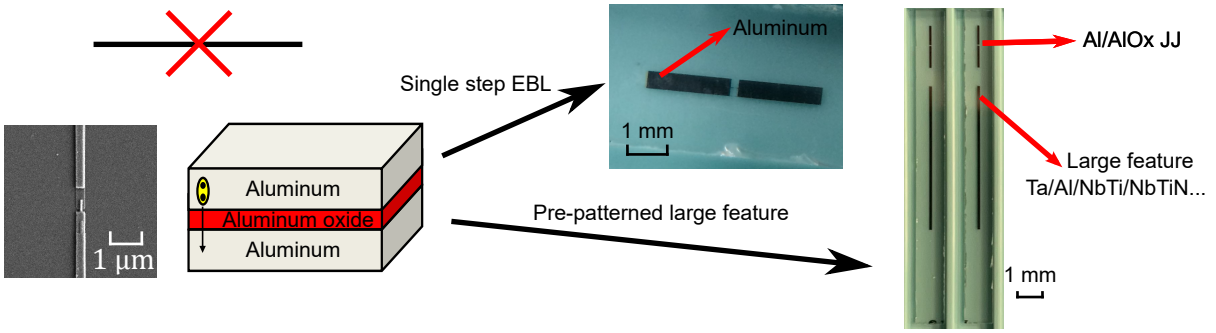

Figure 21: **JJ-based superconducting circuit fabrication.** In our lab, most superconducting circuit fabrication focuses on making high quality Josephson junctions with precise critical currents. We adopt two basic and general fabrication techniques: first, single step EBL, in which we use EBL to finish all the features in one exposure and deposit metal once. Another way is patterning the large structures first and then only using EBL to write JJs, which are usually ohmically connected to the large features.

In our lab, the superconducting circuit fabrication focuses almost exclusively on JJ-based devices. In lots of scenarios, making the sure JJs are as well controlled as possible is the primary consideration. During my PhD, our lab has worked in two primary styles of fabrication (as shown in Fig. 21). Before 2019, single step E-beam Lithography (EBL) was generally used, which means the whole pattern of the chip, including the Josephson

junctions, will be done in a single EBL write step. The metal is then deposited in a single step through the resultant mask. Even though this way is more straightforward, the writing time (typically overnight) and stability in our older Raith E-line EBL were a big challenge. Moreover, the residues of resist and the interactions between the Josephson junctions and the surrounding big features can be quite challenging. For example, typically, we have to write several hundreds of microns of the antennas that form our transmons before the dose in a dose test resembled the dose of an actual transmon. After 2019, we rebuilt the fabrication following Houck's tantalum transmons, with kind assistance from Andrew Houck and Alex Place [50]. Rather than finishing everything in one step, we first fabricate all large features in tantalum (Ta), adding the aluminum (Al) JJs in a final step.

In this chapter, I'll first discuss basic fabrication techniques before discussing specific issues with Josephson junction fabrication. This is covered in two sections. in Sec. 3.1, several basic superconducting fabrication steps are presented in detail. Then in Sec. 3.2, I will focus on fabrication of different sizes and shapes of Josephson junctions in different scenarios via the tools we have introduced.

3.1 Superconducting circuit fabrication steps

In this section, I present three main fabrication steps. The first step is the fabrication of large features ($\sim> 5\,\mu$m) with Al or Ta. The second step is depositing metal for subsequent patterning. Finally comes JJs fabrication with e-beam lithography. Details of common recipes are shown at the end of this section in a table for readers' easy use.

3.1.1 Large feature fabrication

Typically, superconducting circuits have been fabricated on silicon or sapphire substrates. In the Hatlab we use only two wafer types: silicon wafer (exclusively for amplifiers) which are double-sided polished with thickness of $250\,\mu$m, resistance around $3000 - 5000\,\Omega/$cm and crystal direction (100). Silicon wafers allow for conducting layers at room temperature to

reduce effects of static discharge, while becoming insulators at low temperature. They are also much easier to saw. Everything else is patterned on sapphire wafers (in early years from University Wafers and now from Crystek) with thickness of 430 μm, double-sided polished with crystal direction in C-M plane. Sapphire substrates are often believed to have less internal loss, thus potential higher Qs in microwave circuits. However, some groups and also major organizations such as IBM show excellent performance in Silicon qubits and circuits[51].

Before doing anything else, we generally clean the wafer (sapphire or silicon) by sonicating in acetone and isopropyl alcohol (IPA) for 5 minutes, then hard baking at 175 °C for 3 minutes to remove any potential particles or residues.

Next comes large feature fabrication. Here, large features refer to any metal of size bigger than 5 μm, which can be directly patterned with optical lithography. Practically, this includes ground planes for lumped elements, coplanar waveguides and other transmission lines, antennas or capacitor designs in superconducting circuits, (e.g. transmon-like circuits) and so on. In short, this process has the following five sub-steps:

1. Metal deposition
2. Spinning optical resist
3. Optical lithography
4. Metal etching
5. Stripping resist.

Note that this is a subtractive process in which we first cover the entire wafer in metal and then remove it where we don't want it to be in the final circuit.

Metal deposition. We'll cover the details in Sec. 3.1.2. For now, assume we have successfully deposited the large features we need. Normally, the metal will be a superconductor, and for us, we most often use aluminum or tantalum for this step.

Next, spinning optical resist. In general, there are many aspects that need to be considered in choosing the right resist. For example, the chemicals we are going to use in the following step (i.e. wet etching, R.I.E., etc.), the thickness of resist we need, and the

uniformity of the result. Here, due to the fact that we are going to go through several strong acid procedures, we have chosen AZ1518 as our mask.

One important thing to remember for spinning the resist is that you want absolute uniformity and consistency every time you execute the procedures. The recipe we are using is following:

Table 1: AZ1518 spinning recipe

Step	Description
1	20s 500 RPM with 100 RPM/s
2	20s 1000 RPM with 100 RPM/s
3	90s 4000 RPM with 500 RPM/s
4	30s 0 RPM with 500 RPM/s
5	Bake on hot plate at 100 °C for 3 mins.

And for uniformity's consideration, the center of the round wafer need to be put at the center of the spinner using an aligner; for non-round shape wafer, a pre-deposited marker can be used to keep the same position for each spinning.

Then, optical lithography. Immediately after spinning the resist (to prevent any unnoticed exposure on the resist), a direct photolithography can be applied on the sample. In our lab, we have used the Heidelberg MLA100 direct write lithographer to carry out the process. One thing to notice here is that an inverse pattern is written on the chip, which means unwanted metal will be etched away in the later process. After that, by immersing the chip in the AZ300 MIF solution at room temperature for 85 seconds followed by rinsing in DI water for 30 seconds, the chip can be properly developed. Before we move on, we generally bake the chip again at 115 °C for 2 minutes to keep the sample dry.

Metal etching. After putting the inverse mask on top of the metal we have deposited on the substrate, we can etch the unwanted metal away. In order to clean any residues coming from previous steps, we first put the sample into the plasma asher to let oxygen plasma remove hydrocarbons. Here, the asher has been set to 30 mTorr O_2 with 20W/200W RF/ICP coil power for 120 seconds. Then, based on the material we have deposited, the

whole wafer is dipped into tantalum etchant 111 for 26 seconds or aluminum etchant type A for 4 minutes. According to Houck's lab's latest result [50], for tantalum etching, very small differences in etching time could result in different performance. Maybe in the future, diluted tantalum etchant 111 or dry etching [52] could be tried for tantalum etching.

Stripping resist. Last, the sample is sonicated in toluene, acetone, methanol and IPA ('TAMI-cleaned') for 5 minutes each to fully remove any residue resist or other chemicals. And before the next step, we also put the chip into piranha solution ($2:1$ H_2SO_4 and H_2O_2) for 20 minutes followed by rinsing in three cups of DI water, 10 seconds each. In the end, the sample is rinsed in the IPA one more time for 30 seconds and baked at 175 °C for 5 minutes.

3.1.2 Metal deposition

Metal deposition can be tricky and complicated during the fab process. The whole process normally includes three steps: first, ion milling; then, environment conditioning; last, metal deposition. For each step, there are several parameters that could be optimized to get a proper result. However, to prevent main points have been distracted, we use several recipes as examples and explain the purpose of each step.

First, **ion milling**. A very similar step we have used in plasma asher, ion milling is the process of removing the top amorphous layer on a material to reveal the pristine sample surface for high-resolution imaging and post-processing. One example of recipe is following:

As we can see from the recipe, ion milling is a physical etching process whereby the ions of an inert gas (e.g. Ar) are accelerated from a wide beam ion source into the surface of a substrate in vacuum which can also be described as 'ionic sandblasting'.

The steps themselves are pretty straightforward. First, Ar is admitted in the proximity of a filament, then by DC discharging the filament, electrons are produced by thermionic emission. These electrons in turn ionize some Ar gas atoms.

After we stabilize the gas injection, the power of ion source and accelerator are directly related to the milling strength. In general, higher strength can remove the amorphous layer more efficiently, however, sometimes we also use suspending structures which are very easily destroyed by those ions (e.g. in Fig. 32 a3)). The number we have recorded in the recipe

Table 2: Ion milling

Step	Description
1	Gas inject: Argon (Ar) until 8.0 sccm in chamber
2	Start DC discharging ion beam to 40 V
3	Gas stable: Change Ar to required pressure: 4.0 sccm
4	Ramping up ion beam to 400 V and 22 mA with 80 V acceleration voltage
5	Wait recipe time: 30 seconds
6	Turn off ion beam
7	Turn off Ar

could be a good start developing new one in the future.

Then, **environmental conditioning**. Before the deposition, we perform another step called conditioning. The purpose of this step is to make sure the machine always starts with the same environment. Titanium thin film is used as an adhesive thin film to hold particles on the chamber wall which can prevent unwanted particles from falling on the chips.

Lastly, **metal deposition**. In our lab, depositing thin film on a substrate could use either sputtering coating or e-beam evaporation methods. As shown in Fig. 22, sputtering coating is a physical vapor process which starts by electrically charging a sputtering cathode which in turn forms a plasma causing material to be ejected from the target metal. We can think that the material is bonded to the cathode, and the magnetron sputtering gun is used to ensure stable and uniform erosion of the material. At a molecular level, the target material is directed at the substrate through a momentum transfer process. The high energy target material impacts the substrate and is driven into the surface of the substrate, forming a very strong bond at an atomic level. The material becomes a permanent part of the substrate, rather than an applied coating or plating of the surface. The benefit of sputter coating is the stable plasma created, which in turn provides a more uniform deposition, meaning the coating is consistent and durable.

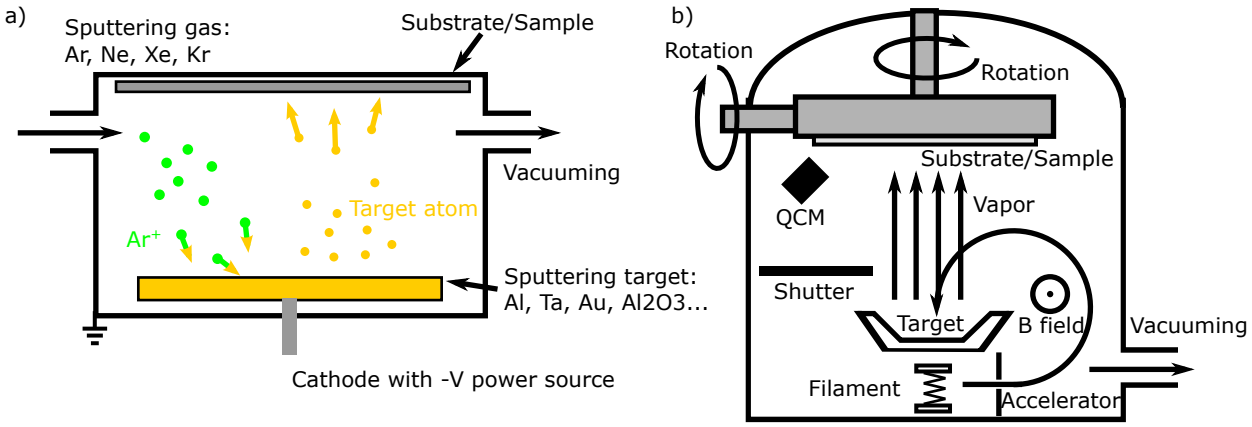

Figure 22: **Sputtering and e-beam evaporation.** a) Sputtering coating. Sputtered atoms ejected from the target impact energetically on the substrate or vacuum chamber (causing resputtering), sometimes, magnetron is also used behind the negative cathode to trap electrons over the negatively charged target material so they are not free to bombard the substrate, allowing for faster deposition rates. b) E-Beam or Electron Beam Evaporation is a form of Physical Vapor Deposition in which the target material to be used as a coating is bombarded with an electron beam from a charged tungsten filament to evaporate and convert it to a gaseous state for deposition on the material to be coated. Here QCM stands for quartz crystal microbalance which is an extremely sensitive mass balance that measure nanogram to microgram level changes in mass per unit area.

Another method of vapor deposition is e-beam evaporation, which first generates an electron beam by a charged tungsten filament under high vacuum. Then the target metal anode is bombarded with the electron beam (e-beam) to transform into the gaseous phase. These atoms then precipitate into solid form, coating everything in the vacuum chamber (within line of sight).

In the end, one major difference between sputtering and e-beam evaporation is directionality, where the first has better uniformity in sacrifice of directionality, and the second can control direction precisely without any sacrifice at some level. Someone may argue e-beam

evaporation has limitation on uniformity, however, the use of masks and planetary motion (both rotatory and tilting motion) can mitigate this problem.

3.1.3 E-beam lithography (EBL)

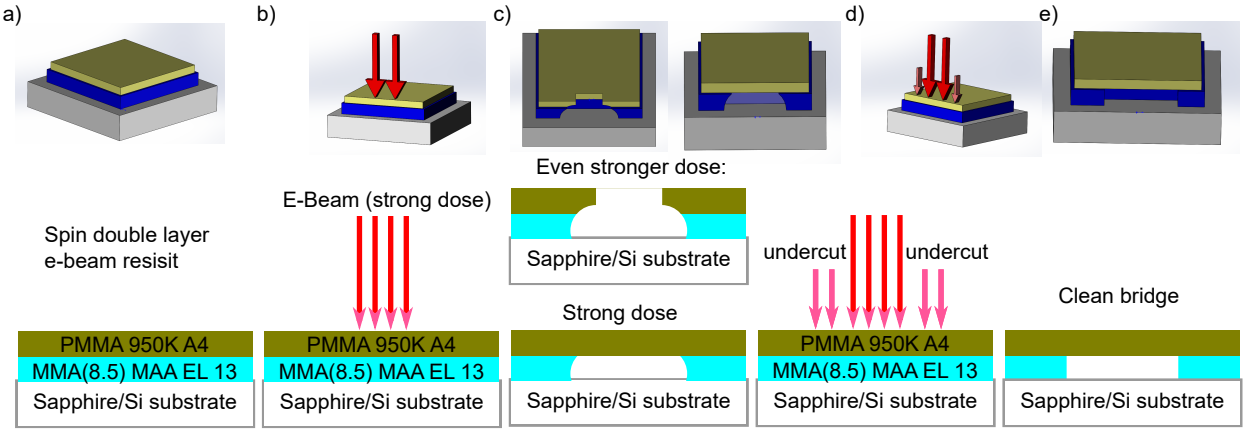

Figure 23: **Double layers of resists for EBL.** a) First two different resists are spun on top of the substrate. In general, the top resist is stronger than the bottom (e.g. MMA and PMMA); b, c) By changing the dose factor of e-beam, either both resists or only the bottom one is removed; at the same time, proximity effect can be observed in the bottom one. d, e) By adding undercut around strong dose, a very sharp edge can be created in bottom layer. Also, a floating layer can be created by tuning a proper dose.

Now we're ready for some small ($< 5\,\mu$m) features' fabrication. In our lab, e-beam has been used on resist to form a mask that is generated in a mask design software. The Raith e-LINE system we have has a maximum accelerating voltage up to 30 kV and the area dose we set up in the machine is 300 μC/cm. The whole process has exactly the same steps as its large feature fabrication; however, there are some details that are totally different.

First, instead of single layer resist, double layers of resists have been chosen where the bottom one is methyl methacrylate (MMA) and the top one is poly-methyl methacrylate (PMMA). Due to the relatively weak chemical bond, MMA is easier to remove than PMMA. There are several reasons we have chosen these two; one of the main reason is for making a

suspending bridge (as shown in Fig. 23). We also find double layers of resists make lifting off small features much easier than the single layer does, where the unwanted metal and wanted metal may form a connection after deposition.

To be specific, the resists we are using are MMA(8.5) MAA EL 13 and PMMA 950K A4, and the spinning recipe has been attached in Table. 3. The process itself is pretty straightforward, but there are two things I want to point out: First, even though the volume of resist is labeled, in the real process, it is very hard to control the exact volume since we want to prevent any air bubbles. Maybe a better way to control volume could be explored. Second, in the 6th step, cooling down the substrate with compressed N_2, can efficiently improve the uniformity of second layer.

Table 3: Double layers of resists

Step	Description
1	First layer: MMA EL 13: 240 mL
2	10s 500 rpm with 100 RPM/s
3	90s 2000 rpm with 500 RPM/s
4	30s 0 rpm with 500 RPM/s
5	Bake the substrate for 90 sec at 175 °C
6	Cool down the substrate and clean the spinner
7	Second layer: PMMA 950K A4: 210 mL
8	10s 500 rpm with 100 RPM/s
9	90s 3000 rpm with 500 RPM/s
10	30s 0 rpm with 500 RPM/s
11	Bake the substrate for 90 sec at 175 °C

Regarding lithography process, the very first thing to be considered is the accumulation of negative charge during the e-beam writing. Compared to silicon with $0.1\,\Omega\cdot\mathrm{m}$ resistivity, sapphire has $10^{14}\,\Omega\cdot\mathrm{m}$ resistivity at room temperature, which make the sapphire substrate a very good reservoir accumulating negative charge. As shown in Fig. 24, depositing another thin (40 nm) film of aluminum can efficiently solve the problem. Later, the thin film can

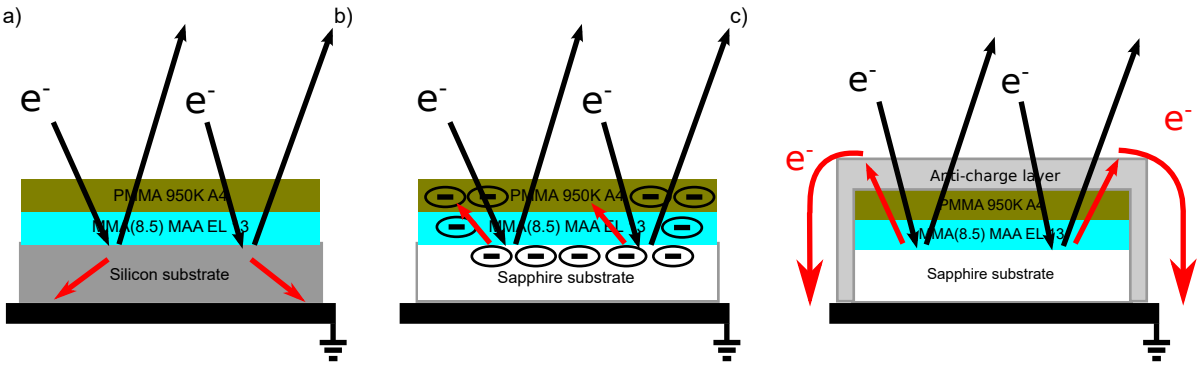

Figure 24: **Anti-charge layer.** Here the thickness of each layer doesn't indicate any real thickness. a) For the conductive substrate, like silicon, the charges can go through the substrate and dissipate into the ground. b) Without anti-charge layer, sapphire substrate could be a great reservoir accumulating negative charges, very soon the resists will be over exposed. c) By depositing a thin anti-charge layer (i.e. 40 nm aluminium), the negative charges could distribute into the ground.

be easily removed using different solution (e.g. MF-319). People also have started using high resistivity silicon wafer these days; an anti-charge layer is also required in this scenario. And there are other options for an anti-charge layer. For example, Espacer, an aqueous solution that doesn't contain any organic solvent, is another choice if metal contamination is a problem during the process. Another thing is that we have found different thicknesses of aluminum film could result in different doses in EBL. However, no significant quality difference has been observed in the later process.

Following the regular EBL process laid out, the coming step will vary for different circuit designs and instruments used. Specifically, due to the features' sizes and shapes, the proximity effect of the electron beam can be an extremely concerning point regarding the quality of exposure. We'll try to give some examples and analyze the difficulties of making them, especially making Josephson junctions, in Sec. 3.2. At this point, let's just say the resist has been successfully exposed. Next, we remove the anti-charge layer. In our lab, we put the chip in MF-319 for 4 minutes at room temperature, followed by rinsing in DI water.

After that, the wafer is ready for developing.

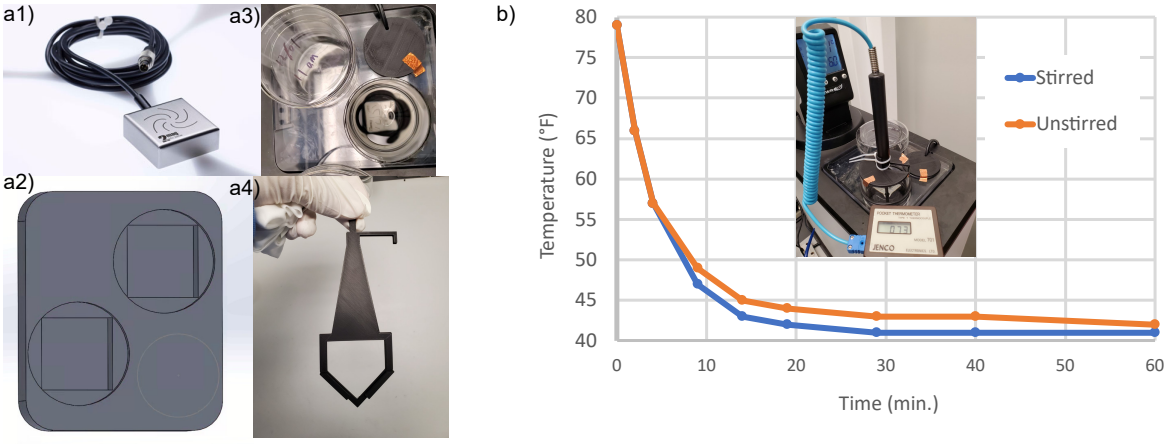

Figure 25: **post-EBL developing.** a) Details of post-EBL developing: a1) the submersible magnetic stirrer; a2) 3D printed holder for stirrer and beaker inside cold bath; a3) Developing setup; a4) chip holder for fixing the developing position and direction. b) The temperature of developing solution has been tracked with or without magnetic stirrer.

In order to control the speed of development and increase the success rate, the developing process is finished in a cold bath at 4 °C. The solution we are using is a mix of IPA and DI water with 2.4 : 1 mass ratio. Again, to strictly control the environment, a submersible magnetic stirrer (as shown in Fig. 25 a1)) has been used in this process. Moreover, both the depth and direction of the wafer inside the beaker need to be consistent between each run to minimize any environmental fluctuation. One bonus point of using the magnetic stirrer is that the solution is well-mixed after a shorter time. In general, the chip is put into the solution for 2 minutes and then rinsed in DI water for another 30 seconds.

After that, the sample is ready for deposition. Because of the precise mask design, it is suited for directional deposition using the e-beam evaporation process. Most of JJs in our lab are fabricated during this step, and based on the techniques people use, the deposition rate, angle and thickness of the thin film can be precisely controlled to get high quality JJs.

In the end, the unwanted deposited metal need to be lifted off. We are using hot acetone for the stripping process. Typically, the chip is immersed in the acetone at 80 °C for 2-3 hours depending on the samples' size. We don't have any solid evidence showing too long

stripping time damages the sample. Using room temperature acetone can also strip the resist. It is safer with room temperature acetone; however, the process requires about twice the time.

3.1.4 Summarized recipe

In this section, the several processes mentioned above have been summarized step-by-step in table format for easy use. The four processes include: 1. Aluminum base layer 2. Tantalum base layer; 3. Sapphire dielectric deposition; 4. EBL procedure and dicing process.

Table 4: Al base layer

Aluminum coating	Clean wafer: Sonicating in Acetone, IPA and DI water for 5 mins each;
	Deposition: Deposit 150nm Al on cleaned Si wafer;
Photolithography	AZ1518 resist (20s 500 RPM; 20s 1000 RPM; 90s 4000 RPM; 30s 0 RPM) then heat 3 mins on hotplate at 100 °C.
	Doing MLA writing with 200 mJ/μm^2 dose setting.
	Developing: 85s in AZ300 MIF; and rinse in DI water.
	Heat 2 mins on hotplate at 115 °C.
Aluminum Etching	Asher cleaning: 2 mins in 30 mTorr O_2 with 20W/200W RF/ICP coil power.
	Al etching: Stirring in Aluminum etchant A for 4 mins; then clean it with 3 cups of DI water;
	Clean wafer: Sonicating in Acetone, IPA and DI water for 5 mins each;

Table 5: Ta base layer

Tantalum coating	Deposition;
	Piranha-clean: 2:1 H_2SO_4 and H_2O_2 for 20 mins; And stirring in 3 cups of DI water after; dipping into IPA to clean in the end.
	Heat 5 mins on hotplate at 140 °C.
Photolithography	AZ1518 resist (20s 500 RPM; 20s 1000 RPM; 90s 4000 RPM; 30s 0 RPM) then heat 3 mins on hotplate at 100 °C.
	Doing MLA writing with 210 mJ/μm^2 dose setting.
	Developing: 85s in AZ300 MIF; and rinse in DI water.
	Heat 2 mins on hotplate at 115 °C.
Tantalum Etching	Asher cleaning: 2 mins in 30 mTorr O_2 with 20W/200W RF/ICP coil power.
	Tantalum etching: Stirring in Tantalum etchant 111 for 30 secs; then clean it with 3 cups of DI water.
	Sonicating in toluene, acetone, methanol and IPA ("TAMI-cleaned") for 5 mins each.
	Piranha-clean again.
	Heat 5 mins on hotplate at 140 °C.

Table 6: Sapphire dielectric deposition

Sapphire dielectric	AZ1518 resist (20s 500 RPM; 20s 1000 RPM; 90s 4000 RPM; 30s 0 RPM) then heat 3 mins on hotplate at 100 °C.
	Doing MLA writing with 200 mJ/μm^2 dose setting.
	Developing: 85s in AZ300 MIF; and rinse in DI water.
	Heat 2 mins on hotplate at 115 °C.
	Asher cleaning: 2 mins in 30 mTorr O_2 with 20W/200W RF/ICP coil power.
	Deposition: Deposit 60nm Sapphire on developed wafer;
	Lifting off: Sonicating in Acetone, IPA and DI water for 15 mins each;

Table 7: E-beam Lithography(EBL) procedure and dicing procedure

E-beam Lithography	Spin: MMA El13 (10s 500 RPM; 5s 2000 RPM; 90s 2000 RPM; 10s 0 RPM) heat 90s at 175 °C.
	2nd Layer: Then PMMA 950K A4 (10s 500 RPM; 5s 3000 RPM; 90s 3000 RPM; 10s 0 RPM) heat 15mins at 175 °C.
	Anti-charge layer: deposit 40 nm Al on the chip.
	EBL writing
	Remove anti-charge layer: 4 mins in MF-319; and rinse in DI water.
	Developing: stirring in IPA/DI water (2.4:1 mass ration) at 4 °C for 2 mins; Then rinse in DI water for 30s.
	Plassys: Double-angle deposition.
	Lifting off: 2 hours in hot (80 °C) acetone, then briefly sonicate.
Dicing	Protecting Layer: S1805 (5s 500RPM; 60s 1000RPM) heat 3 mins at 80 °C.
	Dicing.
	Clean protecting layer: rinse in acetone for 10s.

3.2 Josephson junction fabrication

Now after all the details we have discussed in the previous section, we're finally ready to make some Josephson junctions. In order to make the junction precious enough (as close as designed), people have tried lots of different methods for different sizes and shapes of junctions. In our lab, the two main ways of making JJs are the Dolan technique and Manhattan technique. This section starts from introducing these two ways, then shares some basic difficulties we have encountered during fabrication. In the end, the pros and cons are discussed to let people choose which way is better for a specific sample.

3.2.1 Dolan technique

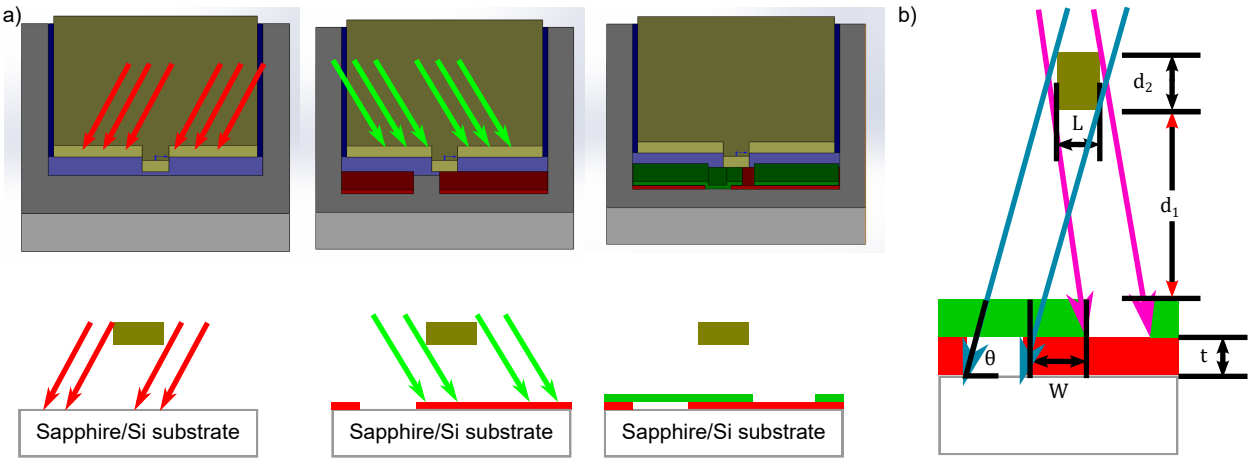

Figure 26: **Dolan bridge with double angle deposition.** a) Dolan bridge with double layers of resists then deposit aluminum with two different angles; b) JJ size's dependence. Depending on the evaporation angle, the shadow image of the mask is projected onto different position on the substrate. By carefully choosing the angle for each material to be deposited, adjacent openings in the mask can be projected on the same spot, creating an overlay of two thin films with a well-defined geometry.

The Dolan technique traces back to 1977 [53]. It is also called Niemeyer-Dolan technique, since Niemeyer first used this idea to make the junctions [54]. Normally, people think of

this technique as shadow evaporation, which is a thin-film lithographic method to create nanometer-sized overlapping structures.

As shown in Fig. 26, the key feature in the Dolan technique is the suspending bridge which can be created using double layer resist (shown in Fig. 23). Then, metal deposition is deposited with mask. In our lab, the JJs are mainly made of Al−AlOx−Al, which makes the whole deposition process only need one type of metal with an oxidation step in between the two depositions. By carefully choosing the deposition angle during the e-beam evaporation process (discussed in Sec. 3.1.2), an overlay of two thin films can be created.

The regular recipe in our lab of the double angle deposition is following:

Table 8: Double angle deposition

Step	Description
1	20 nm aluminum deposition at rate of 0.5 nm/s with 50 °
2	Oxidation process with O_2 @ 95 mbar for 30 minutes.
3	Another 30 nm aluminum deposition at rate of 0.5 nm/s with −50 °

To calculate the junction size exactly, based on the parameters labeled on the Fig. 26 b), the overlay width W can be calculated as :

$$W = 2d_2/\tan\theta - L \tag{44}$$

where d_2 is the thickness of the MMA resist, θ is the deposition angle, and L is the width of suspending bridge. Normally, θ and L are fixed between different runs, and the sizes of JJs A can be easily controlled by changing the structures of bridges.

As shown in Fig. 27, the blue regions (weak dose blocks) in the GDSII files can be treated as the suspending area, and the red regions (strong dose blocks) are deposited in two different angles which can overlay with each other. Normally, based on the oxidation time and oxygen pressure we have used during the deposition procedure, the current density J_c of JJs is fixed between different samples. Then the critical current of JJs I_c can be easily calculated as $I_c = J_c \cdot A$.

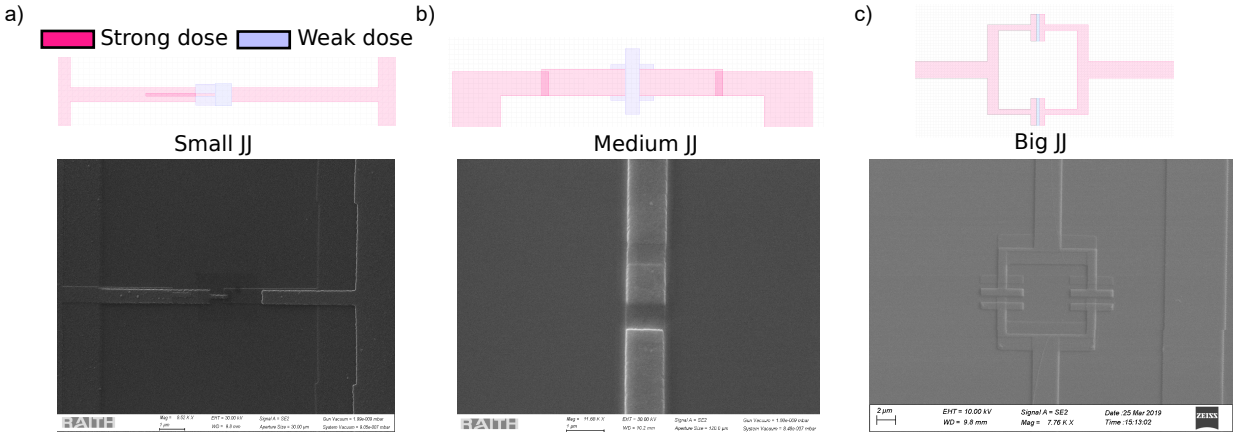

Figure 27: **SEM images of small, medium and Big JJs.** The first row represents the corresponding GDSII files for fabrication, where red blocks mean stronger dose in EBL and blue ones mean weaker dose. And the second row is the associated SEM images.

However, in real life, the Dolan technique is sometimes tricky to implement, regardless of the size of the JJs. For instance, when several in-series JJs (normally, odd number of) are needed, they can be realized using the Dolan technique. However, due to the close proximity effect, the JJs are never symmetric. In order to solve this problem, several different dose tests need to be performed. In general, people can apply different dose factors on each red block shown in Fig. 28 a), or an intentionally asymmetric design can be used to compensate for the proximity effect.

Regarding small JJs, more challenges arise. Let alone the proximity effect, which can be solved by adding more blocks with different doses to correct, there are still lots of fluctuations on deposition angles, thickness of resists, and oxidation layer growth. It is quite common that the junction ends up having a different size than designed. Moreover, because we're trying to use the overlay of two different depositions, the edge of each deposition becomes very critical. Additionally, the side of the resist is not as sharp as we expect. All of these factors lead us to the fact that the exact size of JJs cannot be easily controlled.

From the experience in our lab, we think reproducible results rely on a controllable environment, which includes every step starting from spinning resist until stripping the

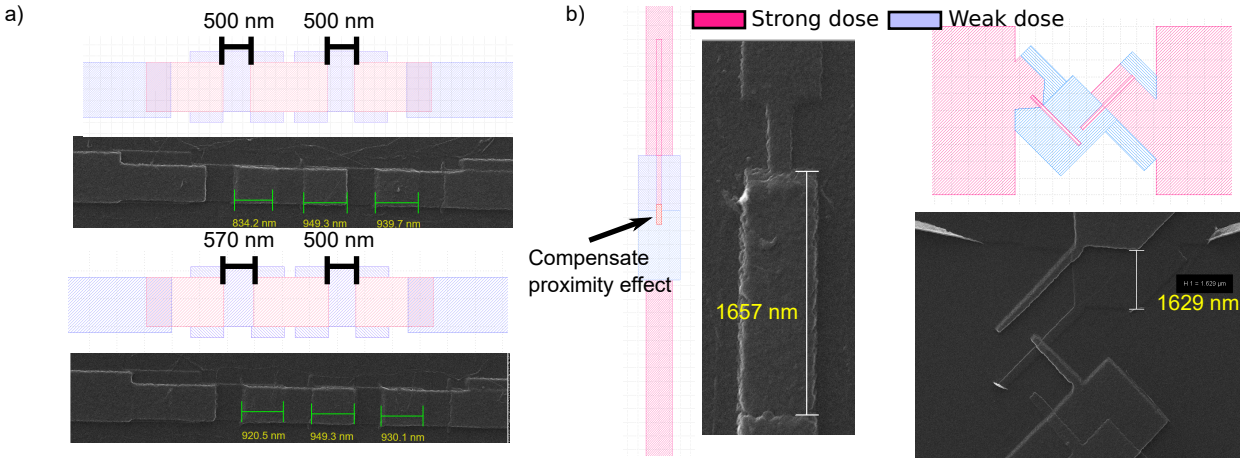

Figure 28: **JJs fabrications could be hard.** a). One difficulty could be the asymmetry of JJs in series. And based on the SEM results, intentionally controlling different blocks' size could be a solution for a given size JJ. b) Another one is that the edge of the small JJ's bridge is not as sharp as expected which results in fluctuated overlay width. If the finger's width can be easier to control, the finger crossing pattern may be used in the design.

resist. As we have discussed in the previous section, all parameters in each step have been strictly recorded, and we also try our best to minimize any uncontrolled process including random hand movement (one example is shown in Fig. 25). Furthermore, we're also trying to develop new patterns forming the JJs. Instead of using the edge of each deposition, the finger crossing feature (as shown in Fig. 28 b)) may have better performance under some conditions. Even though we don't have solid proof that controlling the width of fingers is actually easier than controlling the deposition shift, the former is more dependent on a stable dose and the latter is more dependent on the thickness of resist and deposition angle.

One thing we want to emphasize here is that in the experiments, the resistances of JJs are first measured before we cool down the sample. Via the **Ambegaokar-Baratoff relation [55]**, we can derive the corresponding critical current I_c in the superconducting regime from the resistance R_N at normal state regime ($\Delta = 0$).

$$L_J = \frac{\hbar}{\pi\Delta} R_N = \frac{\varphi_0}{I_c} \tag{45}$$

where Δ is the superconducting energy gap and φ_0 is the reduced flux quantum.

In the experiments, we often use this relation to decide the JJ's inductance before we cool down the sample. However, it is important to realize that: first, R_N is the junction's normal state resistance or tunneling resistance which only considers the resistance coming from metal-insulator-metal tunneling. This number can be precisely measured around $1.4-4.2\,\mathrm{K}$, and the room temperature resistance we generally measured includes not only tunneling resistance but also electrical resistance. Since both parts relate to the temperature, there is a coefficient between room temperature resistance R_J and tunneling resistance R_N. In our lab, we assume $R_J = 1.12R_N$; however, please keep in mind this number can vary between different antenna shapes and probe positions. At the same time, the superconducting energy gap for different thickness of aluminum film might also be different. The number we generally use is $182.412\,\mu\mathrm{eV}$, even though different numbers can be found in other articles [56].

Based on the above truth, we'd like to keep the deposition thickness and antenna shapes the same across samples. By fitting the relation between resistance measured at room temperature R_J and L_J calculated after cool down, a confident coefficient can be extracted in a period of time (half year to a year).

3.2.2 Manhattan technique

Correspondingly, the Manhattan technique is a younger technique [57], which was first developed in 2008. This technique can easily print large scale/numbers of qubits, and the overall pattern is like the 'Avenue' and 'Street' in Manhattan - that's where the name came from. And more interestingly, compared to the Dolan technique, where the metal is deposited at symmetric angle, in Manhattan technique, the metal is actually deposited at perpendicular angle.

For the single JJ design, the mask is simple, with only a cross where the JJ forms. Here, even without suspending structure, we still use double layers as resist for the following two reasons: 1. The metal is easier to strip, especially with a small deposition angle when the metal is connected together. 2. The thickness of resists can be stacked up. Notice here, you actually want the thickness of the resist for the Manhattan technique to be as large as

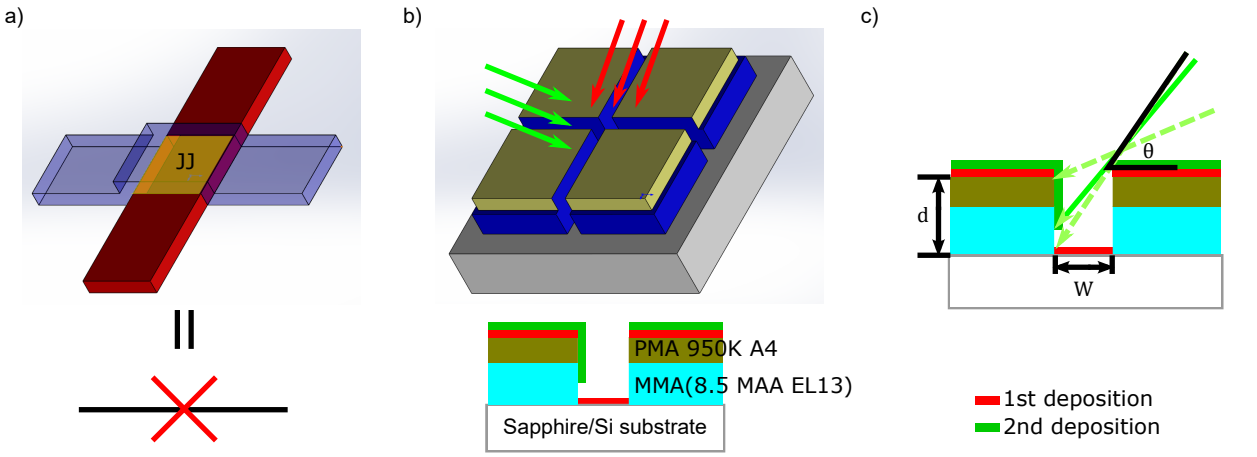

Figure 29: **Manhattan pattern for JJ fabrication.** a) Schematic representation of the Manhattan pattern, where the red and blue blocks indicate aluminum deposition with perpendicular planar angle; b) 3D representation of two deposition. By depositing at different angles, two sets of overlapping strips are formed. c) Based on the thickness of resists and the width of strips, the deposition angles have a minimum value.

possible instead of carefully controlling it to get designed junctions. For the second point, Fig. 29 is clearer to explain. As we can see, the perpendicular deposition will deposit all metal on the resist, as long as $\arctan\theta > d/W$. That's also why we want a thick stack to allow making as big JJs as possible.

And one advantage of Manhattan technique is the precision for the small junctions since now the size of junctions is related to the width of the trenches and how clean they are. Without suspending structure, the ion milling before deposition could be much stronger than before, since the resist itself is actually very hard to destroy. In this case, by ion milling the trench with stronger power only, the mask can have better shape. One way we can calibrate for the stability of this technique is by sweeping both the dose factor and the junction area to see how sensitively the resistance changes. As shown in Fig. 31, we find the relation is pretty linear ($\sim 1\%$) at some ranges. When the JJs are too small, the deviation becomes relatively large.

Again, even though we're trying to claim Manhattan pattern is better for making small

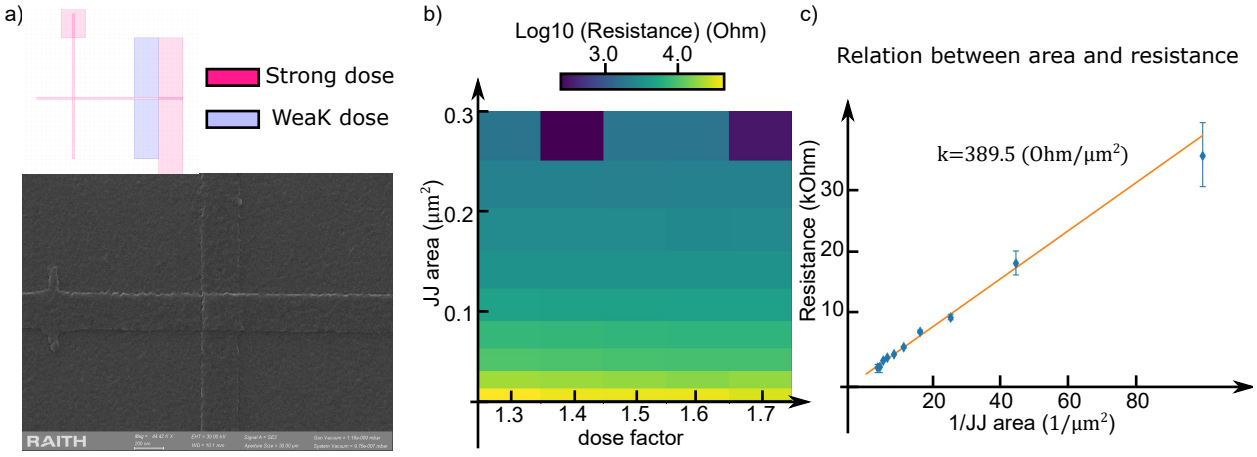

Figure 30: **SEM images of Manhattan pattern stability analysis.** a) SEM image of Manhattan pattern and the corresponding GDSII file; b) By changing the dose factor and the width of the strips, the resistances of formed JJs are tracked. c) By fitting the relation between resistance and 1/area, first order linear relation can be extracted (i.e. R = k/A).

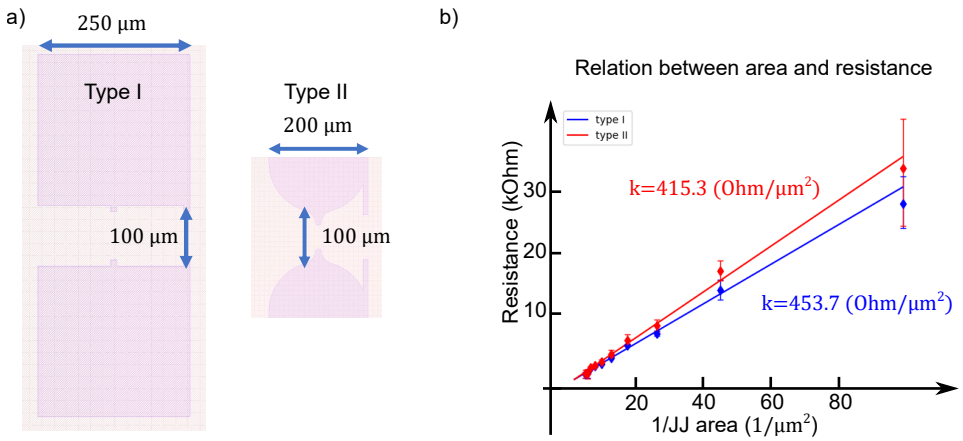

Figure 31: **The effect of different antenna shapes on resistances.** a) Two different shapes of antenna in the tranmon design; b) Fitted relation between junctions' size and resistances.

JJs because of its stability, the resistance between different designs and patterns for various experiments still can be different because of the proximity effect. In this case, we think a dose test for each different sample is still necessary if a precise resistance is needed.

3.2.3 Summary

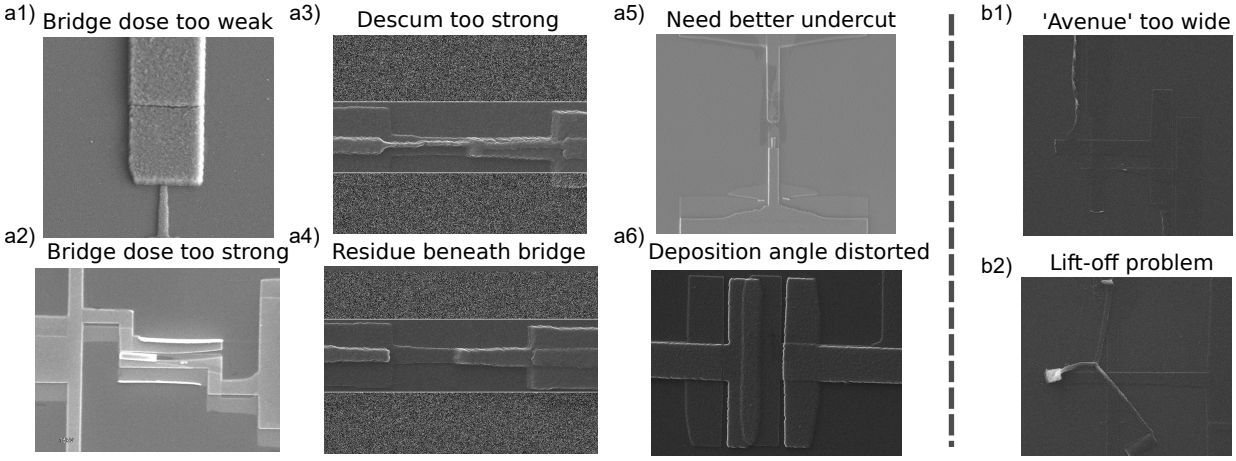

Figure 32: **Failed examples of JJs fabrication.** a) Possible failed reasons for Dolan bridge technique. Notice here, the reasons causing failed JJs are not excluded, most of time the failure is coming from many aspects; b) Possible failed reasons for Manhattan technique.

In the end of this section, we want to restate the difficulty of making junctions. Even though with industry has joined the game, and lots of large scale junctions have been made in the last three to five years, the quality of single junction is still be a topic people are trying to explore. In order to give the readers a more straightforward vision of failure during the fabrication, Fig. 32 shows several failed examples of making JJs both in Dolan techniques and Manhattan techniques. For each failure, the reasons may be due to multiple aspects, which also means the problem probably can be fixed in various ways. Despite the fact that sometimes changing a parameter in one step results in another failure in the other step, it is still worth trying different combinations to get a stable pattern.

Comparing the two different techniques we have discussed, we think the Dolan technique is still very good making different sizes' junctions, ranging from $0.01\,\mu\mathrm{m}^2$ to $10\,\mu\mathrm{m}^2$, as long

as with a stable pattern the junctions can be made consistently. Moreover, it is very simple making several odd numbers of junctions in series.

On the other hand, the Manhattan technique is really good at making small, precise junctions. Getting rid of suspending features in small junction fabrication offers the chance to aggressively ion mill and clean the substrate with mask before metal deposition, which results in a more controllable junction fabrication. Nonetheless, designing multiple junctions in series or fabricating large junctions sometimes can be quite grueling with this technique.

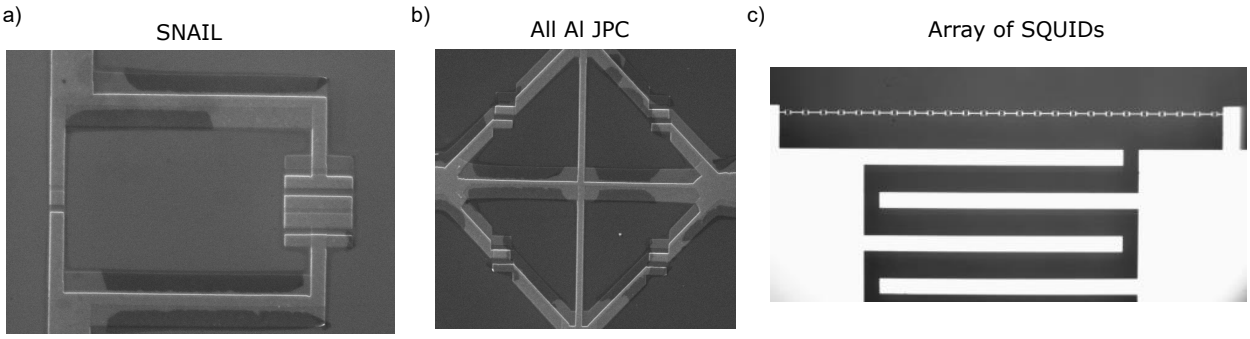

Figure 33: **SEM of different devices.** Here, we show some real examples of superconducting device based on Josephson junctions.

Lastly, we'd like to present several examples of real samples in our lab. Most of the fabrications we have done are related to the JJs themselves and based on the requirements we need. The JJs can be shunted with different sizes of capacitors and inductors. With all the techniques discussed and a bit of imagination, quantum engineering could be as easy as building Lego blocks.

4.0 Hardware Philosophy and Setup

After two chapters, we have completed the theory and prepared the sample, now we can finally cool down the sample and start measurement. Generally speaking, quantum measurements can be divided into two main categories: steady-state measurements and dynamical measurements. Most of the time, the former can be directly done in the frequency domain and the latter is done in the time domain. Sometimes the two kinds of measurements overlap to capture the whole picture. As shown in Fig. 34, choosing the right tools for specific jobs can be a challenge sometimes.

Thus, this chapter is divided into three sections and is following the same organization followed in Ch.3. First, we discuss the basic measurement techniques in different domains in Sec. 4.1, then in Sec. 4.2, qubit measurement is used as an example to go through all the techniques and also the tools we have used during the calibration and optimization of qubit operations. Last, Sec. 4.3 introduces parametric operations in experiments and explains the details on how to tuneup and calibrate a good parametric gate.

4.1 Basic measurement techniques

This section focuses on basic techniques that have been used in quantum measurement, which can be divided into frequency domain and time domain. Instead of discussing the quantum mechanics behind the measurement, I want the reader to have a clearer vision on how to operate different instruments for various measurements.

4.1.1 Frequency domain measurement

For the frequency domain measurements, the two most important instruments are the vector network analyzer (VNA) and the spectrum analyzer (SA). The VNA always compares the signal coming out from the dilution refrigerator with the signal sent in, while the SA

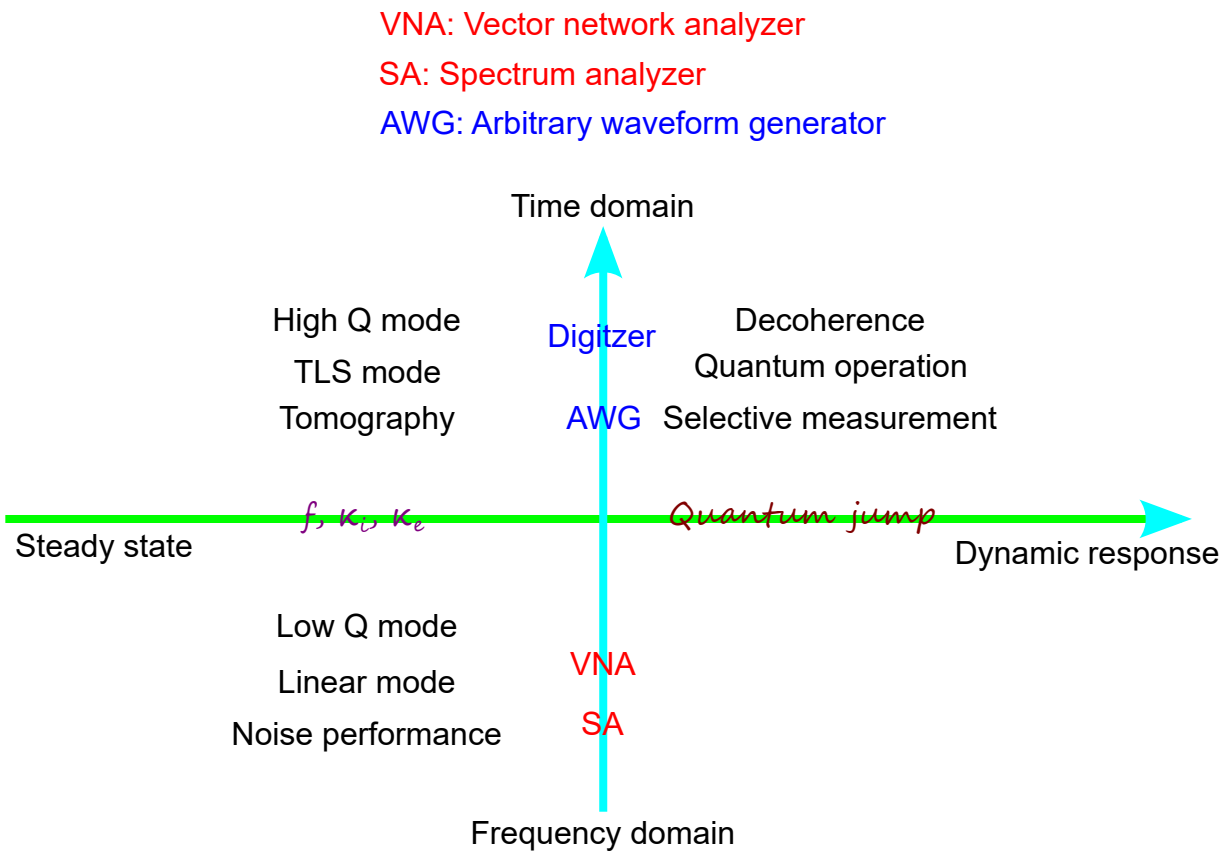

Figure 34: **Introduction of superconducting circuits measurement.** In most of the cases, quantum measurement is trying to figure out either steady state solutions or dynamics responses for a given system by using both frequency domain and time domain techniques to fully characterize the system under study.

monitors the power coming out in a range of frequencies. In the following part, I am going to introduce several experiments that these two instruments can perform to give an idea about what we can do with them.

VNA experiment. First, a very common experiment that a VNA can do is measuring the scattering parameters of a linear mode or a nonlinear mode with small anharmonicity ($\alpha/\kappa < 0.1$). The steady state solution has already been predicted in Sec. 2.1.2. As we have calculated in theory section, the mode we measured could have reflection response or

transmission response. But in practice, since the cryogenic input and output are always different, which means we always measure $S_{21} = \frac{V_2^-}{V_1^+}|_{V_2^+=0}$ in the VNA.

Another common experiment a VNA can perform is two-tone spectroscopy. It is a very useful tool in the dispersive coupled system, and we are going to introduce several examples in the qubit measurement experiments (Sec.4.2). The general idea of spectroscopy is using VNA to constantly measure one of the coupled mode, and another generator is used to sweep the frequency on the other mode. If two modes have dispersive coupling between them, when the generator 'hits' another mode, the response in the VNA will be different. By doing this, we can find a high-Q mode easily or a nonlinear mode.

SA experiment. The SA is widely used in amplifier measurements, which is not this thesis' topic. However, we still want to emphasize here that the SA can measure the background noise from the output. For example, in the cryogenic output line, the signal goes through three amplifiers: quantum-limited amplifier (JPC, TWPA, ...), HEMT @ 4K stage, and room temperature amplifier. One quick thing people could test is turning on the amplifier from high temperature to low temperature one by one and monitor the background noise change. If the noise doesn't change, that may be because the amplifier just turned on has very limited gain; however, if the noise increases too much, that may indicate the noise of this amplifier is too high.

One other thing SA can do is calibrate input signals. For the next section, time domain measurement, the quality of the input signal is a critical component which could relate to many aspects of the experiment. First, since most of the signal we are sending into the system is finite, choosing a good modulated signal is important because their Fourier transformation could be very bad (spurious tones, higher harmonics, and wide primary tone from short pulses) in frequency domain. Second, all signals go through lots of room temperature RF elements before they are sent into the fridge. For each element, they could have very different saturation power, working range, insertion loss and multi-port unbalance, which could distort the signal dramatically. Because of all the above reasons, if we always check the signal in SA before sending it into the fridge, we can save lots of time and trouble.

4.1.2 Time domain measurement

Another big category of the measurement is time domain measurement. In time domain measurement, we use an arbitrary waveform generator (AWG) sending a signal into the system in ns scale and demodulate the output in a digitizer also in ns scale. The whole process involve several RF elements for frequency conversion, up-conversion for input and down-conversion for output. As shown in Fig. 35, it forms a closed loop from input to output. More importantly, the whole setup makes a copy of the input, and mixes with the demodulate generator forming a reference signal to cancel any hardware drifts.

Let's take a close look at the readout setup. First, the AWG generates a signal shape (e.g. a Gaussian shape) and then the signal mixes with the LO generator at mode frequency to create a Gaussian modulated signal: $s_1(t) = A(t)\cos(\omega_a \cdot t + \phi_1)$. Here $A(t)$ is the pulse shape, ω_a is the mode frequency and ϕ_1 is the random phase coming from the first generator.

Then the signal s_1 is sent into the fridge to interact with the system, and carry both amplitude and phase information coming out from the fridge: $s_2(t) = B(t)\cos(\omega_a \cdot t + \phi_1 + \phi(t)$, where $B(t)$ and $\phi(t)$ is the complex information we cared about. The signal first go through an image rejection (IR) mixer, where the LO is the second generator with frequency $\omega_a - 50\,\text{MHz}$. Here the $50\,\text{MHz}$ difference makes the signal down-convert to $50\,\text{MHz}$ and the reason we choose $50\,\text{MHz}$ is because our digitizer sample rate is $500\,\text{MSample/s}$, and it is much harder to extract complex information from a DC signal. One more point I want to make here is the reason we choose IR mixer is because it can generate both LO-RF and RF-LO signal, in our case it is $+50\,\text{MHz}$ and $-50\,\text{MHz}$. And these two signal automatically average together, resulting in half (power) background noise in the result.

After mixing, the signal becomes $s_3(t) = B(t)\cos(50\,\text{MHz}\cdot t + \phi_1 - \phi_2 + \phi(t))$, where ϕ_2 is the random phase coming from the second generator. At the same time, a copy of generator one also mixes with generator two to create a reference signal $s_r(t) = C\cos(50\,\text{MHz} \cdot t + \phi_1 - \phi_2)$. At this point, the logic looks obvious: we want to use the reference signal to cancel the random process drift in $s_3(t)$, but this process cannot automatically finish in any RF element, which means we need to calculate it in the software.

So, both $s_r(t)$ and $s_3(t)$ send into the digitizer, and we use a digitized $50\,\text{MHz}$ oscillator

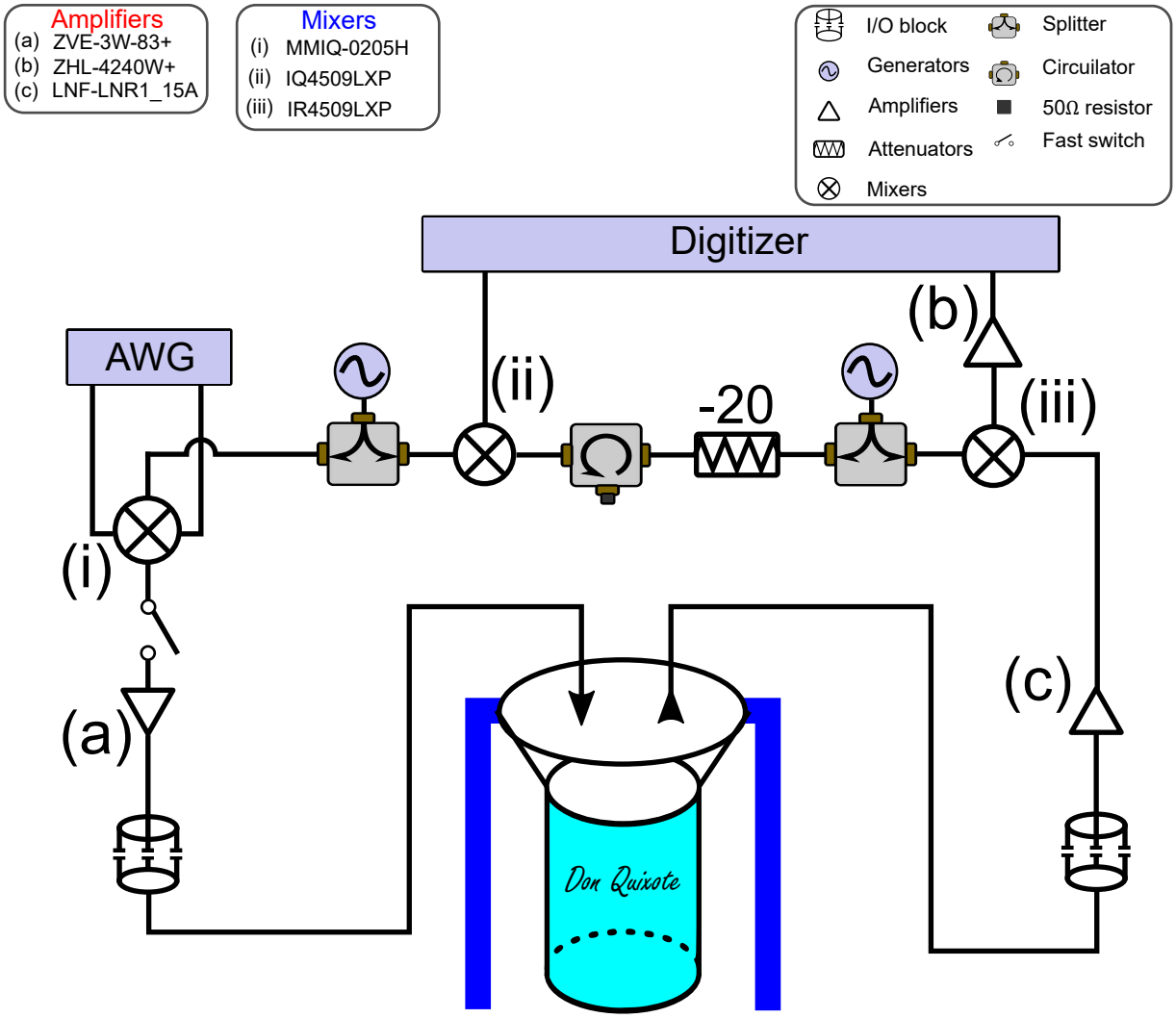

Figure 35: **Interferometric readout setup.** Schematic representation of an input-output measurement setup with interferometric readout.

to demodulate both signal:

$$\begin{aligned} \tilde{I} &= \int_t s(t) \cdot \cos(50\,\mathrm{MHz} \cdot t) dt \\ \tilde{Q} &= \int_t s(t) \cdot \sin(50\,\mathrm{MHz} \cdot t) dt \end{aligned} \tag{46}$$

After demodulation, we can get four arrays: $\tilde{I}_s$, $\tilde{Q}_s$ for $s_3(t)$ and $\tilde{Q}_s$, $\tilde{Q}_s$ for $s_r(t)$. Next, we need to rotate the random phase drift away from the real signal:

$$
\begin{aligned}
I &= (\tilde{I}_s \cdot \tilde{Q}_s + \tilde{Q}_s \cdot \tilde{Q}_s)/\sqrt{(\tilde{Q_s}^2 + \tilde{Q_s}^2)} \\
Q &= -(\tilde{I}_s \cdot \tilde{Q}_s + \tilde{Q}_s \cdot \tilde{Q}_s)/\sqrt{(\tilde{Q_s}^2 + \tilde{Q_s}^2)}
\end{aligned}
\tag{47}
$$

Now the I, Q are the real demodulation of signal coming out from the fridge. If the system we probed is a cavity, the I, Q are the cavity response in the $I-Q$ plane.

Above is the basic principle of the time domain measurement. In practice, based on the different manipulation of the qubit and cavity, the experiment could become very complicated. However, in the end, the last thing we measure is always a cavity response carrying the system information. We start introducing more complicated experiment in the next section.

4.2 Qubit measurement and calibrations

In this section, we take transmon qubit measurement as an example going through all the steps during the measurement using techniques we have mentioned in the previous section. After reading this section, we want the readers to have a straight idea about what is measurement, and how to calibrate a qubit from the very scratch.

4.2.1 Frequency domain measurement

4.2.1.1 Identify cavity mode

Everything starts from the frequency domain, and for transmon qubit measurement, even before we try to find the qubit frequency, we need to figure out the readout mode information first. And in most cases, this mode is a cavity mode, no matter in 2D or 3D.

Following the protocol, we have introduced in Sec. 4.1.1, we can find the cavity mode and get the basic information, frequency f and decay rate κ, about the cavity. Then the first interesting thing happens, a quick check to see if there is a qubit or not.

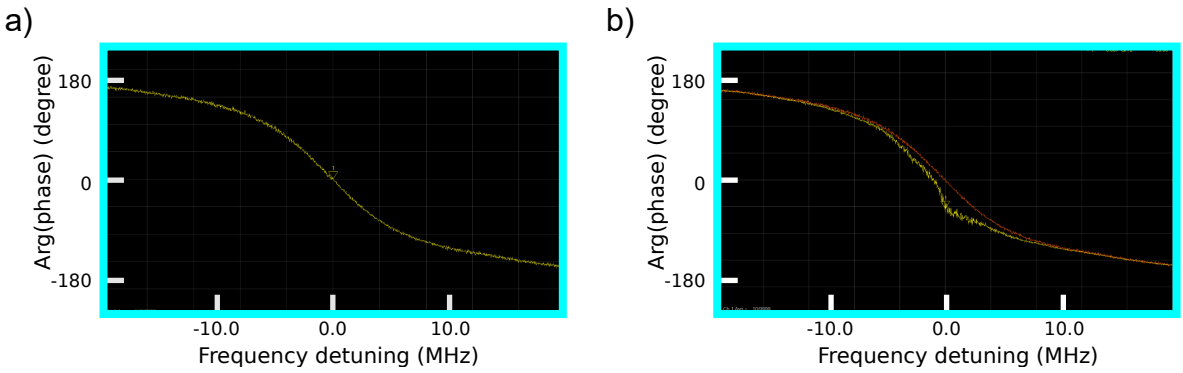

Figure 36: **Cavity response and high power response.**.

Based on the truth that transmon qubit has a strong anharmonicity ($\sim 200\,\mathrm{MHZ}$) and relatively strong coupling between cavity and qubit ($g/\Delta \sim 0.1$, where g is the coupling strength, and $\Delta = \omega_c - \omega_q$ is the frequency difference between two modes), the cavity itself also has a self-anharmonicity around $10 - 100\,\mathrm{KHz}$. As long as we have successfully put over 100 photons into the cavity, the cavity response will be distorted naturally, which can prove the existence of qubit (as shown in Fig. 36 b)).

4.2.1.2 CW spectroscopy

Next, find the frequency of qubit, **CW spectroscopy**. Again, for the Hamiltonian of qubit-cavity system, we have

$$\hat{H} = \omega_c c^\dagger c + \omega_q q^\dagger q + \alpha(q^\dagger q^\dagger q q) + \chi(q^\dagger q c^\dagger c) = (\omega_c + \chi\langle q^\dagger q\rangle)c^\dagger c + \omega_q q^\dagger q + \alpha(q^\dagger q^\dagger q q) \quad (48)$$

where, ω_c, ω_q are the resonant frequency of qubit and cavity; and α, χ is the anharmonicity of qubit and dispersive coupling between qubit and cavity. One thing we noticed from Hamiltonian, due to the existence of qubit and dispersive coupling between two modes, the occupation in the qubit mode automatically changes the cavity frequency which means if we can use another generate trying to 'hit' qubit frequency, then the cavity response will also change. That is also the key point of **two-tone spectroscopy**.

In practice, **1).** we first move to cavity resonate frequency, then change the frequency span on VNA to 0 Hz. Then **2).** a second generator is used to send a continues wave into qubit drive port, and by sweeping the frequency of the second generator, if the qubit mode has been 'hit', the cavity response in VNA will be changed. One thing that needs to be clarified is this protocol is a good example of quantum Zeno effect: when one generator is trying to drive the qubit, the VNA keeps measuring cavity to reset the qubit (or with small possibility, qubit jumps). On the other hand, because the cavity has been driven all the time, there is a relatively not small amount ($\sim$ 10 $\sim$ 100) of photons inside the cavity resulting in qubit frequency shift. With all the above, in order to get a clear spectroscopy, the power of both generator and VNA, and also VNA center frequency need to be fine-tuned. Last, there is also one bonus point of CW spectroscopy: most of the cases, because the qubit drive is strong enough, not only f_{ge}^{q} transition, but also f_{ef}^{q} and $\frac{1}{2}f_{gf}^{q}$ can be observed during the protocol.

4.2.2 Time domain measurement

After figuring out the basic parameters of two modes, we can move on to time domain measurement, analyzing more details on qubit itself. In the following, I'm going to first introduce qubit routine examination, then briefly discuss some other parameters' measurement, optimization and benchmarking techniques are presented in the end.

4.2.2.1 Qubit routine examination

Cavity response. First, examining cavity by sending some photon into system. With the development of quantum operation, cavity drive signal could be exotic for different purpose: e.g. bright states' readout [58], fast reset of cavity, increasing measurement fidelity. Here, we're just going to use a flat top modulated signal as an example, explaining the basic technique of measuring qubit via measuring cavity. A finite tanh function has been used for the modulated signal: $s(t) = \tanh\left(k \cdot t - b\right) - \tanh k \cdot (t - w) - b$, where k can be treated as ramp rate, b is the truncated point, and w is the signal width. Like we have calculated cavity response in Sec. 2.1.2, and by applying the techniques we have introduced in Sec. 4.1.1,

the exact same response we have predicted from theory can be presented from experiments. More interestingly, if the experiment has been repeated multiple times (depends on SNR), the averaged data is the solution of the cavity response, and the standard deviation is the amplified half photon noise determined by the Heisenberg uncertainty. At this point, we can also integrate the response to get a Gaussian blob where the center is at $\bar{n}\kappa T_m$, where $\bar{n}$ is the average driving strength, κ is the cavity decay rate and T_m is the measurement length. By keeping increase the driving strength or measurement length, two blobs may show up due to the dispersive shift and finite temperature of qubit, where the angle between them is $2 \cdot \arctan(\chi/\kappa)$, where χ is the dispersive shift between qubit and cavity.

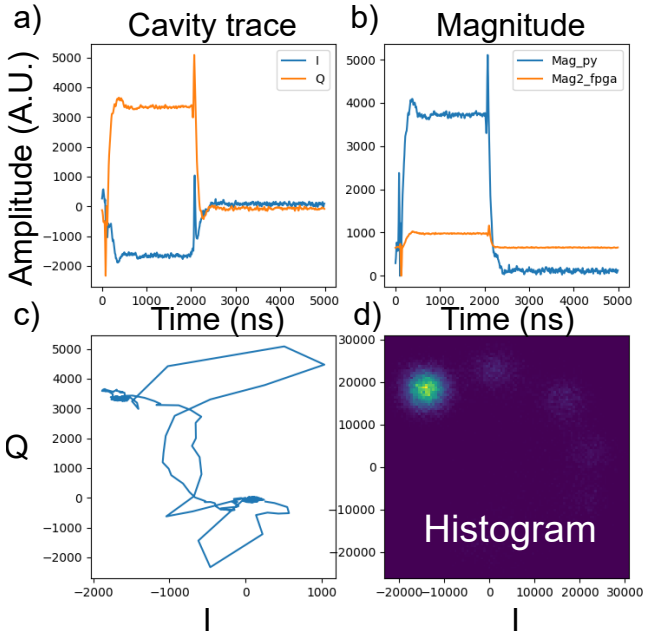

Figure 37: **Cavity response and histogram.** a) Demodulation of cavity response; b) Calculate the magnitude of cavity response, one is calculating $\sqrt{\bar{I}^2 + \bar{Q}^2}$ (Mag_py), and another is calculating $\sqrt{\bar{I^2 + Q^2}}$ (Mag_FPGA); c) The cavity response in I-Q plane; d) 10,000 repetition of measurement histogram.

A good cavity readout and histogram has been shown in Fig .37. After we have determined the best cavity driving frequency and π-pulse for qubit, we can calculate the **mea-**

surement fidelity as :

$$\sum \left(\left| \frac{\text{Histo}_e}{\sum \text{Histo}_e} - \frac{\text{Histo}_g}{\sum \text{Histo}_g} \right| \right) \cdot \frac{1}{2} \tag{49}$$

A high fidelity readout could make the following qubit measurement much easier, and provide the conditions for complicated experiments. A simple example is that we can add an extra measurement before every sequence to reset qubit, and only select ground state results for following sequences. However, for routine measurement, this is not necessary. As long as we have the ability of probing the cavity, we can start measuring the qubit as follows:

Pulse spectroscopy. Since in CW spectroscopy, we cannot control the exact photon in cavity or qubit (again, Zeno effect), and due to the AC Stark shift, the $f_g^g e$ transition we find could be off by several MHz. The very first thing we can do is finding a more precise resonate frequency of qubit by pulse spectroscopy.

A very long (several times longer than qubit coherence time) and weak qubit drive has been first applied on the qubit to saturate the qubit to $\rho = |g\rangle\langle g| + |e\rangle\langle e|$ (a purely mixed state), then applying a cavity drive to measure the state of qubit. By sweeping the frequency of qubit drive, once the cavity response shows difference, indicating the qubit has been 'hit'. In this scenario, we have guaranteed that the cavity is almost empty when probe the qubit which can give us a precise resonate frequency. In practice, the qubit coherence time could vary a lot, sometimes a very long coherence time qubit may need over 100 μs pulse to saturate, which results in a very narrow peak in the spectroscopy. Sometimes, in order to save some time, a shorter ($5 - 10\,\mu$s) pulse could use to do a rough spectroscopy, however, different amplitudes may need to be tried in case accidentally drive qubit back to ground state.

After that, **π-Pulse tune up.** After we have found qubit frequency, we can start controlling qubit starting from tuning up a π-pulse on qubit driving from the ground state to excited state. Here, the driving pulse we have chosen is a Gaussian modulated signal, since the Fourier transform of Gaussian is still Gaussian making the pulse can be easily controlled in both time and frequency domain. By sweeping the amplitude of the Gaussian pulse, a beautiful sinusoidal trace can be observed, which is also been called as **power Rabi oscillation.** In one example shown in Fig. 38, the qubit start from ground state, after half

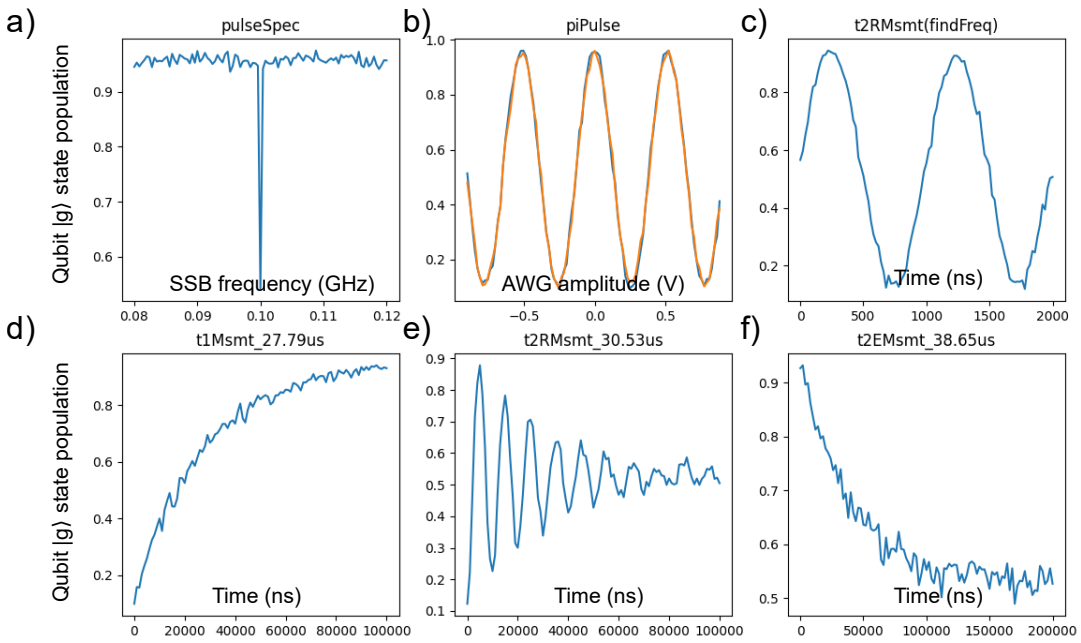

Figure 38: **Qubit routine examination.** The routine examination including the following steps: 1. Pulse spectroscopy to find qubit frequency, here the x-axis is the Single Side Sand (SSB) frequency which is easily swept in AWG; 2. Rough π-pulse tune up; 3. Use a short T_2 Ramsey measurement to find a more accurate qubit frequency; 4. Redo π-pulse tune up; 5. T_1 measurement; 6. Real T_2 Ramsey measurement; 7. T_2 Echo measurement.

period of sinusoidal trace, the qubit reaches excited state, and the corresponding amplitude is the π-pulse amplitude.

Then, T_1 **measurement.** In order to measure the energy decay of qubit, the only thing we need is driving the qubit to excited state, which is actually can be any population except for the thermal equilibrium state, and after a various width of time, measuring qubit. No matter where the qubit starts, you can see an exponential decay of the qubit population to the thermal equilibrium state. By fitting the trace to $y = A\exp(-t/T_1) + b$, the T_1 decay can be extracted. Also, here b can roughly indicate the thermal population of qubit mode.

Next, T_2 **Ramsey, and** T_2 **echo measurement.** Except for the energy decay, there is also phase decoherence T_ϕ. In the experiment, it could be very hard to directly separate two

losses. Instead, we can measure T_2 of the qubit, which is defined as $1/T_2 = 1/(2\ T_1) + 1/T_\phi$. The sequence is still quite easy: applying two $\pi/2$-pulse on qubit and vary the time width between them, following by an immediate measurement. After the first $\pi/2$-pulse, the qubit starts decoherence and decay at the same time. Depending on the qubit drive is exactly on resonance or not, the qubit and the driving signal may oscillate at different frequency, which results in the next $\pi/2$-pulse could lead the qubit onto any point of the projection on Z-axis. This is a very good way to precise tune up the qubit frequency to $1/T_2$ level by fitting the result to $y = A\exp(-t/T_2)\cdot\cos(\delta t + \phi) + b$. One trick we have always done is after T_2 Ramsey measurement, we can also add one more π-pulse between two $\pi/2$-pulse to echo any low frequency decoherence noise by flipping the qubit from $|+X\rangle$ to $|-X\rangle$. For example, if you have intentionally driven qubit several kHz away, the echo pulse can automatically correct the off-resonance drive and extract T_2 from an exponential decay: $y = A\exp(-t/T_1) + b$. On the other hand, if you have observed a big difference between T_{2R} and T_{2E}, the qubit may suffer from low frequency noise, but if $T_{2R} \approx T_{2E} < 2\ T_1$, the qubit suffers from high frequency noise. Sometimes, you may find your T_{2E} is smaller than T_{2R}, which definitely violates the physics of law. We think the reasons could be the qubit is not stable and the decoherence vary a lot in a short period of time, or you just don't have a good enough π-pulse, especially after you have changed driving frequency of qubit recently.

4.2.2.2 Other parameters

Except for the above measurements, there are also several parameters that related to the performance of the qubit. Multiple mature protocols have already been developed to perform the measurement, here I'm going to take some examples explaining the idea of these protocols and discuss the points of measuring these parameters. One thing that need to be noticed here is that the most obstacle of different protocols is actually coming from the truth that the noise and error could come from lots of aspects, like state preparation and measurement (SPAM) error, gate error, or hardware instability. How to isolate all errors from the measurement itself could be a very challenge question. Even though the protocols could have limitations, it is still very valuable understanding the idea behind the protocols.

Anharmonicity α measurement. Two-tone spectroscopy is a very good tool to probe different transitions in the system. Since the π-pulse has already tuned up, we can directly prepare the qubit to excited state and then sweeping the driving frequency to 'hit' the f_{ef}^q transition. Then the anharmonicity can be simply calculated as $\alpha = f_{ge}^q - f_{ef}^q$ for transmon-like qubit.

The reasons we cared about anharmonicity are following: first, for transmon-like qubit, $\alpha = -E_C$, where E_C is the capacitance energy of transmon qubit. This number can directly give us an idea between simulation and fabrication, since E_L could be much harder to directly measure. Second, after tuning up the $e - f$ pulse, other protocols becomes possible, one simple example is shelving the qubit [59] to increase measurement fidelity.

Dispersive shift χ measurement. The difficulty of measuring χ highly depends on the ratio between χ and κ, the decay rate of cavity. With a big χ/κ, we can weakly populate the cavity and at the same time doing the spectroscopy, as shown in Fig. 39. This is also a common way of calibrating the photon number in a linear mode, especially a high Q linear mode, by fitting the coherent state distribution.

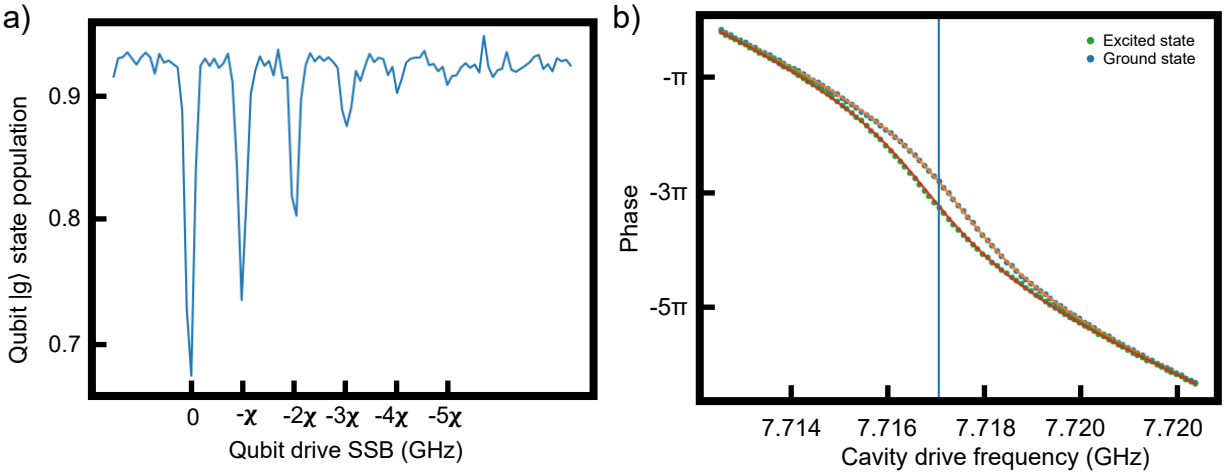

Figure 39: **Dispersive shift measurement.** a) When $\chi > \kappa$, we can first populate cavity and do pulse spectroscopy on qubit. b) When $\chi < \kappa$, we can selectively measure steady states of cavity.

On the other hand, for small χ/κ (< 1), pulse spectroscopy is relatively hard since multi-

ple peaks could be not differentiable at all. However, if we recall the definition of dispersive shift from Sec. 2.1.1.2, χ is actually twice the frequency difference of cavity when qubit in ground state and in excited state. Since qubit state can already be easily manipulated in time domain, then the only problem is how do we know the cavity resonance frequency at given condition in time domain. As we have recalled, cavity response is the dynamical solution at driving frequency, as long as a long enough pulse ($> 5/\kappa$) driving cavity to its steady state, we can integrate the time domain data and treat it as the steady state response at particular frequency. Then simply sweeping the cavity driving frequency, we can generate the exact same response from VNA. Now the protocol becomes straightforward: we prepare the qubit to ground and excited state separately, and then sweep the cavity driving frequency.

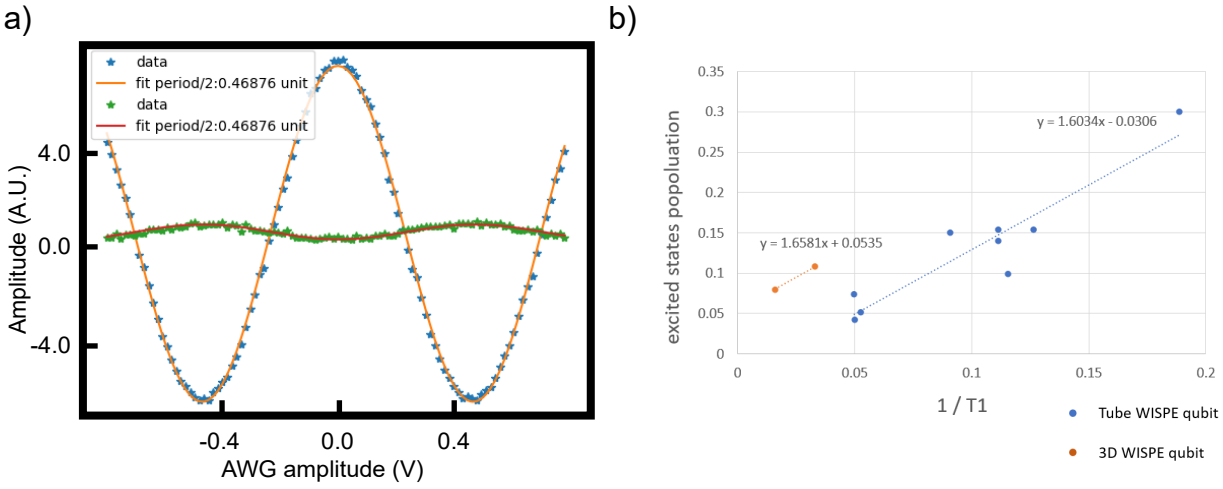

Figure 40: **Rabi population measurement and temperature coherence relation.** a) From the two oscillations amplitudes, an estimate of the population and its associated standard deviation can be calculated from $P_e = A_e/(A_e + A_g)$. b) With different devices, we have observed a strong relation between qubit $|e\rangle$ state population and $1/T_1$.

One example is shown in Fig. 39, we can see two clear separable trace representing the frequency domain cavity response when qubit in ground or excited state. By fitting these two response to its analytical solution (in Sec.2.1.2), dispersive shift can be calculated as $\chi = \frac{1}{2}\left(f_g^c - f_e^c\right)$. One more point that can be emphasized here is that by sweeping the cavity driving frequency, we can also find a point where the cavity response has the most big

difference when qubit in different states. This point is also the best cavity driving frequency for good readout.

Population measurement. One of the common technique measuring the qubit population is 'Rabi population measurement' (RPM), which has been well introduced in K. Geerlings's dissertation [41]. Here, we just use a measurement example showing the idea of RPM. Moreover, we have kept tracking the population of a same qubit in multiple cooldowns. By changing the packaging and shelving of the system, we can intentionally change the qubit temperature. At the same time, we have found the decay rate of the qubit has a very linear relation with the qubit temperature.

At this point, we have figured out most related parameters of a cavity-qubit system, here we use a table of results at the end showing our lab's current (2021's) progress on this kind of system:

Table 9: **A general cavity qubit system parameters.**

Cavity frequency (GHz)	6.998044
Cavity κ (MHz)	2.385
Qubit frequency (GHz)	4.867723
α (MHz)	188
χ (MHz)	0.504
χ/κ	0.211
T_1 (μs)	92.9
T_{2R} (μs)	48.8
T_{2E} (μs)	60.0
n_{thermal}	3.39%

4.2.2.3 Optimization and benchmarking

After we have measured all numbers we cared about the system, next step we need to do is fine-tuning up the gate and benchmark how good the gate is. At this moment, we

only have a single qubit involved in the whole system, so the target will be how good a single-qubit gate can be tuned.

First, we need to understand where the gate error could come from. In most of the sense, all errors can be divided into two parts: hardware side and physics side. For the hardware part, it is mostly because of the driving power, detuning and X-Y skewness; and for the physics part, it is often due to the coherence and the Hamiltonian of the system. Apparently, coherence limit is not something that can be fixed in room temperature, however, Hamiltonian limit may could be fixed using pulse engineering techniques (not always).

Let's start from hardware error. In general, after a good π-pulse tune up, the gate error is smaller than 1%. In order to correct this 1%, we need to first amplify this error using some pulse combination. One straightforward idea is using multiple π-pulse to accumulate single-qubit gate error. At the same time, via sweeping the driving power and detuning, an optimized gate can be easily found.

Another idea fixing the hardware error is 'AllXY' sequence, which has been introduced in Dr. Reed's thesis [60] in details. The benefit of 'AllXY' is that by using 21 difference pulse combinations, the most three common hardware errors, power, detuning and X-Y skewness have different sensitivities, and different patterns of the experiment results reveal different errors in the gates. Here we use an experiment data to show how convenient this approach fine-tuning up the π-pulse.

For the physics error, the sources could come from many aspects. As I have mentioned, sometimes the coherence limit gives us the upper limit of the gate fidelity. But on the other hand, there are also lots of approaches trying to suppress the gate time to get higher fidelity. For example, a Gaussian-modulated pulse is not necessary the best pulse shape, since it is always during the ramping process. One extreme approach is Gradient Ascent Pulse Engineering (GRAPE) [61], where you literally program each single time bin of the pulse. With the large freedom and good calculation power, a best optimized pulse should be able to find. However, the cap of this approach in the end is how much power you can send into the system: at some point, because of the power you need for the single-qubit gate is too high, the dilution fridge will warm up first. Alternatively, according to Mingkang's work (in preparation) using parametric single-qubit gate, if the gate is not necessary on resonance, it

can solve a nature conflict between strong qubit drive and long coherence time. The details of the parametric gate is going to be discussed in the later section.

Another kind of error in the physics side is the infinite energy level in the transmon qubit. When a $g-e$ transition is fast enough, it is inevitable that part of the photon leak into f state or even high energy level. Fortunately, tuning up a good gate doesn't care what happened during the pulse, but only after the pulse. A very mature approach, Derivative Removal by Adiabatic Gate (DRAG) [61], can be adapted here to prevent leaking into high-energy level after the pulse. By adding a derivative of the original pulse onto the perpendicular driving axis, the leaking error can be fixed till the first order level. In practice, two combinations in 'AllXY' sequence can perfectly amplify the high level leaking effect with different sign. By sweeping the DRAG factor, we can easily find the optimized point.

With the development of quantum operation techniques, there are lots of new idea that have been invented. There are even companies focusing on optimizing gate performance on software level, like Q-CTRL. However, as a quantum engineer background, I think understanding where the error comes from and what's the physics limitation mean more to develop better techniques.

Benchmarking. After gate optimization, we want to know how good our gate really is. The idea of gate benchmarking is trying to separate the gate error and SPAM error, then using the Clifford gates set to move the qubit onto each polar point on the Bloch sphere to test all combinations of Clifford gates, no matter single-qubit gate or two-qubit gate. A mature example is randomized benchmarking (RB) [62, 63] and interleaved randomized benchmarking (iRB) [64] for measuring single gate fidelity. Since both theory and experiment have already been well introduced in the literature, this section we're going to only focus on how do we realize the protocol in our lab, a superconducting transmon system.

Single-qubit RB. For the single-qubit gate, there are 24 Clifford gates. Here, we write down all 24 gates decomposed by π_x, π_y, $\pi_x/2$ and $\pi_y/2$ in the Table. 10 (The end of this chapter).

Alternatively, we can also add virtual-Z gate for decomposition, which can reduce the number of gates per Clifford from 1.875 to 1.167. However, we don't think it is necessary for gate benchmarking using virtual-Z gate, still, it can test if phase tracking work in the

system. After the gates has all been decomposed, in practice, we only need to generate a sequence of random number from 1 to 24, and then calculate which Clifford gate can bring the qubit state back to ground state using brute force sweeping. Here we show an example of single-qubit RB result in our lab in Fig. 41. According to the fitting result, we can calculate the average Clifford gate error is $r = (1 - 0.9988)/2 = 0.0006$, in this case, each single qubit gate fidelity is 99.968%.

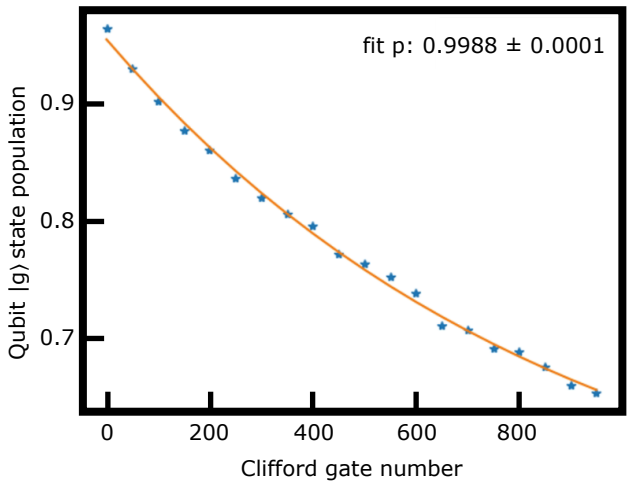

Figure 41: **Single-qubit gate RB.** Here the trace has been fitted to $y = Ap^m + B$, wehre A and B absorb state preparation and measurement errors as well as the error on the final gate, and m is the number of Clifford gate. The average gate error rate r is defined as $r = 1 - p - (1 - p)/d$, where d is the dimension of qubits' space.

Two-qubit RB. For the two-qubit Clifford gates set, there are totally 11,520 gates. The math details behind it could be massive, here we take a shortcut, defining four distinct classes of the two-qubit Clifford group. Before we introduce all four classes, we first define two gates group: $\mathcal{C}_i$ is the group of single-qubit Clifford gate (which has 24 different elements) and $S_i = \{I, R_S, R_S^2\}$ where $R_S = \exp[-i(X + Y + Z)\pi/(3\sqrt{3})]$. The latter group is simply the rotation that exchanges all the axes of the Bloch sphere (from $x - y - z$ to $y - z - x$). In practice, S_i can be written as:

Now, the first class, which consists of 576 elements (24^2), represents all single qubit Clifford operations.

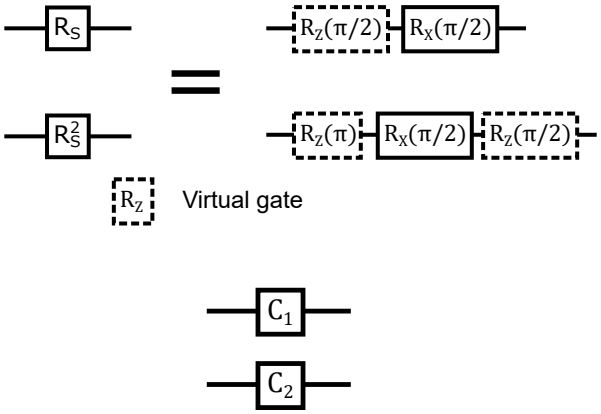

The second class, iSWAP-like class, has 5184 elements ($24^2 \times 3^2$) and represents all combinations of the following sequences:

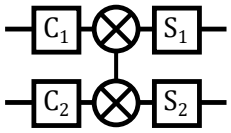

The third class, CNOT-like class, also has 5184 elements ($24^2 \times 3^2$):

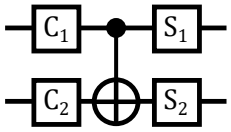

And the last is SWAP-like class, and contains 576 elements (24^2):

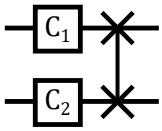

We think this is the optimal decomposition of the two-qubit Clifford group in terms of number of iSWAP gate as it can be shown that implementing a CNOT requires two iSWAPs and a SWAP requires three. However, we don't think this is a general expression for all two-qubit Clifford gates. If the building block is $\sqrt{i\text{SWAP}}$, there is better decomposition [65] possible. Back to the topic, since we use iSWAP as our building block, the following replacements for the two-qubit entangling gates of the above classes has been used:

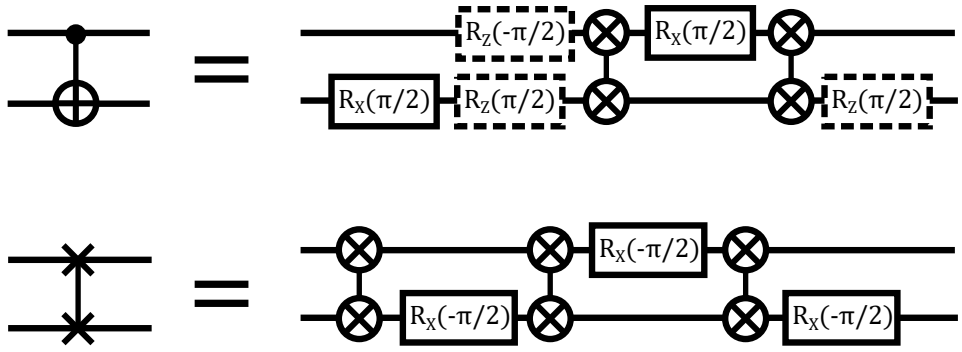

After all Clifford gates have been prepared, we can follow the same order as single-qubit RB protocol to finish the benchmarking. In general, there is no other difference between single-qubit and two-qubit RB.

Except for the randomized benchmarking, there is also an interleaved randomized benchmarking to test single gate fidelity. And the only difference in the sequence is for each original Clifford gate in the sequence, there is an extra added Clifford gate, no matter single-qubit gate or two-qubit gate. By doing this, we can interleave any specific gate we want to test, more specifically, we can separate this single gate error from all other gates' error. This is especially useful in testing two-qubit gate. In this case, if we obtain a fitted parameter $\bar{p}$ from RB and p from iRB, we can calculate the single gate error as:

$$r_C = \frac{(d-1)(1-\bar{p}/p)}{d} \tag{50}$$

Again, we use a lab's current (2021's) result as an example to show the two-qubit RB result:

From the fitting result, we can calculate the iSWAP gate fidelity is 98.2%. However, by comparing the result with interleaving with identity gate, we can claim that our two-qubit gate is only limited by the coherence of the system. The next step we can improve is either have a better coherence time or faster gate speed.

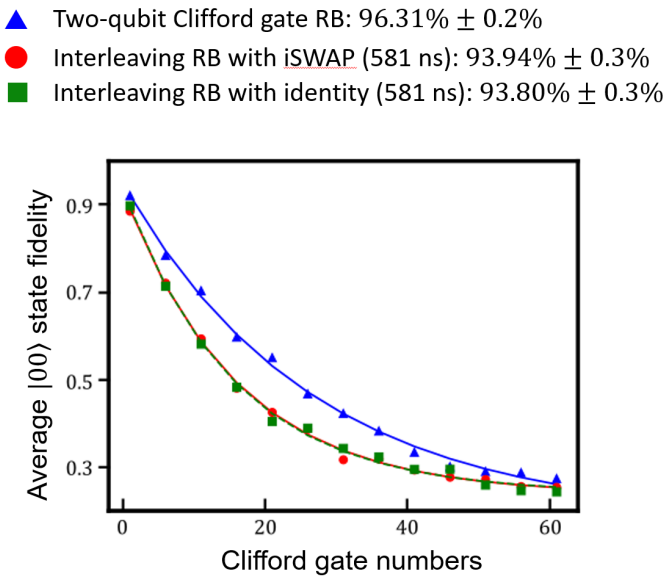

Figure 42: **Two-qubit RB.** One useful experiment we can do is interleaving both two-qubit gate and identity gate with same time. By doing this, we can determine if the gate is only limited by the coherence of the system or not.

4.3 Parametric gate tune up

During my graduate study, one important gates set family I have used is the parametric gate, including single-qubit and two-qubit gate. The theory behind parametric gate has already been discussed in Sec. 2.1.3, and in this section, we're going to only focus on three-wave mixing parametric gate by coupling the qubits onto a SNAIL element which generates three-wave coupling across the whole system.

4.3.1 Single-qubit parametric gate tune up

For the single-qubit parametric gate, we're considering the following simplified Hamiltonian system:

$$\hat{H}_0/\hbar = \omega_q \hat{a}^\dagger \hat{a} + \frac{\alpha}{2}\hat{a}^\dagger \hat{a}^\dagger \hat{a}\hat{a} + g_{\text{eff}}\left(\hat{a} + \hat{a}^\dagger\right)\langle \hat{s}^\dagger \hat{s}\rangle \tag{51}$$

As we have mentioned in theory, this process transfer two pumping photons into a single qubit photon. The only difference comparing to the on resonance drive is that all pumping photon is half resonance. Even though due to the existence of AC Stark shift, the pumping frequency is not exactly half of the f_{ge}^{q} transition, but lots of techniques above can be directly adopted in parametric gate.

Find the time Rabi for the parametric process. Just like single-qubit on resonance gate starting from pulse spectroscopy, the first step tuning up parametric gate is also using spectroscopy to find the transition. Using the same protocol as mentioned in **two-tone spectroscopy**, we can sweep the frequency near the $\frac{1}{2}f_{ge}^{q}$ to find the right transition frequency. Next, instead of power Rabi we have used in π-pulse tune up, we can do a time Rabi with frequency tuning to generate a 'chevron' pattern Rabi oscillation like in Fig. 43. The reason we don't use power Rabi in the parametric system is because the pumping frequency is dependent on the pumping amplitude that comes from AC Stark shift. Power Rabi cannot separate these two freedoms, making the tuning up process even harder. And by looking at the 'chevron' pattern, the first point reaching the excited state is the condition forming the parametric π-pulse gate.

Fine-tuning the parametric π-pulse. Similarly, fine-tuning the parametric gate adopt the same idea: accumulating errors to amplify the syndromes, and multiple π-pulse, different pulses combinations can be used again. In Mingkang's work (in preparation), he has systematically introduced how to tune up the single-qubit parametric gate from rough-tuning to fine-tuning with different sequences. One example is shown in Fig. 44.

Track the phase change. One last thing I want to emphasize here is the phase tracking during a parametric gate. Because the resonance frequency of qubit could change during the parametric pumping process, the qubit could capture some extra phase. Understanding where the phase comes from and tracking the phase change is a very important part of operations.

In order to easily explain and track the phase change, we have used a flat top (finite tanh) function as the modulated signal. The phase change can be divided into two parts: the constant phase change coming from the ramping process and the time-dependent phase change coming from the frequency difference between driving frame and resonance frame.

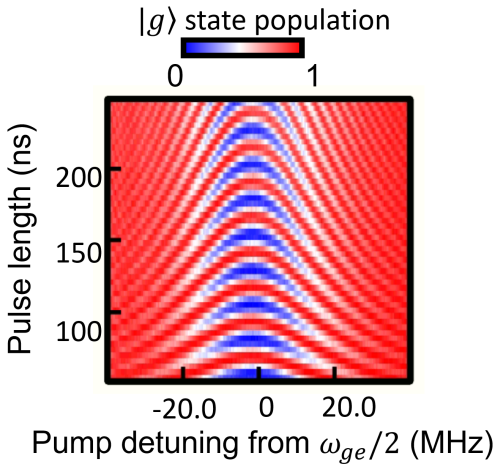

Figure 43: **Time Rabi of single-qubit parametric process.** Here, the y-axis is the parametric pumping length, the x-axis is the pumping frequency, and the color represents the qubit $|g\rangle$ state population. In general, the center of the first blue zone is the condition of a π-pulse.

The first part is very easily to understand, because when the pump signal starts ramping, the amplitude of the drive keeps changing during this process, resulting in the resonate frequency of the qubit is also changing. However, it is not necessary to make the pump frequency change with the driving amplitude, (even though this could be a solution.) as long as the ramping width is same, we can average the phase difference:

$$\int_{t=t_0}^{t_0+t_{\text{ramp}}} \Delta(t)dt = \bar{\Delta} \cdot t_{\text{ramp}} = \phi_c \tag{52}$$

to compensate every time there is a ramping process. And In practice, there is no problem directly sweeping the compensation phase to find the optimized point.

The second part is relatively interesting, because we need to understand a fact that everything keeps oscillating even you didn't look at it. This truth has already been used in T_2 Ramsey experiment, where we have intentionally driven the qubit off-resonance, we can see the measurement results is oscillating between $|g\rangle$ and $|e\rangle$ states. Notice this is not because the qubit is oscillating, but there is frequency difference between qubit drive and

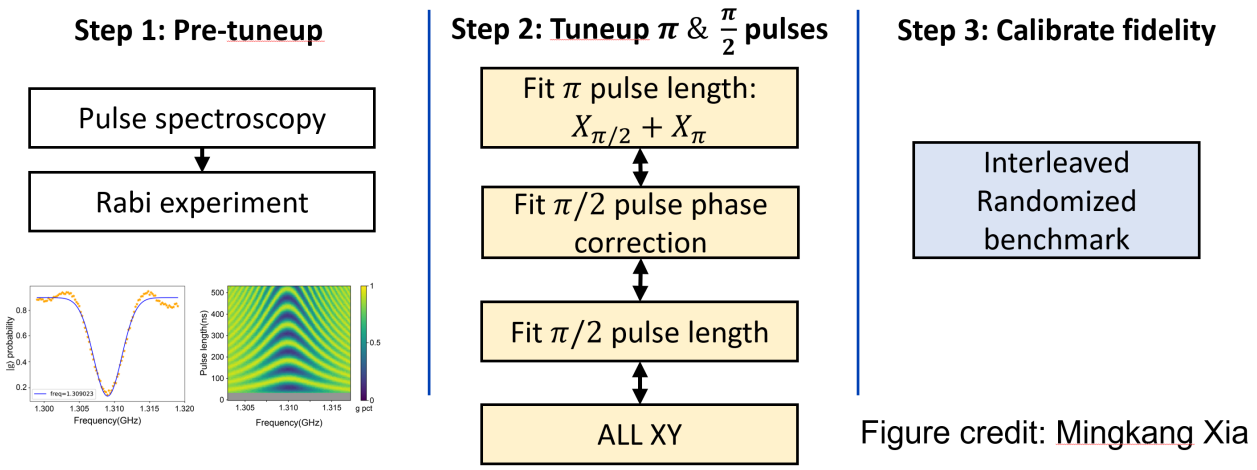

Figure 44: **Tuning up the parametric single-qubit gate.** In general, tuning up process can be divided into three steps: 1. pre-tuneup to find a rough single-qubit gate; 2. By using difference pulses combinations, fine-tuning different parameters separately; 3. Using iRB to accumulate the errors in a large scale to do a very fine-tuning.

qubit resonance. Similar idea, it is inevitable that the qubit driven frame and non-driven frame are different with each other. In order to solve this problem, we need to add an extra phase in the qubit driven frame. Assume the qubit non-driven resonance frequency is f_{ge}^{q} and the driven resonance is $\tilde{f_{ge}^{q}} = f_{ge}^{q} + \delta_p$, then at each time t in sequence, the phase difference between two frames is $\delta_p \cdot t$. In this case, every time a parametric single-qubit gate has been used, we simply add an extra phase $\delta_p \cdot t$ on it, the problem can be solved. It is also not a problem if an on-resonance gate and a parametric gate haven been used simultaneously.

4.3.2 Two-qubit parametric gate tune up

Before we move on to the two-qubit gate, one thing we want to emphasize here again is that all gate operations are based on non-phase modulation AWG with RF generator mixing together. And till this point, we assume all single qubit gates have already been well tuned and phase locked. In the following section, iSWAP is taken as an example explaining the technique of tuning up a parametric gate. We believe different two-qubit gates have

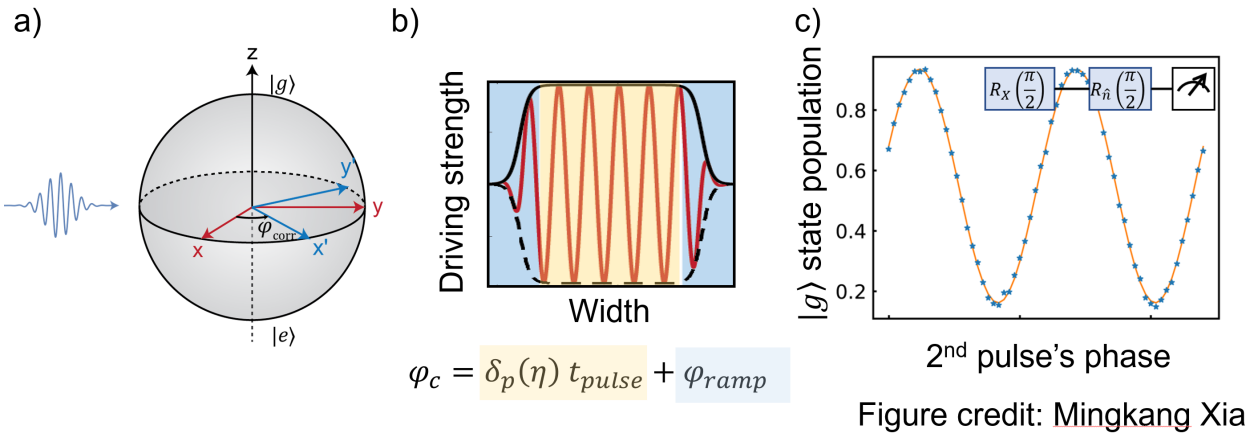

Figure 45: **Phase tracking of the parametric single-qubit gate.** a) Schematic representation of the driven frame and non-driven frame. b) The phase compensation mainly comes from the ramping process and pumping duration, where the latter relates to the gate time in the sequence. c) One example of finding the ramping phase compensation by preparing the qubit to $|-Y\rangle$ then sweeping the phase of the second $\pi/2$-pulse.

different techniques to operate, however, for all parametric gates, they should share the same principles.

Find the photon conversion between two modes. It starts from a very similar protocol in single-qubit gate tuneup: finding the photon exchanging process. Since iSWAP exchanges the photon between two qubits, for a three-wave mixing parametric system, the pumping frequency is the frequency difference between two qubits. So we can again start from 'two-tone spectroscopy' around $|\omega_2 - \omega_1|$. After we find a rough pumping frequency, the pump length and pump frequency can be simultaneously swept to generate a two-qubit 'chevron' pattern Rabi oscillation between two qubits.

Fine-tuning a photon conversion gate. By looking at 'chevron' pattern between two qubits, we can first find a rough photon conversion gate. The reason we cannot call it a iSWAP gate but a photon conversion gate is because the phase change could be very complicated, which will be addressed later. Back to the topic, after we have rough tuned, we can apply multiple gates to accumulate the errors. In practice, we find the most efficient

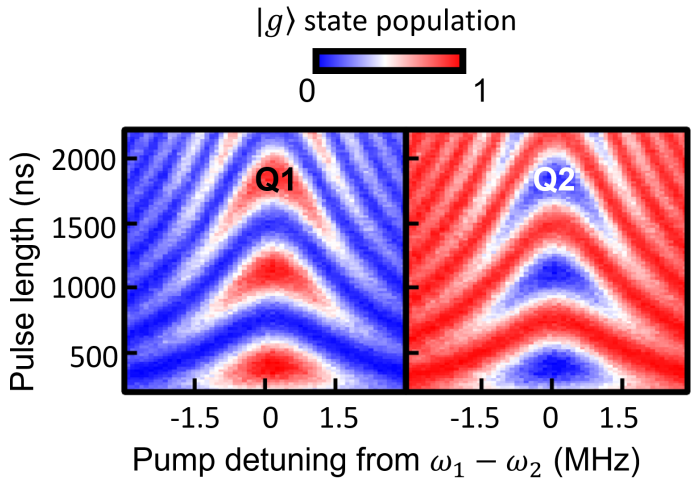

Figure 46: **Time Rabi of two-qubit parametric process.** Here, the y-axis is the parametric pumping length, the x-axis is the pumping frequency, and the color represents the qubit $|g\rangle$ state population. In practice, we can measure two qubits simultaneously, monitoring the photon moves back and forth.

tuneup approach is applying even number of gates, i.e. num $= 2, 4, 6, 8, ..., 2n + 1$, then measure two qubit simultaneously. At the same time, we tune the gate amplitude, gate frequency and gate width separately, till we see two longest exponential decay on qubits. After this approach, the gate error can reach smaller than 0.5%. Due to the coherence limit, we couldn't make any better two-qubit gate before I graduate.

Track the phase change. Now finally the fun part. Even though in the Schrödinger picture, for the given effective two-body coupling $\hat{H}_g = g_{\text{eff}}(a^\dagger b + ab^\dagger)$, the evolution operator $U = \exp i\hat{H}_g t$ at $t = \pi/(2g_{\text{eff}})$ is exactly an iSWAP gate (e.g. $g_{\text{eff}} = 10\,\text{MHZ}$, iSWAP takes 25 ns). However, in the real life, due to the truth of RF mixing, the phase change is way more complicated than simulation. Let's use a simple protocol to explain the process: Fig. 47.

Start at $t = T_0^b$, two qubits have been pre-selected to ground state without any phase, then two generators with SSB have been used to control qubits (not necessary). We record the driving phase is following: $\varphi_a = (G_a + S_a) \cdot T_0^b$ and $\varphi_b = (G_b + S_b) \cdot T_0^b$. Notice here, we assume all SSB generated from AWG also carry phase (also explained in 4.3.1), which

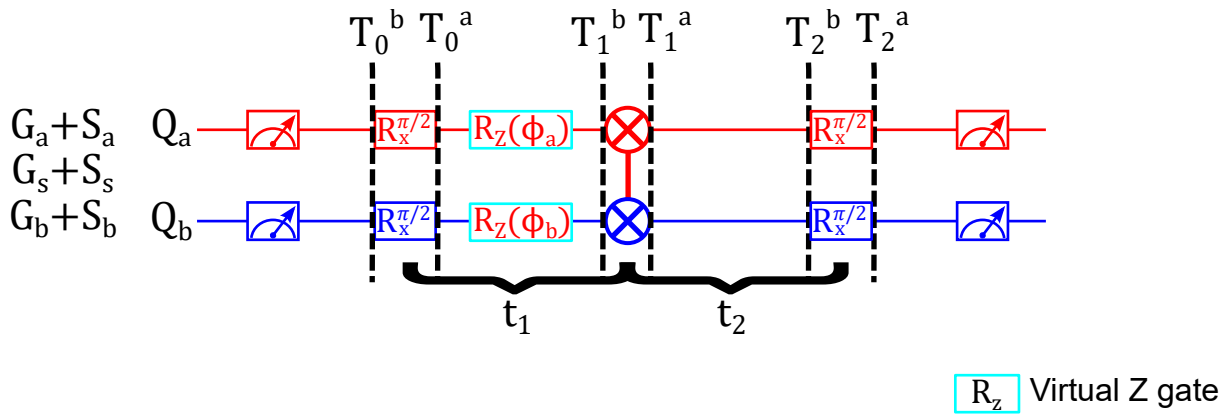

Figure 47: **Phase tracking of two qubit gate.** Here $t_{1/2}$ is the time in each sequence and T is absolute time from powering on the generators, and superscript b and a represents before and after the pulse. While $G_{a/b/s}, S_{a/b/s}$ represent corresponding generator and single-side band (SSB) frequency.

could be different for other pulse programming technique. After the first single qubit gates, both qubits start oscillating at their resonate frequency, $\omega_{a/b}$. Since $G_{a/b} + S_{a/b} = \omega_{a/b}$, we can assume driving pulse and qubit oscillate at same frequency (this is also one benefit to let SSB carry phase). There are potentially virtual-Z gates following the sequence, where we can record all virtual phase before two-qubit gates as ϕ_a, ϕ_b.

Next, we send parametric pumping tone into the system, where the generator accumulated phase is $\varphi_s = G_s \cdot T_1^b$. Deriving from the evolution operator U, we have:

$$U = \exp i \begin{pmatrix} 0 & 0 & 0 & 0 \\ 0 & 0 & g_{\text{eff}}t + \varphi_s & 0 \\ 0 & g_{\text{eff}}t - \varphi_s & 0 & 0 \\ 0 & 0 & 0 & 0 \end{pmatrix} = \begin{pmatrix} 1 & 0 & 0 & 0 \\ 0 & \cos(g_{\text{eff}}t) & i\sin(g_{\text{eff}}t)e^{i\varphi_s} & 0 \\ 0 & i\sin(g_{\text{eff}}t)e^{-i\varphi_s} & \cos(g_{\text{eff}}t) & 0 \\ 0 & 0 & 0 & 1 \end{pmatrix}. \quad (53)$$

which forms an iSWAP gates' set family. Due to the truth that only off-diagonal elements have phase added, assuming $t = \pi/(2g_{\text{eff}})$ doesn't lose generality for the gates' family.

Before we track the phase change, let's quick review what happened with iSWAP gate with initial state $\psi_i = (|\alpha|\exp(i\phi_\alpha),\ |\beta|\exp(i\phi_\beta),\ |\gamma|\exp(i\phi_\gamma),\ |\eta|\exp(i\phi_\eta))^T$:

$$\psi_t = U(i\text{SWAP})\psi_i = (|\alpha|\exp(i\phi_\alpha),\ i|\gamma|\exp(i\phi_\gamma),\ i|\beta|\exp(i\phi_\beta),\ |\eta|\exp(i\phi_\eta))^T \tag{54}$$

Since iSWAP swap the phase of two middle elements in ψ, let's deal with virtual phase first:

$$\begin{aligned} U(i\text{SWAP})Z_1(\phi_a)Z_2(\phi_b) &= \begin{pmatrix} 1 & 0 & 0 & 0 \\ 0 & 0 & i & 0 \\ 0 & i & 0 & 0 \\ 0 & 0 & 0 & 1 \end{pmatrix} \cdot \begin{pmatrix} 1 & 0 & 0 & 0 \\ 0 & e^{i\phi_a} & 0 & 0 \\ 0 & 0 & 1 & 0 \\ 0 & 0 & 0 & e^{i\phi_a} \end{pmatrix} \cdot \begin{pmatrix} 1 & 0 & 0 & 0 \\ 0 & 1 & 0 & 0 \\ 0 & 0 & e^{i\phi_b} & 0 \\ 0 & 0 & 0 & e^{i\phi_b} \end{pmatrix} \\ &= \begin{pmatrix} 1 & 0 & 0 & 0 \\ 0 & 0 & ie^{i\phi_b} & 0 \\ 0 & ie^{i\phi_a} & 0 & 0 \\ 0 & 0 & 0 & e^{i(\phi_a+\phi_b)} \end{pmatrix} \end{aligned} \tag{55}$$

In order to carry on the virtual phase, there are two ways we can do:

1. Manually exchange (ϕ_a, ϕ_b) in the software.

2. Add extra phase on parametric pump: $U = \exp i(\hat{H}_g t + \phi_p)$, where $\varphi_p = \phi_b - \phi_a$ when $\omega_b < \omega_a$ or vice versa.

For the iSWAP, there is no difference on both ways, however, for the iSWAP gates' set family, the first one doesn't work, but the second still holds based on:

$$\exp\left(i(\hat{H}_g t)\right) Z_1(\phi_a)Z_2(\phi_b) = Z_1(\phi_a)Z_2(\phi_b)\exp\left(i(\hat{H}_g t + \phi_b - \phi_a)\right) \tag{56}$$

Then parametric pumping phase accumulation. Assuming the pumping pulse is a flat top modulated signal with finite width of ramp-up and ramp-down, due to the non-zero AC Stark shift in the system, both qubits have a fixed phase change during the ramping time and a pulse width dependent phase change during the flat top time. In practice, these two kinds of phases can be counted together as $\varphi_{\text{two},a}, \varphi_{\text{two},b}$, which can be fixed by adding virtual-Z gates on both qubits immediately after two-qubit gate.

However, there is one more compensation that could be easily overlooked. Before the two qubit gate, the accumulated real phase of two qubit can be written as: $\varphi_a = (G_a + S_a) \cdot T_0^b + \omega_a \cdot t_1$ and $\varphi_b = (G_b + S_b) \cdot T_0^b + \omega_b \cdot t_1$. And if we assume, $\widetilde{\omega_{a/b}}$ is the average resonate frequency during pumping, and $\tilde{\Delta}$ is the frequency difference. Then $\tilde{\Delta}$ is also the pumping frequency we sent into the system, $G_s + S_s = \tilde{\Delta}$. After two qubit gate, φ_a becomes $(G_b + S_b) \cdot T_0^b + \omega_b \cdot t_1 + \tilde{\Delta} \cdot T_1^b$. Ignoring absolute phase at this moment (phase relate to T), let's focus on relative phase first. With time moving on, the qubit is going to keep oscillating at their own resonate frequency, which means $\omega_b \cdot t_1 + \tilde{\Delta} \cdot (T_1^b - T_0^b)$ actually determines the driving axis for the following pulse. In order to let driving pulse and qubit oscillate at the same phase, we can calculate:

$$\varphi_{\tilde{s}} = \omega_a \cdot (T_1^b - T_0^b) - (\omega_b \cdot t_1 + \tilde{\Delta} \cdot (T_1^b - T_0^b)) = (\Delta - \tilde{\Delta}) \cdot t_1 \tag{57}$$

As we can see, there is a time dependent phase difference for every time a two qubit gate has applied, and two qubits has exact same phase offset with different sign. In this case, we can either add $(\Delta - \tilde{\Delta}) \cdot t_1$ onto the parametric pumping signal or on each qubit with different sign.

Again, similar idea for the absolute phase, but even more tricky. For φ_a, excluding the relative phase, it still has $(G_b + S_b) \cdot T_0^b + (G_s + S_s) \cdot T_0^b$ left. And this part need to align with $(G_a + S_a) \cdot T_0^b$ for each sequence repetition. Apparently, SSBs generated from AWG have been synchronized through the digital board, which could be done in software. On the other hand, generators' phase could be random if we cannot control the absolute time between each sequence repetition, which is exactly the situation we have in our lab. To solve this problem, we have intentionally chosen $|G_a - G_b| = G_s$ to cancel absolute phase generated from generators. Moreover, during the experiment, we have found different generators could have different random phases over hours even an external rubidium clock and temperature control have been used. To stabilize the phase drift, we have used the same technique in interferometric readout: by mixing G_a and G_b to generate the LO signal for parametric pumping, all random phase drifts can be automatically cancelled, and $|G_a - G_b| = G_s$ also holds in this situation.

One thing I want to point out is that this also proves the benefits of direct digital synthesis (DDS) in signal generation. DDS can much more easily control all phases across the whole system, which is a crucial point in parametric control. Even though, we still need to consider all phase drifts from physics side, e.g. AC Stark shift, any phase drifts in hardware side can be monitored and corrected.

At this point, the iSWAP gate has finally been applied without any additional phase recorded in software. **In summary**, there are four parts that need to be considered during two qubits parametric gate: 1. Pumping phase $(\phi_a - \phi_b)$ to compensate virtual phase; 2. Pumping phase $(\Delta - \tilde{\Delta}) \cdot t_1$ to compensate AC Stark shift difference between qubits; 3. Each qubit adding constant phase offset due to its own AC Stark shift; 4. Using G_a and G_b to mix the LO signal for parametric pumping to cancel any hardware phase drifts.

After that, the following pulses can be treated the same way we have described from start, no matter single-qubit or two-qubit gates.

Table 10: **Single qubit Clifford sequences.** The average gate number (decomposed without virtual-Z gate) per Clifford is 1.875 if identity gate has also been considered.

Effective gate	Sequences	No VZ	with VZ
Identity	C_1	'I'	'I'
	C_2	$\pi_x/2$, $\pi_y/2$, $-\pi_x/2$	$\pi_z/2$
	C_3	π_x, π_y	π_z
	C_4	$\pi_x/2$, $-\pi_y/2$, $-\pi_x/2$	$-\pi_z/2$
π-pulse	C_5	π_y	π_y
	C_6	$\pi_x/2$, $\pi_y/2$, $\pi_x/2$	π_x, $-\pi_z/2$
	C_7	π_x	π_x
	C_8	$\pi_x/2$, $-\pi_y/2$, $\pi_x/2$	π_x, $\pi_z/2$
$-\pi_y/2$-pulse	C_9	π_x, $\pi_y/2$	π_z, $-\pi_y/2$
	C_{10}	$-\pi_y/2$	$-\pi_y/2$
	C_{11}	$-\pi_y/2$, $\pi_x/2$	$-\pi_y/2$, $\pi_x/2$
	C_{12}	$-\pi_y/2$, $-\pi_x/2$	$-\pi_y/2$, $-\pi_x/2$
$\pi_y/2$-pulse	C_{13}	π_x, $-\pi_y/2$	π_z, $\pi_y/2$
	C_{14}	$\pi_y/2$, $-\pi_x/2$	$\pi_y/2$, $-\pi_x/2$
	C_{15}	$\pi_y/2$	$\pi_y/2$
	C_{16}	$\pi_y/2$, $\pi_x/2$	$\pi_y/2$, $\pi_x/2$
$-\pi_x/2$-pulse	C_{17}	$-\pi_x/2$, $-\pi_y/2$	$-\pi_x/2$, $-\pi_y/2$
	C_{18}	$-\pi_x/2$, $\pi_y/2$	$-\pi_x/2$, $\pi_y/2$
	C_{19}	$-\pi_x/2$, π_y	$\pi_x/2$, π_z
	C_{20}	$-\pi_x/2$	$-\pi_x/2$
$\pi_x/2$-pulse	C_{21}	$\pi_x/2$, $-\pi_y/2$	$\pi_x/2$, $-\pi_y/2$
	C_{22}	$\pi_x/2$	$\pi_x/2$
	C_{23}	$\pi_x/2$, π_y	$-\pi_x/2$, π_z
	C_{24}	$\pi_x/2$, $\pi_y/2$	$\pi_x/2$, $\pi_y/2$

5.0 Josephson-Junction based Frequency comb

5.1 Introduction to frequency comb

While the circuit QED (cQED) architecture has built its success on strongly-coupled qubit-cavity experiments [10, 12, 13, 9], it has also been firmly established as a versatile platform to realize a broader variety of quantum nonlinear systems [28]. A key factor determining the breadth of realizable quantum nonlinear devices, and thus feasibility of future applications, is understanding the diverse dynamical regimes enabled by Josephson-junctions [17].

A nonlinear dynamical regime that has yet to be realized via a Josephson-junction mediated Kerr nonlinearity is that of frequency comb formation. Distinct from Kerr-nonlinear amplifiers which operate in regimes with at least one classically stable fixed point in phase space, frequency comb formation is marked by a system undergoing stable periodic excursions around *unstable* fixed points. In the optical domain, coherently-driven microresonators utilizing the Kerr nonlinearity have emerged as the leading platform for frequency comb generation [66, 67, 68, 69, 70, 71]; however the typically weak Kerr nonlinearity of optical microresonators [72] means that contemporary comb generation requires $\sim \mu$W power input [73], corresponding to millions of circulating cavity photons [74]. Similar results have been achieved in superconducting circuits using the weak nonlinearity of kinetic-inductance in very long resonators [75]. As a result, vacuum fluctuations amplified by the comb-generating nonlinear process are much weaker in comparison [76].

In this section [17], we harness the Josephson junction to realize a minimal version of Kerr-mediated microwave frequency combs based on a recent theoretical proposal [78]. Our minimal realization within cQED consists of just two coupled modes, of which only one possesses a Kerr nonlinearity furnished by Josephson junctions, as shown in Fig. 49. Although our device is based on familiar cQED components, it operates in a distinct regime within the landscape of nonlinear cQED devices: while strongly-coupled like transmon-cavity systems [40], its nonlinearity is in fact weaker and is operated under much stronger driving. On the other hand, the device exhibits stronger couplings yet smaller detunings and weaker

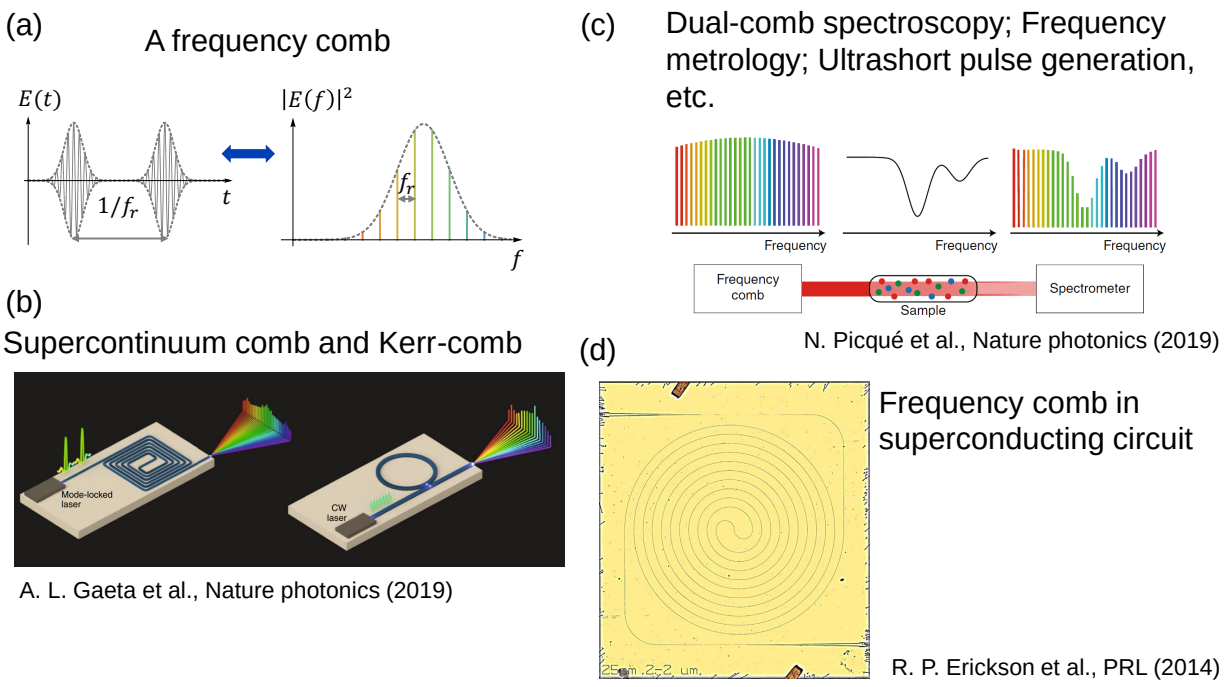

Figure 48: **Frequency comb.** (a) In general, frequency comb in time domain is a series of wave packets with the same time interval. After Fourier transform, multiple signals with the same spacing can be observed in frequency domain. (b) In optical domain, there are two ways generating frequency comb: supercontinuum comb and Kerr-comb[72]. (c) Multiple applications have been applied using frequency comb in optical regime, including spectroscopy, metrology and pulse generation[77]. (d) The same idea has been applied in microwave regime where people use superconducting circuits with tiny Kerr[75].

drives than Kerr-mediated bifurcation and parametric amplifiers [79, 32]. This allows us to realize an unstable regime where a single frequency drive tone generates coherent frequency combs over a large parameter space.

Crucially, the strong engineerable nonlinearities in cQED and operation at cryogenic temperatures brings quantum fluctuations to the fore ahead of thermal and dephasing effects in our comb synthesizer: the phase coherence of the generated combs is fundamentally limited by vacuum fluctuations that are amplified by the nonlinear comb-generating process

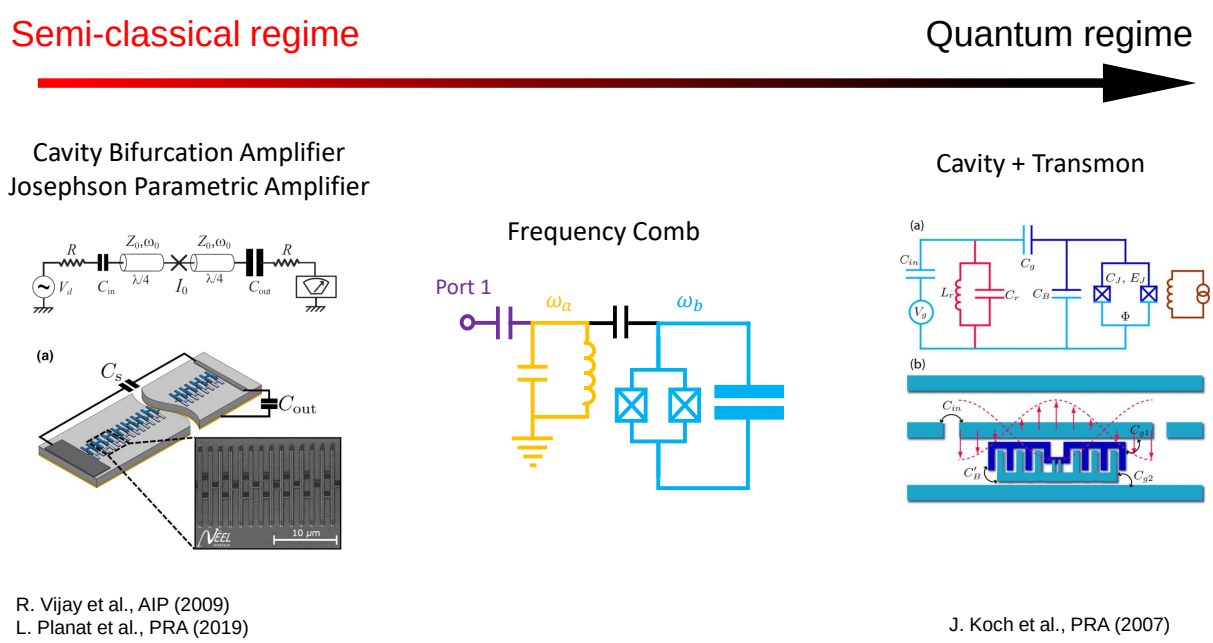

Figure 49: As described in the theory proposal[78], the superconducting circuit forming frequency comb is very common in circuit QED[9]. As shown in the figure, with stronger anharmonicity in the nonlinear mode, the circuit can be a general cavity + transmon system[40]; On the contrary, decreasing the anharmonicity will result in a semi-classical Josephson parametric amplifier[32, 80].

itself. A microscopic nonlinear quantum theory of our two-mode device, in addition to providing precise operating parameters for this comb-generating regime, enables us to quantify this quantum limit on comb phase coherence. By also characterizing and explaining the dependence of coherence on operating parameters like detuning and drive power, we provide a detailed quantitative study of the phase coherence of frequency combs near the quantum limit.

Built up of fundamentally quantum components, we believe this highly-controllable cQED realization can serve as a necessary building block for Kerr-nonlinear systems operating in classically-unstable *and* deeply-quantum regimes, exploring dynamics beyond coherent

frequency comb formation. For certain parameter regimes, our device exhibits temporal instabilities marked by large, irregular excursions in phase space, distinct from regular comb dynamics and reminiscent of chaos. More excitingly, while our work indicates that strong quantum fluctuations limit the coherence of generated frequency combs, they are also features of deeply-quantum regimes necessary for displaying quantum effects such as squeezing, entanglement, and generation of non-Gaussian states. Our realization thus marks a promising first step in exploring the potentially competing role of strong quantum fluctuations in quantum dynamics within classically unstable regimes.

5.2 Theory analysis

5.2.1 Stochastic description of quantum dynamics via the Positive-P representation

The Hamiltonian of our device consists of a linear mode $\hat{a}$ with uncoupled resonant frequency ω_a, linearly coupled with strength g to a nonlinear mode $\hat{b}$ with uncoupled resonant frequency ω_b; see Fig. 52(a). The linear mode is driven by a coherent tone with frequency ω_d and amplitude η, and the system Hamiltonian in the frame rotating with this drive takes the form:

$$\begin{aligned}\hat{\mathcal{H}}/\hbar = & -\Delta_{da}\hat{a}^\dagger\hat{a} - \Delta_{db}\hat{b}^\dagger\hat{b} - \frac{\Lambda}{2}\hat{b}^\dagger\hat{b}^\dagger\hat{b}\hat{b} \\ & + g(\hat{a}^\dagger\hat{b} + \hat{a}\hat{b}^\dagger) + \eta(\hat{a} + \hat{a}^\dagger)\end{aligned} \tag{58}$$

where $\Delta_{da/db} = \omega_d - \omega_{a/b}$ and $\Lambda > 0$ is the strength of the Kerr nonlinearity.

The derivation of the system Hamiltonian and master equation we consider in this section is quite standard in cQED; in particular, it may be found in detail in the previous work [78], and we thus do not repeat the derivation here. Instead, we begin with the master equation description, derive its corresponding classical description making use of a positive-P phase-space description, and analyze the stability of the resulting system.

For convenience, we reproduce here the master equation describing the dynamics of the two-mode system:

$$\dot{\hat{\rho}} = -i[\hat{\mathcal{H}}, \hat{\rho}] + \kappa\mathcal{D}[\hat{a}]\hat{\rho} + \gamma\mathcal{D}[\hat{b}]\hat{\rho} + \gamma_\varphi\mathcal{D}[\hat{b}^\dagger\hat{b}]\hat{\rho} \tag{59}$$

where the system Hamiltonian in the frame rotating with the drive is given by Eqs. 58.

In the weakly nonlinear regime relevant to the experiment, $\Lambda/\kappa \sim O(10^{-2}) - O(10^{-3})$, strong driving leads to large mode occupations $\sim O(10^2) - O(10^3)$, rendering the standard master equation and even stochastic wavefunction approaches intractable for direct simulation. Such operating regimes are particularly suited to analysis using a phase-space approach to the dynamics of the density operator $\hat{\rho}$. In this section, we describe the approach used in this work, that of the Positive-P representation of the density operator, and the resulting stochastic differential equations (SDEs) it yields.

We employ a representation of the density operator in a non-diagonal coherent state basis over both modes $\hat{a}$ and $\hat{b}$:

$$\begin{aligned}\hat{\rho}(t) &= \int d^2\zeta\ P(\vec{\zeta}, t)\ \hat{\Xi}_\alpha \otimes \hat{\Xi}_\beta \\ &\equiv \int d^2\zeta\ P(\vec{\zeta}, t) \cdot \frac{|\alpha\rangle \left\langle \alpha^{\dagger *}\right|}{e^{\alpha\alpha^\dagger}} \otimes \frac{|\beta\rangle \left\langle \beta^{\dagger *}\right|}{e^{\beta\beta^\dagger}}\end{aligned} \tag{60}$$

where $\vec{\zeta} = (\alpha, \alpha^\dagger, \beta, \beta^\dagger)$ are complex variables describing a classical phase space, $\vec{\zeta} \in \mathbb{C}^4$. For convenience of notation, we use ζ_i to refer to the ith element of the vector $\vec{\zeta}$, for $i = 1, \ldots 4$, and define $d^2\zeta \equiv \prod_i d^2\zeta_i$ as the integration measure over the entire phase space.

Eq. (60) is simply an expansion of $\hat{\rho}(t)$ in terms of non-diagonal projection operators $\hat{\Xi}_\alpha \otimes \hat{\Xi}_\beta$, with weights given by the time-dependent function $P(\vec{\zeta}, t)$. For the above definition of $\hat{\Xi}_\alpha \otimes \hat{\Xi}_\beta$, $P(\vec{\zeta}, t)$ is a positive-definite function that satisfies a Fokker-Planck equation, and therefore may be meaningfully thought of as a classical distribution function; in particular, $P(\vec{\zeta}, t)$ is referred to as the Positive-P distribution[81, 82].

$$d\vec{\zeta} = \vec{A}_c(\vec{\zeta})dt + \sqrt{\Gamma}\mathbf{B}_1(\vec{\zeta})d\vec{W}_1(t) + \sqrt{\gamma_\varphi}\mathbf{B}_2(\vec{\zeta})d\vec{W}_2(t) \tag{61}$$

where $d\vec{W}_i$ are vectors of real, independent Wiener increments. The noise matrices $\mathbf{B}_1$, $\mathbf{B}_2$ are related to the square root of the diffusion matrix, $\mathbf{D}_{\rm st} = \mathbf{B}_{\rm st}\mathbf{B}_{\rm st}^T$, where $\mathbf{B}_{\rm st} = \sqrt{\Gamma}\mathbf{B}_1 + \sqrt{\gamma_\varphi}\mathbf{B}_2$. They can be written compactly in block form:

$$\mathbf{B}_1 = \begin{pmatrix} \mathbf{0} & \mathbf{0} \\ \mathbf{b}_1 & \mathbf{0} \end{pmatrix}, \ \mathbf{B}_2 = \begin{pmatrix} \mathbf{0} & \mathbf{0} \\ \mathbf{0} & \mathbf{b}_2 \end{pmatrix} \tag{62}$$

where the 2-by-2 component matrices $\mathbf{b}_1$ and $\mathbf{b}_2$ are given by:

$$\mathbf{b}_1 = \begin{pmatrix} e^{i\theta/2}\beta & 0 \\ 0 & e^{-i\theta/2}\beta^\dagger \end{pmatrix}, \ \mathbf{b}_2 = \sqrt{\frac{\beta^\dagger\beta}{2}} \begin{pmatrix} e^{i\pi/4} & e^{-i\pi/4} \\ e^{-i\pi/4} & e^{i\pi/4} \end{pmatrix} \tag{63}$$

Finally, we have defined the parameters Γ and θ via:

$$\Gamma e^{i\theta} \equiv i\Lambda - \gamma_\varphi \implies \Gamma = \sqrt{\Lambda^2 + \gamma_\varphi^2}, \ \theta = \arctan\left(-\frac{\Lambda}{\gamma_\varphi}\right) \tag{64}$$

Eqs. (61) are the central equations we employ to analyze the dynamics of the two-mode system.

5.2.2 Classical limit, fixed points, and linear stability

While Eqs. (61) describe the quantum dynamics of the two-mode system, they also allow us to analyze a well-defined classical limit, where the stochastic terms in Eqs. (61) vanish. Clearly, the dephasing contribution $\propto \sqrt{\gamma_\varphi}\mathbf{B}_2$ can be dropped by setting $\gamma_\varphi = 0$. However, simply setting taking $\Lambda = 0$ will render the two-mode system linear and eliminate the comb dynamics we are interested in.

Instead, a simple scaling argument allows us to understand the classical limit of the two-mode system. We consider reducing the nonlinearity by a factor $\Lambda \to \Lambda/k$ ($k > 1$), and simultaneously transforming $\vec{\zeta} \to \sqrt{k}\vec{\zeta}$, $\eta \to \sqrt{k}\eta$. Under this transformation, we find that Eqs. (61) become ($\gamma_\varphi = 0$):

$$d\vec{\zeta} = \vec{A}_{\rm c}(\vec{\zeta})dt + \frac{1}{\sqrt{k}}\sqrt{\Lambda}\mathbf{B}_1(\vec{\zeta})d\vec{W}_1(t) \tag{65}$$

More precisely, the drift vector $\vec{A}_{\rm c}(\vec{\zeta})$ is *invariant* under this transformation, while the stochastic terms are scaled by a factor of $1/\sqrt{k}$. Physically, this transformation indicates

that as the strength of the nonlinearity decreases, the deterministic dynamics remain unchanged provided the drive is suitably increased, upto a scaling of the mode amplitudes $\vec{\zeta}$. The stochastic dynamics, on the other hand, are suppressed. The appropriate classical limit that retains nonlinear dynamics can thus be realized by considering weak nonlinearities under sufficiently strong driving. The dynamical equations that describe this classical limit are thus given by:

$$d\vec{\zeta} = \vec{A}_{\rm c}(\vec{\zeta})dt \quad \text{(classical limit, } k \to \infty) \tag{66}$$

Upon dropping the stochastic terms, it is clear to see from the now *ordinary* differential equations above (when written out) that $\alpha^\dagger = \alpha^*$, $\beta^\dagger = \beta^*$; as a result, the deterministic dynamics in the classical limit, Eqs. (66), can finally be written down entirely in terms of α, β:

$$\dot{\alpha} = \left(i\Delta_{da} - \frac{\kappa}{2}\right)\alpha - ig\beta - i\eta \tag{67a}$$

$$\dot{\beta} = \left(i\Delta_{db} - \frac{\gamma}{2}\right)\beta + i\Lambda|\beta|^2\beta - ig\alpha \tag{67b}$$

For completeness, we note here that the above system is the same as that obtained by writing down the equations of motion for operator averages $\{\langle\hat{a}\rangle, \langle\hat{b}\rangle\}$, neglecting correlations (namely performing replacements of the form $\langle\hat{b}^\dagger\hat{b}\hat{b}\rangle \to \langle\hat{b}^\dagger\rangle\langle\hat{b}\rangle\langle\hat{b}\rangle$), and finally replacing operator expectation values by complex amplitudes, $\{\langle\hat{a}\rangle, \langle\hat{b}\rangle\} \to \{\alpha, \beta\}$; the derivation here provides some context to the approximations underlying this dropping of correlations.

The linearity of both mode $\hat{a}$ and the coupling $\propto g$ enables the linear mode to be integrated out, leading to a single effective dynamical equation for the nonlinear mode amplitude [78]:

$$\begin{aligned}\dot{\beta} = &\left(i\Delta_{db} - \frac{\gamma}{2}\right)\beta + i\Lambda|\beta|^2\beta - ig\chi_a\eta \\ &- g^2\int_0^t d\tau\ F(\tau)\beta(t-\tau)\end{aligned} \tag{68}$$

where we have introduced the linear mode susceptibility $\chi_a = (-i\Delta_{da} + \frac{\kappa}{2})^{-1}$, and where the memory kernel for the self-interaction is given by:

$$F(\tau) = e^{(i\Delta_{da} - \kappa/2)\tau} \tag{69}$$

The classical steady-state of the two-mode system $(\bar{\alpha}, \bar{\beta})$ may be obtained by setting $\dot{\bar{\beta}} = 0$ in Eq. (68). This requirement simplifies the self-interaction term and is exactly equivalent to performing a Markov regime reduction of the same. The result is a cubic polynomial in $|\bar{\beta}|^2$ that can be solved exactly for the steady-state nonlinear mode amplitude $\bar{\beta}$:

$$\left[\left(\widetilde{\Delta}_{db} + \Lambda|\bar{\beta}|^2\right)^2 + \frac{\widetilde{\gamma}^2}{4}\right]|\bar{\beta}|^2 = g^2|\chi_a|^2\eta^2 \tag{70}$$

where we have introduced the renormalized nonlinear mode detuning and damping parameters respectively:

$$\begin{aligned}\widetilde{\Delta}_{db} &= \omega_d - (\omega_b + g^2|\chi_a|^2\Delta_{da}) \\ \widetilde{\gamma} &= \gamma + g^2|\chi_a|^2\kappa\end{aligned} \tag{71}$$

The steady-state linear mode amplitude may then be determined by requiring $\dot{\bar{\alpha}} = 0$ in Eq. (67a), which simply relates $\bar{\alpha}$ to $\bar{\beta}$:

$$\bar{\alpha} = -\chi_a\left(ig\bar{\beta} + i\eta\right) \tag{72}$$

Once the steady-state amplitudes $(\bar{\alpha}, \bar{\beta})$ have been determined, we perform a stability analysis for small fluctuations around these steady-state(s). Formally, such an analysis can be performed on the linearized version of the effective nonlinear mode dynamical equation, which can be studied analytically *exactly* in the Laplace domain, and is particularly tractable for the special case where $\Delta_{da} = 0$. Full details of such an analysis are provided in Ref. [78].

However, the current experiment explores more general operating conditions where $\Delta_{da} \neq 0$ in general. In this case, it proves most convenient to simply perform a numerical stability analysis based on the Jacobian matrix of the original two-mode system. Performing the linearized stability analysis requires expanding Eqs. (66) around the classical steady state $(\bar{\alpha}, \bar{\beta})$. For notational convenience, we define the vector of steady-state amplitudes $\vec{Z}$ and small fluctuations, $\vec{z}(t)$ respectively:

$$\vec{Z} = (\bar{\alpha}, \bar{\alpha}^*, \bar{\beta}, \bar{\beta}^*)^T \tag{73a}$$

$$\vec{z}(t) = (\delta\alpha(t), \delta\alpha^*(t), \delta\beta(t), \delta\beta^*(t))^T \tag{73b}$$

Then, we expand the variables $\vec{\zeta}(t)$ around the steady-state $\vec{Z}$:

$$\vec{\zeta}(t) = \vec{Z} + \vec{z}(t) \tag{74}$$

and linearize Eqs. (66) in small fluctuations $\vec{z}(t)$, obtaining the set of equations:

$$\frac{d\vec{z}}{dt} = \mathbf{J}[\vec{Z}] \cdot \vec{z}(t) \tag{75}$$

where $\mathbf{J}[\vec{Z}]$ defines the Jacobian matrix of the two-mode system evaluated at the classical steady-state; its entries are given by $J_{ij} = \partial_j A_{\rm c}^i$, where $A_{\rm c}^i$ is the ith element of $\vec{A}_{\rm c}$; more explicitly the Jacobian matrix takes the form:

$$\mathbf{J}[\vec{Z}] = \begin{pmatrix} +i\Delta_{da} - \frac{\kappa}{2} & 0 & -ig & 0 \\ 0 & -i\Delta_{da} - \frac{\kappa}{2} & 0 & ig \\ -ig & 0 & +i\Delta_{db} - \frac{\gamma}{2} + i2\Lambda|\bar{\beta}|^2 & i\Lambda(\bar{\beta}^2) \\ 0 & ig & -i\Lambda(\bar{\beta}^*)^2 & -i\Delta_{db} - \frac{\gamma}{2} - i2\Lambda|\bar{\beta}|^2 \end{pmatrix} \tag{76}$$

The stability of Eqs. (75) is determined by the eigenvalues of the above Jacobian matrix, obtained by setting $\det \mathbf{J} = 0$; these are used to determine the stability boundaries, and in Fig. 50 of the following section.

5.2.3 Numerical phase diagram and Lyapunov stability

Regions in the classical phase diagram with no stable fixed points, can give rise to a rich class of dynamics. Amongst various metrics to characterize such dynamics, we employ the standard technique of computing the maximal Lyapunov exponent $\lambda_{\rm M}$, which describes the sensitivity of dynamical trajectories to small perturbations in the long-time limit.

The maximal Lyapunov exponent $\lambda_{\rm M}$ we calculate is plotted for Device A parameters in drive-Δ_{db} space in Fig. 50; the panel on the right framed in blue shows the region of drive-Δ_{db} space which will be explored later (also in experiments). The blank regions indicate regions where $\lambda_{\rm M} < 0$, indicating a stable fixed point; perturbations near this point decay over time, settling back towards the fixed point. This is visible in the projection of the steady-state dynamics onto the nonlinear mode phase space, plotted in Fig. 50 (a); in the long time limit, the system has returned to the stable fixed point indicated by the orange cross. The gray

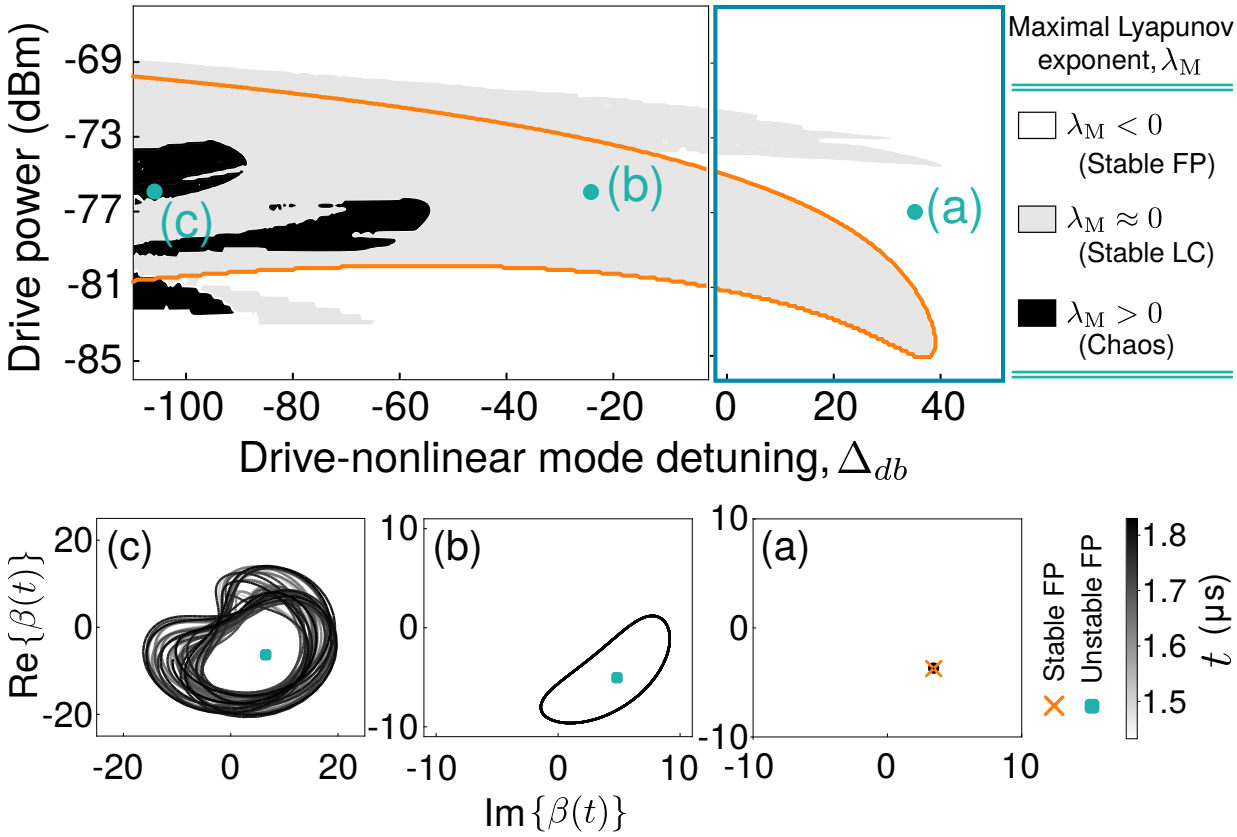

Figure 50: **Calculated maximal Lyapunov exponent λ_M in Drive-Δ_{db} space.** The panel on the right framed in blue indicates the detuning range explored in Figs. 2, 3 of the main text. Solid orange curve indicates the linear stability boundary. In the white regions, $\lambda_M < 0$ is negative and the system is therefore stable. In the light gray regions, $\lambda_M \approx 0$, indicating a stable limit cycle. The dark regions are where $\lambda_M > 0$, and the system exhibits chaotic dynamics. Typical long-time dynamics projected in the nonlinear mode phase space are plotted in (a)-(c) corresponding to dynamics in the stable fixed point, stable limit cycle, and chaotic regimes respectively.

regions indicate $\lambda_M \approx 0$, signifying a stable limit cycle attractor [83]. Steady-state dynamics here follow a stable phase space orbit, as shown in Fig. 50 (b), around a classically unstable fixed point (green square). The periodic orbits yield combs in the frequency domain, as observed in Fig. 50.

Finally, the dark regions indicate $\lambda_{\mathrm{M}} > 0$. Here, perturbations grow without bound over time, manifesting in dynamical chaos observed in numerical simulations of the classical system. The steady-state dynamics plotted in Fig. 50 (c) show how over time a single fixed orbit does not emerge and the system explores a large region of phase space in an irregular manner. The region framed in blue in the phase diagram describes the detuning range explored in the experiment, Figs. 2, 3 of the main text, where the system exhibits stable limit cycle dynamics, consistent with observations in the main text. However, for much more negative Δ_{db} it is possible to observe chaos with the same system. This indicates the potential of the two-mode system for controlled studies of chaos in the quantum regime.

5.2.4 Quantum simulations: comb coherence and estimating pure dephasing rate

$$d\vec{\zeta}(t) = \vec{A}_{\mathrm{c}}(\vec{\zeta})\ dt + \mathbf{B}_{\mathrm{st}}(\vec{\zeta}, \Lambda, \gamma_{\varphi}) d\vec{W}(t) \tag{77}$$

Simulating Eqs. (61) allows us to calculate the output coherence function:

$$G^{(1)}(\tau) = \lim_{t\to\infty} \frac{\langle I(t)I(t+\tau)\rangle - \langle I(t)\rangle^2}{\langle I(t)^2\rangle - \langle I(t)\rangle^2} \tag{78}$$

This enables us to extract the coherence time T_{coh}. The only parameter required to simulate the SDEs that we are unable to directly measure is the pure dephasing rate γ_{φ}; the weak nonlinearity of the nonlinear mode prevents standard Ramsay measurement of the pure dephasing rate, and indirect methods based on cavity measurement are limited by the large disparity between the dephasing rate and the cavity linewidth κ.

However, the coherence of frequency combs is affected by the known nonlinearity and the unknown pure dephasing rate; as a result, by simulating Eqs. (77) for various values of γ_{φ} and comparing with experimental observations, we can estimate γ_{φ}. In Fig. 51, we show the numerically obtained value of T_{coh} across the same cross-section of the phase diagram included in the main text, Fig. 2(b), for $\gamma_{\varphi}/(2\pi) \in [0.0, 1.0, 2.0, 3.0]$ kHz. Also shown is the experimental result. From these results we conclude that the pure dephasing rate may be

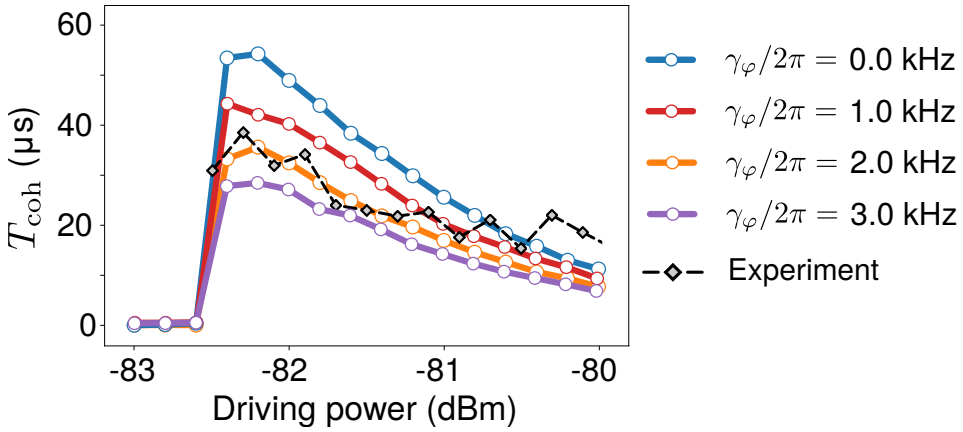

Figure 51: **Coherence times as a function of γ_φ.** Colored lines and points show numerically obtained T_{coh} values from the simulation of Eqs. (77) as a function of drive power, while dashed-diamonds indicate experimental values.

well approximated to lie within $\gamma_\varphi/(2\pi) \in [1.0, 3.0]$ kHz. Furthermore, the best fit is found to be for $\gamma_\varphi/(2\pi) \simeq 2.0$ kHz.

5.3 Nearly quantum-limited Josephson-junction Frequency Comb synthesizer

5.3.1 System schematic and device overview

In our experiment (Fig. 52(c)), the nonlinear mode is realized as a Superconducting QUantum Interference Device (SQUID) [84] array: Device A: 25 SQUIDs; Device B: 5 SQUIDs. The SQUIDs act together as a flux-tunable, nonlinear inductor, which is shunted with a planar interdigitated capacitor/antenna to form a nonlinear microwave mode. Weakly asymmetric SQUIDs (with critical current ratio of 1.2:1) are used to build up the array, alleviating otherwise large hysteresis effects at the cost of a reduction in tunability of the nonlinear mode frequency [85]. The device is deposited on a sapphire substrate and capacitively coupled to the $\lambda/4$ mode of a coaxial 3-D copper cavity [86]. This driven-dissipative

system is then described by the master equation:

$$\dot{\hat{\rho}} = -i[\hat{\mathcal{H}}, \hat{\rho}] + \kappa\mathcal{D}[\hat{a}]\hat{\rho} + \gamma\mathcal{D}[\hat{b}]\hat{\rho} + \gamma_\varphi\mathcal{D}[\hat{b}^\dagger\hat{b}]\hat{\rho} \tag{79}$$

which includes linear damping rates κ (γ) for modes $\hat{a}$ ($\hat{b}$), and pure dephasing (γ_φ) for the flux-tunable nonlinear mode; thermal fluctuations are neglected. By sweeping the flux through the SQUIDs to tune the nonlinear mode frequency, and making a measurement of the reflection coefficient $S_{11}(\omega)$, we extract (Fig. 52(c)) a coupling strength of $g/2\pi = 87.6956\,\mathrm{MHz}$ between the modes, and linear mode damping rate $\kappa/2\pi = 10.9308\,\mathrm{MHz}$. Via pump-probe measurements 5.4.2 we also extract a Kerr nonlinearity of $\Lambda/2\pi = 5.96\,\mathrm{kHz}$, such that $\Lambda/\kappa \sim 10^{-3}$, stronger than typical values of $\sim 10^{-5}$ for optical microresonators [72].

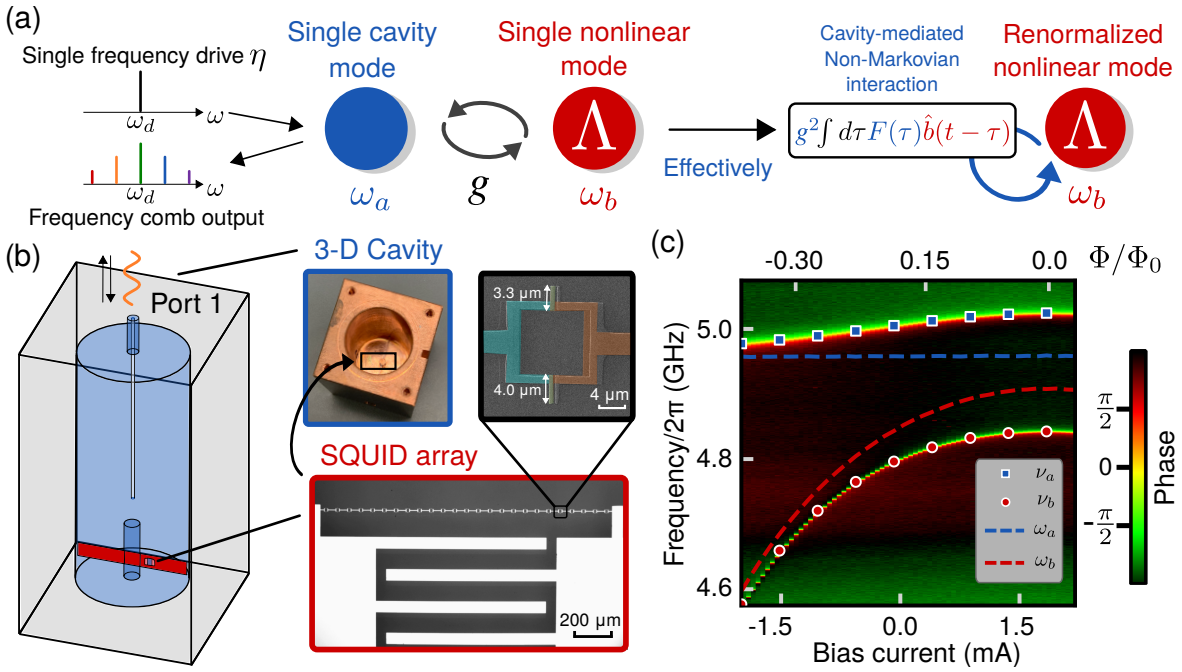

Figure 52: **System schematic and flux sweep.** (a) The two-mode device can be represented by a single cavity mode (blue, ω_a) coupled linearly to a single Kerr mode (red, ω_b). (b) Circuit QED implementation of the schematic in (a). The nonlinear mode inductance is formed by 25 Superconducting QUantum Interference Devices (SQUIDs) in series; False-color SEM image of a component SQUID indicates the small asymmetry employed to alleviate hysteresis. The SQUID array is coupled to an antenna that both forms the capacitance of the nonlinear mode and controls its dipole coupling with the linear mode; the latter is the $\lambda/4$ mode of a coaxial 3-D cavity, fabricated of copper to permit the passage of an external DC flux that threads all the SQUIDs. The input signal drives the cavity through port 1, and $S_{11}(\omega)$ is monitored. (c) Color plot of reflected signal vs. frequency from port 1 ($S_{11}(\omega)$) for a range of applied coil bias currents/applied SQUID fluxes. The linear and nonlinear mode frequencies are highlighted by blue squares and red dots respectively. By fitting for the bare mode frequencies, we determine $g/2\pi = 87.6956$ MHz, as well as the bare mode frequencies, represented by the dashed lines.

As shown in Fig 52, we create a comb in this device by driving with a carefully chosen, single microwave drive of strength η at frequency ω_d, which interacts with the device to

create a series of tones at regularly spaced output frequencies (the 'comb'). The linear mode plays the role of mediating a delayed self-interaction of the nonlinear mode (right panel), with kernel $F(\tau) = e^{-\tau/\chi_a}$. In the strong coupling regime, the interaction's non-Markovian nature fundamentally modifies the nonlinear mode's stability, enabling comb formation.

Table 11: **Device parameters.** Coupling strength g, nonlinearity Λ, and bare cavity damping rate κ for Device A (25 SQUIDs) and Device B (5 SQUIDs); nonlinearity suppression by a factor ~ 25 is measured, as designed.

	Device A (25 SQUIDs)	Device B (5 SQUIDs)
$\omega_b/2\pi$(GHz)	4.956806	4.951073
$g/2\pi$(MHz)	87.6956	89.25
$\Lambda/2\pi$(MHz)	5.96×10^{-3}	152.6×10^{-3}
$\kappa/2\pi$(MHz)	10.9308	22.84

5.3.2 Comb generation and phase diagram

Analysis of this system in Ref. [78] showed that the linear mode effectively equips the nonlinear mode with a delayed self-interaction (see Fig. 52(a)), whose influence is dictated by the coupling g and the linear mode susceptibility $\chi_a = (-i\Delta_{da} + \frac{\kappa}{2})^{-1}$. Under suitable coupling, drive, and detuning conditions, this two-mode system can go beyond typical bifurcation dynamics associated with Kerr nonlinear devices to exhibit frequency comb formation. To illustrate this, we plot the classical phase diagram for measured Device A parameters in Fig. 53(a), as a function of drive detunings Δ_{da}, Δ_{db} (see Sec. 5.2.2). For each pair of detunings, we consider a range of experimentally accessible drive powers (-132 dBm to -67 dBm), and classify phases according to the number of fixed points (FPs) and stable fixed points (SFPs) observable within this driving range. For large $|\Delta_{da}|$ (small $|\chi_a|$) relative to g, only two types of phases are exhibited: blank regions, where the system admits one SFP for all driving powers considered, or hatched regions, where for some subset of driving powers, three FPs exist. In either case, at least one fixed point is always stable. These phases are

reminiscent of the standard Kerr bistability, and unsurprisingly so: in this regime, the effective coupling $g|\chi_a|$ is weak, and the mediated interaction may be treated within a Markov approximation.

However, for intermediate $|\Delta_{da}|$ such that $g|\chi_a| \gtrsim 1$ (on resonance, we require $g > \kappa/2$, comfortably satisfied by Device A), the non-Markovian nature of the interaction manifests in a qualitative change of the nonlinear mode's stability, marked by regions (shaded red) where no stable fixed points exist for a subset of the driving powers considered. Here, classical Lyapunov analysis reveals the possibility of our device exhibiting stable limit cycles with period $T = \frac{2\pi}{\Delta}$ and comb-like frequency spectra with spacing Δ, and even chaotic dynamics deeper into the unstable regime, namely at more negative detunings and stronger drive powers (see Sec 5.2.3).

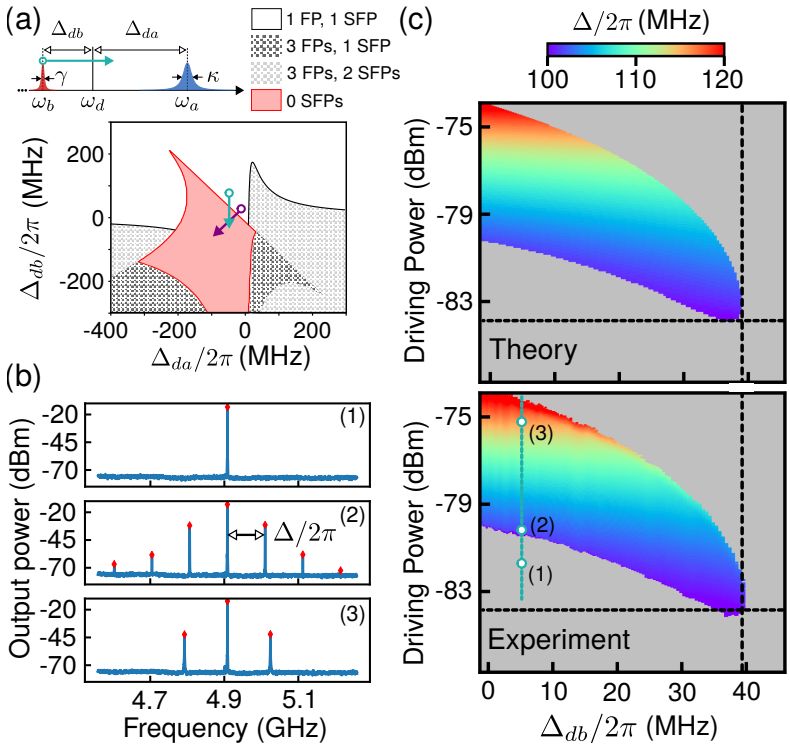

Figure 53: **Phase diagram and comb spectrum**. (a) Theoretically predicted phase diagram in Δ_{db}-Δ_{da} space, indicating observable phases characterized by number and stability of classical fixed points (FPs) over a range of experimentally accessible drive powers (-132 dBm to -67 dBm). Here, the unstable regime (shaded red) exhibiting no stable fixed points (SFPs) is entered by fixing the drive frequency to $\omega_d = 4.9085(2\pi)$ GHz, varying the nonlinear mode frequency along the direction of the green arrow via a flux sweep, and observing the output power spectra. (b) Typical power spectra as a function of increasing drive power, along the indicated cross section of the experimental phase diagram in (c). The theoretical phase diagram is plotted in the top panel of (c) for comparison.

To observe the response of our quantum device in this rich dynamical regime, we enter the unstable region along the green arrow in Fig. 53 (a), by fixing the drive frequency so that $\Delta_{da}/2\pi = -47.8\,\text{MHz}$, and flux tuning the nonlinear mode frequency. In search of the frequency domain signature of comb formation, we measure the frequency response in drive-Δ_{db} parameter space using a spectrum analyzer, with typical results at fixed Δ_{db} shown in Fig. 53(b). At low powers (1), the system exhibits a single frequency response at the drive

frequency, corresponding to the stable fixed point. However, as the power is increased, a multifrequency spectrum emerges with equidistant peaks (2 and 3). The spacing Δ extracted from these power spectra are used to construct the experimental phase diagram in Fig. 53(c), with the theoretical result over the same parameter space provided for comparison. We find remarkable agreement between theory and experiment; only a single fitting offset is used to account for scaling factors along the drive power axis.

5.3.3 Temporal coherence and dynamical response

Power spectrum measurements provide a key signature of comb formation but are insensitive to the nontrivial phase dynamics of these complex nonlinear solutions. While the central comb peak has a definite phase set by the incident coherent tone, the relative phase $\theta(t)$ of generated sidebands relative to the central peak phase is free to diffuse [87, 88]. This diffusion sets the comb linewidth and thus provides the ultimate limit to any precision measurements made using the comb in question [89]. To quantify the phase coherence, we measure the *steady-state* first-order temporal coherence function $G^{(1)}(\tau)$, defined as [90]:

To do so, we first obtain the time-domain cavity output $I(t)$ using a single side band (SSB) mixer to downconvert the dominant sideband peak to around the 100 MHz regime, followed by homodyne detection via a 500 MSample/s digitizer to demodulate the output signal, and finally compute its time-domain autocorrelation. The normalized coherence function $G^{(1)}(\tau)$ decays from its maximum value of unity (at $\tau = 0$) towards $G^{(1)}(\tau) = 0$ over a timescale T_{coh} determined by the loss mechanisms affecting the system dynamics. We measure $G^{(1)}(\tau)$ in the parameter space explored in Fig. 53(c), and extract T_{coh} as the decay constant of the observed function envelopes; the results are plotted in Fig. 54(a). Focusing in particular on the indicated cross-section at $\Delta_{db}/2\pi = 25.2$ MHz, we plot the measured $G^{(1)}(\tau)$ functions at positions $\{1, 2, 3\}$ in the top panel of Fig. 54(c). Outside the comb regime (1), $G^{(1)}(\tau)$ decays on a timescale of ~ 13 ns, set by the fastest decay rate, namely the bare cavity loss κ. However, a qualitative change is observed in $G^{(1)}(\tau)$ when the system transitions into the comb regime (2), with a sharp increase in coherence time to a maximum of 36.7 μs, significantly longer than the timescale set by κ. This observation,

together with the decrease in T_{coh} with increasing drive power (3), highlights a key feature of the self-oscillating regime: the intrinsic energy loss of the system is overcome and coherence is therefore no longer determined by the bare energy loss rates.

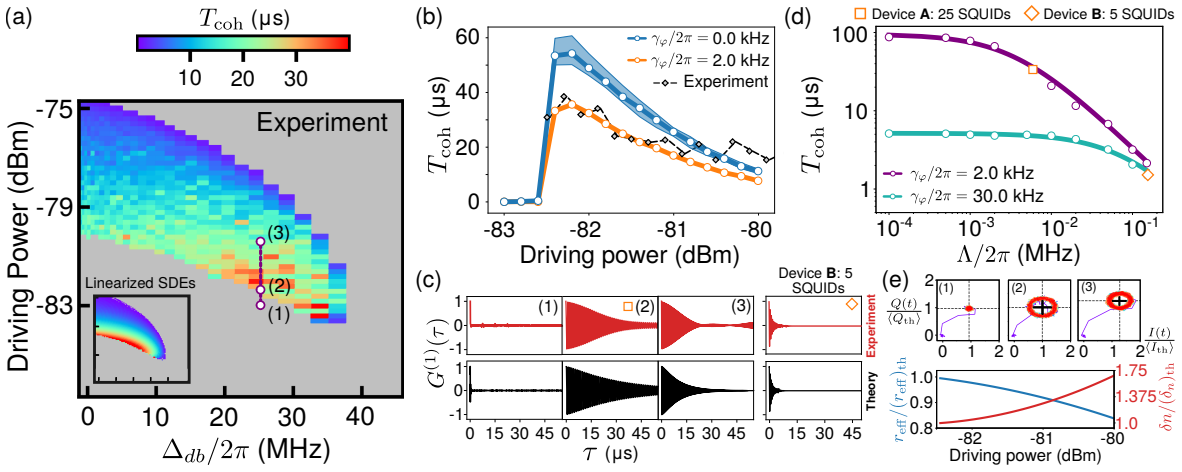

Figure 54: **Comb coherence.** (a) Coherence time $T_{\rm coh}$ extracted by measuring $G^{(1)}(\tau)$ (Eq. 78) for the same operating parameters as Fig. 53 b. Inset: approximate $T_{\rm coh}$ calculated using Floquet analysis of linearized SDEs (see text). (b) Cross section of phase diagram along the dashed line in a, in black. The blue curve and shaded region indicates the theoretically calculated coherence time due to nonlinearity alone (pure dephasing $\gamma_\varphi = 0$). The orange curve shows $T_{\rm coh}$ for $\gamma_\phi = 2.0(2\pi)$ kHz, showing good agreement with the experimental result. (c) Experimental (top panel) and theoretical (lower panel) $G^{(1)}(\tau)$ for $\gamma_\varphi = 2.0(2\pi)$ kHz at positions 1 (stable regime), 2 (threshold of comb formation), and 3 (higher drive power in comb regime). (d) Numerical results for variation of coherence time with nonlinearity. Purple and green points correspond to parameters for Device A (25 SQUIDs) and B (5 SQUIDs) respectively, obtained by varying the nonlinearity alone. Experimental results for the devices are shown by the orange square and diamond; corresponding $G^{(1)}(\tau)$ are marked by the same symbols in (c). (e) Top panel: I-Q trace at positions {1,2,3}, showing 2-D projection of the limit cycle orbit which decreases in radius with increasing power. Lower panel: theoretical effective radius of limit cycle $r_{\rm eff}$ (solid blue) and standard deviation of noise projected tangential to limit cycle, δn (solid red, right hand axis) scaled by their values at threshold. The relative decrease in $r_{\rm eff}$ combined with the increase in δn point towards a reduction in coherence time with increasing drive power.

This naturally raises the question: what limits the observed phase coherence? The answer lies in the full quantum description of the strongly-driven, weakly nonlinear two-

mode system. In this regime, we employ a phase-space approach based on the Positive-P representation [78, 82, 81], obtaining a set of stochastic differential equations (SDEs) for phase space variables $\vec{\zeta} = (\alpha, \alpha^\dagger, \beta, \beta^\dagger)^T$ associated with operators $(\hat{a}, \hat{a}^\dagger, \hat{b}, \hat{b}^\dagger)^T$. The SDEs take the general form:

$$d\vec{\zeta}(t) = \vec{A}_{\rm c}(\vec{\zeta})\ dt + \mathbf{B}_{\rm st}(\vec{\zeta}, \Lambda, \gamma_\varphi) d\vec{W}(t) \tag{80}$$

The deterministic contribution ($\propto \vec{A}_{\rm c}$) describes noise-free classical dynamics of the two-mode system, which yields perfectly coherent combs. The remaining stochastic terms $\propto d\vec{W}(t)$ (vector of independent Wiener increments) then describe deviations from classical dynamics, here including fluctuations due to the quantum nonlinearity Λ and pure dephasing γ_φ. These fluctuations are ultimately responsible for phase diffusion that limits comb coherence. The stochastic terms take the explicit form $\mathbf{B}_{\rm st}(\vec{\zeta}, \Lambda, \gamma_\varphi) d\vec{W}(t) = \sqrt{\Gamma}\mathbf{B}_1(\vec{\zeta}) d\vec{W}_1(t) + \sqrt{\gamma_\varphi}\mathbf{B}_2(\vec{\zeta}) d\vec{W}_2(t)$, where $\Gamma = \sqrt{\Lambda^2 + \gamma_\varphi^2}$. Crucially, we note that even in the absence of pure dephasing, $\gamma_\varphi \to 0$, the stochastic terms do not vanish: a contribution due to the intrinsic nonlinearity of the system always remains, setting a fundamental limit on comb coherence. This is verified by simulating Eqs. (80) for $\gamma_\varphi = 0$ and the experimentally measured nonlinearity of $\Lambda/2\pi = 5.96$ kHz, and obtaining $T_{\rm coh}$[91, 92]; the results are shown by the blue curve in Fig. 54(b), with the blue shaded region being a 95% confidence bound accounting for uncertainty in Λ. The maximum $T_{\rm coh}$ is thus limited to around 55 μs by amplified quantum fluctuations due to the device nonlinearity alone under these operating conditions. This of course exceeds the maximum observed $T_{\rm coh}$ since $\gamma_\varphi \neq 0$. For $\gamma_\varphi/2\pi \simeq 2.0$ kHz (orange) we find good agreement with experiment (gray); simulated $G^{(1)}(\tau)$ at positions $\{1, 2, 3\}$ are shown (Fig. 54 c, black) for comparison. The relatively small γ_φ is not unexpected given both the narrow modulation range of the asymmetric SQUID array [85] and operation at $\Phi/\Phi_0 \lesssim 0.12$, close to the flux noise sweet spot (see Fig. 52 (c)).

Since Λ cannot be varied *in-situ* while holding other parameters fixed, we confirm its influence on $T_{\rm coh}$ by employing Device B; this 5-SQUID device is engineered to have the same total inductance as Device A, while possessing a 25-fold stronger nonlinearity [93] of $\Lambda/2\pi = 152.6$ kHz. While we obtain similar multifrequency behavior, coherence times for this device are much shorter, $T_{\rm coh} \lesssim 1.5$ μs (see Fig. 54(c)) for measured and simulated

$G^{(1)}(\tau)$ at typical operating parameters). Although Device B is operated away from the flux-noise sweet spot, and thus experiences a larger estimated $\gamma_\varphi/2\pi \simeq 30\,\mathrm{kHz}$, we find that its much stronger nonlinearity is dominant in limiting comb coherence. To confirm the dependence of T_{coh} on Λ and γ_φ numerically, we simulate T_{coh} at fixed positions on the phase diagrams of both devices, while varying Λ. The results are plotted in Fig. 54(d), in purple (green) for Device A (Device B) parameters, with the experimental result indicated by the square (diamond). They are well described by fits to $T_{\mathrm{coh}} = a(\gamma_\varphi + b\Lambda)^{-1}$ (curves); we find $b = (\mathrm{A}\colon 0.40, \mathrm{B}\colon 0.55) \neq 1$, consistent with Λ and γ_φ-contributions to dephasing originating from different stochastic terms in Eqs. (80). More importantly, both devices clearly operate in the regime where $b\Lambda \gtrsim \gamma_\varphi$, and thus T_{coh} is predominantly set by the nonlinearity.

However, as observed in Fig. 54(a), T_{coh} also depends nontrivially on *operating* parameters (e.g. drive power, detuning), even if Λ, γ_φ are held fixed. This dependence is intimately related to the nature of the dynamical comb regime, where the system traverses a periodic trajectory in phase space. The shape of this trajectory, which changes with operating parameters, controls its susceptibility to noise, as well as the noise itself when the latter is *multiplicative* (dependent on $\vec{\zeta}(t)$, as $\mathbf{B}_{\mathrm{st}}$ is). This connection can be made precise via a linearized Floquet analysis [94, 88, 95] of the SDEs around the *classical* limit cycle trajectory $\vec{\zeta}_{\mathrm{c}}(t)$. In this weak-fluctuations approach [96], the phase $\theta(t)$ of the limit cycle solution evolves according to the SDE: $r_{\mathrm{eff}}\dot{\theta} = n(t)$, and the coherence time T_{coh} can be related to the variance of this diffusing phase, $T_{\mathrm{coh}}^{-1} \propto \langle[\theta(T) - \theta(0)]^2\rangle$. Here r_{eff} is the effective limit cycle radius, defined via $r_{\mathrm{eff}}\Delta = \sqrt{\frac{1}{T}\int_0^T dt\ ||\vec{v}(t)||^2}$ where $\vec{v}(t) = \dot{\vec{\zeta}}_{\mathrm{c}}(t)$ is the tangential velocity of limit cycle traversal. Secondly, $n(t)$ is the projection of stochastic terms $\mathbf{B}_{\mathrm{st}}(\vec{\zeta}_{\mathrm{c}}(t))d\vec{W}$ onto the limit cycle trajectory. Noise projected onto the limit cycle therefore provides an impulse that causes $\theta(t)$ to diffuse, while r_{eff} provides an inertial term: the larger the radius, the more $\theta(t)$ resists diffusion. We plot the average projected noise standard deviation, $\delta n = \sqrt{\frac{1}{T}\int_0^T dt\ \langle n(t)^2\rangle}$ and the effective limit cycle radius r_{eff} along the indicated cross-section of Fig. 54(a), scaled by their values at the threshold of comb formation. The limit cycle radius (blue) decreases with increasing power; this is also seen experimentally in I-Q traces (top panel), positions 2 to 3, which can be viewed as a 2-D Poincaré section of the limit cycle trajectory. Additionally, the noise strength δn (red, right-hand axis) increases, in a

clear manifestation of its multiplicative nature. Both effects tend to reduce T_{coh}, as captured by both the linearized analysis (Fig. 54(a), inset) and full SDE simulations (Fig. 54(b)).

Finally, we note that multiplicative noise can also manifest in non-exponential decay of phase coherence. However, for the operating parameters explored in Fig. 54, theoretical simulations predict deviations from exponential decay to be minimal, and experimentally observed weak non-exponential signatures (such as (3) in Fig. 54(c)) can be attributed to electronic $1/f$ noise. With the use of additional probing systems and judicious choice of operating parameters[97, 98, 99], this system could be used to study non-exponential phase decoherence due to quantum fluctuations.

5.3.4 Temporal instabilities and further explorations

While we have demonstrated the formation of stable frequency combs with this minimal two-mode Kerr system, even more complex dynamical phenomena may be observed deeper in the regime with no stable fixed points. We explore this region by fixing $\omega_b = 4.91$ GHz and varying ω_d instead, now entering the unstable region along the purple arrow in Fig. 55(a). The experimental phase diagram in Fig. 55(a) plots spacings Δ where combs are observed, together with a dark gray region where the spectrum no longer exhibits a comb. The typical variation in spectrum is shown in Fig. 55(b). For $\Delta_{db}/2\pi \gtrsim -30$ MHz, a clear comb spectrum is observed with a spacing that varies with ω_d; the system polariton frequencies ν_a, ν_b (unchanged with ω_d) are marked in dashed pink, confirming that comb peaks do not always coincide with passive modes of the two-mode system.

For $\Delta_{db}/2\pi \lesssim -30$ MHz, the spectrum abruptly changes, exhibiting a single broad peak and an increased noise background. Analyzing I-Q traces in Fig. 55(c), dynamics in this region (2) show large deviations with time and while recurringly confined to a region of phase space do not follow a regular trajectory, even on short timescales (inset), in stark contrast to regular periodic dynamics for stable comb operation (1). Note that these temporal instabilities disagree with results of a weak quantum fluctuations analysis in this regime (Fig. 55(a), inset), which simply predicts frequency combs with finite coherence akin to Fig. 54 (although instabilities do manifest for more negative detunings. Curiously, quantum dynamics here are

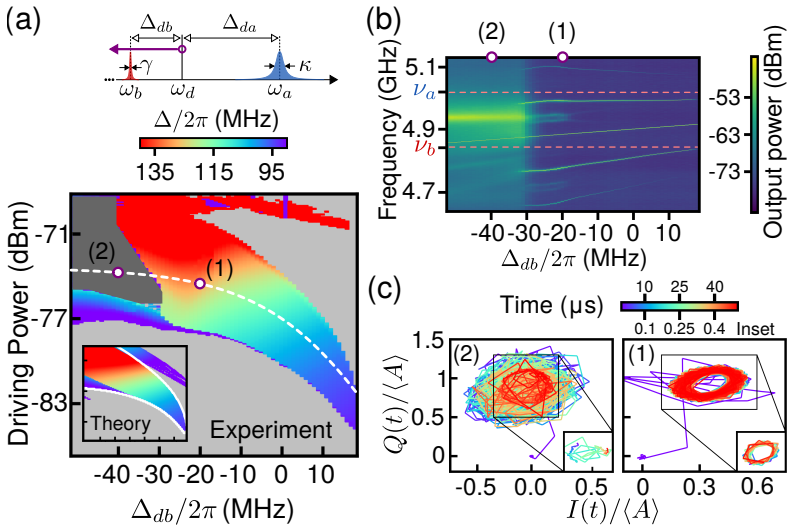

Figure 55: **Temporal instabilities.** (a) By fixing ω_a, ω_b and varying ω_d (top panel), the system can be driven to the regime with no stable fixed points along the purple arrow in Fig. 53 (a), while leaving the underlying mode structure unchanged. The resulting phase diagram plotting observed comb spacing Δ is shown, with the theoretical prediction in the inset. For $\Delta_{db}/2\pi \lesssim -30$ MHz and strong enough driving, a distinct regime emerges (dark gray) where the output spectrum broadens significantly. In (b), we show the typical evolution of the spectrum across the white dashed line, chosen to show a large variation in comb spacing. In dashed red are the underlying polariton resonances, indicating that the emergent comb peaks do not exactly coincide with these resonances. (c) Time dynamics as observed via I-Q traces, with both axes scaled by $\langle A\rangle = \sqrt{\langle I^2\rangle + \langle Q^2\rangle}$ at position 1, for ease of direct comparison. In the stable comb regime (1), the cavity response settles into an obvious orbit as before; the inset shows a 500 ns trace after $t = 40$ μs, demonstrating the stable orbit. In the unstable regime (2), the response shows large deviations over time and no periodic phase space trajectory is observed.

also too complex to be captured by simulating the exact SDEs in Eqs. (80), which run into familiar numerical difficulties encountered in the application of phase-space stochastic approaches to strong-quantum systems [100]. This could be indicative of qualitative deviations

from classically stable limit cycles not captured by a linearized treatment of quantum fluctuations, and merits further study of this system as a platform for exploring complex dynamics of quantum nonlinear systems.

5.4 Supplementary experimental details and methods.

5.4.1 Phase diagram for Device B (5 SQUIDs)

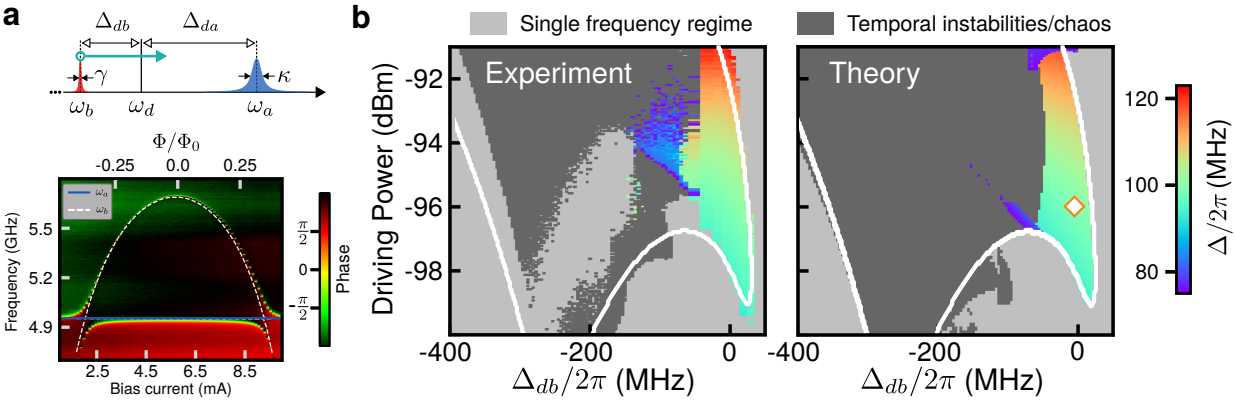

Figure 56: **Device B measurements.** (a) Flux sweep showing the system polariton modes and the avoided crossing as the nonlinear mode is swept across the linear mode resonance. The horizontal blue line indicates the bare linear mode frequency, while the white dashed line indicates the bare nonlinear mode frequency. (b) Experimental and theoretical phase diagram in Drive-Δ_{db} space, as the nonlinear mode frequency is swept (see schematic in (a)). The observed comb spacing Δ in the multifrequency regime is plotted, alongside the single frequency regime (light gray) and regime with temporal instabilities (dark gray). White curve in both phase diagrams is the analytically obtained boundary enclosing the classically unstable region. Orange diamond indicates the drive power (-96 dBm) and detuning ($\Delta_{db}/2\pi = -5.87$ MHz) for which coherence function results are plotted in Fig. 3(c) of the main text for Device B.

In addition to Device A, which employs a 25 SQUID array, we explore the impact of nonlinearity on comb dynamics by fabricating Device B, which employs a 5 SQUID array

and therefore possesses an approximately 25-fold stronger nonlinearity. In Fig. 56 (a), we show the flux sweep of this device, indicating the polariton resonances of the two-mode system. Fitting to the avoided crossing reveals a coupling strength of $g/2\pi = 89.25$ MHz, similar to Device A (by design), and a bare linear mode linewidth of $\kappa/2\pi = 22.84$ MHz.

Having verified that the device satisfies the strong coupling condition $g > \frac{\kappa}{2}$ at resonant driving ($\Delta_{da} = 0$, see main text), we can explore the classically predicted unstable regime as was done for Device A. Fixing the driving frequency at $\omega_d/2\pi = 4.9085\,\mathrm{GHz}$, we change the external flux through the SQUIDs to sweep the nonlinear mode frequency, as shown schematically in the top panel of Fig. 56 (a). Device B has a much larger flux modulation range than Device A, enabling us to explore a wider range of drive-nonlinear mode detunings Δ_{db}. The resulting phase diagram in drive power-Δ_{db} space is shown in Fig. 56 (b), with the theoretically predicted phase diagram shown in the right panel, both plotted with the same axes. The light gray regions indicate the single frequency regime, which gives way to a multifrequency comb regime at appropriate drive strengths for small $|\Delta_{db}|$. The experiment and theory agree quite well both in terms of the critical detuning where the combs emerge, as well as the observed comb spacing. Finally, the orange diamond in the theory plot indicates the position on the phase diagram for which coherence function results are plotted in Fig. 3 of the main text.

Note that for more negative Δ_{db}, a region (dark gray) emerges where the system exhibits temporal instabilities similar to Device A, in both the experimental and theoretical phase diagrams. Numerical simulations here indicate that the system exhibits chaotic dynamics (maximal Lyapunov exponent $\lambda_{\mathrm{M}} > 0$). We also find greater disparity between experiment and theory here; in addition to possible deviations from classical predictions due to quantum effects, the dynamics exhibit temporal instabilities that require careful processing. Such dynamical regimes therefore merit further detailed investigation. The white contour in both figures depicts the analytically predicted unstable region, as determined by the linearized dynamics; it agrees well with both experiment and numerical simulations, in particular for small $|\Delta_{db}|$.

5.4.2 Kerr nonlinearity measurement

To demonstrate the dependence of comb coherence on the quantum nature of the device nonlinearity, knowledge of this engineered Kerr nonlinearity strength is of crucial importance. Typically, one would do so via a standard pump-probe measurement that measures the Kerr-induced frequency shift of the nonlinear mode as the pump power incident on it increases. However, for the two-mode system such a measurement accesses the frequency shift of the renormalized *polariton* modes of the system, which of course depends on the degree of hybridization between linear and nonlinear modes. In this section we clarify how measured polariton mode frequency shifts can be used to extract the bare nonlinear mode Kerr interaction strength.

We begin by rewriting below, for convenience, the full system Hamiltonian ($\hbar = 1$) from Eq. 58 in Seq. 5.2.1:

$$\hat{\mathcal{H}} = -\Delta_{da}\hat{a}^\dagger\hat{a} - \Delta_{db}\hat{b}^\dagger\hat{b} - \frac{\Lambda}{2}\hat{b}^\dagger\hat{b}^\dagger\hat{b}\hat{b} + g(\hat{a}^\dagger\hat{b} + \hat{a}\hat{b}^\dagger) + \eta(\hat{a} + \hat{a}^\dagger) \tag{81}$$

Next, we consider the linear Hamiltonian $\hat{\mathcal{H}}_{\mathrm{L}}$ that determines the polariton modes:

$$\hat{\mathcal{H}}_{\mathrm{L}} = \omega_a\hat{a}^\dagger\hat{a} + \omega_b\hat{b}^\dagger\hat{b} + g(\hat{a}^\dagger\hat{b} + \hat{a}\hat{b}^\dagger) \equiv \begin{pmatrix}\hat{a}^\dagger & \hat{b}^\dagger\end{pmatrix} \underbrace{\begin{pmatrix}\omega_a & g \\ g & \omega_b\end{pmatrix}}_{\mathbf{H}_{\mathrm{L}}} \begin{pmatrix}\hat{a} \\ \hat{b}\end{pmatrix} \tag{82}$$

which is obtained from Eq. (58) by neglecting the nonlinearity and drive terms, and returning to the lab frame. The above Hamiltonian may be diagonalized by introducing the matrix of eigenvectors $\mathbf{P}$ and diagonal matrix of eigenvalues $\mathbf{D}$ for the matrix $\mathbf{H}_{\mathrm{L}}$, such that $\mathbf{H}_{\mathrm{L}} = \mathbf{P}\mathbf{D}\mathbf{P}^{-1}$. The Hamiltonian then becomes:

$$\hat{\mathcal{H}}_{\mathrm{L}} = \nu_a\hat{c}_a^\dagger\hat{c}_a + \nu_b\hat{c}_b^\dagger\hat{c}_b, \quad \begin{pmatrix}\hat{c}_a \\ \hat{c}_b\end{pmatrix} = \mathbf{P}^{-1}\begin{pmatrix}\hat{a} \\ \hat{b}\end{pmatrix}, \ \mathbf{D} = \begin{pmatrix}\nu_a & 0 \\ 0 & \nu_b\end{pmatrix} \tag{83}$$

which serves to define the polariton modes $\hat{c}_a$, $\hat{c}_b$, and corresponding frequencies ν_a, ν_b.

We can now rewrite the Kerr nonlinear term of the full Hamiltonian, Eq. (58), in the polariton basis. Writing the nonlinear term $\hat{\mathcal{H}}_\Lambda$ as:

$$\hat{\mathcal{H}}_\Lambda = -\frac{\Lambda}{2}\hat{b}^\dagger\hat{b}^\dagger\hat{b}\hat{b} \tag{84}$$

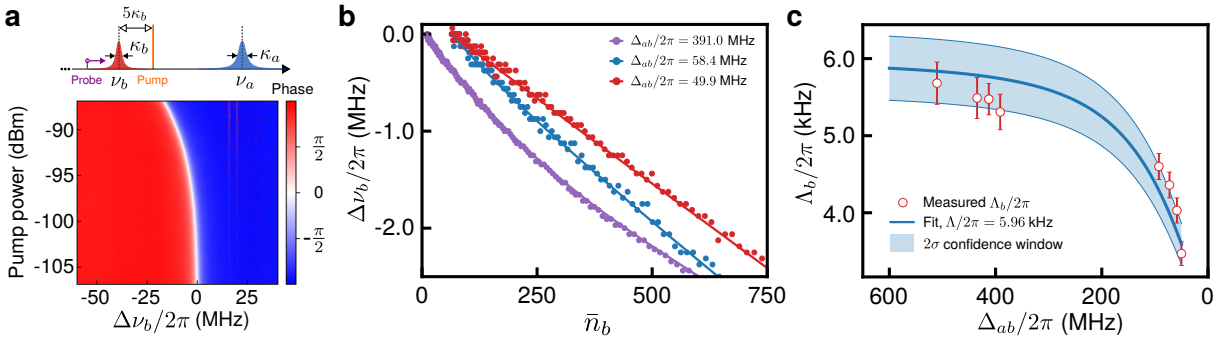

Figure 57: **Kerr nonlinearity measurement.** (a) Left column: schematic showing the pump-probe setup. Note that modes shown are *polariton* modes, not the bare modes. A strong pump tone (orange) is applied 5 linewidths positively detuned from $\hat{c}_b$ (see text), and the modified polariton resonance frequency identified using a weak probe (purple). Increasing polariton mode occupation $\bar{n}_b$ by increasing pump tone power, the frequency shift $\Delta\nu_b$ of polariton mode is measured versus $\bar{n}_b$ for various detunings between the bare linear and nonlinear modes, $\Delta_{ab} = \omega_a - \omega_b$. Lines are fits to $-\Lambda_b\bar{n}_b + \epsilon O(\bar{n}_b^2)$ where higher order terms $\propto \epsilon$ become important as pump power increases. The fits are used to extract the polariton mode nonlinearity Λ_b. With decreasing detuning Δ_{ab}, the initial slope of the fit decreases, indicating a decrease in the strength of the $\hat{c}_b$ mode nonlinearity as the hybridization increases. (b) Measured Kerr nonlinearity Λ_b of polariton mode $\hat{c}_b$ (red circles) extracted from (a), as a function of detuning Δ_{ab}. Solid blue line is the best fit to Eq. (92), with the obtained fit value of $\Lambda/2\pi = 5.96$ kHz. The shaded region indicates the 2σ confidence interval for the fit.

and noting from Eq. (83) that:

$$\hat{b} = \mathbf{P}_{21}\hat{c}_a + \mathbf{P}_{22}\hat{c}_b = \sum_n \mathbf{P}_{2n}\hat{c}_n \tag{85}$$

the nonlinear Hamiltonian in terms of polariton modes takes the form:

$$\hat{\mathcal{H}}_\Lambda = -\frac{\Lambda}{2}\sum_{nmrs} \mathbf{P}^*_{2n}\mathbf{P}^*_{2m}\mathbf{P}_{2r}\mathbf{P}_{2s}\hat{c}^\dagger_n\hat{c}^\dagger_m\hat{c}_r\hat{c}_s \equiv -\frac{\Lambda}{2}\sum_{nmrs}\mathcal{A}_{nmrs}\hat{c}^\dagger_n\hat{c}^\dagger_m\hat{c}_r\hat{c}_s \tag{86}$$

Therefore, the coupling transforms the localized nonlinearity of mode $\hat{b}$ into self- and cross-Kerr interactions between the polariton modes of the system. The Kerr-induced frequency

shift observed for either polariton mode will be a combination of these terms, making it complicated to determine in general.

However, we can obtain a simplified expression by assuming operation near a stable fixed point and assuming a strong polariton mode occupation, both conditions that are expected to be valid for the typical pump-probe measurement scheme. The experimental scheme proceeds similarly to the case for a single nonlinear mode: a strong pump tone is applied to the system at a positive detuning of five linewidths away from *polariton* mode $\hat{c}_b$, predominantly pumping this mode, although also residually (weakly) pumping mode $\hat{c}_a$ (see schematic in Fig. 57 (a)). The resulting steady-state polariton amplitudes, and therefore occupations, can be conveniently determined by first obtaining the nonlinear and linear mode amplitudes $\bar{\beta}$, $\bar{\alpha}$ by solving Eqs. (B6) and (B8) respectively, reproduced below:

$$\left[\left(\widetilde{\Delta}_{db} + \Lambda|\bar{\beta}|^2\right)^2 + \frac{\widetilde{\gamma}^2}{4}\right]|\bar{\beta}|^2 = g^2|\chi_a|^2\eta^2 \tag{87a}$$

$$\bar{\alpha} = -\chi_a\left(ig\bar{\beta} + i\eta\right) \tag{87b}$$

recalling the renormalized nonlinear mode detuning and damping parameters respectively:

$$\begin{aligned}\widetilde{\Delta}_{db} &= \omega_d - (\omega_b + g^2|\chi_a|^2\Delta_{da}) \\ \widetilde{\gamma} &= \gamma + \gamma_\varphi + g^2|\chi_a|^2\kappa\end{aligned} \tag{88}$$

where $\chi_a = (-i\Delta_{da} + \frac{\kappa}{2})^{-1}$. Then, the steady-state polariton amplitudes, $\bar{c}_a$, $\bar{c}_b$, are easily determined via the transformation matrix introduced in Eq. (83):

$$\begin{pmatrix}\bar{c}_a \\ \bar{c}_b\end{pmatrix} = \mathbf{P}^{-1}\begin{pmatrix}\bar{\alpha} \\ \bar{\beta}\end{pmatrix} \tag{89}$$

Finally, the application of a weak probe determines Kerr-mediated frequency shifts, as dictated by the nonlinear Hamiltonian, Eq. (86). We are only interested in shifts to the polariton mode $\hat{c}_b$; the corresponding terms of the nonlinear Hamiltonian are given by:

$$\begin{aligned}\hat{\mathcal{H}}_\Lambda \approx &-\frac{\Lambda}{2}\left[\mathcal{A}_{2222}\hat{c}_b^\dagger\hat{c}_b + 4\mathcal{A}_{2121}\hat{c}_a^\dagger\hat{c}_a + 2\mathcal{A}_{2221}\hat{c}_b^\dagger\hat{c}_a + 2\mathcal{A}_{2122}\hat{c}_a^\dagger\hat{c}_b\right]\hat{c}_b^\dagger\hat{c}_b \\ &+ (\hat{c}_a^\dagger\hat{c}_a - \text{only and non Kerr shift terms})\end{aligned} \tag{90}$$

We now perform a semiclassical approximation, linearizing the above Hamiltonian around the fixed point defined by Eqs. (89), under which the effective Kerr-mediated shift $\Delta\nu_b$ of the polariton frequency ν_b is given by:

$$\Delta\nu_b = -\Lambda\left[\mathcal{A}_{2222}|\bar{c}_b|^2 + 2\mathcal{A}_{2121}|\bar{c}_a|^2 + 2\mathcal{A}_{2221}\bar{c}_b^*\bar{c}_a + \mathcal{A}_{2122}\bar{c}_a^*\bar{c}_b\right] \tag{91}$$

Finally, the effective measured Kerr constant Λ_b is obtained by determining the frequency shift per photon occupying the polariton mode, $\bar{n}_b = |\bar{c}_b|^2$:

$$\Lambda_b = -\frac{\Delta\nu_b}{\bar{n}_b} = \Lambda\left[\mathcal{A}_{2222} + 2\mathcal{A}_{2121}\frac{|\bar{c}_a|^2}{|\bar{c}_b|^2} + 2\mathcal{A}_{2221}\frac{\bar{c}_a}{\bar{c}_b} + \mathcal{A}_{2122}\frac{\bar{c}_a^*}{\bar{c}_b^*}\right] \tag{92}$$

Clearly, $\Delta\nu_b$ and the measured Kerr constant Λ_b depend on $\mathcal{A}_{nmrs}$ and consequently on the detuning between the bare linear and nonlinear modes, $\Delta_{ab} = \omega_a - \omega_b$, as well as the strength of their coupling g. As a result, both will vary as the nonlinear mode frequency ω_b is swept, even though the bare nonlinear mode Kerr constant Λ remains unchanged. In addition to this dependence on ω_b, Eq. (92) also accounts for the small but nonzero occupation of polariton mode $\hat{c}_a$ due to this mode being weakly driven, and the corresponding cross-Kerr shifts this mediates.

Experimentally, a single pump-probe measurement with pump frequency ω_P at a fixed nonlinear mode frequency populates the polariton mode $\hat{c}_b$ as the pump power P is increased. We first calibrate the polariton mode occupation with the applied pump power via $\bar{n}_b = |\bar{c}_b|^2 = \frac{\kappa_b}{\Delta_P^2 + (\kappa_b/2)^2}\frac{P}{\hbar\omega_P}$, where κ_b is the linewidth of polariton mode $\hat{c}_b$, and $\Delta_P = 5\kappa_b$ is the detuning between the pump frequency and the bare polariton mode frequency [92]. The observed frequency shift $\Delta\nu_b$ as a function of $\bar{n}_b$ is shown in Fig. 57 (a) for various detunings between the bare linear and nonlinear modes Δ_{ab}. By fitting the observed frequency shift to $\bar{n}_b$, we obtain the measured polariton mode Kerr constant Λ_b. Each such measurement yields Λ_b at the given Δ_{ab}. By sweeping the nonlinear mode frequency, we obtain Λ_b as a function of Δ_{ab}, with the results plotted in red in Fig. 57 (b). Note that as the detuning Δ_{ab} decreases, the measured Kerr nonlinearity strength also decreases, since increased hybridization dilutes the nonlinearity of the originally nonlinear mode. By fitting the experimental results to Eq. (92) with the bare nonlinearity Λ as the only fitting parameter, we obtain the solid blue curve in Fig. 57 (b), with the fit value $\Lambda/2\pi = 5.96$ kHz. The shaded blue region

indicates the 2σ confidence interval of the fit, which finally yields the bare nonlinearity of $\Lambda/2\pi = 5.96 \pm 0.2$ kHz for Device A.

5.4.3 Typical Kerr nonlinearity strength of optical microresonators

In this subsection we calculate the typical Kerr nonlinearity strength, or equivalently the Kerr-mediated frequency shift per photon, for nonlinear optical microresonators. For an optical microresonator with center frequency ω_{op}, refractive index n, second-order nonlinear refractive index n_2, and mode volume V_0, the Kerr shift per photon, Λ_{op} is given by [71]:

$$\Lambda_{\text{op}} = \frac{\hbar\omega_0^2 c n_2}{n^2 V_0} \tag{93}$$

where c is the speed of light in vacuum. Using parameter values for silicon nitride optical microresonators [72] - a popular and successful material choice - we have: $\omega_{\text{op}}/(2\pi) = 100$ THz (equivalently, wavelength $\lambda \simeq 1.55$ μm), $n = 2$, $n_2 = 2.5 \times 10^{-19}$ m^2 W^{-1}, and $V_0 = (\lambda/n)^3$, we obtain:

$$\Lambda_{\text{o}}/(2\pi) \simeq 100 \text{ Hz} \tag{94}$$

which is about two orders of magnitude lower than the realized Λ for Device A. Optical microresonators are engineered to have high quality factors; we consider a large value of $Q \simeq 10^7$. For $\omega_{\text{op}}/(2\pi) = 100$ THz, this implies microresonator loss rates of $\kappa_{\text{op}}/(2\pi) \simeq 10$ MHz. As a result, the ratio of Λ_{op} to the loss rate is $\Lambda_{\text{op}}/\kappa_{\text{op}} \simeq 10^{-5}$, again about two orders of magnitude smaller than the smallest value realized by devices in our experiment.

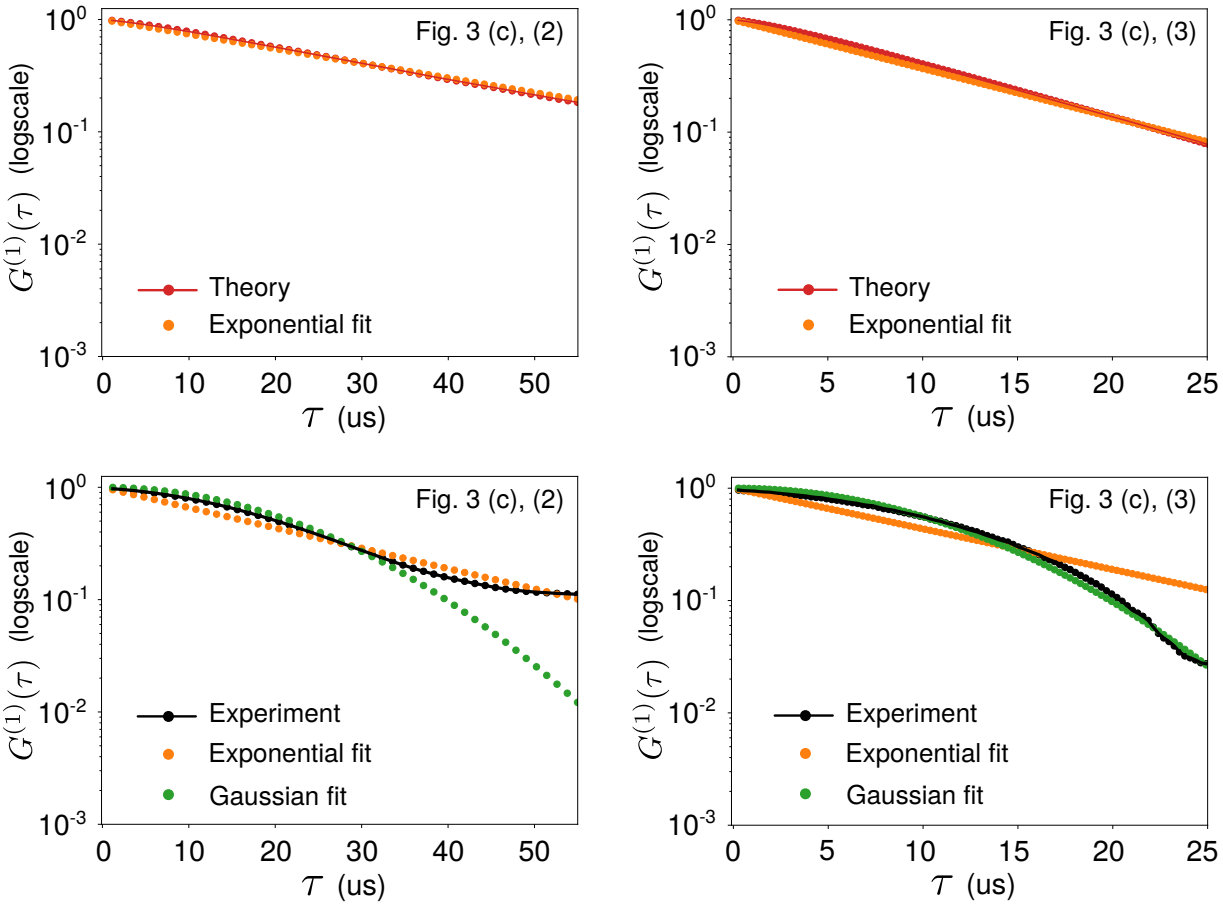

Figure 58: **Non-exponential signatures of phase decoherence.** Top panels: Theoretically calculated decay of $G^{(1)}(\tau)$ peaks as a function of time in logscale (red), and exponential fit (orange). Left and right plots correspond to $G^{(1)}(\tau)$ plotted in Fig. 3(c), positions (2) and (3) respectively of the main text. Lower panels: Same as the top panel, but now showing experimentally obtained decay of $G^{(1)}(\tau)$ peaks as a function of time (black). In addition to the exponential fit (orange), a Gaussian fit is also shown (green), corresponding to contributions from $1/f$ noise.

5.4.4 Non-exponential signatures in phase decoherence

Generally, the multiplicative nature of the noise described by Eqs. (80) allows for non-exponential decay of the phase coherence captured by $G^{(1)}(\tau)$. Signatures of this can be

better seen by extracting the theoretically calculated coherence function peaks and plotting in logscale, as shown in Fig. 58, top panel. However, we find numerically that these nonexponential signatures are minor in the explored parameter regime, as can be seen by the very small deviation from a straight line in logscale. As a result the theoretical decay envelope can be considered to be exponential to a very good approximation.

For the experimentally-obtained coherence function, we have also observed that the decay envelope of the correlation function is not always perfectly exponential. We believe that the observed experimental decay is further complicated by signatures of $1/f$ noise in the system, which would lead to a Gaussian decay envelope. From typical plots of the coherence function peaks as a function of time in logscale, we find that the actual experimental decay envelope is quite close to exponential, but with some signatures of Gaussian decay. Fig. 3(c) at position 3 is a somewhat atypical example, with more pronounced nonexponential features; we usually find decay characteristics more similar to Fig. 3(c), position 2.

Various techniques have been developed to characterize environmental noise in nature and artificial spin systems [Nature Physics 7, 565(2011), Nature Communications 4, 2337 (2013), Nature Physics, 15, 1123 (2019)]. However, the efficacy of these methods requires sensitivity to the specific frequency distribution of the noise, e.g.: large anharmonicity, thus limiting our ability to remove this noise contribution from the experimental results, or include its effect on the theoretical calculations. Noting further that we generally find the experimental decay to be close to exponential just like the theoretical results in this parameter regime, we have used an exponentially decaying envelope to fit to both theory and experiment results and extract the coherence time. Furthermore, adding a probing system to characterize the environmental noise can also be a future research about quantum coherence in the unstable regime.

5.4.5 Cavity ringdown method and theoretical simulations

Even when a two-level description of the nonlinear mode is not feasible, Eqs. (95) indicate that under weak driving it should still be possible to observe the effect of pure dephasing on the nonlinear mode moments. To do so, one would ideally like to probe the nonlinear

mode dynamics directly, without having to observe the linear mode. This requires effectively decoupling the nonlinear mode from the linear mode (by being detuned far away) while still retaining a coupling to the outside world. However, the 3-D transmon design isolates the nonlinear mode from a direct coupling to the environment, successfully allowing for a much higher-Q nonlinear mode than lumped-element or coplanar waveguide architectures. While this design usefully reduces both the relaxation rate γ and pure dephasing rate γ_φ [101], it also means that we only have direct access to linear mode quadratures, $\hat{I}_a$, $\hat{Q}_a$.

$$\frac{d}{dt}\vec{v} = \mathbf{M}\vec{v} + \vec{d} \tag{95}$$

As such, one is restricted to determining the dephasing rate by monitoring moments of cavity quadratures. The approach one would employ is a ringdown setup [91]: a coherent drive is placed on the system to initialize it to a nontrivial state in phase space, following which the drive is turned off and the resulting ringdown dynamics of the measured first and second order cavity moments recorded as the two-mode system returns to the undriven steady-state. Comparing the rates of relaxation for first and second order moments then enables a calculation of the pure dephasing rate γ_φ.

To explore the feasibility of such an approach, we perform numerical simulations of Eqs. (95) under this ringdown setup. We assume a much larger pure dephasing rate $\gamma_\varphi/2\pi =$ 50.0 kHz than estimated for either of our devices, for reasons that will become clear shortly. The typical initialization and ringdown evolution is shown in Fig. 59 (a). The drive η is turned on at $t = -0.8$ μs, and then turned off at $t = 0$, following which the cavity undergoes relaxation to return to the undriven steady-state. The ringdown dynamics are shown in Fig. 59 (b) for two different detunings between the linear and nonlinear modes, Δ_{ab}. We fit exponentials with decay constants λ_1, λ_2 to the moments $\langle \hat{I}_a(t) \rangle$, $\langle \hat{A}_a^2(t) \rangle$ (see Eq. (96) respectively, and define the *dephasing rate experienced by the linear mode* as $\gamma_\varphi^a = \lambda_1 - \lambda_2/2$. When the detuning is large compared to the coupling (i), the linear and nonlinear modes are effectively decoupled, so that the linear mode should experience no pure dephasing and γ_φ^a is vanishingly small. With decreasing detuning (ii), the linear and nonlinear modes hybridizes, and the linear mode inherits some dephasing, so that γ_φ^a increases.

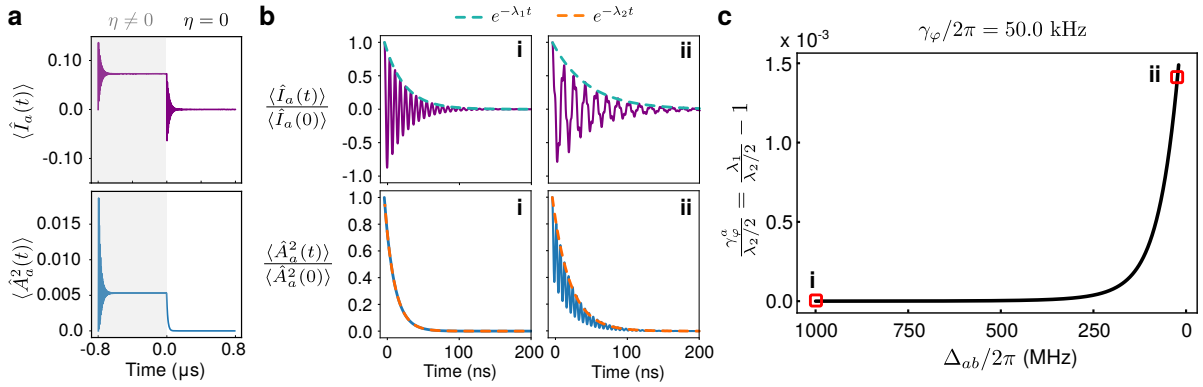

Figure 59: **Theoretical analysis of dephasing in the linear regime via cavity ringdown.** (a) Typical dynamics of cavity quadrature moments under the initialization drive (gray region) and when the drive is turned off (blank region), displaying ringdown. (b) (i) and (ii) show ringdown dynamics for $\langle \hat{I}_a(t) \rangle$ (top panel) and $\langle \hat{A}_a(t) \rangle$ (bottom panel) at the indicated values of detuning Δ_{ab} between the linear and nonlinear mode in (c). Also shown are fits to exponential decays; the top (bottom) panel shows fits with rates determined by the eigenvalue λ_1 (λ_2) for $\langle \hat{I}_a(t) \rangle$ ($\langle \hat{A}_a(t) \rangle$), computed from the dynamical matrix $\mathbf{M}_1$ ($\mathbf{M}_2$) in the ringdown regime ($\eta = 0$). (c) Extracted decay rates from ringdown dynamics as a function of Δ_{ab}. For (b), (c), we choose the actual nonlinear mode dephasing rate $\gamma_\varphi/2\pi = 50.0$ kHz, which is larger than the estimated dephasing rates in the comb generation regimes for both experimental devices.

$$\hat{A}_j^2 \equiv \hat{I}_j^2 + \hat{Q}_j^2 = \langle \hat{d}_j^\dagger \hat{d}_j \rangle \tag{96}$$

The dephasing experienced by the linear mode γ_φ^a as a function of Δ_{ab} is plotted in Fig. 59 (c), scaled by $\lambda_2/2$. While in principle such an approach may be used to extract the pure dephasing rate γ_φ, Fig. 59 (c) brings to light a number of technical difficulties. Firstly, the variation due to pure dephasing is superimposed on the very fast cavity decay rate; the *relative* difference in decay rates $\sim \gamma_\varphi/\kappa$ is therefore very small and difficult to extract experimentally, even though we have assumed a dephasing rate here much larger than those

obtained in the main text. In contrast, spectroscopy of the two-level system compares γ_φ directly to γ. Secondly, since this is a direct temporal measurement, its accuracy is limited by the DAC resolution. Small changes in the very short cavity relaxation time are therefore more uncertain.

Both these issues mean that obtaining the pure dephasing rate from direct cavity ringdown measurements under moderate to strong hybridization is likely to be inaccurate. As a result, we instead employ the strategy of obtaining γ_φ in the *nonlinear* regime, in particular within the frequency comb regime. Here, the effect of the bare mode decay rates γ and κ is overcome since the system starts to undergo self-oscillation, as discussed in the main text. Then, the comb coherence is limited entirely by the nonlinearity strength and the pure dephasing rate. By measuring the nonlinearity strength via a pump-probe measurement of the hybridized system, as discussed in Section 5.4.2, we are able to use SDE simulations of comb coherence to obtain an estimate of γ_φ.

5.5 Conclusion

We have realized a minimal two-mode Kerr system for generating coherent frequency combs under excitation by a single coherent tone. The phase coherence of the generated combs is fundamentally limited by the intrinsic nonlinearity strength in the quantum modes which form the device. The excellent agreement between theory and experiment points toward a highly controllable experimental platform for the study of complex nonlinear dynamics in the quantum regime. Our device realizes a classically-unstable Kerr-nonlinear regime, ideally suited to understand the potentially competing role of strong quantum fluctuations as a source of decoherence and non-classicality in moderate to strongly nonlinear quantum devices.

Finally, the versatility of the cQED platform admits extensions of our device to multimode systems, and to realizations employing tunable parametric couplers [42], paving the way towards an *in-situ* engineerable multifrequency light source. Such frequency combs could enable multiplexed quantum measurement [102] using a single monochromatic incident tone.

The generated combs could also function as multifrequency pumps to phase-coherently drive multiple parametric processes simultaneously in a single device for Hamiltonian engineering applications [21, 103, 104, 105]. This could include the intriguing possibility of multifrequency pumps exhibiting non-classical coherence, using comb generators operating in the deep-quantum regime.

6.0 Modular quantum computer

6.1 Introduction to modular quantum computer

Building quantum information processors of increasing size and complexity requires meticulous management of both qubit-environment and qubit-qubit interactions. Suppressing interaction with the external environment has always been recognized as the central difficultly in maintaining coherence in a system. In the long term this challenge will be met by fault tolerantly encoding much smaller logical machines inside a qubit fabric; in the present so-called Noisy Intermediate-Scale Quantum (NISQ) era we must simply run short circuits. However, in both the short and long term we face choices about which architecture of machine we build. In many current large-scale processors based on a monolithic fabric of nearest-neighbor interactions we pay a price in spectator qubit errors and cross-talk [1, 2, 3] as well as the fabrication cost of needing all components to perform flawlessly on a single die [106].

Modular quantum systems offer a very promising alternate route to large scale quantum computers, allowing us to sidestep many of these difficulties, and instead operate using smaller, simpler quantum modules linked via quantum communication channels[5, 6, 7, 8]. Such machines allow us to replace faulty components and test sub-units separately, which can greatly ease requirements for flawless fabrication, while also allowing distant qubits to communicate with many fewer intermediate steps, potentially enhancing fidelity in near-term quantum[107].

The key element that determines the performance of a modular machine is its quantum communication bus. For atomic scale qubits (which form the basis for many of the early proposals for modular quantum computing) communicating using optical-frequency states, it is infeasible to couple photons into a communication channel with very high efficiency. This loss of information precludes light from simply being transferred from module to module, instead one must herald instances in which transmission is successful [108, 109, 110, 111, 112]. However, once light has been coupled into an optical fiber, it can be readily distributed over

kilometer and longer distances, which readily supports long-range entangled state generation and distributed quantum computation[113, 114]. In superconducting circuits, there have also been several recent demonstrations of similar measurement-based protocols[115, 35, 116, 117].

However, superconducting circuits can also transfer states directly. For this form of direct state exchange we require strong, switchable couplings from module to the communication channel to enable rapid operations, low losses in the channel, and a dense, reconfigurable network of couplings among many modules[118, 119]. Realizations to date have focused on pairs of quantum modules, with transmission-line based 'quantum bus' communication channels and controllable module-bus couplings based on the nonlinearity of Josephson junctions [120, 121, 122, 123, 124, 125, 126, 127] or driven exchange via a driven, nonlinear coupling mode [128, 129, 130].

In this chapter, we propose and experimentally implement a new scheme for creating a modular superconducting network, which instead creates a nonlinear 'quantum state router' with fixed, dispersive couplings to individual quantum modules. The strong, parametrically driven nonlinearity of the quantum state router allows us to only virtually occupy its modes, and thus achieve efficient operations over the router with only modest requirements for router quality. There is no use of measurement in the router system, operations over the bus can be thought of as direct, parametrically actuated gates between quantum modules. The state router naturally supports all-to-all coupling among several quantum modules, and is naturally extensible to a larger modular network. We have realized the quantum state router using a Superconducting Nonlinear Assymetric Inductive eLement (SNAIL)-based nonlinearity[42], and used it to operate a four module quantum processor.

6.2 Theory of router operation

The basic structure of our modular quantum computer consists of two major parts: a quantum state router and multiple modules, as shown in Figure 60. Each module consists of a variable number of qubits (one in our present experiment) which have controllable local coupling with each other. In each module, there should also be at least one 'communication'

mode which couples to both the qubits in the module and the quantum state router. This communication mode can either be a qubit, or, as in our work, a long-lived harmonic oscillator which can store information for exchange over the router.

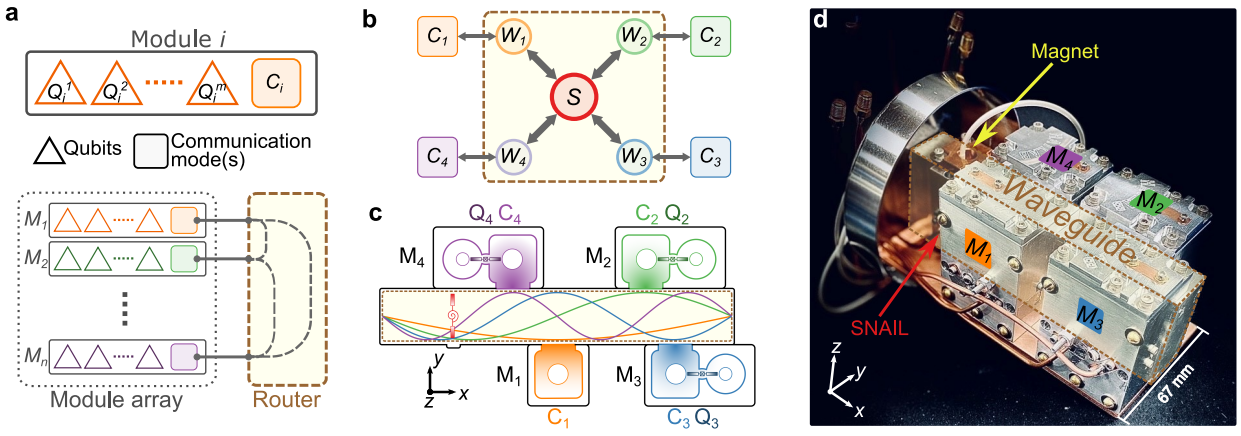

Figure 60: **Schematic representation and picture of the modular quantum computer device.** (a) Basic structure of our modular quantum computer, in which a number of quantum modules are connected via their communication modes to a quantum state router. (b) Coupling scheme between the router and four communication modes. The brown dashed square represent the router with four waveguide modes ($\mathrm{W}_1 - \mathrm{W}_4$) and a SNAIL (S). Each waveguide mode is dispersively coupled to a single communication cavity mode ($\mathrm{C}_1 - \mathrm{C}_4$). (c) Schematic drawing of the full system consisting four modules and the central quantum state router. The colored curves inside the router represent the E electric field distribution of the first four waveguide $\mathrm{TE}_{10n} (n = 1, 2, 3, 4)$ eigenmodes. The SNAIL chip (represented in red) is placed at a location where it couples to all the waveguide modes being used. Each module (for M_2 to M_4) consists of a qubit ($\mathrm{Q}_2 - \mathrm{Q}_4$), a communication cavity ($\mathrm{C}_2 - \mathrm{C}_4$) and a readout cavity (for module M_1 the qubit has been omitted). (d) Photograph of the assembled device.

We have realized our modular quantum computer as a 3D superconducting circuit, and have adopted several design rules to guide our efforts. First, the communication modes we use are superconducting 3D cavities, rather than qubits, as they accommodate multiple qubit encoding schemes, including both the Fock encoding we use in this work as well as

cat states[131], binomial encodings[132], GKP-encodings[133], etc. This allows our router to be compatible with a wide array of future module designs. Secondly, we emphasize the "modularity" of our system in the additional sense that each module and the router itself exist as independent units which can operate individually, instead of the whole system forming a monolithic block. This offers a tremendous advantage in the laboratory, as defective components can be easily replaced, and the different components can be tested separately and then assembled. Thirdly, the router operates via coherent photon exchange based on parametric driving of a 3-wave-mixing Hamiltonian, in which the third order non-linearity is introduced by a SNAIL device. Finally, we have designed the router to minimize both the need for precise frequency matching between router and module modes, and also minimize the requirements for high Q router elements. To accomplish this, we couple all modes in the computer dispersively.

The only nonlinear element is a central SNAIL-mode S (with corresponding annihilation operator $\hat{s}$), which is very strongly coupled to an input line for strong parametric driving, and flux biased via a nearby copper-sheathed electromagnet. As such, it has a low quality factor Q ($\sim 10,000$). The remainder of the router is composed of a rectangular, superconducting 3D waveguide. The first four transverse electric modes ($\mathrm{TE}_{10i}, i = 1, 2, 3, 4$) of the waveguide W_i (with operators $\hat{\mathrm{w}}_i$) are each used as an intermediate mode coupling to both the SNAIL and a corresponding communication mode C_i (with operator $\hat{c}_i$ in the i^{th} module). The SNAIL is flux biased to a point where its even order non-linear terms are negligible[42, 105] while the third order term is strong, resulting in the Hamiltonian of the router, which has been divided into mode energies, interactions, and nonlinear terms, respectively:

$$\begin{aligned}\hat{\mathcal{H}}_R/\hbar &= \hat{\mathcal{H}}_{R,0}/\hbar + \hat{\mathcal{H}}_{R,\mathrm{int}}/\hbar + \hat{\mathcal{H}}_{R,\mathrm{nl}}/\hbar \\ &= \left[\omega_s \hat{s}^\dagger \hat{s} + \sum_i \omega_{\mathrm{w}_i} \hat{\mathrm{w}}_i{}^\dagger \hat{\mathrm{w}}_i\right] + \left[\sum_i g_{\mathrm{w}_i s}(\hat{\mathrm{w}}_i^\dagger \hat{s} + \hat{\mathrm{w}}_i \hat{s}^\dagger)\right] \\ &+ \left[g_{sss}(\hat{s} + \hat{s}^\dagger)^3\right].\end{aligned} \tag{97}$$

In this Hamiltonian, the waveguide modes are naturally orthogonal, and each is coupled to the SNAIL with strength $g_{\mathrm{w}_i s}$; g_{sss} is the strength of the SNAIL's third-order term. We

parametrically drive photon exchange between a pair of waveguide modes by driving the SNAIL at the difference of their frequencies. This scheme has been long used in parametric amplifiers and circulators, where it goes by the name 'noiseless photon conversion' [134, 21, 103]). To have independently controllable couplings, we have chosen the SNAIL frequency and waveguide dimensions so that all mode frequencies and frequency differences are unique, with all difference frequencies below the lowest mode frequency (see Fig. 61)

As all frequencies are widely separated, we can rediagonalize the system to eliminate the interaction term, slightly shifting all mode frequencies and definitions(for simplicity's sake we omit any change of variable representation for the new, hybrid eigenmodes), and inducing all possible self- and cross-three-wave couplings among the waveguide modes and SNAIL. This is analogous to common techniques used in circuit QED[46, 47], with a third- rather than fourth-order nonlinearity. Retaining only the parametric coupling terms we will use in the router, which is safe as long as all other processes are well separated from any desired process in frequency, we write the effective Hamiltonian of the router as

$$\hat{\mathcal{H}}_R^{\text{eff}}/\hbar = \hat{\mathcal{H}}_{R,0}/\hbar + \sum_{i \neq j} g^{\text{eff}}_{\text{w}_i\text{w}_j s}(\hat{\text{w}}_i^\dagger \hat{\text{w}}_j \hat{s} + \hat{\text{w}}_i \hat{\text{w}}_j^\dagger \hat{s}^\dagger). \tag{98}$$

The effective three-wave interaction strengths are given by, $g^{\text{eff}}_{\text{w}_i\text{w}_j s} \approx 6 g_{sss} (\frac{g}{\Delta})_{\text{w}_i s} (\frac{g}{\Delta})_{\text{w}_j s}$, where $\Delta_{\text{w}_i s} = \omega_{\text{w}_i} - \omega_s$. Note, however, that in our experiment we never directly populate these waveguide modes or drive their difference frequencies. Instead, these terms serve as a 'scaffold' in the router to create similar terms among the module communication modes, as detailed below. The hybridization strengths $(\frac{g}{\Delta})_{\text{w}_i s}$ are key parameters as they both limit the eventual parametric coupling strengths and determine how much longer-lived the waveguide modes can be compared to the low-Q SNAIL mode.

Next, we combine our router with the modules' communication modes. As shown in Fig. 60 b), we accomplish this by creating four modules, each containing one mode with a frequency near one of the router's waveguide modes, and coupled to the router via an aperture in their shared wall. This coupling is again deliberately dispersive, with the strength controlled by a combination of waveguide-communication mode detuning, coupling aperture size, and placement along the router's length. The router plus communication mode

Hamiltonian is written as:

$$\begin{aligned}\hat{\mathcal{H}}_{RC}/\hbar &= \hat{\mathcal{H}}_R/\hbar + \hat{\mathcal{H}}_{C,0}/\hbar + \hat{\mathcal{H}}_{RC,\mathrm{int}}/\hbar \\ &= \hat{\mathcal{H}}_R/\hbar + \left[\sum_i \omega_{c_i} \hat{c_i}^\dagger \hat{c_i}\right] + \left[\sum_i g_{c_i \mathrm{w}_i} (\hat{c_i}^\dagger \hat{\mathrm{w}}_i + \hat{c_i} \hat{\mathrm{w}}_i^\dagger)\right].\end{aligned} \tag{99}$$

The second and third terms denote the communication mode's energy and the communication mode-waveguide mode interactions, respectively. As before, we diagonalize this Hamiltonian to eliminate the direct interactions among the modes without changing variable representation, and neglect all but the cavity-cavity third order interactions to find the new effective Hamiltonian for the composite router plus communication modes system:

$$\hat{\mathcal{H}}^{\mathrm{eff}}_{RC}/\hbar = \hat{\mathcal{H}}_{R,0}/\hbar + \hat{\mathcal{H}}_{C,0}/\hbar + \sum_{i \neq j} g^{\mathrm{eff}}_{c_i c_j s} (\hat{c_i}^\dagger \hat{c_j} \hat{s} + \hat{c_i} \hat{c_j}^\dagger \hat{s}^\dagger). \tag{100}$$

The new effective three body interaction strength is $g^{\mathrm{eff}}_{c_i c_j s} \approx g^{\mathrm{eff}}_{\mathrm{w}_i \mathrm{w}_j s} (\frac{g}{\Delta})_{c_i \mathrm{w}_i} (\frac{g}{\Delta})_{c_j \mathrm{w}_j}$.

The use of a network of hybridization, linking the cavity modes to the central SNAIL via intermediate cavity modes comes with advantages: choosing each dispersive coupling $g/\Delta \simeq 0.1$ the communication modes can live up to 10^4 times longer than the SNAIL mode and 100 times longer than the waveguide modes, greatly decreasing the need for long lifetime components in the router. More, the dispersive couplings and parametric driving are insensitive to modest errors in mode frequencies, again reducing the need for precision fabrication, unlike photon exchange techniques based on resonant mode couplings[135, 123]. It is certainly possible to remove the intermediate waveguide modes in a monolithic version of our design, though this comes with both greatly reduced flexibility in combining disparate elements and more stringent requirements for the SNAIL's lifetime.

In operation, the parametrically driven two-body exchange rate, for example between modes C_i and C_j, is $\sqrt{n_s} g^{\mathrm{eff}}_{c_i c_j s}$, where n_s is the pump strength expressed as a photon number (see Sec. 6.5.2.1). It is here that we find the price for our hybridization network: the effective three body coupling has been greatly reduced ($g^{\mathrm{eff}}_{c_i c_j s} \simeq 6 \times 10^{-4} g_{sss}$). To achieve rapid gates with feasible pump strengths, we must both engineer g_{sss} to be large and carefully design the pump line (and the SNAIL itself) to tolerate very strong drives to compensate this dilution of nonlinearity.

It is also important to note that Eq. 100 represents only our desired coupling terms, in practice all modes inherit both self- and cross- three-wave mixing terms from the SNAIL. Of particular concern are couplings between a cavity and non-adjacent waveguide modes (e.g. C_3 to W_4), in practice we choose a minimum waveguide to cavity spacing of $\sim 100\,\mathrm{MHz}$ to suppress cross-talk with these couplings. This difference frequency is comparable to the anharmonicity of transmon qubits; similarly, we can use variants of the DRAG[61] technique to drive rapid iSWAP gates among the communication modes without leakage to unwanted modes (see Sec.6.5.3).

6.3 Experimental results

In table 12 we list the measured parameters of all key modes in our device. All numbers have been directly measured and calibrated in the experiments at the operation bias of the SNAIL, they are also used in our master equation simulations (see Methods, Numerical simulations in main text). The measurement fidelity is calculated using single qubit tomography. The single qubit gate fidelity is measured using interleaved randomized benchmarking[136].

Table 12: **Devices parameters.**

	Q_2	Q_3	Q_4	C_1	C_2	C_3	C_4	SNAIL††
$\omega/2\pi$ (GHz)	3.067984	4.040709	3.566572	4.477662	4.812500	5.474195	6.180769	3.914900
T_1 (μs)	60.442	9.065	8.385	22.771†	27.230	13.795	20.065	0.975
T_{2R} (μs)	18.386	6.295	7.997	44.643†	47.320	11.303	22.691	1.05124
T_{2E} (μs)	23.745	7.568	8.018					
$\alpha/2\pi$ (MHz)	-141.3	-118.1	-125.8					
$\chi_{qc}/2\pi$ (MHz)	-0.112	-1.719	-0.862					
Measurement fidelity *	93.61%	83.00%	88.00 %					
Single gate error **	0.48% ± 0.04%	3.74% ± 0.5%	3.21% ± 0.6%					

* Calculated from single qubit's tomography measurement
** Calculated from randomized benchmarking of single qubit gates [136]
† Measured using coherent state
†† Measured at operation point

One natural advantage of our router design is that the parametric pumps are all well-

separated in frequency from all modes. This allows us to protect all quantum modes while still strongly pumping the parametric processes. As we can see from Fig 61, the communication modes and SNAIL mode itself are all at least 2 GHz higher than the parametric pumping frequencies.

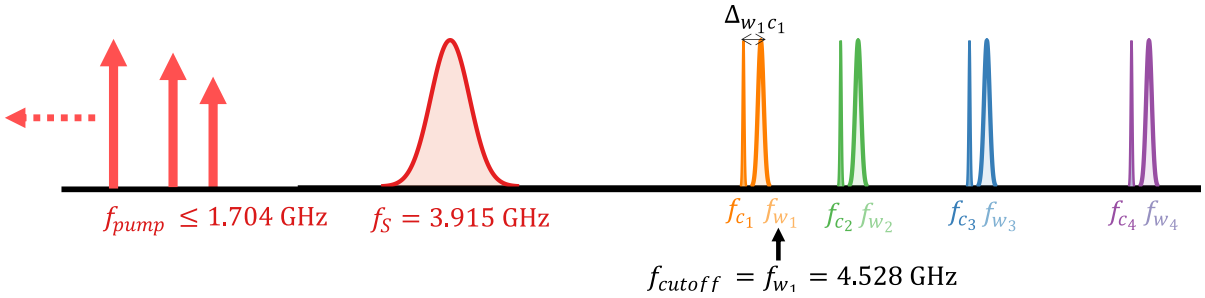

Figure 61: **Frequency spectrum of all linear modes, SNAIL mode and pumping frequency.** Since the maximum pumping frequency on the SNAIL $f_{pump}^{max} \approx f_{c_4} - f_{c_1} =$ 1.704 GHz, which is way below the waveguide cutoff frequency $f_{cutoff} = f_{w1} = 4.528$ GHz. The router naturally protects pumping tones from propagating into modules. Meanwhile, the frequency of communication modes don't have to be precisely controlled, so the router can be easily adaptive to different modules. Also, since the maximum pumping frequency is also lower than the SNAIL frequency $f_{pump}^{max} < f_s = 3.915$ GHz, a low-pass-filter (e.g. VLF-2250+) is added to the SNAIL pump port, so that strong pump can be applied to SNAIL while the SNAIL mode lifetime is still protected.

6.3.1 Basic router characterization with coherent states

For initial experiments, we connected our router to four simple modules, but omitted the module qubits. Each communication mode is driven and read out via a 'weak' port whose induced relaxation rate is much smaller than the mode's internal loss rate. Figure 62a shows an experimental pulse sequence for swapping coherent states between the module communication modes C_2 and C_4. First, a short on-resonance drive is applied to C_4 through the weakly coupled port, which creates a coherent state in this cavity. Then, a pump tone is applied to the SNAIL mode near the $C_2 - C_4$ difference frequency: $\omega_p = \omega_{c_4} - \omega_{c_2} + \delta$, where

δ is the pump detuning relative to the measured frequency difference between two cavity modes. Meanwhile, the light in these two cavities are monitored by receiving the I-Q voltage leaking out from each cavity's weakly coupled port. By varying the applied pump frequency and time, we can determine both the swap rate and resonant condition for pumping.

The experiment results are shown in Fig. 62b, c. There is good agreement between the envelope of the swap trace (green and purple lines) and the hybridized decay trace, indicating that the state is only swapping between these two cavities without leaking into other modes, and that the fidelity of state exchange is mainly limited by the lifetime of these two cavities. The same experiment was performed for all the six possible pairs of the four communication modes, the fastest full-swap time was 375 ns, and the slowest was 1248 ns, with an average swap time of ~ 760 ns (see Sec. 6.5.2.2). On average, the pump frequency required to fully swap light between the two cavities was detuned by several hundred kHz (-416 kHz for the data in Figure 62). We attribute this to a combination of SNAIL- and communication-mode static and dynamic Kerr effects. This has strong parallels to saturation effects in parametric amplifiers [137, 105, 80, 138], though here the primary consequence is just that we must track these shifts in our control electronics.

6.3.2 Operation as a modular quantum computer with single-qubit modules

Next, we added the transmon qubits to complete modules 2-4 (Module one's qubit was omitted), and operated the full device as a small, modular, quantum computer. Each single-qubit-module consists of one communication cavity C_i, one transmon Q_i and one readout cavity R_i. The machine's layout is shown schematically in Fig. 60 c). For simplicity, our qubit states throughout the system are the Fock states $|0\rangle$ and $|1\rangle$, although the communication modes could in principle support a variety of more complex encodings. We create intra-module gates between the qubit and cavity in each module using qubit-cavity cross-Kerr to implement doubly-driven parametric photon exchange (see Ref. [35, 120, 125] and Sec. 6.5.3 for details), which are indicated as paired drives in Fig. 63 b).

In the simple algorithms that follow we refer to the operation of these exchange interactions as variations on iSWAP gate, as is typical for gates based on coherent photon exchange

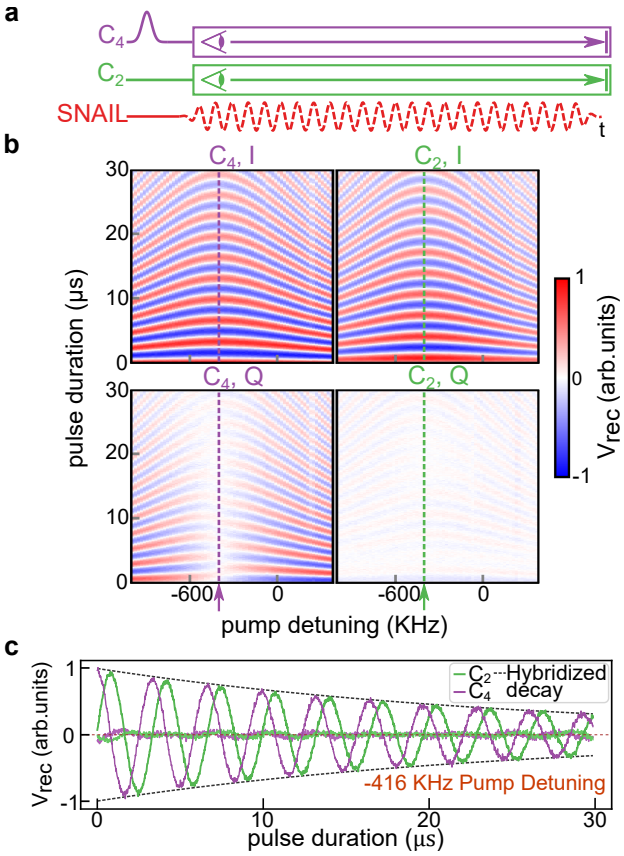

Figure 62: **Coherent state exchange between communication cavities.** (a) Pulse sequence of the swap experiment. We begin by displacing one cavity to create a coherent state, which we then swap between a pair of cavities by applying a parametric drive to the SNAIL. We continuously monitor the I-Q voltage in each cavity during the swap process. (b) In- and quadrature-phase received voltage from the two cavities versus pulse duration and pump detuning from the nominal difference frequency. The dashed vertical line denotes the optimal detuning frequency for full photon exchange. (c) Line-cut of (b) at the optimal full-swap detuning. The grey dashed envelope represents the theoretical hybridized decay trace of C_2 and C_4, given by $\exp[-2t(1/\tau_2 + 1/\tau_4)]$, where τ_2 and τ_4 are the decoherence times of C_2 and C_4, respectively.

[128, 35, 129, 125, 127, 130]. We exclusively use these gates to swap coherent states or Fock states fully from a source cavity to a formerly empty target cavity. In this scenario the gates

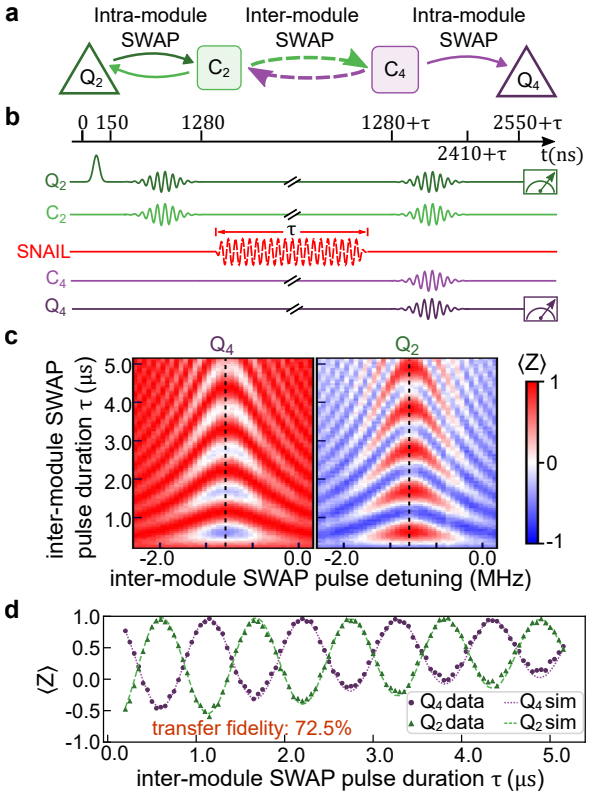

Figure 63: **Fock state swap experiment between remote qubits.** (a) Illustration of the photon swap protocol, in which a photon, originating in Q_2 is fully swapped to C_2, and then, depending on the variable inter-module pulse duration, routed to Q_4 or returned to Q_2. (b) Experiment pulse sequence. A photon is created in Q_2, then swapped to C_2. Next it is swapped (or not) to C_4 with a variable duration inter-module iSWAP pulse, and finally the light in $C_{2,4}$ are routed via further intra-module iSWAP to their respective qubits, which are then measured. The upper black bar indicates the total experimental duration with τ. (c) Measurement result of Q_2 and Q_4 for different SNAIL pump detuning and duration. Here the color of 2D sweep indicates the measurement along qubits' z-axis. (d) A cut of the swap data along the dotted line indicated in (c). The green triangles and purple circles and are Q_2 and Q_4 data, respectively, and the dashed lines are the corresponding simulation results.

act as a combination of SWAP and a z-rotation for both Fock and coherent states. However, this analogy breaks down for both intra- and inter-module exchange of Fock states between a

qubit and cavity and a pair of cavities, when we consider arbitrary pulse lengths and certain joint qubit-cavity or cavity-cavity Fock states (e.g. $|1,1\rangle$). For this reason some researchers choose to refer to such gates between pairs of cavities as 'beam splitters'[125, 139] for their obvious resemblance to the optical component of the same name. This analogy, however, fails for our qubit-cavity interactions, and so we choose instead to refer to these gates via the exponent which determines their unitary relative to a full iSWAP gate, i.e., a $\sqrt{i\text{SWAP}}$ is described by $U_{i\text{SWAP}}^{\frac{1}{2}}$. As we only swap light into empty qubits/cavities in our protocols, and so never occupy states containing two or more photons, this inexact analogy will yield both a simple graphical and conceptual picture of our gates as well as correct intuition about the system's evolution during our protocols. This issue, however, must obviously be revisited for alternate qubit encoding choices, and when both send- and receive- modes are in arbitrary states (for instance, for coherent states between cavities the identification of the gates as iSWAP is again exact). For further discussion see Sec. 6.5.1.

We next use the module transmons and intra-module iSWAP operations to swap Fock states across the router, transferring single photons between distant qubits as shown in Fig. 63 a), b). The protocol begins with all qubits and cavities prepared in their ground states. A $R_x(\pi)$ pulse is first applied to Q_2 and brings it to the excited state. Next, an intra-module iSWAP gate is performed between Q_2 and C_2. This fully swaps the excitation from Q_2 to C_2. Third, the photon is swapped between C_2 and C_4 across the router by pumping on the SNAIL mode, just as demonstrated in Figure 62. The SNAIL pump duration is varied, which will result in an effective Rabi oscillation between the two qubits when the protocol is completed. Finally, we apply two more intra-module iSWAP gates, C_2 to Q_2 and C_4 to Q_4, which fully transfer the states of C_2 and C_4 to their module qubits, which are then measured simultaneously using dispersive readout of the readout (R) modes. The results are shown in Fig. 63 c) and 63 d). The transfer fidelity between Q_4 and Q_2 is 72.5 ± 1.17 %. We perform Lindblad master equation simulations assuming ideal interactions, with the only defects being all modes' measured coherences(see Methods); the simulation results (dotted curves) show good quantitative agreement with our data, indicating that, as with coherent state operation, the primary fidelity limit in our system is the ratio of gate time to our modes' coherence times. The uncertainty given for the Fock state transfer fidelity, and all

following quoted fidelities, is calculated following the 'bootstrap method' in[140, 141]. No correction is applied for State Preparation and Measurement (SPAM) errors. Details of our data processing and experimentally determined SPAM errors can be found in Methods, Sec. 6.4.

6.3.3 Inter-module Bell state generation

Next, we use such a gate, a $\sqrt{i\text{SWAP}}$, created by shortening the first intra-module iSWAP gate from Figure 63 by close to 1/2 in duration to create inter-module Bell states. The $\sqrt{i\text{SWAP}}$ has the effect of taking the single photon in the qubit and coherently 'sharing' it between the qubit and cavity, creating a Bell state between the two modes. Overall, the sequence first creates a Bell-pair inside a module, and then shifts the communication cavity's component to a qubit in a second module. The quantum circuit is shown in Fig. 64 a). Tomography is performed on both qubits, while the communication cavities are not measured. The measurement results are shown in Fig. 64 b). From this tomographic data, we can reconstruct the density matrix of the Q_2 and Q_4. We achieve a Bell fidelity of 76.9 ± 0.76 %. The same experiments were performed on the other two qubit pairs $Q_2 - Q_3$ and $Q_4 - Q_3$) with fidelity of 58.7 ± 2.40 % and 68.2 ± 0.83 %, respectively. The results were again compared with Lindblad master equation simulations (red rectangles in Fig. 64 b), and show that the dominant source of infidelity remains the modes' lifetimes.

6.3.4 Parallel operations

Another advantage of our architecture is that we can drive multiple parametric operations in the router simultaneously, which enables parallel operation and new ways to create entanglement. We have demonstrated the simplest implementation of parallel operations by swapping light between two pairs of modules simultaneously. Here, M_2 and M_4 are treated as one sub-system, while M_3 and M_1 form a second. We swap a photon from Q_2 to Q_4 and Q_3 to C_1 across the router simultaneously. The gate sequence is shown in Fig. 65 a1). The two cross module swap interactions, $C_2 - C_4$ and $C_3 - C_0$, are turned on simultaneously by pumping the SNAIL mode at the two frequency differences using a room-temperature

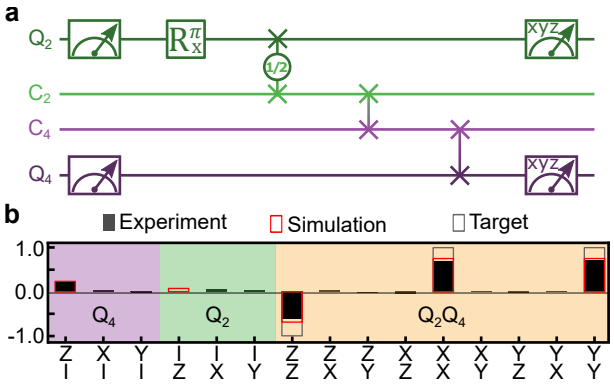

Figure 64: **Inter-module Bell state generation.** (a) Quantum circuit for generating a Bell state between Q_2 and Q_4. Entanglement is first generated between Q_2 and C_2 using a $\sqrt{i\text{SWAP}}$ gate, the cavity component is then moved to Q_4 using two full-iSWAP gates. (b) Tomography of the joint Q_2, Q_4 Bloch vector, in which each bar represent a joint measurement of the two qubits in the basis indicated (I indicates no measurement). Here the black bars indicate the experiment result, the red rectangles are master-equation simulation results, while the gray rectangles are the target pure Bell state. The fidelity to target Bell state $\frac{1}{\sqrt{2}}(|01\rangle + |10\rangle)$ is $76.9 \pm 0.76\%$, which agrees very well with the simulation prediction of 77.2%.

combiner. The SNAIL pumps are applied for a variable period. The protocol concludes with SWAP gates between all cavity-qubit pairs and measurement of all qubits. The results (Fig. 65 a2) show that Fock states can swap between both pairs of modules simultaneously without interference or enhanced relaxation, as shown by comparison to master equation simulations. The drive frequencies for parallel swap processes in the router needs frequency adjustments on order $\sim$100 kHz compared to the single iSWAP case, which we attribute to dynamic and static cross-Kerr effects due to the paired SNAIL drives. We reduced the pump strengths, slowing the gates from 600 ns to 1300 ns as we saw excess decoherence when running two parallel processes at maximum pump strength. We do not believe this is a fundamental limitation, but can be improved in future experiment by optimized SNAIL and router design.

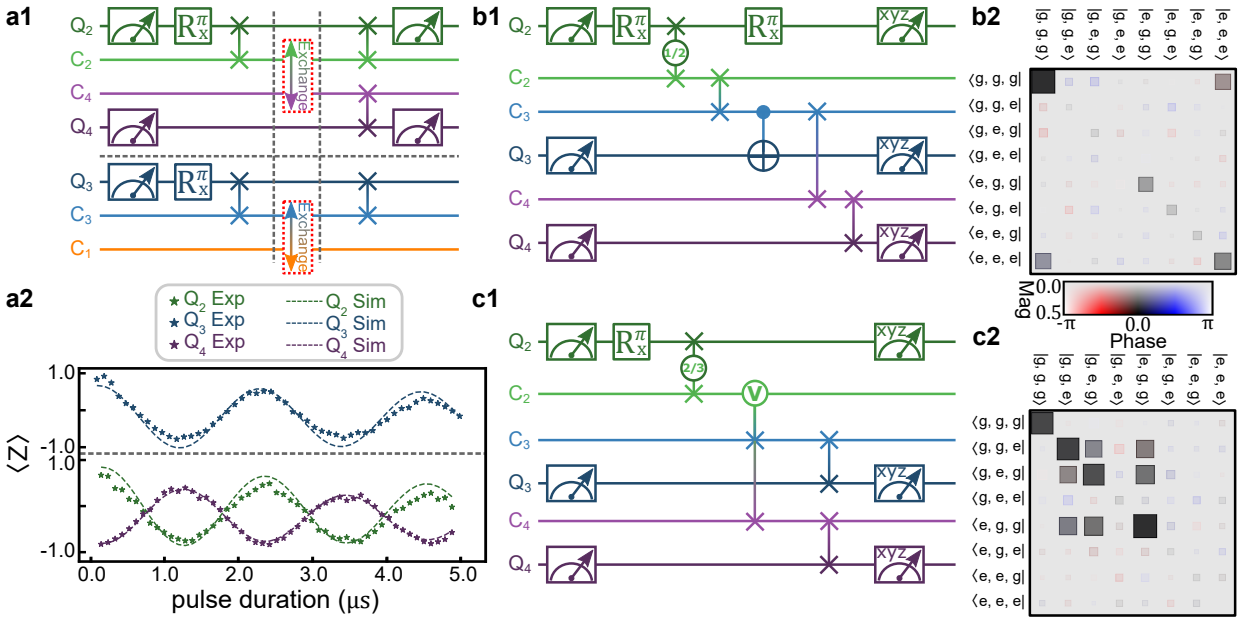

Figure 65: **Parallel *i*SWAP, GHZ and W state generation experiments.** (a1) Gate sequence for parallel photon exchange over the router. (a2) Photon population of all three qubits vs. router swap time. The dots here are the experimental results, and the corresponding dashed lines are simulation results. (b1) GHZ state generation sequence. (b2) GHZ state generation density matrix reconstructed from tomography. Here the size of each block represents the magnitude of each element in density matrix, and the 2-D color scale represents each element's phase as a function of both color and magnitude, with bright colors for large elements fading to neutral gray for small magnitudes to avoid drawing the eye to small, noisy matrix elements. The observed fidelity state is 48.9 ± 5.27 % (c1) W state generation pulse sequence. Together, the $i\text{SWAP}^{2\arctan(\sqrt{2})/\pi}$ and 'V-*i*SWAP' gates create a W state distributed across Q_2, C_3, and C_4. The subsequent *i*SWAPs redirect the latter two components to Q_3 and Q_4, respectively. (c2) Hinton diagram of results of W-state generation sequence; the observed fidelity state is 53.4 ± 2.56 %.

As further proof of the quantum coherence of parallel operations in the router, we also repeated the Bell state generation protocol between Q_2 and Q_4 with the $M_1 - M_3$ *i*SWAP activated in parallel. Again, the pump strengths were decreased, slowing the inter-module

swap time. We achieved a Bell state fidelity of 68.1 ± 0.79 %, while the simulated fidelity is 68.4 %. Here the decrease of fidelity compared to the single Bell state generation process (which has a fidelity of 76.9 ± 0.76 %) is due to the longer gate time used for the $C_2 - C_4$ iSWAP in the presence of a parallel iSWAP operation (see details in Sec. 6.5.4). Currently, the utility of this multi-parametric gate is limited by this slowdown compared to individual iSWAPs. However, we believe this kind of multi-parametrically-pumped process should be further investigated, as it could also be used to generate other multi-qubit gates in one step. Given the overhead in composing multi-qubit gate with a series of two-qubit and single-qubit gates (for example decomposing a Toffoli gate into 6 C-NOTs), performing multi-qubit gates in this way might still give better performance in terms of gate fidelity by shortening overall sequence time/gate count even if operating at a lower rate.

Full-router sequences To this point, we have listed only state fidelities, which are limited both by the mode lifetimes in our system, as well as the number of gates required to perform both intra- and inter-module operations in the same pulse sequence. We can estimate the performance of the router itself by estimating the 'average' fidelity of the inter-module gates. Given the average gate time of $T_{gate,avg} \simeq 760\,\text{ns}$, and the average decoherence time of our communication modes of $T_{C,avg} \simeq 22\,\mu\text{s}$ we find $F_{avg} = 1 - \frac{T_{gate,avg}}{T_{C,avg}} = 0.97$. Even given this performance, extending to still longer sequences which can entangle all qubits in the system is very challenging due to the further decay caused by increased gate count and the delicacy of larger entangled states. Nevertheless, we implemented two further router-wide sequences to demonstrate further capabilities of our system.

First, we explored the use of two simultaneous swap processes which link one 'source' cavity to two 'target' cavities, which we refer to as a 'V-iSWAP'. As shown in Sec. 6.5.2.3, this form of swap for a certain duration empties the source cavity, coherently and symmetrically swapping its contents into the target cavities. By combining the V-iSWAP with a $(i\text{SWAP})^{2\arctan(\sqrt{2})/\pi}$ (which leaves 1/3 photon in the source mode) as shown in Fig. 65c1, we can take a single photon from Q_2 and use our inter-module V-iSWAP to create a W-state shared among all three modules. We achieve a fidelity for this state of 53.4 ± 2.56 % (see state reconstruction in Fig. 65 c2).

We also sought to create a GHZ state shared among all three modules' qubits. As we

implement it in Fig. 65 b1), this protocol require one additional entangling gate: an intra-module CNOT. We achieve this using a state selective qubit π-pulse [142]. We reconstruct the final state from tomography as shown in Fig. 65 b2), and find a fidelity of 48.9 ± 5.27 %, just below the threshold for provable entanglement. While both results fall below the threshold for provable entanglement, they point to our ability to implement an extensive gate set in the router.

6.4 Methods

Device fabrication The device in Fig. 60 d) contains a SNAIL on a sapphire chip, three transmon qubits on individual sapphire chips, and multiple 3D resonator modes coupled with each other as shown in Fig. 60 c). The coupling between the SNAIL and waveguide modes is determined by the shape of the SNAIL antenna (Extended Data Fig. 66 b), which is fabricated using photolithography and acid etching from a 200-nm thin tantalum film on a c-plane sapphire substrate[50]. Two windows were opened on the 3D waveguide above and below the SNAIL chip to place a copper magnet and a pump port into the waveguide close to the SNAIL to enable flux bias and strong pumping (Extended Data Fig. 66 a).The antennae of the transmon qubits are fabricated using the same tantalum etching technique, while both the SNAIL and transmon junctions are made of Al-AlO_x-Al layers fabricated using a standard Dolan bridge method.

SNAIL mode characterization. The SNAIL mode is characterized by measuring the transmission signal from the SNAIL pump port to a side port on the waveguide using a network analyzer. By sweeping the bias current applied to the magnet (Extended Data Fig. 66 c) we can measure how the frequency of the SNAIL and waveguide modes are changed by flux biasing the SNAIL loop.

Experimental setup. The modular quantum computer is installed at the base ($\sim$ 18 mK) plate of a cryogenic set-up (Extended Data Figure 1). Here, all pulse sequences are generated by h Keysight M3202A (1 GSa/s) and M3201A (500 MSa/s) Arbitrary Waveform Generators (AWGs). The baseband microwave control pulses are generated at an intermedi-

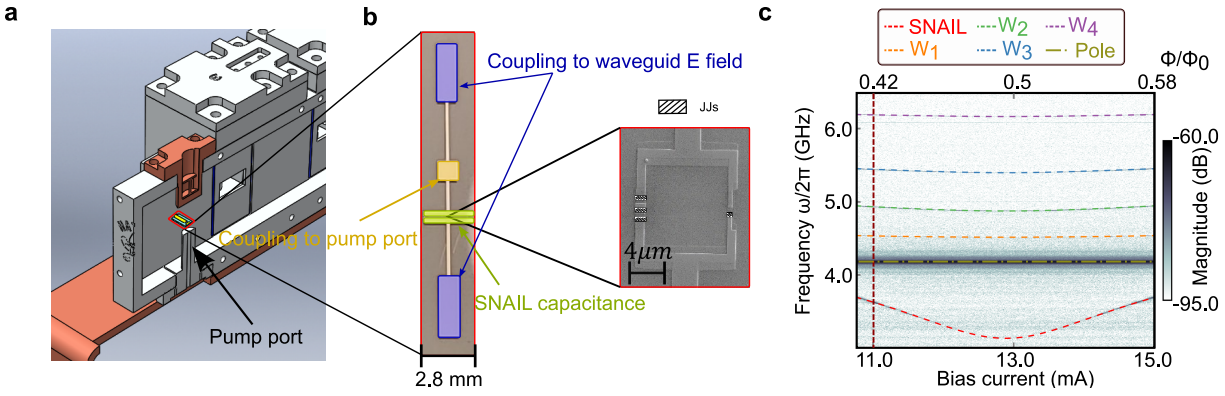

Figure 66: **SNAIL mode details.** (a) Physical position of the SNAIL chip and pumping port. The SNAIL is flux-biased via a copper-sheathed electromagnet protruding into the waveguide above it, and is strongly coupled to a microwave drive line introduced via an aluminum cylinder below the SNAIL. (b) False color optical and SEM image of the SNAIL, indicating its essential components. (c) Color plot of the magnitude of transmission signal versus the frequency from SNAIL pumping port ($|S_{21}(\omega)|$) for a range of applied coil bias current/applied SNAIL flux. The dotted lines indicate the dressed modes of the waveguide modes and snail, as well as the 'pole mode' of the aluminum cylinder containing the drive port. The vertical dark red dash line indicates the operating flux of the SNAIL.

ate frequency (IF) of 100 MHz and upconverted to microwave frequencies using IQ mixers. Image rejection (IR) mixers have been used for downconverting the detected signals to 50 MHz, which are then digitized using a control system based on Keysight M3102A Analog-to-Digital converters with a sampling rate of 500 MSa/s and on-board Field-Programmable Gate Arrays (FPGA) for signal processing.

Numerical simulations. We simulate the behavior of our system by analyzing the behavior of seven modes participating in the experiments: three qubit modes and four communication modes. We treat the gates as ideal parametric interactions, and work in the rotating frame of the system. The Hamiltonian, then contains single qubit controls, cavity-cavity inter-module interactions, and qubit-cavity intra-module interactions listed respectively to give:

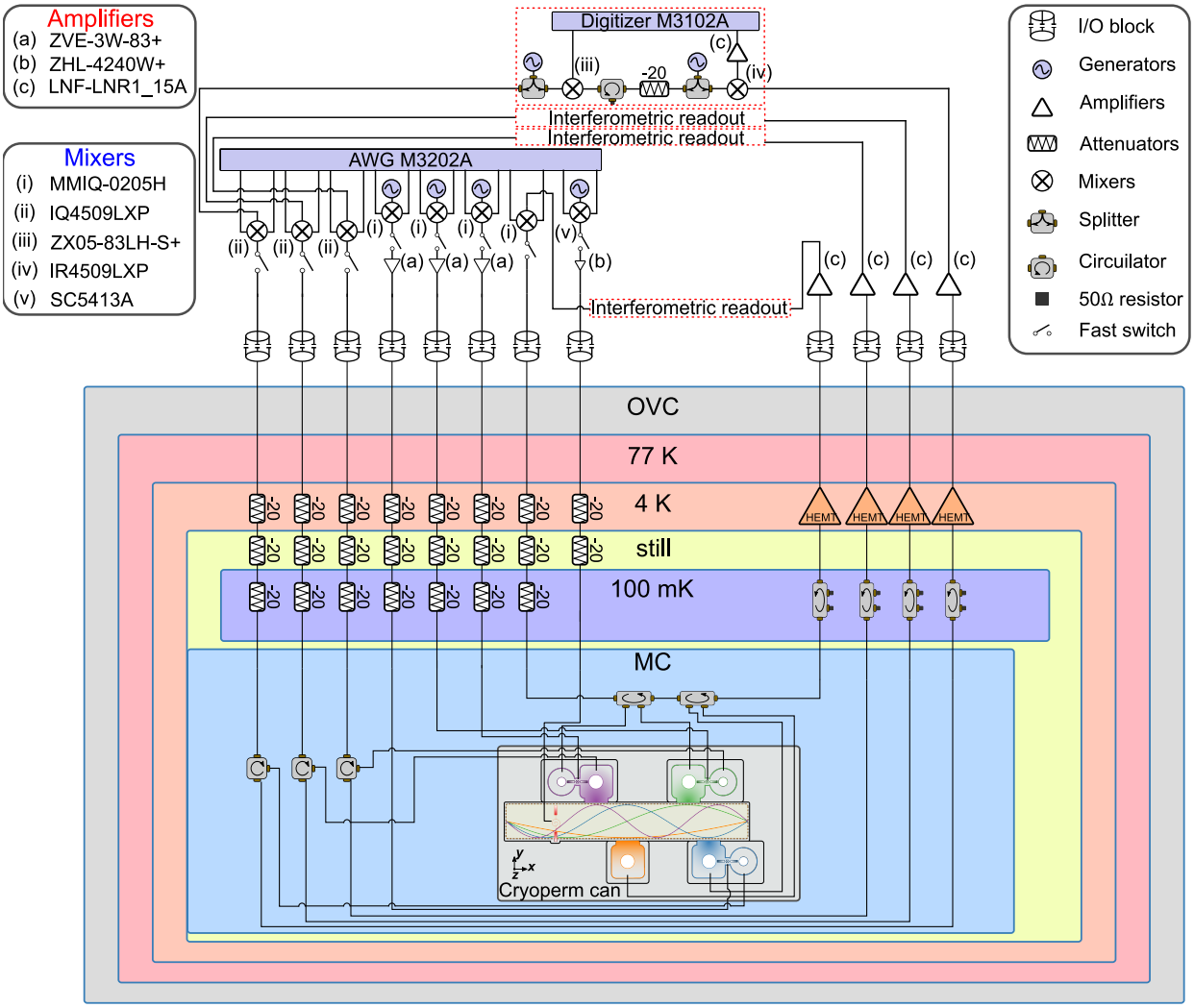

Figure 67: **Schematic of the experimental setup**

$$\frac{\hat{\mathcal{H}}_{QC}}{\hbar} = \sum_{m=2,3,4} \eta_m(\hat{q}_m^\dagger + \hat{q}_m) + \sum_{\substack{i,j=1,2,3,4 \\ i\neq j}} \eta_{ij}\, g_{c_i c_j s} \left(\hat{c}_i^\dagger \hat{c}_j + \hat{c}_i \hat{c}_j^\dagger\right) + \sum_{k=2,3,4} \eta_k\, g_{q_k q_k c_k c_k} \left(\hat{c}_k^\dagger \hat{q}_k + \hat{c}_k \hat{q}_k^\dagger\right), \tag{101}$$

where $\hat{q}_i$ indicates the qubit mode in each module and $\eta(t)$ represents the time-dependent strength of a given pulse, which follows the shapes and durations used in the experiment.

To capture the effects of photon loss and decoherence in the system, we add loss operators with rates corresponding rates to the measured values listed in the Table. 12 and simulate the evolution of the system via Lindblad master equation[143] using QuTiP[144]:

$$\dot{\rho}(t) = -\frac{i}{\hbar}\left[\hat{H}_{QC}(t), \rho(t)\right] + \sum_n \mathcal{D}\left[\hat{C}_n\right](\rho) \tag{102}$$

where ρ represents the density matrix of the system and

$$\mathcal{D}[C_n](\rho) = \hat{C}_n \rho \hat{C}_n^\dagger - 1/2\left(\hat{C}_n^\dagger \hat{C}_n \rho + \rho \hat{C}_n^\dagger \hat{C}_n\right) \tag{103}$$

is the interaction between the system and the environment for different collapse operators.

For all experiments reported in the main text, we have applied same pulse sequences in the simulation, and record the final states after half of the measurement time (to account for decay during the measurement process). Results are very consistent between experiments and simulation, which indicates that our device is primarily limited by the coherence times of our modes.

Data processing. For all quoted fidelities in the main text, we have first reconstructed the density matrix ρ from tomographic measurements, and for a given target state σ, the fidelity of the results is calculated using:

$$F(\rho, \sigma) = \left(\mathrm{tr}\sqrt{\sqrt{\rho}\sigma\sqrt{\rho}}\right)^2 \tag{104}$$

Furthermore, a bootstrap method[141] has been used to estimate the uncertainty of the reported fidelity. In experiments, all final datasets contain more than 10,000 averages; we restructure the data set into $N_{\mathrm{boot}} = 1,000$ data sets each containing $N = 10,000$ points obtained by Monte Carlo sampling of the original set of $10,000$ points. During Monte Carlo sampling, the probability that a data point is picked is 1/N irrespective of whether it has been picked before. In the end, we calculate the standard deviation of the bootstrap data sets s_{x^B}.

In general, s_{x^B} should have the relation with the uncertainty of the original sample σ_x as:

$$\sigma_x = \sqrt{\frac{N}{N-1}} s_{x^B} \tag{105}$$

Since, in our case, $N = 10,000$ is sufficiently large, the square root can be replaced by unity.

6.5 Supplementary experimental details and methods.

6.5.1 Effect of exchange interaction VS mode type and state encoding

As noted previously, depending on the qubit encoding in Hilbert space of the state being swapped, the same parametric coupling (i.e. $\hat{\mathcal{H}}^{\text{eff}} = g^{\text{eff}}_{c_i c_j}(\hat{c}_i^\dagger \hat{c}_j + \hat{c}_i \hat{c}_j^\dagger)$) can result in very different state evolution. To clarify this, we compare different initial states and different kinds of modes (transmon qubit or cavity) at times $t = \pi/g^{\text{eff}}, 2\pi/g^{\text{eff}}, 3\pi/g^{\text{eff}}$ and $4\pi/g^{\text{eff}}$.

As shown in Tabel. 13, between two two-level-systems (TLS), the effective conversion process can perform a perfect iSWAP gate. However, if the coupled objects include one linear mode, the situation becomes more complicated. For example, in the Fock state basis, the conversion process between two linear modes is more like a 'beam splitter' process[139, 125]; and in the coherent state basis, the process becomes a non-entangling exchange.

6.5.2 Parametric photon iSWAP gate using 3-wave-mixing

6.5.2.1 Parametric regime analysis

Here we analyze the parametric exchange process in the system. Without loss of the generality, we have excluded the qubit and readout cavity modes from the total Hamiltonian, and focused on the parametric coupling between the communication cavities.

$$\begin{aligned}\hat{\mathcal{H}}_0/\hbar = &\sum_{i=1,2,3,4} \left[\omega_{\mathrm{w}_i} \hat{\mathrm{w}}_i{}^\dagger \hat{\mathrm{w}}_i + g_{\mathrm{w}_i s}(\hat{\mathrm{w}}_i{}^\dagger \hat{s} + \hat{\mathrm{w}}_i \hat{s}^\dagger)\right] + \sum_{i=1,2,3,4} \left[\omega_{c_i} \hat{c}_i{}^\dagger \hat{c}_i + g_{c_i \mathrm{w}_i}(\hat{c}_i{}^\dagger \hat{\mathrm{w}}_i + \hat{c}_i \hat{\mathrm{w}}_i{}^\dagger)\right] \\ &+ \omega_s \hat{s}^\dagger \hat{s} + g_3(\hat{s} + \hat{s}^\dagger)^3,\end{aligned} \tag{106}$$

Table 13: Transmon to transmon exchange. We consider the final states of different initial states under evolution operation U^p, where U is defined as $U = \exp(-i\hat{\mathcal{H}}t)$, as $t = 2\pi/g^{\text{eff}}$. The exponent of U simply means $U^p = \exp(-i\ \hat{\mathcal{H}}(pt))$. Here, U^p creates an iSWAP family gate between the two qubits; $U^{1/2} = \sqrt{i\text{SWAP}}$ could be used to create Bell state given an initial state $|1,0\rangle$. Note that U performs an iSWAP gate, which could also be used to create entanglement between two qubits.

$\|\psi_{\text{init}}\rangle$	$\|1,0\rangle$	$\|1,1\rangle$	$\alpha\|0,0\rangle + \beta\|0,1\rangle + \gamma\|1,0\rangle + \eta\|1,1\rangle$
$U^{1/2}\|\psi_{\text{init}}\rangle$	$\frac{\sqrt{2}}{2}(\|1,0\rangle - i\|0,1\rangle)$	$\|1,1\rangle$	$\alpha\|0,0\rangle + \frac{\sqrt{2}}{2}(\beta - i\gamma)\|0,1\rangle + \frac{\sqrt{2}}{2}(\gamma - i\beta)\|1,0\rangle + \eta\|1,1\rangle$
$U\|\psi_{\text{init}}\rangle$	$-i\|0,1\rangle$	$\|1,1\rangle$	$\alpha\|0,0\rangle - i\gamma\|0,1\rangle - i\beta\|1,0\rangle + \eta\|1,1\rangle$
$U^{3/2}\|\psi_{\text{init}}\rangle$	-$\frac{\sqrt{2}}{2}(\|1,0\rangle + i\|0,1\rangle)$	$\|1,1\rangle$	$\alpha\|0,0\rangle - \frac{\sqrt{2}}{2}(\beta + i\gamma)\|0,1\rangle - \frac{\sqrt{2}}{2}(\gamma + i\beta)\|1,0\rangle + \eta\|1,1\rangle$
$U^2\|\psi_{\text{init}}\rangle$	$-\|1,0\rangle$	$\|1,1\rangle$	$\alpha\|0,0\rangle - \beta\|0,1\rangle - \gamma\|1,0\rangle + \eta\|1,1\rangle$

Table 14: Transmon to cavity exchange. We consider the Fock state basis as for transmon-cavity coupling, coherent states could result in an even more complicated scenario. Here the U^p operator can still behave like a tunable beam-splitter if either the cavity or qubit is prepared to an empty/ground state. However, for initial states like $|1,n\rangle$, where $n \geq 1$, the U^p operator will no longer keep the state unchanged.

$\|\psi_{\text{init}}\rangle$	$\|1,0\rangle$	$\|1,1\rangle$ *
$U^{1/2}\|\psi_{\text{init}}\rangle$	$\frac{\sqrt{2}}{2}(\|1,0\rangle - i\|0,1\rangle)$	$\frac{\sqrt{2}}{2}(\|1,1\rangle - i\|0,2\rangle)$
$U\|\psi_{\text{init}}\rangle$	$-i\|0,1\rangle$	$-i\|0,2\rangle$
$U^{3/2}\|\psi_{\text{init}}\rangle$	-$\frac{\sqrt{2}}{2}(\|1,0\rangle + i\|0,1\rangle)$	$-\frac{\sqrt{2}}{2}(\|1,1\rangle + i\|0,2\rangle)$
$U^2\|\psi_{\text{init}}\rangle$	$-\|1,0\rangle$	$-\|1,1\rangle$

* Here, the unitary is defined as $U = \exp(-i\hat{\mathcal{H}}t')$, where $t' = t/\sqrt{2}$.

Table 15: Cavity to cavity exchange. For two cavities prepared to Fock states, U^p operator still behaves as a 'beam splitter', while for coherent state basis, it will only exchange photon between the two cavities but will not create entanglement.

$\|\psi_{\text{init}}\rangle$	$\|1,0\rangle$	$\|1,1\rangle$	$\|\alpha,0\rangle$	$\|\alpha,\beta\rangle$
$U^{1/2}\|\psi_{\text{init}}\rangle$	$\frac{\sqrt{2}}{2}(\|1,0\rangle - i\|0,1\rangle)$	$\frac{\sqrt{2}}{2}(\|2,0\rangle + \|0,2\rangle)$	$\|\alpha/2, -i\ \alpha/2\rangle$	$\|\alpha/2 - i\ \beta/2, \beta/2 - i\ \alpha/2\rangle$
$U\|\psi_{\text{init}}\rangle$	$-i\|0,1\rangle$	$\|1,1\rangle$	$\|0, -i\ \alpha\rangle$	$\|-i\ \beta, -i\ \alpha\rangle$
$U^{3/2}\|\psi_{\text{init}}\rangle$	$-\frac{\sqrt{2}}{2}(\|1,0\rangle + i\|0,1\rangle)$	$\frac{\sqrt{2}}{2}(\|2,0\rangle + \|0,2\rangle)$	$\|-\alpha/2, -i\ \alpha/2\rangle$	$\|-\alpha/2 - i\ \beta/2, -\beta/2 - i\ \alpha/2\rangle$
$U^2\|\psi_{\text{init}}\rangle$	$-\|1,0\rangle$	$\|1,1\rangle$	$\|-\alpha,0\rangle$	$\|-\alpha,-\beta\rangle$

After re-diagonalizing the second order terms in Eq. 106, all dressed modes in the router inherit third order nonlinearity. The terms we are going to use for the parametric pumping scheme are three-wave mixing terms:

$$g_{c_i c_j s}\left(\hat{c_i}^\dagger \hat{c_j}\hat{s} + \hat{c_i}\hat{c_j}^\dagger \hat{s}^\dagger\right),\ (i,j=1,2,3,4; i\neq j). \tag{107}$$

Here the $\hat{c_i}$ and $\hat{s}$ operators represent the dressed modes after re-diagonalization, and $g_{c_i c_j s}$ is the 3-wave-mixing coefficient. In the weak coupling regime where $(\frac{g}{\Delta})_{c_i \mathrm{w}_i}, (\frac{g}{\Delta})_{\mathrm{w}_i s} \sim 0.1$, the coefficient $g_{c_i c_j s}$ is approximately $g_3(\frac{g}{\Delta})_{c_i \mathrm{w}_i}(\frac{g}{\Delta})_{\mathrm{w}_i s}(\frac{g}{\Delta})_{c_j w_j}(\frac{g}{\Delta})_{w_j s}$, where $\Delta_{\mathrm{w}_i s} = \omega_{\mathrm{w}_i} - \omega_s$.

To realize iSWAP gates between communication cavities based on Eq. 107, we apply a strong single-tone pump on the SNAIL at the frequency difference of two cavities, $\omega_p = \left|\omega_{c_i} - \omega_{c_j}\right|$, where $i,j=1,2,3,4; i\neq j$. The time-dependent pumping term can be written as $\hat{\mathcal{H}}_P/\hbar = \epsilon(t)(\hat{s}+\hat{s}^\dagger)$, where $\epsilon(t)$ is represented by:

$$\epsilon(t) = \begin{cases} \epsilon^x(t)\cos(\omega_p t) + \epsilon^y(t)\sin(\omega_p t), & 0 < t < t_g \\ 0, & \text{otherwise,} \end{cases} \tag{108}$$

Thus, the total system Hamiltonian under pumping can be written as $\hat{\mathcal{H}}' = \hat{\mathcal{H}}_0 + \hat{\mathcal{H}}_P$. To study the effect of this pumping term in the total Hamiltonian, we apply a unitary transformation on $\hat{\mathcal{H}}$ with displacement operator:

$$D(t) = \exp[(zs^\dagger - z^* s)], \tag{109}$$

where $z = -\frac{(\epsilon^x + i\epsilon^y)/2}{\omega_p - \omega_s} e^{-i\omega_p t} + \frac{(\epsilon^x - i\epsilon^y)/2}{\omega_p + \omega_s} e^{i\omega_p t}$. This results in a new Hamiltonian $\hat{\mathcal{H}}^D$, in which the $\hat{\mathcal{H}}_P$ term is canceled and $\hat{s} \to \hat{s} - z$. Specifically, the 3-wave mixing term in Eq. 107 becomes:

$$g_{c_i c_j s} \hat{c_i}^\dagger \hat{c_j} \left(\hat{s} \frac{(\epsilon^x + i\epsilon^y)/2}{\omega_p - \omega_s} e^{-i\omega_p t} - \frac{(\epsilon^x - i\epsilon^y)/2}{\omega_p + \omega_s} e^{i\omega_p t} \right) + h.c. \tag{110}$$

Then we apply a rotating frame transformation at the frequency of all the router modes (SNAIL + waveguide) and communication modes in the system:

$$R(t) = \exp\left[i\omega_s \hat{s}^\dagger \hat{s} + \sum_{i=1,2,3,4} i \left(\omega_{\mathrm{w}_i} \hat{\mathrm{w}}_i^\dagger \hat{\mathrm{w}}_i + \omega_{c_i} \hat{c_i}^\dagger \hat{c_i} \right) \right], \tag{111}$$

Note that $\omega_p = \left| \omega_{c_i} - \omega_{c_j} \right|$. Assume the all the other frequency differences in the system are several linewidths away from the pumping frequency. Then the only slowly rotating term after the transformation is

$$\hat{\mathcal{H}}^{\mathrm{RWA}}/\hbar = \eta \; g_{c_i c_j s} \left(\hat{c}_i^\dagger \hat{c}_j + \hat{c}_i \hat{c}_j^\dagger \right), \tag{112}$$

where $\eta = (\epsilon^x + i\epsilon^y)\omega_s / (\omega_d^2 - \omega_s^2)$.

Equation 112 shows that pumping at $\omega_p = \left| \omega_{c_i} - \omega_{c_j} \right|$ activates the spontaneous photon exchange process between communication mode c_i and c_j. The iSWAP speed depends on the pumping strength and the three-wave mixing coefficient $g_{c_i c_j s}$. By controlling the length of the pulse, $i\mathrm{SWAP}^{1/n}$ gates can be performed between the two modes. Also, the existence of all the 3-wave-mixing terms between different modes allows us to pump multiple parametric process simultaneously, e.g. we can perform iSWAP gate between two different cavity pairs at the same time by simultaneously pumping the SNAIL mode at the two difference frequencies.

6.5.2.2 iSWAP gate time for all six cavity pairs

By preparing coherent states in all four different cavities, we can perform six pairs of inter-module iSWAP. We list all iSWAP gate times in Table. 16. The average gate time is 760 ns.

Table 16: **iSWAP gate times between all six possible communication cavity pairs.** The data is measured by preparing a coherent state in one cavity and swap it to another cavity. For each swap pair, the listed iSWAP gate time is based on the maximum iSWAP speed measured by tuning up the SNAIL pump power until we see obvious decrease of mode lifetime.

iSWAP pair	iSWAP time (ns)
$C_1 \leftrightarrow C_2$	1248
$C_1 \leftrightarrow C_3$	651
$C_1 \leftrightarrow C_4$	535
$C_2 \leftrightarrow C_3$	942
$C_2 \leftrightarrow C_4$	832
$C_3 \leftrightarrow C_4$	375

6.5.2.3 Multi-end router iSWAP

One benefit of the router design is that we can apply multiple pump tones on the SNAIL at the same time to activate multiple exchange processes simultaneously, which give us lots of freedom for more complicated gates. In order to test this idea, we have designed two experiments: one realizing multiple iSWAPs in parallel, and a second realizing "V-iSWAP" from one source cavity to two target cavities.

The protocol and experimental results are shown in Fig. 68. All protocols are based on coherent states. First, we have tried the parallel iSWAP (as shown in Sec. 68): Here, C_3 and C_4 have been first displaced with short Gaussian pulses, then we turn on the iSWAP

pump on $S_{C_1C_4}$ and $S_{C_2C_3}$ simultaneously. At the same time, the voltage output from all the cavities are measured through weakly-coupled ports. Comparing to the single iSWAP, a small extra pump detuning (~ -250KHz) has been observed on both pumps, which will attribute to the dynamic-Kerr from driven SNAIL.

For the "V-iSWAP", we have displaced C_2 first, then we turn on the SNAIL pumps for $S_{C_2C_3}$ and $S_{C_2C_4}$ simultaneously, and similarly, we have recorded the voltage output from all three cavities. One thing is different from parallel iSWAP is that the rate of two iSWAPs between each pair need to be precisely identical. In our case, as C_3 and C_4 have been perfectly overlapped with each other, thus, C_2 to C_3 and C_2 to C_4 share the same iSWAP rate with each other. Again, a small extra pump detuning (~ -60KHz) is added on both pumps to compensate the dynamic-Kerr effect.

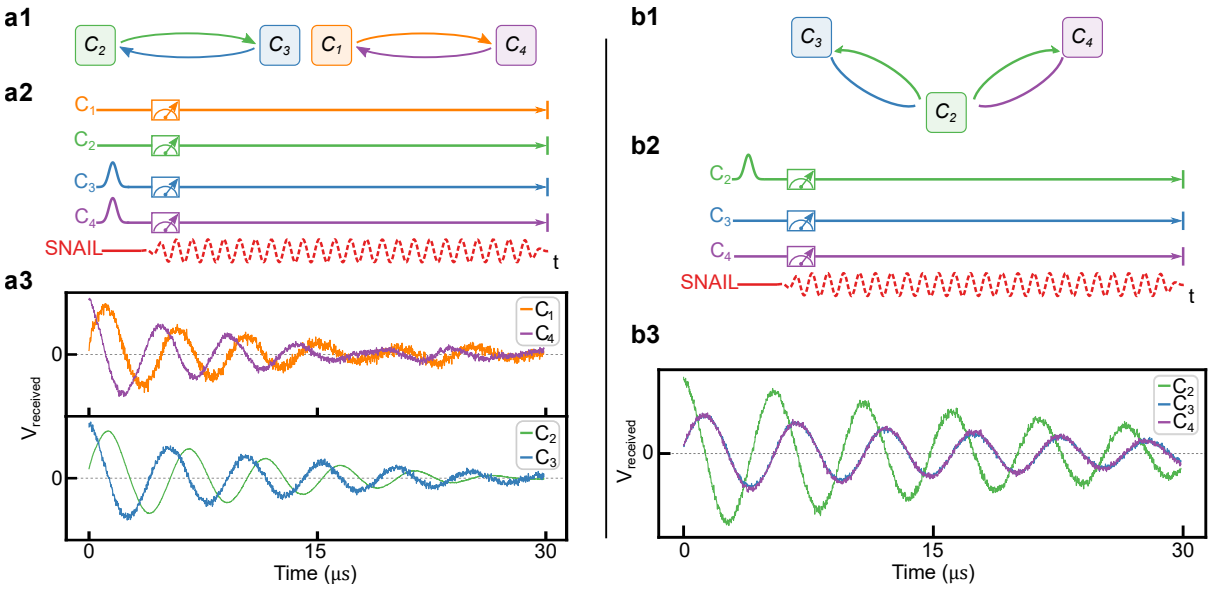

Figure 68: **Simultaneous iSWAPs between multiple cavities.** (a) Parallel SWAP between C_1, C_4 and C_2, C_3; (a1, a2) Pulse sequence and schematic. (a3) We have rotated the output results so that the quadrature components equal to zero, and plot only the in-phase voltages vs time for all four cavities. (b) V-iSWAP from C_2 to C_3 and C_4. In this case, the light can go back and forth between one cavity and two cavities. We have carefully tuned the pump frequencies and amplitudes so that the voltage trace for C_3 and C_4 perfectly overlap with each other. If C_2 is prepared to Fock state $|1\rangle$ at the beginning, and C_3 and C_4 are both prepared to empty states, then at the moment when C_2 is empty, a bell state is created between C_3 and C_4.

6.5.3 Intra-module iSWAP

The next ingredient, previously termed an intra-module iSWAP[35], swaps information between qubits and communication cavities. In the experiment, the qubit is first prepared to its excited state, which gives module state $|e0\rangle$. Next, two side-band tones are applied near to the qubit and cavity frequencies. Here the detunings are around 10κ ($\sim$ 20 MHz) away from each mode to avoid any undesired mode excitation. Then, both iSWAP time and cavity side-band (CSB) detuning δ are swept to determine the optimized iSWAP condition. The average fidelity of a iSWAP gate is 94%, which is mainly limited by how fast the iSWAP gate is compared to T_1 and T_ϕ of qubit and cavity.

6.5.4 Generating Bell states during parallel operations

Due to the coherence time of all modes, the Bell states' fidelity has been limited by the iSWAP gate time in all operations. Here we use one example showing the limitation of the experiments. As we have mentioned in text, because of the saturation power when operating with multiple tones during parallel operations on the SNAIL, we need to slow down the iSWAP rate. As shown in Fig. 70, when the iSWAP gate time increase from 600 ns to 1300 ns, the fidelity of bell states decrease from 76.9% to 68.1%, but no additional side effect is added due to cross-talking or other source.

6.6 Discussion and outlook

In this work we have demonstrated a coherent quantum state router for microwave photons and used it to realize a small modular quantum computer. A key feature is the use of a SNAIL mode to create three-wave couplings in the router itself, rather than rely on nonlinear couplers embedded in each module. The router enables us to create all-to-all couplings among a set of quantum modules, to parametrically drive gates between the communication modes of those modules, and even create three-qubit and parallel iSWAP operations

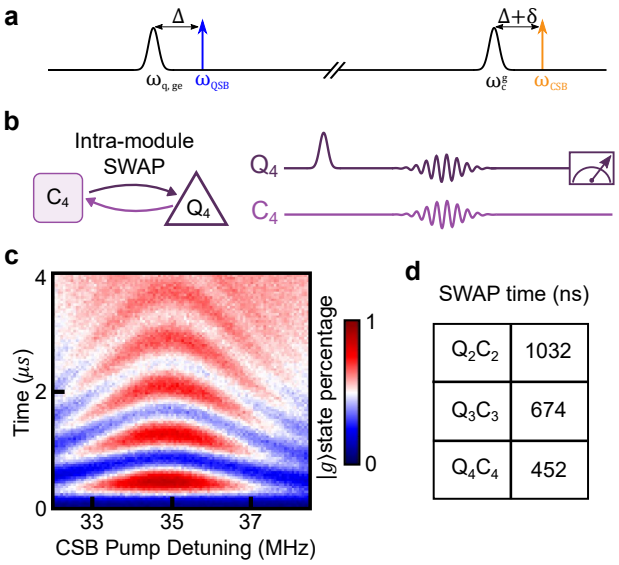

Figure 69: **Intra-module iSWAP.** (a) Schematic of qubit and communication cavity frequencies and pump tones. Two pump tones have been applied near the qubit and cavity frequencies to generate iSWAP between qubit and cavity. (b) Schematic and pulse sequence. The qubit is prepared in its excited state via a $R_x(\pi)$ pulse at $\omega_{q,ge}$, then two sideband pulses are applied at ω_{QSB}, detuned by Δ from $\omega_{q,ge}$, and ω_{CSB}, detuned by $\Delta+\delta$ from ω_c^g. Finally, projective measurement is applied to the qubit. Both pulse length, and δ are swept to determine an optimized iSWAP gate. (c) Rabi oscillation of the intra-module iSWAP. The vertical axis is the pulse time, and the horizontal axis is the CSB detuning δ, where the color indicates the $|g\rangle$ state population of qubit. (d) Full iSWAP time for all three cavity-qubit pairs in the system

between multiple pairs of communication modes by applying multiple, simultaneous parametric drives.

The current device's performance ($F_{avg} = 0.97$ for gates involving the router) is limited primarily by the qubit/cavity lifetimes involved, though the limitation is primarily in the modules themselves and due to imperfect quantum engineering. Other recent implementations of similar quantum modules[125, 120] have achieved much higher coherence time, with qubit and cavity modes in the $100 - 1000\mu s$ range. With modest improvements in lifetime

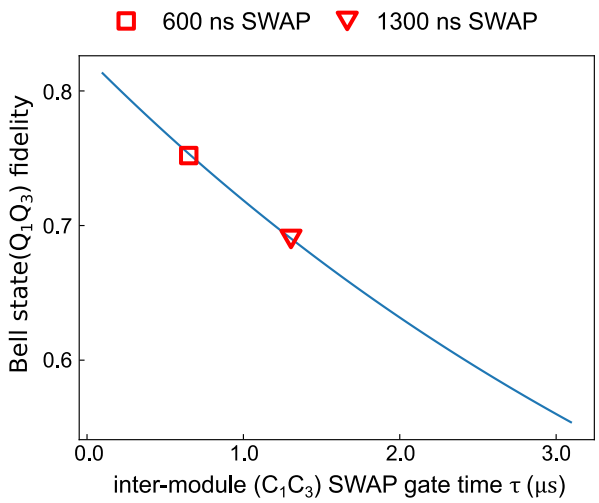

Figure 70: **Bell stated fidelity versus inter-mdoule *i*SWAP gate time.** The blue line represents the simulation of the bell state fidelity between Q_1 and Q_3 when we varying the inter-module iSWAP gate time. And the 600 ns (1300 ns) iSWAP corresponding to the Bell state generation without (with) parallel operations.

to $\sim 10\mu s$ for our router waveguide modes, which we can achieve by retracting our SNAIL into a coupling tube[120], our router will be able to provide sub-microsecond, very high fidelity gates between millisecond scale communication cavities. Retracting the SNAIL into a tube adjacent to the waveguide also has the advantage that we can couple a single SNAIL to multiple router elements, allowing us create inter-router operatoins and hence a scalable modular network.

One vital question requiring further research is how fast we can ultimately drive gates in this system. One straightforward route is to further increase the waveguide mode lifetimes in the router; we can then increase the dispersive coupling strength to their respective communication modes without decreasing the communication mode lifetimes. Doubling our current average coupling to $g/\Delta = 0.2$ will immediately push our average gate time to ~ 100 ns. We must also learn more about how hard we can drive SNAILs with one or more drive tones. This is directly related to the issue of saturation power in parametric amplifiers,

where recent exciting results [105, 145] provide guidance on how we may further optimize our router. Coupled with stronger module-router couplings, it seems feasible to push our overall gate time down to as low as tens of nanoseconds in better optimized, next generation devices.

7.0 Conclusions and perspectives

7.1 Better quantum state router

The story of the modular quantum computer does not end after the work we have published last year. There are ongoing efforts (led by Chao Zhou and Mingkang Xia and certain to become chapters in their theses) to build a better quantum state router from many perspectives. First, we worked to protect the SNAIL from its lossy environment via a 'seamless' design (as shown in Fig. 71 a)) and low pass filters with lower out-of-band loss at the SNAIL frequency. Based on our current SNAIL lifetime (T_1 : 2 μs and T_2 : 3.5 μs), the maximum module coherence we can support is easily around T_1 : 2 ms and T_2 : 3.5 ms, or perhaps even longer.

Second, we have discovered important changes we can make to the machined sample mounts which host our machines. As will be detailed in forthcoming theses from the group, a combination of both polishing seams in 6061 aluminum and OFHC copper and placing the seams to minimize participation in our high Q modes can greatly extend coherence in the router. New max router lifetime XXX us, module cavity lifetime increased to YYY, now standard in all our sample mounts. This may also hold for high purity aluminum or Nb cavities, though it is not clear whether etching or other surface treatments will erase the effects of starting from a mirror-quality surface. Identifying the reason polishing helps may offer us new insights, allowing us to use stronger and more convenient materials such as aluminum alloys, or perhaps pointing the way to how to further improve the quality of high-purity cavities and sample mounts.

Third, we have improved the system's coherence by carefully reworking all filters, magnetic shields, Eccosorb filters, etc. in the system. We have incorporated these improvements in an 'armored' sample shield with cryoperm which incorporates all the final stage filters very near the sample, with all components firmly bolted to a single-piece copper sample mount and allows the whole system to be covered in absorbing Eccosorb foam and almunized mylar.

With the multiple upgrades, we start seeing the coherence of the cavity modes in the

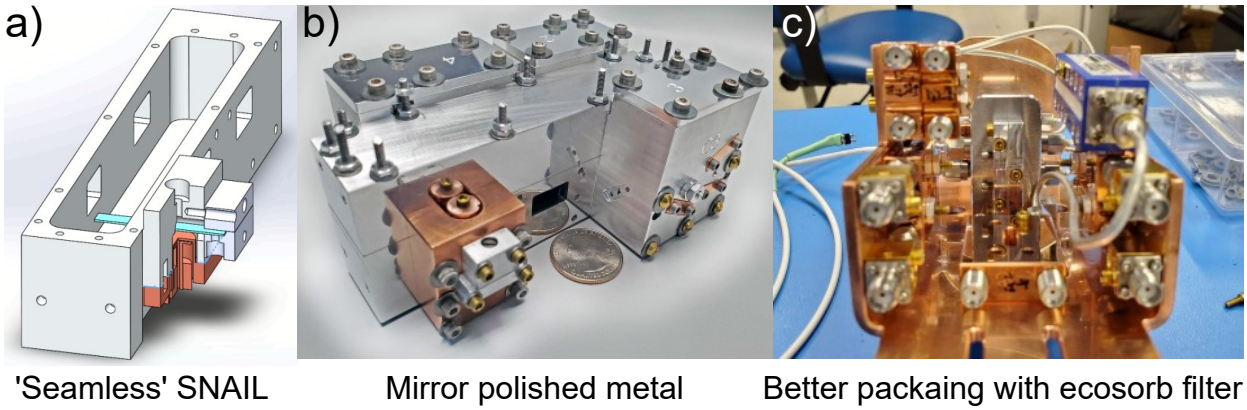

Figure 71: **Better quantum state router.** a) On the one hand, putting the 'seam' at the height with least participation of all the waveguide modes can efficiently prevent the 'seam' loss for the router modes; on the other hand, the SNAIL has been designed to put in a single metal block, which we called 'seamless' SNAIL, as we found its participation in seams which cross the SNAIL's pads to be too high. b) All aluminum metal forming the waveguide and cavities has been carefully polished to a 'mirror' surface finish, and we find this simple trick can significantly increase the quality factor contribution due to the seams (see Chao Zhou's forthcoming thesis). c) An 'armored' cryoperm can has been designed to further suppress the high-frequency noise and filter, attenuator, and sample thermalization.

system can already reach $200 - 500\,\mu$s, even though the iSWAP gate time we made is only around $2\,\mu$s, we see big potential of a much better performance in the short future.

7.2 Compatible quantum module design

We have also been working to develop a quantum module with more than one qubit to accompany the state router. Since we have already built the quantum state router based on SNAILs and all-to-all parametric controls, we decided to apply the same ideas to a transmon-based quantum module. More, because of the simpler two-level energy spectrum the qubit

has, photon conversion between two modes can naturally become an iSWAP family gates with no extra effort.

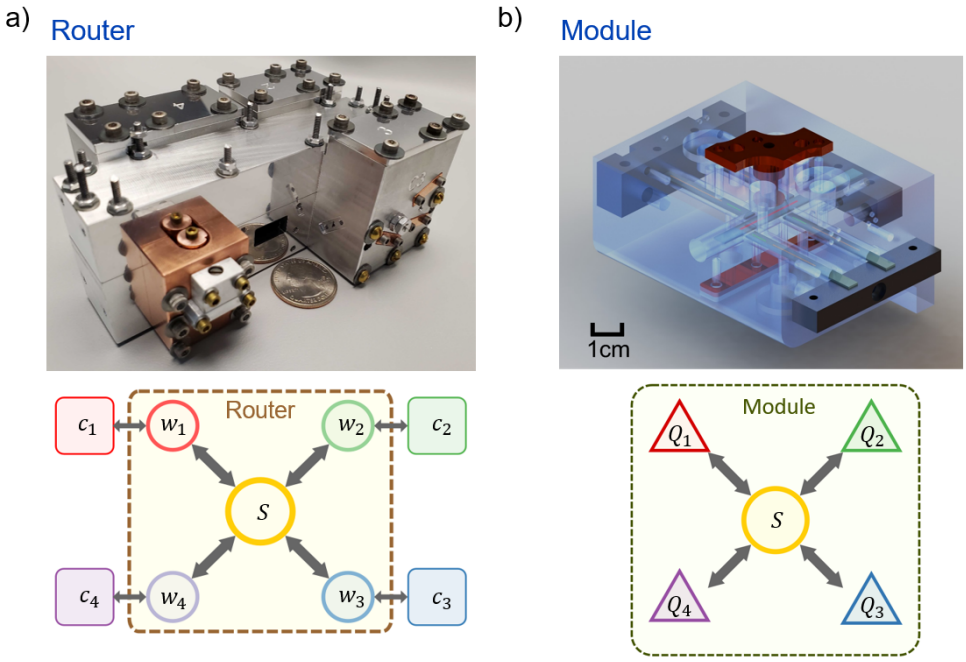

Figure 72: **Comparison between Tree 2.0 and quantum module.** We have tried a pretty similar structure between the router and the module, where the former uses SNAIL couple to linear mode and the latter to nonlinear mode. The operations between each of the modes are very similar: by parametrically pumping frequency difference between any of the two modes, the photon can coherently move back and forth between them.

This year, we have successfully made the quantum module comprised of a central SNAIL coupled with four transmon qubits. Two-qubit interactions are created via three-wave coupling driving the SNAIL at the difference frequency of a pair of qubits. The module's architecture allows us to realize all-to-all two-qubit couplings with experimental iSWAP times of $\sim 300\,\text{ns}$ in our prototype. Moreover, we can also drive single qubit gates in the module as fast as $\sim 20\,\text{ns}$ by driving the central SNAIL at one half of each qubit's resonant frequency, allowing the entire module's gates to be implemented via a single drive line. This 'subharmonic' driving was developed collaboratively among several students in the lab, and will be featured in a forthcoming publication on which I am a co-author. Some preliminary

data for the module is shown in Fig. 73. More detailed data and analysis will be published in later papers and also my colleagues Mingkang Xia and Chao Zhou 's theses. Furthermore, our module design is directly compatible with our previously realized quantum state router.

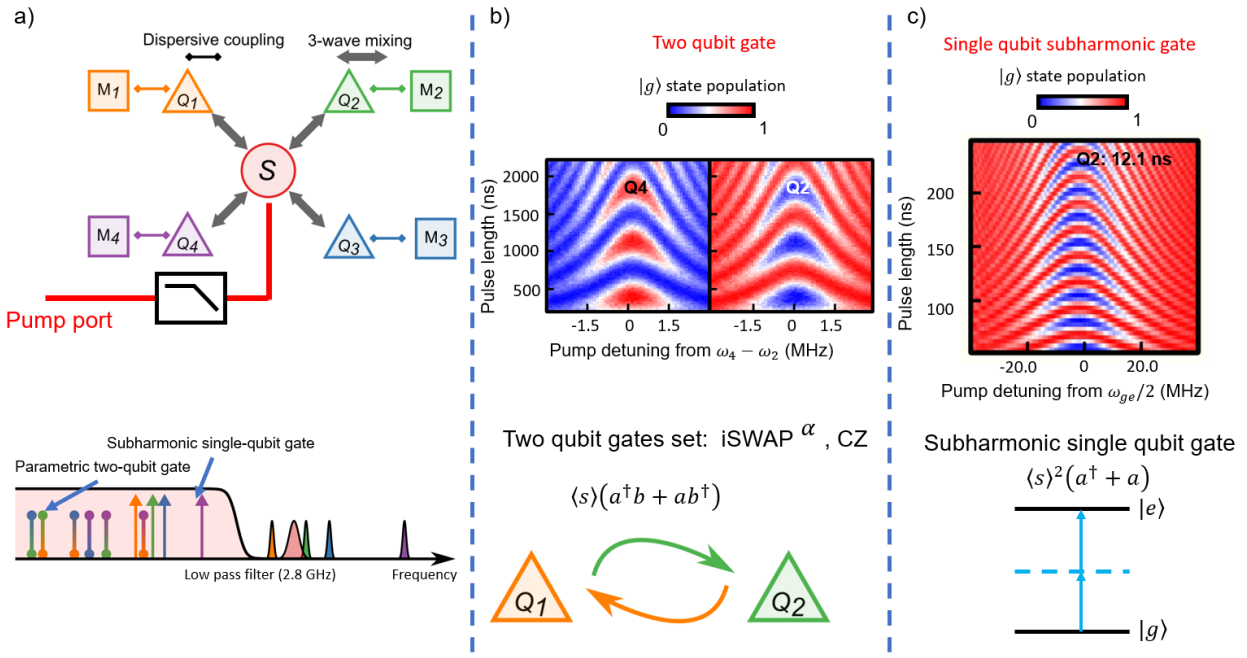

Figure 73: **Quantum module preliminary results.** a) We have carefully designed all coherent modes above the filter's cut-off frequency to let the lossy pumping signal come in and don't let the modes' photon come out. b) Similar idea in the quantum state router, by parametrically pumping the frequency different between two modes, the photon can go back and forth between two qubits. c) Moreover, we can also pump half-resonance of each qubit to perform single-qubit gate with faster rate and no coherence limit.

7.3 Pushing the performance boundary

During the module's development, we found building the modular quantum computer based on parametric controls not only has practical use, but also bring lots of new science question that need to be addressed. One interesting point we are working on is the speed

limit of the photon conversion rate. In both router and module experiments, we find a crucial limit on the parametric pumping strength: as soon as the power is beyond a specific value, the system will go through a phase transition destroying the whole system's coherence. We don't believe this limit to be including in standard theories for gate speed due to parametric driving (which depend on an expansion of the Hamiltonian to finite order) [146]. The results look to relate to the 'chaotic' regime of SNAIL itself in which it oscillates across several minima of its potential. At this moment, we're trying to find a complete theory explaining the result and also push the boundary of the parametric system limit via Hamiltonian engineering with this additional constraint factored in.

Not only this, we're also exploring the potential of the module we have built. A 4-bit quantum system with all-to-all interaction is actually not very common in superconducting circuits because of all kinds of cross talk and frequency crowding problem. During the experiment, we have already proved multiple parametric interactions do not interfere with each other, which gives us the possibilities of applying multiple tones at the same time. In this case, building a three or more-qubit gate is not very far away from what we have now, which again can provide new ideas of quantum circuits decomposition and algorithm optimization.

7.4 Outlook

At this point, we have started seeing the vision of the 'tree' like modular quantum computer. No matter the router or the module, we think they are compatible enough connecting with each other. After we have built the 'Lego' block step by step, the next step naturally becomes putting them together and learning the best route to computation power and/or fault tolerant operation with the least amount of hardware.

We think we're not very far away from a 20-bit modular quantum computer (1 router + 4 modules), and we keep pushing the boundary of the computers' performance and the science we have learned. I think the most important aspect my work has opened is to free us from the structures of existing couplers and gate methods which favor only short-range, one to

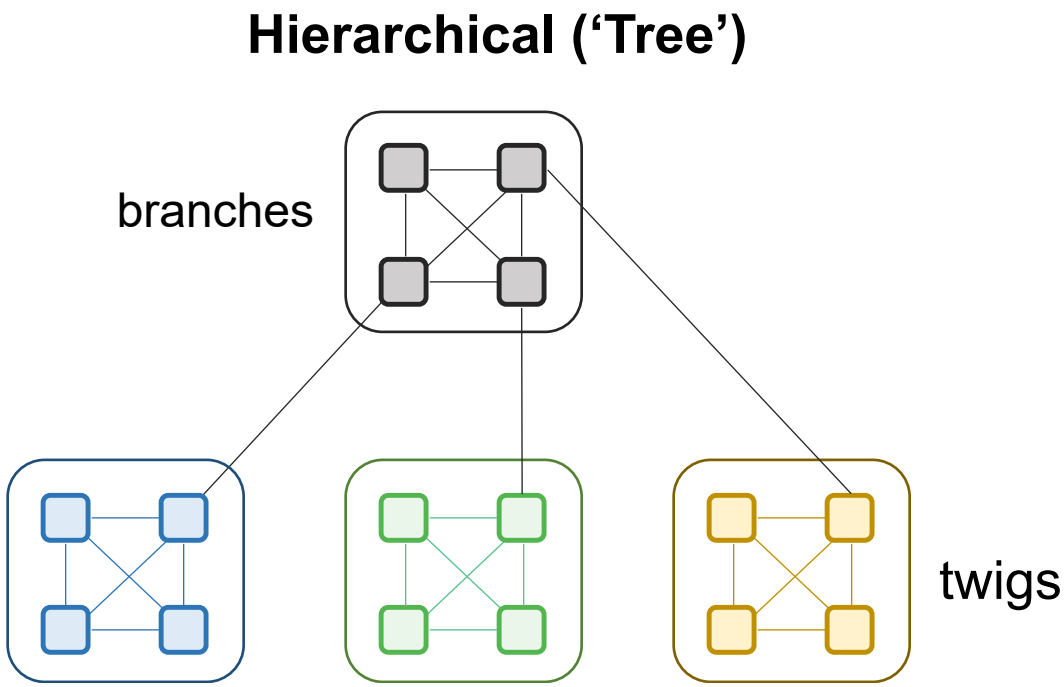

Figure 74: The future of superconducting modular quantum computer.

one, nearest neighbor architectures like the Heavy Hexagon and square lattice architectures, and I am both exciting and hopefully that more and more people will start to adopt and further improve these ideas and used them to power further, more powerful generations of quantum computers.

Bibliography

[1] S. Majumder, L. Andreta de Castro, and K. R. Brown, "Real-time calibration with spectator qubits," npj Quantum Information, vol. 6, no. 1, pp. 1–9, 2020.

[2] S. Krinner, S. Lazar, A. Remm, C. K. Andersen, N. Lacroix, G. J. Norris, C. Hellings, M. Gabureac, C. Eichler, and A. Wallraff, "Benchmarking coherent errors in controlled-phase gates due to spectator qubits," Physical Review Applied, vol. 14, no. 2, p. 024042, 2020.

[3] X. Dai, D. Tennant, R. Trappen, A. Martinez, D. Melanson, M. Yurtalan, Y. Tang, S. Novikov, J. Grover, S. Disseler, et al., "Calibration of flux crosstalk in large-scale flux-tunable superconducting quantum circuits," PRX Quantum, vol. 2, no. 4, p. 040313, 2021.

[4] C. Zhou, P. Lu, M. Praquin, T.-C. Chien, R. Kaufman, X. Cao, M. Xia, R. Mong, W. Pfaff, D. Pekker, et al., "A modular quantum computer based on a quantum state router," arXiv preprint arXiv:2109.06848, 2021.

[5] J. I. Cirac, P. Zoller, H. J. Kimble, and H. Mabuchi, "Quantum State Transfer and Entanglement Distribution among Distant Nodes in a Quantum Network," Physical Review Letters, vol. 78, pp. 3221–3224, Apr. 1997. Publisher: American Physical Society.

[6] H. J. Kimble, "The quantum internet," Nature, vol. 453, pp. 1023–1030, June 2008. Number: 7198 Publisher: Nature Publishing Group.

[7] C. Monroe and J. Kim, "Scaling the ion trap quantum processor," Science, vol. 339, no. 6124, pp. 1164–1169, 2013.

[8] C. R. Monroe, R. J. Schoelkopf, and M. D. Lukin, "Quantum connections," Scientific American, vol. 314, no. 5, pp. 50–57, 2016.

[9] A. Blais, A. L. Grimsmo, S. M. Girvin, and A. Wallraff, "Circuit Quantum Electrodynamics," arXiv:2005.12667 [quant-ph], May 2020. arXiv: 2005.12667.

[10] A. Blais, R.-S. Huang, A. Wallraff, S. M. Girvin, and R. J. Schoelkopf, "Cavity quantum electrodynamics for superconducting electrical circuits: An architecture for quantum computation," Physical Review A, vol. 69, p. 062320, June 2004.

[11] S. M. Girvin, "Circuit QED: superconducting qubits coupled to microwave photons," in Quantum Machines: Measurement and Control of Engineered Quantum Systems, Oxford: Oxford University Press, 2014.

[12] S. M. Girvin, M. H. Devoret, and R. J. Schoelkopf, "Circuit QED and engineering charge-based superconducting qubits," Physica Scripta, vol. T137, p. 014012, Dec. 2009. Publisher: IOP Publishing.

[13] J. M. Martinis, M. H. Devoret, and J. Clarke, "Quantum Josephson junction circuits and the dawn of artificial atoms," Nature Physics, vol. 16, pp. 234–237, Mar. 2020. Number: 3 Publisher: Nature Publishing Group.

[14] A. A. Clerk, K. W. Lehnert, P. Bertet, J. R. Petta, and Y. Nakamura, "Hybrid quantum systems with circuit quantum electrodynamics," Nature Physics, vol. 16, pp. 257–267, Mar. 2020.

[15] T.-C. Chien, O. Lanes, C. Liu, X. Cao, P. Lu, S. Motz, G. Liu, D. Pekker, and M. Hatridge, "Multiparametric amplification and qubit measurement with a Kerr-free Josephson ring modulator," Physical Review A, vol. 101, p. 042336, Apr. 2020.

[16] G. Liu, X. Cao, T.-C. Chien, C. Zhou, P. Lu, and M. Hatridge, "Noise reduction in qubit readout with a two-mode squeezed interferometer," arXiv:2007.15460 [quant-ph], Aug. 2020. arXiv: 2007.15460.

[17] P. Lu, T.-C. Chien, X. Cao, O. Lanes, C. Zhou, M. J. Hatridge, S. Khan, and H. E. Türeci, "Nearly Quantum-Limited Josephson-Junction Frequency-Comb Synthesizer," Physical Review Applied, vol. 15, p. 044031, Apr. 2021. Publisher: American Physical Society.

[18] Wikipedia, "Parametric oscillator — Wikipedia, the free encyclopedia." `http://en.wikipedia.org/w/index.php?title=Parametric%20oscillator&oldid=1074027597`, 2022. [Online; accessed 05-April-2022].

[19] M. Vainio and L. Halonen, "Mid-infrared optical parametric oscillators and frequency combs for molecular spectroscopy," Physical Chemistry Chemical Physics, vol. 18, no. 6, pp. 4266–4294, 2016.

[20] G. Liu, T.-C. Chien, X. Cao, O. Lanes, E. Alpern, D. Pekker, and M. Hatridge, "Josephson parametric converter saturation and higher order effects," Applied Physics Letters, vol. 111, no. 20, p. 202603, 2017.

[21] K. M. Sliwa, M. Hatridge, A. Narla, S. Shankar, L. Frunzio, R. J. Schoelkopf, and M. H. Devoret, "Reconfigurable Josephson Circulator/Directional Amplifier," Physical Review X, vol. 5, p. 041020, Nov. 2015. Publisher: American Physical Society.

[22] N. Bergeal, F. Schackert, M. Metcalfe, R. Vijay, V. Manucharyan, L. Frunzio, D. Prober, R. Schoelkopf, S. Girvin, and M. Devoret, "Phase-preserving amplification near the quantum limit with a josephson ring modulator," Nature, vol. 465, no. 7294, pp. 64–68, 2010.

[23] N. A. Ansari, "Theory of a two-mode phase-sensitive amplifier," Physical Review A, vol. 46, no. 3, p. 1560, 1992.

[24] A. Vrajitoarea, Z. Huang, P. Groszkowski, J. Koch, and A. A. Houck, "Quantum control of an oscillator using a stimulated josephson nonlinearity," Nature Physics, vol. 16, no. 2, pp. 211–217, 2020.

[25] J. M. Gertler, B. Baker, J. Li, S. Shirol, J. Koch, and C. Wang, "Protecting a bosonic qubit with autonomous quantum error correction," Nature, vol. 590, no. 7845, pp. 243–248, 2021.

[26] J. M. Martinis, M. H. Devoret, and J. Clarke, "Experimental tests for the quantum behavior of a macroscopic degree of freedom: The phase difference across a josephson junction," Physical Review B, vol. 35, no. 10, p. 4682, 1987.

[27] H. Walther, B. T. Varcoe, B.-G. Englert, and T. Becker, "Cavity quantum electrodynamics," Reports on Progress in Physics, vol. 69, no. 5, p. 1325, 2006.

[28] S. Haroche, M. Brune, and J. M. Raimond, "From cavity to circuit quantum electrodynamics," Nature Physics, vol. 16, pp. 243–246, Mar. 2020.

[29] J. Aumentado, "Superconducting Parametric Amplifiers: The State of the Art in Josephson Parametric Amplifiers," IEEE Microwave Magazine, vol. 21, pp. 45–59, Aug. 2020. Conference Name: IEEE Microwave Magazine.

[30] M. A. Castellanos-Beltran and K. W. Lehnert, "Widely tunable parametric amplifier based on a superconducting quantum interference device array resonator," Applied Physics Letters, vol. 91, p. 083509, Aug. 2007.

[31] A. Roy and M. Devoret, "Introduction to parametric amplification of quantum signals with Josephson circuits," Comptes Rendus Physique, vol. 17, pp. 740–755, Aug. 2016.

[32] R. Vijay, M. H. Devoret, and I. Siddiqi, "Invited Review Article: The Josephson bifurcation amplifier," Review of Scientific Instruments, vol. 80, p. 111101, Nov. 2009.

[33] T. Yamamoto, K. Inomata, M. Watanabe, K. Matsuba, T. Miyazaki, W. D. Oliver, Y. Nakamura, and J. S. Tsai, "Flux-driven Josephson parametric amplifier," Applied Physics Letters, vol. 93, p. 042510, July 2008.

[34] K. Inomata, Z. Lin, K. Koshino, W. D. Oliver, J.-S. Tsai, T. Yamamoto, and Y. Nakamura, "Single microwave-photon detector using an artificial Λ-type three-level system," Nature Communications, vol. 7, p. 12303, July 2016. Number: 1 Publisher: Nature Publishing Group.

[35] A. Narla, S. Shankar, M. Hatridge, Z. Leghtas, K. M. Sliwa, E. Zalys-Geller, S. O. Mundhada, W. Pfaff, L. Frunzio, R. J. Schoelkopf, and M. H. Devoret, "Robust Concurrent Remote Entanglement Between Two Superconducting Qubits," Physical Review X, vol. 6, p. 031036, Sept. 2016.

[36] A. Poudel, R. McDermott, and M. G. Vavilov, "Quantum efficiency of a microwave photon detector based on a current-biased Josephson junction," Physical Review B, vol. 86, p. 174506, Nov. 2012. Publisher: American Physical Society.

[37] E. D. Walsh, D. K. Efetov, G.-H. Lee, M. Heuck, J. Crossno, T. A. Ohki, P. Kim, D. Englund, and K. C. Fong, "Graphene-Based Josephson-Junction Single-Photon Detector," Physical Review Applied, vol. 8, p. 024022, Aug. 2017. Publisher: American Physical Society.

[38] Y. Nakamura, Y. A. Pashkin, T. Yamamoto, and J.-S. Tsai, "Charge echo in a cooper-pair box," Physical review letters, vol. 88, no. 4, p. 047901, 2002.

[39] Y. Nakamura, Y. A. Pashkin, and J. Tsai, "Coherent control of macroscopic quantum states in a single-cooper-pair box," nature, vol. 398, no. 6730, pp. 786–788, 1999.

[40] J. Koch, T. M. Yu, J. Gambetta, A. A. Houck, D. I. Schuster, J. Majer, A. Blais, M. H. Devoret, S. M. Girvin, and R. J. Schoelkopf, "Charge-insensitive qubit design derived from the Cooper pair box," Physical Review A, vol. 76, p. 042319, Oct. 2007.

[41] K. L. Geerlings, Improving coherence of superconducting qubits and resonators. Yale University, 2013.

[42] N. E. Frattini, U. Vool, S. Shankar, A. Narla, K. M. Sliwa, and M. H. Devoret, "3-wave mixing Josephson dipole element," Applied Physics Letters, vol. 110, p. 222603, May 2017. Publisher: American Institute of Physics.

[43] D. M. Pozar, Microwave engineering. John wiley & sons, 2011.

[44] M. J. Reagor, Superconducting cavities for circuit quantum electrodynamics. Yale University, 2016.

[45] T. Brecht, M. Reagor, Y. Chu, W. Pfaff, C. Wang, L. Frunzio, M. H. Devoret, and R. J. Schoelkopf, "Demonstration of superconducting micromachined cavities," Applied Physics Letters, vol. 107, no. 19, p. 192603, 2015.

[46] S. E. Nigg, H. Paik, B. Vlastakis, G. Kirchmair, S. Shankar, L. Frunzio, M. H. Devoret, R. J. Schoelkopf, and S. M. Girvin, "Black-Box Superconducting Circuit Quantization," Physical Review Letters, vol. 108, p. 240502, June 2012.

[47] Z. K. Minev, Z. Leghtas, S. O. Mundhada, L. Christakis, I. M. Pop, and M. H. Devoret, "Energy-participation quantization of Josephson circuits," arXiv:2010.00620 [cond-mat, physics:quant-ph], Oct. 2020. arXiv: 2010.00620.

[48] C. Wang, Y. Y. Gao, I. M. Pop, U. Vool, C. Axline, T. Brecht, R. W. Heeres, L. Frunzio, M. H. Devoret, G. Catelani, et al., "Measurement and control of quasiparticle dynamics in a superconducting qubit," Nature communications, vol. 5, no. 1, pp. 1–7, 2014.

[49] C. Wang, C. Axline, Y. Y. Gao, T. Brecht, Y. Chu, L. Frunzio, M. Devoret, and R. J. Schoelkopf, "Surface participation and dielectric loss in superconducting qubits," Applied Physics Letters, vol. 107, no. 16, p. 162601, 2015.

[50] A. P. M. Place, L. V. H. Rodgers, P. Mundada, B. M. Smitham, M. Fitzpatrick, Z. Leng, A. Premkumar, J. Bryon, S. Sussman, G. Cheng, T. Madhavan, H. K. Babla, B. Jaeck, A. Gyenis, N. Yao, R. J. Cava, N. P. de Leon, and A. A. Houck, "New

material platform for superconducting transmon qubits with coherence times exceeding 0.3 milliseconds," arXiv:2003.00024 [cond-mat, physics:physics, physics:quant-ph], Feb. 2020. arXiv: 2003.00024.

[51] J. M. Gambetta, J. M. Chow, and M. Steffen, "Building logical qubits in a superconducting quantum computing system," npj Quantum Information, vol. 3, no. 1, pp. 1–7, 2017.

[52] C. Wang, X. Li, H. Xu, Z. Li, J. Wang, Z. Yang, Z. Mi, X. Liang, T. Su, C. Yang, et al., "Towards practical quantum computers: transmon qubit with a lifetime approaching 0.5 milliseconds," npj Quantum Information, vol. 8, no. 1, pp. 1–6, 2022.

[53] G. Dolan, "Offset masks for lift-off photoprocessing," Applied Physics Letters, vol. 31, no. 5, pp. 337–339, 1977.

[54] J. Niemeyer and V. Kose, "Observation of large dc supercurrents at nonzero voltages in josephson tunnel junctions," Applied Physics Letters, vol. 29, no. 6, pp. 380–382, 1976.

[55] V. Ambegaokar and A. Baratoff, "Tunneling between superconductors," Physical Review Letters, vol. 10, no. 11, p. 486, 1963.

[56] A. Ferguson, R. Clark, et al., "Energy gap measurement of nanostructured aluminium thin films for single cooper-pair devices," Superconductor Science and Technology, vol. 21, no. 1, p. 015013, 2007.

[57] S. Gladchenko, D. Olaya, E. Dupont-Ferrier, B. Douçot, L. B. Ioffe, and M. E. Gershenson, "Superconducting nanocircuits for topologically protected qubits," Nature Physics, vol. 5, no. 1, pp. 48–53, 2009.

[58] M. Reed, L. DiCarlo, B. Johnson, L. Sun, D. Schuster, L. Frunzio, and R. Schoelkopf, "High-fidelity readout in circuit quantum electrodynamics using the jaynes-cummings nonlinearity," Physical review letters, vol. 105, no. 17, p. 173601, 2010.

[59] S. S. Elder, C. S. Wang, P. Reinhold, C. T. Hann, K. S. Chou, B. J. Lester, S. Rosenblum, L. Frunzio, L. Jiang, and R. J. Schoelkopf, "High-Fidelity Measurement of Qubits Encoded in Multilevel Superconducting Circuits," Physical Review X, vol. 10, p. 011001, Jan. 2020.

[60] M. Reed, Entanglement and quantum error correction with superconducting qubits. Lulu. com, 2013.

[61] F. Motzoi, J. M. Gambetta, P. Rebentrost, and F. K. Wilhelm, "Simple Pulses for Elimination of Leakage in Weakly Nonlinear Qubits," Physical Review Letters, vol. 103, p. 110501, Sept. 2009.

[62] E. Magesan, J. M. Gambetta, and J. Emerson, "Characterizing quantum gates via randomized benchmarking," Physical Review A, vol. 85, p. 042311, Apr. 2012.

[63] E. Knill, D. Leibfried, R. Reichle, J. Britton, R. B. Blakestad, J. D. Jost, C. Langer, R. Ozeri, S. Seidelin, and D. J. Wineland, "Randomized benchmarking of quantum gates," Physical Review A, vol. 77, p. 012307, Jan. 2008.

[64] E. Magesan, J. M. Gambetta, B. R. Johnson, C. A. Ryan, J. M. Chow, S. T. Merkel, M. P. da Silva, G. A. Keefe, M. B. Rothwell, T. A. Ohki, M. B. Ketchen, and M. Steffen, "Efficient Measurement of Quantum Gate Error by Interleaved Randomized Benchmarking," Physical Review Letters, vol. 109, p. 080505, Aug. 2012.

[65] C. Huang, D. Ding, F. Wu, L. Kong, F. Zhang, X. Ni, Y. Shi, H.-h. Zhao, and J. Chen, "Towards ultra-high fidelity quantum operations: Sqisw gate as a native two-qubit gate," arXiv preprint arXiv:2105.06074, 2021.

[66] P. Del'Haye, A. Schliesser, O. Arcizet, T. Wilken, R. Holzwarth, and T. J. Kippenberg, "Optical frequency comb generation from a monolithic microresonator," Nature, vol. 450, pp. 1214–1217, Dec. 2007. Bandiera_abtest: a Cg_type: Nature Research Journals Number: 7173 Primary_atype: Research Publisher: Nature Publishing Group.

[67] P. Del'Haye, O. Arcizet, A. Schliesser, R. Holzwarth, and T. J. Kippenberg, "Full Stabilization of a Microresonator-Based Optical Frequency Comb," Physical Review Letters, vol. 101, p. 053903, July 2008. Publisher: American Physical Society.

[68] J. S. Levy, A. Gondarenko, M. A. Foster, A. C. Turner-Foster, A. L. Gaeta, and M. Lipson, "CMOS-compatible multiple-wavelength oscillator for on-chip optical interconnects," Nature Photonics, vol. 4, pp. 37–40, Jan. 2010. Bandiera_abtest: a Cg_type: Nature Research Journals Number: 1 Primary_atype: Research Publisher: Nature Publishing Group.

[69] T. Herr, K. Hartinger, J. Riemensberger, C. Y. Wang, E. Gavartin, R. Holzwarth, M. L. Gorodetsky, and T. J. Kippenberg, "Universal formation dynamics and noise of Kerr-frequency combs in microresonators," Nature Photonics, vol. 6, pp. 480–487, July 2012. Bandiera_abtest: a Cg_type: Nature Research Journals Number: 7 Primary_atype: Research Publisher: Nature Publishing Group Subject_term: Frequency combs;Microresonators;Optical physics Subject_term_id: frequency-combs;microresonators;optical-physics.

[70] T. Herr, V. Brasch, J. D. Jost, C. Y. Wang, N. M. Kondratiev, M. L. Gorodetsky, and T. J. Kippenberg, "Temporal solitons in optical microresonators," Nature Photonics, vol. 8, pp. 145–152, Feb. 2014. Bandiera_abtest: a Cg_type: Nature Research Journals Number: 2 Primary_atype: Research Publisher: Nature Publishing Group Subject_term: Frequency combs;Nonlinear optics;Solitons Subject_term_id: frequency-combs;nonlinear-optics;solitons.

[71] T. J. Kippenberg, A. L. Gaeta, M. Lipson, and M. L. Gorodetsky, "Dissipative Kerr solitons in optical microresonators," Science, vol. 361, p. eaan8083, Aug. 2018. Publisher: American Association for the Advancement of Science.

[72] A. L. Gaeta, M. Lipson, and T. J. Kippenberg, "Photonic-chip-based frequency combs," Nature Photonics, vol. 13, pp. 158–169, Mar. 2019.

[73] B. Stern, X. Ji, Y. Okawachi, A. L. Gaeta, and M. Lipson, "Battery-operated integrated frequency comb generator," Nature, vol. 562, pp. 401–405, Oct. 2018. Bandiera_abtest: a Cg_type: Nature Research Journals Number: 7727 Primary_atype: Research Publisher: Nature Publishing Group Subject_term: Frequency combs;Mode-locked lasers;Nanophotonics and plasmonics;Nonlinear optics;Solitons Subject_term_id: frequency-combs;mode-locked-lasers;nanophotonics-and-plasmonics;nonlinear-optics;solitons.

[74] M. Kues, C. Reimer, J. M. Lukens, W. J. Munro, A. M. Weiner, D. J. Moss, and R. Morandotti, "Quantum optical microcombs," Nature Photonics, vol. 13, pp. 170–179, Mar. 2019. Bandiera_abtest: a Cg_type: Nature Research Journals Number: 3 Primary_atype: Reviews Publisher: Nature Publishing Group Subject_term: Fibre optics and optical communications;Frequency combs;Integrated optics;Quantum optics;Silicon photonics Subject_term_id: fibre-optics-and-optical-communications;frequency-combs;integrated-optics;quantum-optics;silicon-photonics.

[75] R. P. Erickson, M. R. Vissers, M. Sandberg, S. R. Jefferts, and D. P. Pappas, "Frequency Comb Generation in Superconducting Resonators," Physical Review Letters, vol. 113, p. 187002, Oct. 2014.

[76] N. R. Newbury and W. C. Swann, "Low-noise fiber-laser frequency combs (Invited)," JOSA B, vol. 24, pp. 1756–1770, Aug. 2007. Publisher: Optical Society of America.

[77] N. Picqué and T. W. Hänsch, "Frequency comb spectroscopy," Nature Photonics, vol. 13, pp. 146–157, Mar. 2019.

[78] S. Khan and H. E. Türeci, "Frequency Combs in a Lumped-Element Josephson-Junction Circuit," Physical Review Letters, vol. 120, p. 153601, Apr. 2018.

[79] I. Siddiqi, R. Vijay, F. Pierre, C. M. Wilson, M. Metcalfe, C. Rigetti, L. Frunzio, and M. H. Devoret, "RF-Driven Josephson Bifurcation Amplifier for Quantum Measurement," Physical Review Letters, vol. 93, p. 207002, Nov. 2004. Publisher: American Physical Society.

[80] L. Planat, R. Dassonneville, J. P. Martínez, F. Foroughi, O. Buisson, W. Hasch-Guichard, C. Naud, R. Vijay, K. Murch, and N. Roch, "Understanding the Saturation Power of Josephson Parametric Amplifiers Made from SQUID Arrays," Physical Review Applied, vol. 11, p. 034014, Mar. 2019. Publisher: American Physical Society.

[81] P. D. Drummond and C. W. Gardiner, "Generalised P-representations in quantum optics," Journal of Physics A: Mathematical and General, vol. 13, pp. 2353–2368, July 1980.

[82] H. J. Carmichael, Statistical Methods in Quantum Optics 1 - Master Equations and Fokker-Planck Equations | Howard J. Carmichael | Springer. Springer, 2002.

[83] H. Haken, "At least one Lyapunov exponent vanishes if the trajectory of an attractor does not contain a fixed point," Physics Letters A, vol. 94, pp. 71–72, Feb. 1983.

[84] J. Clarke and A. I. Braginski, The SQUID Handbook. Weinheim: Wiley-VCH, 2003.

[85] M. D. Hutchings, J. B. Hertzberg, Y. Liu, N. T. Bronn, G. A. Keefe, M. Brink, J. M. Chow, and B. L. T. Plourde, "Tunable Superconducting Qubits with Flux-Independent Coherence," Physical Review Applied, vol. 8, p. 044003, Oct. 2017.

[86] H. Paik, D. I. Schuster, L. S. Bishop, G. Kirchmair, G. Catelani, A. P. Sears, B. R. Johnson, M. J. Reagor, L. Frunzio, L. I. Glazman, S. M. Girvin, M. H. Devoret, and R. J. Schoelkopf, "Observation of High Coherence in Josephson Junction Qubits Measured in a Three-Dimensional Circuit QED Architecture," Physical Review Letters, vol. 107, p. 240501, Dec. 2011.

[87] M. J. Ablowitz, B. Ilan, and S. T. Cundiff, "Noise-induced linewidth in frequency combs," Optics Letters, vol. 31, pp. 1875–1877, June 2006. Publisher: Optical Society of America.

[88] C. Navarrete-Benlloch, T. Weiss, S. Walter, and G. J. de Valcárcel, "General Linearized Theory of Quantum Fluctuations around Arbitrary Limit Cycles," Physical Review Letters, vol. 119, p. 133601, Sept. 2017.

[89] N. Coluccelli, M. Cassinerio, A. Gambetta, P. Laporta, and G. Galzerano, "Frequency-noise measurements of optical frequency combs by multiple fringe-side discriminator," Scientific Reports, vol. 5, pp. 1–10, Nov. 2015. Number: 1 Publisher: Nature Publishing Group.

[90] M. P. da Silva, D. Bozyigit, A. Wallraff, and A. Blais, "Schemes for the observation of photon correlation functions in circuit QED with linear detectors," Physical Review A, vol. 82, p. 043804, Oct. 2010.

[91] O. Maillet, F. Vavrek, A. D. Fefferman, O. Bourgeois, and E. Collin, "Classical decoherence in a nanomechanical resonator," New Journal of Physics, vol. 18, p. 073022, July 2016.

[92] M. Aspelmeyer, T. J. Kippenberg, and F. Marquardt, "Cavity optomechanics," Reviews of Modern Physics, vol. 86, pp. 1391–1452, Dec. 2014.

[93] C. Eichler and A. Wallraff, "Controlling the dynamic range of a Josephson parametric amplifier," EPJ Quantum Technology, vol. 1, p. 2, Dec. 2014.

[94] A. Demir, A. Mehrotra, and J. Roychowdhury, "Phase noise in oscillators: a unifying theory and numerical methods for characterization," IEEE Transactions on Circuits and Systems I: Fundamental Theory and Applications, vol. 47, pp. 655–674, May 2000. Conference Name: IEEE Transactions on Circuits and Systems I: Fundamental Theory and Applications.

[95] P. D. Drummond and P. Deuar, "Quantum dynamics with stochastic gauge simulations," J. Opt. B: Quantum Semiclass. Opt., vol. 5, pp. S281–S289, June 2003.

[96] C. W. Gardiner and M. J. Collett, "Input and output in damped quantum systems: Quantum stochastic differential equations and the master equation," Physical Review A, vol. 31, pp. 3761–3774, June 1985.

[97] J. Bylander, S. Gustavsson, F. Yan, F. Yoshihara, K. Harrabi, G. Fitch, D. G. Cory, Y. Nakamura, J.-S. Tsai, and W. D. Oliver, "Noise spectroscopy through dynamical decoupling with a superconducting flux qubit," Nature Physics, vol. 7, pp. 565–570, July 2011.

[98] F. Yan, S. Gustavsson, J. Bylander, X. Jin, F. Yoshihara, D. G. Cory, Y. Nakamura, T. P. Orlando, and W. D. Oliver, "Rotating-frame relaxation as a noise spectrum analyser of a superconducting qubit undergoing driven evolution," Nature Communications, vol. 4, p. 2337, Dec. 2013.

[99] G. Andersson, B. Suri, L. Guo, T. Aref, and P. Delsing, "Non-exponential decay of a giant artificial atom," Nature Physics, vol. 15, pp. 1123–1127, Nov 2019.

[100] A. Gilchrist, C. W. Gardiner, and P. D. Drummond, "Positive p representation: Application and validity," Phys. Rev. A, vol. 55, pp. 3014–3032, Apr 1997.

[101] H. Paik, D. I. Schuster, L. S. Bishop, G. Kirchmair, G. Catelani, A. P. Sears, B. R. Johnson, M. J. Reagor, L. Frunzio, L. I. Glazman, S. M. Girvin, M. H. Devoret, and R. J. Schoelkopf, "Observation of high coherence in josephson junction qubits measured in a three-dimensional circuit qed architecture," Phys. Rev. Lett., vol. 107, p. 240501, Dec 2011.

[102] A. Essig, Q. Ficheux, T. Peronnin, N. Cottet, R. Lescanne, A. Sarlette, P. Rouchon, Z. Leghtas, and B. Huard, "Multiplexed photon number measurement," arXiv:2001.03217 [cond-mat, physics:quant-ph], Jan. 2020. arXiv: 2001.03217.

[103] F. Lecocq, L. Ranzani, G. A. Peterson, K. Cicak, R. W. Simmonds, J. D. Teufel, and J. Aumentado, "Nonreciprocal Microwave Signal Processing with a Field-Programmable Josephson Amplifier," Physical Review Applied, vol. 7, p. 024028, Feb. 2017. Publisher: American Physical Society.

[104] A. Metelmann and H. E. Türeci, "Nonreciprocal signal routing in an active quantum network," Phys. Rev. A, vol. 97, p. 043833, Apr 2018.

[105] V. Sivak, N. Frattini, V. Joshi, A. Lingenfelter, S. Shankar, and M. Devoret, "Kerr-Free Three-Wave Mixing in Superconducting Quantum Circuits," Physical Review Applied, vol. 11, p. 054060, May 2019. Publisher: American Physical Society.

[106] F. Arute, K. Arya, R. Babbush, D. Bacon, J. C. Bardin, R. Barends, R. Biswas, S. Boixo, F. G. Brandao, D. A. Buell, et al., "Quantum supremacy using a programmable superconducting processor," Nature, vol. 574, no. 7779, pp. 505–510, 2019.

[107] N. LaRacuente, K. N. Smith, P. Imany, K. L. Silverman, and F. T. Chong, "Short-range microwave networks to scale superconducting quantum computation," arXiv preprint arXiv:2201.08825, 2022.

[108] C.-W. Chou, H. De Riedmatten, D. Felinto, S. V. Polyakov, S. J. Van Enk, and H. J. Kimble, "Measurement-induced entanglement for excitation stored in remote atomic ensembles," Nature, vol. 438, no. 7069, pp. 828–832, 2005.

[109] D. L. Moehring, P. Maunz, S. Olmschenk, K. C. Younge, D. N. Matsukevich, L.-M. Duan, and C. Monroe, "Entanglement of single-atom quantum bits at a distance," Nature, vol. 449, no. 7158, pp. 68–71, 2007.

[110] S. Ritter, C. Nölleke, C. Hahn, A. Reiserer, A. Neuzner, M. Uphoff, M. Mücke, E. Figueroa, J. Bochmann, and G. Rempe, "An elementary quantum network of single atoms in optical cavities," Nature, vol. 484, no. 7393, pp. 195–200, 2012.

[111] J. Hofmann, M. Krug, N. Ortegel, L. Gérard, M. Weber, W. Rosenfeld, and H. Weinfurter, "Heralded entanglement between widely separated atoms," Science, vol. 337, no. 6090, pp. 72–75, 2012.

[112] H. Bernien, B. Hensen, W. Pfaff, G. Koolstra, M. S. Blok, L. Robledo, T. Taminiau, M. Markham, D. J. Twitchen, L. Childress, et al., "Heralded entanglement between solid-state qubits separated by three metres," Nature, vol. 497, no. 7447, pp. 86–90, 2013.

[113] S. Wengerowsky, S. K. Joshi, F. Steinlechner, J. R. Zichi, S. M. Dobrovolskiy, R. van der Molen, J. W. Los, V. Zwiller, M. A. Versteegh, A. Mura, et al., "Entanglement distribution over a 96-km-long submarine optical fiber," Proceedings of the National Academy of Sciences, vol. 116, no. 14, pp. 6684–6688, 2019.

[114] Y. Yu, F. Ma, X.-Y. Luo, B. Jing, P.-F. Sun, R.-Z. Fang, C.-W. Yang, H. Liu, M.-Y. Zheng, X.-P. Xie, et al., "Entanglement of two quantum memories via fibres over dozens of kilometres," Nature, vol. 578, no. 7794, pp. 240–245, 2020.

[115] N. Roch, M. E. Schwartz, F. Motzoi, C. Macklin, R. Vijay, A. W. Eddins, A. N. Korotkov, K. B. Whaley, M. Sarovar, and I. Siddiqi, "Observation of measurement-

induced entanglement and quantum trajectories of remote superconducting qubits," Physical review letters, vol. 112, no. 17, p. 170501, 2014.

[116] C. Dickel, J. Wesdorp, N. Langford, S. Peiter, R. Sagastizabal, A. Bruno, B. Criger, F. Motzoi, and L. DiCarlo, "Chip-to-chip entanglement of transmon qubits using engineered measurement fields," Physical Review B, vol. 97, no. 6, p. 064508, 2018.

[117] P. Kurpiers, M. Pechal, B. Royer, P. Magnard, T. Walter, J. Heinsoo, Y. Salathé, A. Akin, S. Storz, J.-C. Besse, et al., "Quantum communication with time-bin encoded microwave photons," Physical Review Applied, vol. 12, no. 4, p. 044067, 2019.

[118] C. Monroe, R. Raussendorf, A. Ruthven, K. R. Brown, P. Maunz, L.-M. Duan, and J. Kim, "Large-scale modular quantum-computer architecture with atomic memory and photonic interconnects," Physical Review A, vol. 89, p. 022317, Feb. 2014. Publisher: American Physical Society.

[119] N. M. Linke, D. Maslov, M. Roetteler, S. Debnath, C. Figgatt, K. A. Landsman, K. Wright, and C. Monroe, "Experimental comparison of two quantum computing architectures," Proceedings of the National Academy of Sciences, vol. 114, pp. 3305–3310, Mar. 2017. Publisher: National Academy of Sciences Section: Physical Sciences.

[120] C. J. Axline, L. D. Burkhart, W. Pfaff, M. Zhang, K. Chou, P. Campagne-Ibarcq, P. Reinhold, L. Frunzio, S. M. Girvin, L. Jiang, M. H. Devoret, and R. J. Schoelkopf, "On-demand quantum state transfer and entanglement between remote microwave cavity memories," Nature Physics, vol. 14, pp. 705–710, July 2018.

[121] P. Campagne-Ibarcq, E. Zalys-Geller, A. Narla, S. Shankar, P. Reinhold, L. Burkhart, C. Axline, W. Pfaff, L. Frunzio, R. J. Schoelkopf, and M. H. Devoret, "Deterministic Remote Entanglement of Superconducting Circuits through Microwave Two-Photon Transitions," Physical Review Letters, vol. 120, p. 200501, May 2018.

[122] P. Kurpiers, P. Magnard, T. Walter, B. Royer, M. Pechal, J. Heinsoo, Y. Salathé, A. Akin, S. Storz, J.-C. Besse, S. Gasparinetti, A. Blais, and A. Wallraff, "Deterministic quantum state transfer and remote entanglement using microwave photons," Nature, vol. 558, pp. 264–267, June 2018.

[123] N. Leung, Y. Lu, S. Chakram, R. K. Naik, N. Earnest, R. Ma, K. Jacobs, A. N. Cleland, and D. I. Schuster, "Deterministic bidirectional communication and remote entanglement generation between superconducting qubits," npj Quantum Information, vol. 5, pp. 1–5, Feb. 2019. Bandiera_abtest: a Cc_license_type: cc_by Cg_type: Nature

Research Journals Number: 1 Primary_atype: Research Publisher: Nature Publishing Group Subject_term: Quantum information;Qubits;Single photons and quantum effects;Superconducting devices Subject_term_id: quantum-information;qubits;single-photons-and-quantum-effects;superconducting-devices.

[124] P. Magnard, S. Storz, P. Kurpiers, J. Schär, F. Marxer, J. Lütolf, T. Walter, J.-C. Besse, M. Gabureac, K. Reuer, et al., "Microwave quantum link between superconducting circuits housed in spatially separated cryogenic systems," Physical Review Letters, vol. 125, no. 26, p. 260502, 2020.

[125] L. D. Burkhart, J. D. Teoh, Y. Zhang, C. J. Axline, L. Frunzio, M. Devoret, L. Jiang, S. Girvin, and R. Schoelkopf, "Error-detected state transfer and entanglement in a superconducting quantum network," PRX Quantum, vol. 2, no. 3, p. 030321, 2021.

[126] S. Hazra, A. Bhattacharjee, M. Chand, K. V. Salunkhe, S. Gopalakrishnan, M. P. Patankar, and R. Vijay, "Long-range connectivity in a superconducting quantum processor using a ring resonator," arXiv preprint arXiv:2012.09463, 2020.

[127] Y. Zhong, H.-S. Chang, A. Bienfait, E. Dumur, M.-H. Chou, C. R. Conner, J. Grebel, R. G. Povey, H. Yan, D. I. Schuster, and A. N. Cleland, "Deterministic multi-qubit entanglement in a quantum network," Nature, vol. 590, pp. 571–575, Feb. 2021. Number: 7847 Publisher: Nature Publishing Group.

[128] A. J. Sirois, M. Castellanos-Beltran, M. DeFeo, L. Ranzani, F. Lecocq, R. Simmonds, J. Teufel, and J. Aumentado, "Coherent-state storage and retrieval between superconducting cavities using parametric frequency conversion," Applied Physics Letters, vol. 106, no. 17, p. 172603, 2015.

[129] D. C. McKay, S. Filipp, A. Mezzacapo, E. Magesan, J. M. Chow, and J. M. Gambetta, "Universal gate for fixed-frequency qubits via a tunable bus," Physical Review Applied, vol. 6, no. 6, p. 064007, 2016.

[130] Y. Sung, L. Ding, J. Braumüller, A. Vepsäläinen, B. Kannan, M. Kjaergaard, A. Greene, G. O. Samach, C. McNally, D. Kim, et al., "Realization of high-fidelity cz and z z-free iswap gates with a tunable coupler," Physical Review X, vol. 11, no. 2, p. 021058, 2021.

[131] B. Vlastakis, G. Kirchmair, Z. Leghtas, S. E. Nigg, L. Frunzio, S. M. Girvin, M. Mirrahimi, M. H. Devoret, and R. J. Schoelkopf, "Deterministically Encoding Quantum

Information Using 100-Photon Schrödinger Cat States," Science, vol. 342, pp. 607–610, Nov. 2013. Publisher: American Association for the Advancement of Science Section: Report.

[132] M. H. Michael, M. Silveri, R. T. Brierley, V. V. Albert, J. Salmilehto, L. Jiang, and S. M. Girvin, "New Class of Quantum Error-Correcting Codes for a Bosonic Mode," Physical Review X, vol. 6, p. 031006, July 2016. Publisher: American Physical Society.

[133] D. Gottesman, A. Kitaev, and J. Preskill, "Encoding a qubit in an oscillator," Physical Review A, vol. 64, p. 012310, June 2001. Publisher: American Physical Society.

[134] N. Bergeal, R. Vijay, V. E. Manucharyan, I. Siddiqi, R. J. Schoelkopf, S. M. Girvin, and M. H. Devoret, "Analog information processing at the quantum limit with a Josephson ring modulator," Nature Physics, vol. 6, pp. 296–302, Apr. 2010. Bandiera_abtest: a Cg_type: Nature Research Journals Number: 4 Primary_atype: Research Publisher: Nature Publishing Group.

[135] R. C. Bialczak, M. Ansmann, M. Hofheinz, M. Lenander, E. Lucero, M. Neeley, A. D. O'Connell, D. Sank, H. Wang, M. Weides, J. Wenner, T. Yamamoto, A. N. Cleland, and J. M. Martinis, "Fast Tunable Coupler for Superconducting Qubits," Physical Review Letters, vol. 106, p. 060501, Feb. 2011. Publisher: American Physical Society.

[136] J. Kelly, R. Barends, B. Campbell, Y. Chen, Z. Chen, B. Chiaro, A. Dunsworth, A. G. Fowler, I.-C. Hoi, E. Jeffrey, A. Megrant, J. Mutus, C. Neill, P. J. J. O'Malley, C. Quintana, P. Roushan, D. Sank, A. Vainsencher, J. Wenner, T. C. White, A. N. Cleland, and J. M. Martinis, "Optimal Quantum Control Using Randomized Benchmarking," Physical Review Letters, vol. 112, p. 240504, June 2014.

[137] N. Frattini, V. Sivak, A. Lingenfelter, S. Shankar, and M. Devoret, "Optimizing the nonlinearity and dissipation of a SNAIL parametric amplifier for dynamic range," Physical Review Applied, vol. 10, no. 5, p. 054020, 2018.

[138] C. Liu, T.-C. Chien, M. Hatridge, and D. Pekker, "Optimizing Josephson-ring-modulator-based Josephson parametric amplifiers via full Hamiltonian control," Physical Review A, vol. 101, p. 042323, Apr. 2020.

[139] W. Pfaff, C. J. Axline, L. D. Burkhart, U. Vool, P. Reinhold, L. Frunzio, L. Jiang, M. H. Devoret, and R. J. Schoelkopf, "Controlled release of multiphoton quantum states from a microwave cavity memory," Nature Physics, vol. 13, pp. 882–887, Sept. 2017.

[140] M. E. J. Newman and G. T. Barkema, Monte Carlo Methods in Statistical Physics. Clarendon Press, 1999. Google-Books-ID: KKL2nQEACAAJ.

[141] P. Young, "Everything you wanted to know about Data Analysis and Fitting but were afraid to ask," arXiv:1210.3781 [cond-mat, physics:physics], Oct. 2014. arXiv: 1210.3781.

[142] D. I. Schuster, A. A. Houck, J. A. Schreier, A. Wallraff, J. M. Gambetta, A. Blais, L. Frunzio, J. Majer, B. Johnson, M. H. Devoret, S. M. Girvin, and R. J. Schoelkopf, "Resolving photon number states in a superconducting circuit," Nature, vol. 445, pp. 515–518, Feb. 2007.

[143] H.-P. Breuer, F. Petruccione, et al., The theory of open quantum systems. Oxford University Press on Demand, 2002.

[144] J. R. Johansson, P. D. Nation, and F. Nori, "QuTiP 2: A Python framework for the dynamics of open quantum systems," Computer Physics Communications, vol. 184, pp. 1234–1240, Apr. 2013.

[145] D. J. Parker, M. Savytskyi, W. Vine, A. Laucht, T. Duty, A. Morello, A. L. Grimsmo, and J. J. Pla, "A near-ideal degenerate parametric amplifier," arXiv:2108.10471 [cond-mat, physics:quant-ph], Aug. 2021. arXiv: 2108.10471.

[146] A. Petrescu, C. L. Calonnec, C. Leroux, A. Di Paolo, P. Mundada, S. Sussman, A. Vrajitoarea, A. A. Houck, and A. Blais, "Accurate methods for the analysis of strong-drive effects in parametric gates," arXiv preprint arXiv:2107.02343, 2021.